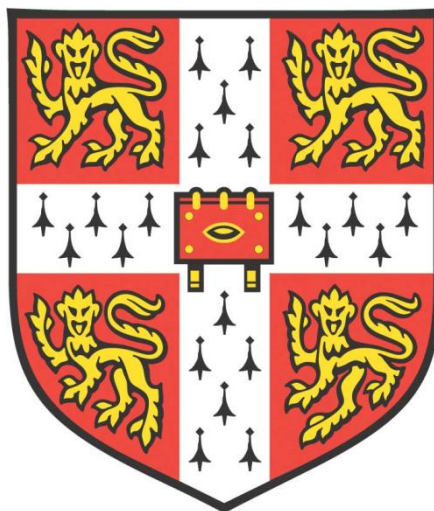


POLYMER WAVEGUIDE BASED OPTICAL INTERCONNECTS FOR HIGH-SPEED ON-BOARD COMMUNICATIONS



JIAN CHEN

JESUS COLLEGE

DEPARTMENT OF ENGINEERING

UNIVERSITY OF CAMBRIDGE

THIS DISSERTATION IS SUBMITTED FOR THE DEGREE OF DOCTOR OF PHILOSOPHY

JUNE 2016

To Shruti, my mother and my parents-in-law

DECLARATION

This dissertation is the result of my own work and includes nothing which is the outcome of work done in collaboration except where specifically indicated in the text. It has not been previously submitted, in part or whole, to any university or institution for any degree, diploma, or other qualification.

In accordance with the Department of Engineering guidelines, this thesis does not exceed 65,000 words, and it contains less than 150 figures.

Jian Chen
Cambridge, June 2016

ACKNOWLEDGEMENTS

First and foremost, I would like to thank my supervisor Prof. Ian H. White for providing me with consistent encouragement, support and guidance throughout the period of my PhD study, without which this thesis would not be possible. His comprehensive knowledge and vision have enabled me to develop a deep understanding of the subject and enlightened me with ideas, whilst his attitude towards details has taught me patience and precision in research.

I would also thank my academic adviser Prof. Richard V. Penty for his advice and insightful suggestions throughout this work. Special thanks must also go to my industrial adviser Dr. David Cunningham. I have particularly benefited from bi-weekly discussions with him from which I not only got to know the most up-to-date industry trends but also gained extensive knowledge in all aspects of optical communications.

I am also very grateful to all the members of the Centre for Photonic Systems (CPS) group who have shared their knowledge with me as well as instructed me with the use of laboratory equipment. Particularly, I would thank Dr. Nikos Bamiedakis, for helping me learn about optical waveguides from scratch, for all the fruitful discussions and for providing great advice in the waveguide simulation and help in laboratory equipment. I also thank Adrian Wonfor for offering technical support on FIMMWAVE software, laboratory equipment and any computer related problems. I would also like to thank Prof. Peter Vasil'ev for sharing his practical experience and knowledge in the ultrafast laser and autocorrelator. My thanks also go to Dr. Jonathan Ingham, Dr. Jinlong Wei, Dr. Jiannan Zhu and Xin Li for the technical discussions and kind help on the simulation of optical communication systems.

I would also wish to acknowledge Dow Corning Corporation for supporting the project and providing polymer waveguide samples. It has been an invaluable opportunity to collaborate with researchers from Dow Corning, and special thanks must go to Dr. Terry V. Clapp, Brandon W. Swatowski and Ken Weidner for their support and useful discussions.

I would also like to show my appreciation to Avago Technologies for providing scholarship that supported my life and education in Cambridge; Great Britain-China Student Awards for partial financial support of my living; Jesus College Research Grants, Department of Engineering, Cambridge Philosophical Society and IET Travel Awards for providing me with generous travel grants for my attendance of international conferences and Jesus College

for offering me Supplementary Hardship Fund for the last few months of my stay at Cambridge and comfortable accommodation throughout my PhD studies.

Finally and faithfully, I would like to give my deepest gratitude to my wife Shruti for her love and support, and my mother and my parents-in-law for their consistent encouragement for all these years. Without them the completion of my doctoral study would not have been possible.

ABSTRACT

This dissertation presents a study of multimode polymer waveguide technology for use in board-level communication links for future data centres and supercomputers. The motivation for this work comes from the severe interconnection bandwidth challenges faced by the conventional electrical interconnections technology and the potential performance advantages of optical interconnections. This thesis presents the work to address the bandwidth bottleneck by developing high-bandwidth multimode polymer waveguides. The use of multimode waveguides provides relaxed alignment tolerances enabling low-cost assembly tools. Siloxane polymer materials developed by Dow Corning Corporation are chosen to form the waveguides in this work due to their favourable optical properties (optical losses as low as 0.03 dB/cm and the ability to withstand temperatures in excess of 350 °C) that allow the waveguides to be directly integrated on printed circuits boards (PCBs) using conventional manufacturing processes. Useful design rules for the use of the multimode polymer waveguides are theoretically derived while the bandwidth-length products are investigated under various launch conditions. Frequency-domain measurements and ultra-short pulse measurements are then carried out to investigate the bandwidth performance of the polymer waveguides under different launch conditions and with lateral misalignments. The instrument-limited frequency-domain measurements show that these waveguides exhibit bandwidth-length products (BLPs) of at least 35 GHz×m, while the pulse broadening measurements reveal the actual BLPs to be in excess of 70 GHz×m under a 50 μm multimode-fibre (MMF) launch and 100 GHz×m for a restricted launch across a wide range of input offsets ($>\pm 10$ μm). This shows the potential for data transmission rates of 100 Gb/s and beyond over a single waveguide channel. A theoretical model is developed using the measured refractive index profile and good agreement with the above experimental results is found. The effects of graded refractive index profiles on the performance of waveguide components (bends, crossings) are also investigated, demonstrating that appropriate refractive index engineering can provide enhanced waveguide loss performance while exhibiting adequate bandwidth. Waveguide bends with excess loss below 1 dB for a radius >6 mm, crossings with loss less than 0.02 dB/crossing while exhibiting adequate link bandwidth (>47 GHz×m) can be achieved for a MMF launch. On this basis, advanced modulation formats are investigated across the board-level waveguide links for further increasing the on-board data rates. Record NRZ-based 40 Gb/s and 56 Gb/s PAM-4 based data transmission over a 1 m long multimode polymer spiral waveguide are theoretically and experimentally demonstrated.

LIST OF PUBLICATIONS

Journal Papers:

- [1] **J. Chen**, N. Bamiedakis, P. Vasil'ev, T. Edwards, C. Brown, R. Penty, and I. White, "High-Bandwidth and Large Coupling Tolerance Graded-Index Multimode Polymer Waveguides for On-board High-Speed Optical Interconnects," *Journal of Lightwave Technology*, vol. 34, no. 12, pp. 2934–2940, November 2015. [Invited paper]
- [2] N. Bamiedakis, **J. Chen**, P. Westbergh, J. S. Gustavsson, A. Larsson, R. V. Penty, and I. H. White, "40 Gb/s Data Transmission Over a 1 m Long Multimode Polymer Spiral Waveguide for Board-Level Optical Interconnects," *Journal of Lightwave Technology*, vol. 33, no. 4, pp. 882–888, November 2014.
- [3] N. Bamiedakis, **J. Chen**, R. V. Penty, and I. H. White, "Bandwidth Studies on Multimode Polymer Waveguides for ≥ 25 Gb/s Optical Interconnects," *IEEE Photonics Technology Letters*, vol. 26, no. 20, pp. 2004–2007, July 2014.

Conference Papers:

- [1] **J. Chen**, N. Bamiedakis, P. Vasil'ev, R. V. Penty, and I. H. White, "Low-Loss and High-Bandwidth Multimode Polymer Waveguide Components Using Refractive Index Engineering," in *Conference on Lasers and Electro-Optics (CLEO)*, p. SM2G.7, San Jose, USA, June 2016.
- [2] **J. Chen**, N. Bamiedakis, P. Vasil'ev, R. V. Penty, and I. H. White, "Bandwidth Enhancement in Multimode Polymer Waveguides Using Waveguide Layout for Optical Printed Circuit Boards," in *Optical Fiber Communication Conference and Exposition (OFC)*, p. W1E.3, Anaheim, USA, March 2016.
- [3] N. Bamiedakis, **J. Chen**, R. V. Penty, and I. H. White, "High-Bandwidth and Low-Loss Multimode Polymer Waveguides and Waveguide Components for High-Speed Board-Level Optical Interconnects," in *Photonics West conference, Proceeding of SPIE*, vol. 9753, pp. 975304–1–9, San Francisco, USA, February 2016. [Invited paper]
- [4] **J. Chen**, N. Bamiedakis, P. Vasil'ev, R. V. Penty, and I. H. White, "Restricted Launch Polymer Multimode Waveguides for Board-level Optical Interconnects with > 100 GHz \times m Bandwidth and Large Alignment Tolerance," in *Asia Communications and Photonics Conference (ACP)*, p. AM3A. 5, Hong Kong, China, November 2015.
- [5] **J. Chen**, N. Bamiedakis, P. Vasil'ev, T. J. Edwards, C. T. A. Brown, R. V. Penty, and

- I. H. White, “Graded-Index Polymer Multimode Waveguides for 100 Gb/s Board-Level Data Transmission,” in *European Conference on Optical Communication (ECOC)*, no. 0613, Valencia, Spain, September 2015.
- [6] N. Bamiedakis, J. Wei, **J. Chen**, P. Westbergh, A. Larsson, R. Penty, and I. White, “56 Gb/s PAM-4 Data Transmission Over a 1 m Long Multimode Polymer Interconnect,” in *Conference on Lasers and Electro-optics (CLEO)*, p. STu4F.5, San Jose, USA, May 2015.
- [7] **J. Chen**, N. Bamiedakis, T. J. Edwards, C. T. A. Brown, R. V. Penty, and I. H. White, “Dispersion Studies on Multimode Polymer Spiral Waveguides for Board-Level Optical Interconnects,” in *Optical Interconnects Conference (OIC)*, p. MD2, San Diego, USA, April 2015.
- [8] R. V. Penty, N. Bamiedakis, **J. Chen**, and I. H. White, “Bandwidth Studies on Multimode Polymer Waveguides for High-Speed Board-Level Optical Interconnects,” in *Photonics West conference, Proceeding of SPIE*, pp. 9368–2, San Francisco, USA, February 2015. [Invited paper]
- [9] N. Bamiedakis, **J. Chen**, R. V. Penty, I. H. White, P. Westbergh, and A. Larsson, “40 Gb/s Data Transmission over a 1 m Long Multimode Polymer Spiral Waveguide,” in *European Conference on Optical Communication (ECOC)*, p. P.4.7, Cannes, France, September 2014.
- [10] **J. Chen**, N. Bamiedakis, R. V. Penty, I. H. White, P. Westbergh, and A. Larsson, “Bandwidth and Offset Launch Investigations on a 1.4 m Multimode Polymer Spiral Waveguide,” in *European Conference on Integrated Optics (ECIO)*, p. P027, Nice, France, June 2014.
- [11] **J. Chen**, N. Bamiedakis, R. V. Penty, I. H. White, P. Westbergh, and A. Larsson, “Bandwidth Studies on a 1.4 m Long Multimode Polymer Spiral Waveguide,” in *Semiconductor and Integrated Optoelectronics Conference (SIOE)*, Cardiff, UK, April 2014.

Publication in Preparation:

- [1] **J. Chen**, N. Bamiedakis, P. Vasil’ev, R. V. Penty, and I. H. White, “Refractive-Index Profile Influences on Multimode Polymer Waveguide Components for On-board High-speed Optical Interconnects,” prepared for submission to *Journal of Lightwave Technology*.

CONTENTS

DECLARATION	II
ACKNOWLEDGEMENTS	III
ABSTRACT	V
LIST OF PUBLICATIONS	VI
CONTENTS	VIII
LIST OF FIGURES	XII
LIST OF TABLES	XXVI
LIST OF ACRONYMS AND ABBREVIATIONS	XXVII
1 INTRODUCTION	1
1.1 MOTIVATION AND RATIONALE	1
1.2 COMPARISONS BETWEEN ELECTRICAL AND OPTICAL INTERCONNECTS	6
1.2.1 Bandwidth Limitation	6
1.2.2 Power Consumption	8
1.3 CHALLENGES FOR OPTICAL INTERCONNECTS	9
1.4 AIM AND CONTRIBUTION OF THE DISSERTATION	10
1.5 OUTLINE OF DISSERTATION	12
1.6 REFERENCES	13
2 TECHNOLOGY CONSIDERATIONS FOR BOARD-LEVEL OPTICAL INTERCONNECTS	17
2.1 INTRODUCTION	17
2.2 TRANSMISSION MEDIUM	18
2.3 POLYMER MATERIALS	21
2.4 WAVEGUIDE FABRICATION	25
2.5 ACTIVE COMPONENTS	28
2.5.1 Optical Sources	28
2.5.2 Optical Receivers	30
2.6 COUPLING SCHEMES	30
2.6.1 Out-of-plane Coupling	31
2.6.2 Butt-coupling	35
2.7 STATE-OF-THE-ART DEMONSTRATORS	37
2.8 SUMMARY	42
2.9 REFERENCES	42

3 FUNDAMENTAL STUDIES OF MULTIMODE POLYMER WAVEGUIDES	52
3.1 INTRODUCTION	52
3.2 WAVEGUIDE GEOMETRY	53
3.3 STEP-INDEX AND GRADED-INDEX WAVEGUIDES	55
3.4 METHODOLOGY	58
3.4.1 Ray Tracing Analysis	58
3.4.2 Electromagnetic Treatment	59
3.4.3 Method Comparison	63
3.5 COUPLING EFFICIENCY CALCULATION	64
3.5.1 SMF Launch	65
3.5.2 50 μm GI MMF Launch	68
3.6 EXPERIMENTAL APPROACH	73
3.6.1 Insertion Loss	73
3.6.2 Alignment Tolerances	75
3.7 DISPERSION STUDIES	77
3.7.1 Ray Tracing Approach	77
3.7.2 Electromagnetic Analysis	79
3.8 BANDWIDTH EVALUATION	81
3.8.1 Overfilled Waveguide	83
3.8.2 SMF Launch	83
3.8.3 50 μm GI MMF Launch	85
3.8.4 Discussion	86
3.9 SUMMARY	87
3.10 REFERENCES	88
4 BANDWIDTH STUDIES ON MULTIMODE POLYMER WAVEGUIDES	90
4.1 INTRODUCTION	90
4.2 FREQUENCY RESPONSE MEASUREMENT	92
4.2.1 1.4 m Long Spiral Waveguide	92
4.2.2 1 m Long Spiral Waveguide	98
4.3 PULSE BROADENING MEASUREMENT	102
4.3.1 Femtosecond Laser	103
4.3.2 Autocorrelator	105
4.4 SHORT PULSE MEASUREMENT ON SPIRAL WAVEGUIDES	108
4.4.1 Waveguide Samples	108

4.4.2 Experimental Setups.....	110
4.4.3 Experimental Results.....	111
4.4.4 Simulation Results.....	116
4.4.5 Discussion	122
4.5 SHORT PULSE MEASUREMENT ON STRAIGHT WAVEGUIDES.....	122
4.5.1 Waveguide Samples.....	123
4.5.2 Experimental Results.....	123
4.6 SUMMARY	126
4.7 REFERENCES.....	126
5 EFFECTS OF REFRACTIVE INDEX PROFILES ON WAVEGUIDE PERFORMANCE	129
5.1 INTRODUCTION	129
5.2 MULTIMODE POLYMER WAVEGUIDE COMPONENTS	132
5.3 EXPERIMENTAL SETUPS.....	135
5.3.1 Power Transmission Studies	135
5.3.2 Dispersion Studies.....	136
5.4 90° BENT WAVEGUIDES	137
5.4.1 Theoretical Approach.....	139
5.4.2 Experimental Results.....	141
5.5 WAVEGUIDE CROSSINGS	142
5.5.1 Theoretical Approach.....	143
5.5.2 Experimental Results.....	145
5.6 BANDWIDTH PERFORMANCE	148
5.6.1 Reference and Spiral Waveguides.....	148
5.6.2 90° Waveguide Bends and 90° Waveguide Crossings.....	150
5.6.3 Discussion	151
5.7 SUMMARY	153
5.8 REFERENCES.....	153
6 HIGH SPEED DATA TRANSMISSION ON MULTIMODE WAVEGUIDES	156
6.1 INTRODUCTION	156
6.2 MODULATION SCHEMES	158
6.2.1 Non-Return-To-Zero (NRZ)	158
6.2.2 Pulse Amplitude Modulation (PAM-N).....	158

6.3 SIMULATION MODELLING.....	159
6.3.1 VCSEL Transmitter.....	160
6.3.2 Waveguide Channel	161
6.3.3 Receiver.....	161
6.3.4 Overall System Response	162
6.3.5 Equalisation	162
6.4 LINK POWER BUDGET	166
6.5 BIT-ERROR-RATIO (BER) CALCULATION	170
6.6 SIMULATION RESULTS.....	176
6.6.1 Signal Generation	177
6.6.2 Signal After VCSEL.....	178
6.6.3 Signal After Waveguide.....	178
6.6.4 Signal After Receiver.....	179
6.6.5 Signal After Equalisation	180
6.7 POWER BUDGET ANALYSIS	181
6.8 EXPERIMENTS.....	184
6.8.1 40 Gb/s NRZ.....	184
6.8.2 56 Gb/s PAM-4.....	189
6.9 SUMMARY	192
6.10 REFERENCES.....	193
7 CONCLUSIONS AND FUTURE WORK	196
7.1 CONCLUSIONS	196
7.2 FUTURE WORK	200
7.2.1 Waveguide Modelling.....	200
7.2.2 Launch Conditions	201
7.2.3 Optimisation of Refractive Index Profiles and Waveguide Layout	202
7.2.4 Toward 100 Gb/s Data Transmission	203
7.2.5 All-plastic Optical Circuits	207
7.3 REFERENCES.....	209
APPENDIX	211
UV MASK DESIGN	211

LIST OF FIGURES

FIGURE 1-1 CISCO GLOBAL IP TRAFFIC FORECAST, 2014-2019 (BY APPLICATION CATEGORY) [2].	2
FIGURE 1-2 INCREASE IN COMPUTING POWER IN SUPERCOMPUTER APPLICATIONS [4].	2
FIGURE 1-3 COMPARISON OF TRANSMISSION CAPACITY OF ELECTRICAL AND OPTICAL INTERCONNECTIONS [11].	3
FIGURE 1-4 HISTORICAL TIMELINE AND PREDICTED TRENDS IN THE DEPLOYMENT OF OPTICAL TECHNOLOGY FOR VARIOUS INTERCONNECTION HIERARCHIES [12].	4
FIGURE 1-5 (A) SCHEMATIC OF OPTICAL INTERCONNECTIONS: ON-CHIP, CHIP-TO-CHIP AND CARD-TO-CARD INTERCONNECTIONS AND (B) A BLADE SERVER [20].	5
FIGURE 1-6 PHOTONIC ROADMAP FOR OPTICAL INTERCONNECTS IN SUPERCOMPUTING [21].	6
FIGURE 1-7 (A) THE COST OF OPTICS BECOMES RELATIVELY LOWER THAN ELECTRICAL INTERCONNECTS AS DATA RATES INCREASE AND (B) THE COST TRENDS FOR OPTICAL AND ELECTRICAL INTERCONNECTS AT DIFFERENT APPLICATION LEVEL [47], [48].	10
FIGURE 1-8 STRUCTURE OF THE DISSERTATION WITH INDICATED FOCUS OF EACH CHAPTER.	12
FIGURE 2-1 (A) NO VISIBLE CRACKING SHOWN IN TWISTED POLYMER WAVEGUIDES DURING THE TWIST AND (B) LARGE-AREA FLEXIBLE POLYMER WAVEGUIDE DEMONSTRATORS [21], [22].	20
FIGURE 2-2 NEGLIGIBLE EFFECT OF TEMPERATURE ON THE OPTICAL TRANSMISSION OF BULK GENERIC PDMS [33].	23
FIGURE 2-3 (A) DEGRADATION TEMPERATURE AND OPTICAL LOSS COMPARISON OF DIFFERENT POLYMER FAMILIES [34] AND (B) MEASURED PROPAGATION LOSS OF DOW CORNING SILOXANE MATERIAL [21].	23
FIGURE 2-4 SCHEMATIC ILLUSTRATION OF PROCEDURES FOR (A) PHOTORESIST-BASED PATTERNING, (B) DIRECT LITHOGRAPHIC PATTERNING AND (C) LASER DIRECT WRITING [30].	26
FIGURE 2-5 SCHEMATIC ILLUSTRATION OF PROCEDURES FOR (A) MICROTRANSFER MOULDING (MTM) AND (B) MICROMOULDING IN CAPILLARIES (MIMIC) [30], [40].	27

FIGURE 2-6 FABRICATION PROCEDURE FOR THE SILOXANE POLYMER WAVEGUIDES EMPLOYED IN THIS THESIS.	28
FIGURE 2-7 (A) VCSEL SPEED RECORDS VERSUS TEMPERATURE AND (B) SPEED RECORDS VERSUS YEAR OF DEVELOPMENT SINCE 2001 [57].	29
FIGURE 2-8 ILLUSTRATION OF COUPLING SCHEMES: (A) OUT-OF-PLANE AND (B) BUTT-COUPLING [80].	31
FIGURE 2-9 EXAMPLES OF WAVEGUIDE INTEGRATED 45° MIRRORS USING FABRICATION METHODS OF (A) LASER ABLATION [82], (B) DICING [28], (C) MICRO-MILLING [33], (D) EMBOSSING [92] (E) UV PHOTOLITHOGRAPHY [93] AND (F) X-RAY LITHOGRAPHY [94]. ...	32
FIGURE 2-10 BEAM DELIVERY TECHNIQUES: (A) DIRECTLY COUPLING, (B) WITH MICRO-LENSES AND (C) WITH OPTICAL PILLARS [96].	33
FIGURE 2-11 EXAMPLES OF INTERCONNECTION SYSTEMS EMPLOYING INTEGRATED 45° MIRRORS AND VARIOUS BEAM DELIVERY SCHEMES EMPLOYING (A) DUAL-LENS [28], (B) AND (C) OPTICAL PILLARS [98], [99].	33
FIGURE 2-12 ILLUSTRATION OF COUPLING SCHEME EMPLOYING CONVENTIONAL FIBRE RIBBON ARRAYS: (A) SYSTEM SCHEMATIC, (B) SCHEMATICS FOR SINGLE-LAYER AND MULTI-LAYER CONNECTION AND (C) DETAILED COUPLING CONFIGURATION [100]–[102].	34
FIGURE 2-13 ILLUSTRATION OF COUPLING SCHEME EMPLOYING AN EVANESCENT FIBRE RIBBON COUPLER: (A) SYSTEM SCHEMATIC AND (B) ACTUAL IMPLEMENTATION [103].	34
FIGURE 2-14 ILLUSTRATION OF COUPLING SCHEME EMPLOYING A TILTED SURFACE GRATING: (A) SYSTEM SCHEMATIC, (B) SCHEMATIC OF COUPLING A SURFACE-NORMAL INPUT LIGHT INTO WAVEGUIDE AND (C) A TILTED GRATING STRUCTURE [104], [105].	34
FIGURE 2-15 ILLUSTRATION OF A BUTT-COUPLED SCHEME EMPLOYING AN MT-COMPATIBLE RIBBON FIBRE CONNECTOR PROPOSED BY IBM ZURICH: (A) SCHEMATIC, (B) ACTUAL IMPLEMENTATION AND (C) THE MT CONNECTOR [106], [107].	35
FIGURE 2-16 ILLUSTRATION OF A BUTT-COUPLED SCHEME EMPLOYING AN MT-COMPATIBLE RIBBON FIBRE CONNECTOR AND VCSEL/PD ARRAY PROPOSED BY XYRATEX AND UCL: (A) SCHEMATIC, (B) ACTUAL IMPLEMENTATION OF A LINE-CARD AND (C) THE MT-PLUG AND MT-SOCKET INTERPOSER [108], [109].	36

FIGURE 2-17 ILLUSTRATION OF A BUTT-COUPLED SCHEME EMPLOYING AN L-SHAPED CONNECTOR: (A) CROSS SECTION OF AN OE PCB WITH L-SHAPED CONNECTOR, (B) AND (C) SCHEMATICS OF THE L-SHAPED CONNECTOR [113].	36
FIGURE 2-18 ILLUSTRATION OF A BUTT-COUPLED SCHEME EMPLOYING CHANNELS FORMED IN THE POLYMER LAYER: (A) A U-GROOVE FORMED IN POLYMER, (B) A CLEAVED FIBRE PLACED IN A V-GROOVE IN SUBSTRATE AND (C) SPIN-COATING AND UV PHOTOLITHOGRAPHIC PATTERNING [110]–[112].	37
FIGURE 3-1 SCHEMATIC OF POLYMER WAVEGUIDES: (A) ARRAY OF WAVEGUIDE FACETS AND (B) CROSS SECTION OF A $50 \times 50 \text{ mm}^2$ WAVEGUIDE.	54
FIGURE 3-2 CONFINEMENT FACTOR OF (A) THE FUNDAMENTAL MODE AND (B) A HIGHER ORDER MODE FOR INDEX STEP $\Delta n = 0.005$, WAVEGUIDE WIDTH $w = 50 \text{ mm}$.	55
FIGURE 3-3 (A) WAVEGUIDE SAMPLE FABRICATED ON A SILICON SUBSTRATE COMPRISING OF $50 \times 50 \text{ mm}^2$ WAVEGUIDES WITH SEPARATION DISTANCE OF 250 mm AND (B) $50 \times 50 \text{ mm}^2$ WAVEGUIDE ILLUMINATED WITH WHITE LIGHT.	55
FIGURE 3-4 REFRACTIVE INDEX PROFILES WITH DIFFERENT INDEX EXPONENT VALUES FOR A WAVEGUIDE WITH CORE WIDTH OF 50 mm .	56
FIGURE 3-5 (A) CROSS SECTION AND REFRACTIVE INDEX PROFILES FOR STEP-INDEX ($s = t = \infty$) AND GRADED-INDEX ($s = t = 2$) WAVEGUIDES AND (B) LIGHT PROPAGATIONS INSIDE THE STEP-INDEX AND GRADED-INDEX WAVEGUIDES.	57
FIGURE 3-6 ILLUSTRATION OF TOTAL INTERNAL REFLECTION (TIR).	58
FIGURE 3-7 BASIC CONCEPT OF EFFECTIVE INDEX METHOD (EIM): DIVIDING THE 2-D PROBLEM INTO TWO 1-D PROBLEMS IN EACH TRANSVERSE DIRECTION [7].	62
FIGURE 3-8 ILLUSTRATION OF FILM MODE MATCHING METHOD (FMM) ON THE CROSS SECTION OF A RIDGE WAVEGUIDE.	62
FIGURE 3-9 EFFECTIVE INDEX FOR GUIDED MODES COMPUTED WITH EIM AND FMM METHODS FOR A $50 \times 50 \text{ mm}^2$ WAVEGUIDE WITH INDEX STEP OF 0.02 .	63
FIGURE 3-10 (A) SCHEMATIC OF THE COUPLING CONFIGURATION FOR A SMF INPUT AT A DISTANCE D_{GAP} FROM THE WAVEGUIDE FACET AND (B) ILLUSTRATION OF THE FREE-SPACE EXPANSION OF GAUSSIAN BEAM.	66

FIGURE 3-11 (A) -3 dB ALIGNMENT TOLERANCE (UNIT IN MM) AS A FUNCTION OF WAVEGUIDE PARAMETERS FOR HORIZONTAL OFFSETS FOR A SMF INPUT, (B) INPUT COUPLING LOSS AS A FUNCTION OF INPUT SMF POSITIONS ON A $50 \times 50 \text{ mm}^2$ WAVEGUIDE WITH $\Delta n = 0.02$ (-3 dB ALIGNMENT TOLERANCES INDICATED IN RED DASHED LINE) AT $\lambda = 850 \text{ nm}$	68
FIGURE 3-12 SCHEMATIC OF THE COUPLING CONFIGURATION FOR A 50 MM GI MMF INPUT: (A) WELL-ALIGNMENT AND (B) TRANSVERSE MISALIGNMENT WITH NO LONGITUDINAL OFFSETS.	68
FIGURE 3-13 REFRACTIVE INDEX PROFILE THE 50 MM GI MMF EMPLOYED.	69
FIGURE 3-14 INPUT COUPLING LOSS FOR A 50 MM GI MMF AS A FUNCTION OF WAVEGUIDE WIDTH w AND INDEX STEP Δn AT $\lambda = 850 \text{ nm}$	71
FIGURE 3-15 INPUT COUPLING LOSS AS A FUNCTION OF THE INPUT POSITIONS FOR A $50 \times 50 \text{ mm}^2$ WAVEGUIDE WITH AN INDEX STEP $\Delta n = 0.02$ FOR A 50 MM GI MMF INPUT AT $\lambda = 850 \text{ nm}$	72
FIGURE 3-16 (A) -1 dB AND (B) -3 dB ALIGNMENT TOLERANCES (UNIT IN MM) AS A FUNCTION OF WAVEGUIDE PARAMETERS FOR HORIZONTAL OFFSETS FOR A 50 MM GI MMF INPUT AT $\lambda = 850 \text{ nm}$	72
FIGURE 3-17 ILLUSTRATION OF THE DEFINITION OF INSERTION LOSS: (A) BACK-TO-BACK OPTICAL LINK AND (B) OPTICAL LINK WITH THE DEVICE UNDER TEST.....	73
FIGURE 3-18 EXPERIMENTAL SETUP EMPLOYED FOR MEASUREMENT OF INSERTION LOSS WITH AXIS DEFINITION NOTED.....	75
FIGURE 3-19 NORMALISED RECEIVED POWER AS A FUNCTION OF INPUT OFFSETS FOR A $50 \times 50 \text{ mm}^2$ WAVEGUIDE FOR (A) A SMF AND (B) A 50 MM GI MMF LAUNCH. INDEX MATCHING GEL IS EMPLOYED.....	76
FIGURE 3-20 (A) A UNIFORM RAY POWER DISTRIBUTION (IN RED) AND IMPULSE RESPONSE DUE TO MULTIMODE DISPERSION (IN BLUE), (B) BLP AND DISPERSION PER UNIT OF LENGTH AS A FUNCTION OF INDEX STEP Δn	79
FIGURE 3-21 ILLUSTRATION OF (A) THE RESTRICTED CENTRE LAUNCH AND (B) OVERFILLED LAUNCH.	82
FIGURE 3-22 BLPs (GHz \times m) AS A FUNCTION OF WAVEGUIDE WIDTH w AND INDEX STEP Δn ASSUMING A UNIFORM MODE POWER DISTRIBUTION.....	83

FIGURE 3-23 (A) SCHEMATIC OF A WELL-ALIGNED SMF INPUT, (B) EXAMPLE OF A GENERATED MODE POWER DISTRIBUTION FOR A $50 \times 50 \text{ mm}^2$ WAVEGUIDE WITH $\Delta n = 0.02$ AND (C) CALCULATED BLPs (GHz \times M) AS A FUNCTION OF WAVEGUIDE WIDTH W AND INDEX STEP Δn FOR A SMF INPUT.....	84
FIGURE 3-24 (A) SCHEMATIC OF A WELL-ALIGNED 50 MM GI MMF INPUT, (B) UNIFORM MODE POWER DISTRIBUTION IN A 50 MM GI MMF, (C) EXAMPLE OF A GENERATED MODE POWER DISTRIBUTION FOR A $50 \times 50 \text{ mm}^2$ WAVEGUIDE WITH $\Delta n = 0.02$ AND (D) CALCULATED BLPs (GHz \times M) AS A FUNCTION OF WAVEGUIDE WIDTH W AND INDEX STEP Δn FOR AN OVERFILLED 50 MM GI MMF INPUT.	85
FIGURE 3-25 ESTIMATED BLPs (GHz \times M) AS A FUNCTION OF INPUT POSITION FOR A $50 \times 50 \text{ mm}^2$ WITH AN INDEX STEP Δn OF 0.02 FOR A 50 MM GI MMF INPUT.	86
FIGURE 4-1 PHOTOGRAPHS OF (A) THE 1.4 M LONG SPIRAL WAVEGUIDE ILLUMINATED WITH RED LIGHT AND (B) INPUT FACET OF THE WAVEGUIDE [10].	92
FIGURE 4-2 EXPERIMENTAL SETUP FOR THE S_{21} MEASUREMENT FOR (A) THE BACK-TO-BACK LINK AND (B) THE WAVEGUIDE LINK UNDER A QUASI-OVERFILLED 50/125 MM LAUNCH CONDITION.	93
FIGURE 4-3 NEAR FIELD IMAGES OF THE OUTPUT FACET OF THE FIBRES EMPLOYED: (A) A QUASI-OVERFILLED 50/125 MM MMF AND (B) A 100/140 MM MMF.....	94
FIGURE 4-4 NORMALISED FREQUENCY RESPONSE OF THE 1.4 M LONG SPIRAL WAVEGUIDE FOR DIFFERENT INPUT HORIZONTAL OFFSETS UNDER (A) A 9/125 MM SMF, (B) A QUASI-OVERFILLED 50/125 MM MMF AND (C) A 100/140 MM MMF LAUNCH.....	95
FIGURE 4-5 EXPERIMENTAL SETUP FOR THE OFFSET LAUNCH MEASUREMENT FOR THE 1.4 M LONG SPIRAL WAVEGUIDE UNDER A QUASI-OVERFILLED 50/125 MM LAUNCH CONDITION.	96
FIGURE 4-6 THE FWHM OF RECEIVED SIGNAL AND THE NORMALISED RECEIVED OPTICAL POWER OVER THE 1.4 M LONG SPIRAL WAVEGUIDE FOR DIFFERENT HORIZONTAL OFFSETS UNDER (A) A 9/125 MM SMF, (B) A QUASI-OVERFILLED 50/125 MM MMF AND (C) A 100/140 MM MMF LAUNCH.....	97
FIGURE 4-7 PHOTOGRAPHS OF (A) THE 1 M LONG SPIRAL WAVEGUIDE ILLUMINATE WITH RED LIGHT AND (B) THE WAVEGUIDE OUTPUT FACET ILLUMINATED WITH 850 NM LIGHT.....	98

FIGURE 4-8 NEAR FIELD IMAGES AT THE INPUT FIBRE END UNDER THE DIFFERENT LAUNCH CONDITIONS STUDIED: (A) A 4/125 MM SMF, (B) A TYPICAL 50/125 MM MMF, (C) A QUASI-OVERFILLED 50/125 MM MMF AND (D) A 100/140 MM MMF.....	99
FIGURE 4-9 NORMALISED FREQUENCY RESPONSE OF THE 1 M LONG SPIRAL WAVEGUIDE FOR DIFFERENT INPUT HORIZONTAL OFFSETS UNDER (A) A 4/125 MM SMF, (B) A TYPICAL 50/125 MM MMF, (C) A QUASI-OVERFILLED 50/125 MM MMF AND (D) A 100/140 MM MMF LAUNCH.	101
FIGURE 4-10 NEAR FIELD IMAGES OF THE WAVEGUIDE OUTPUT UNDER (A) A 4/125 MM SMF, (B) A TYPICAL 50/125 MM MMF, (C) A QUASI-OVERFILLED 50/125 MM MMF AND (D) A 100/140 MM MMF LAUNCH ACROSS DIFFERENT INPUT OFFSETS.....	102
FIGURE 4-11 AUTOCORRELATION TRACES OF THE PULSES FROM THE TWO SHORT PULSE GENERATION SYSTEMS: (A) FWHM = ~250 FS AT $\lambda = 850$ NM AND (B) FWHM = ~450 FS AT $\lambda = 787$ NM.	103
FIGURE 4-12 GAUSSIAN BEAM WIDTH $w(z)$ AS A FUNCTION OF THE DISTANCE z ALONG THE BEAM (w_0 : BEAM WAIST; b : DEPTH OF FOCUS; z_R : RAYLEIGH RANGE; θ : TOTAL ANGULAR SPREAD).....	104
FIGURE 4-13 EXPERIMENTAL SETUP FOR SECOND HARMONIC GENERATION IN THE SHORT PULSE GENERATION SYSTEM 2.	104
FIGURE 4-14 SPECTRUMS OF THE (A) ORIGINAL PULSE (PEAK AT ~1574 NM) AND (B) GENERATED SECOND HARMONIC PULSE (PEAK AT ~787 NM).	105
FIGURE 4-15 (A) TOP VIEW SCHEMATIC AND (B) SIDE VIEW SCHEMATIC OF THE FR-103MN FOR THE SHG AUTOCORRELATION MEASUREMENT WITH NON-COLLINEAR BEAM USED IN THE SHORT PULSE GENERATION SYSTEM 1 [20].	106
FIGURE 4-16 EXPERIMENTAL SETUP FOR THE SHG AUTOCORRELATION MEASUREMENT WITH TWO COLLINEAR BEAMS USED IN THE SHORT PULSE GENERATION SYSTEM 2.	106
FIGURE 4-17 PHOTOGRAPH OF (A) THE 105.5 CM LONG SPIRAL AND (B) THE 19.2 CM LONG REFERENCE WAVEGUIDE ILLUMINATED WITH A RED LASER SOURCE.	109
FIGURE 4-18 MEASURED REFRACTIVE INDEX PROFILE OF THE (A) SI AND (B) GI WAVEGUIDE AT THE WAVELENGTH OF 678 NM.	109

FIGURE 4-19 EXPERIMENTAL SETUP USED FOR THE (A) BACK-TO-BACK LINK; (B) 105.5 CM LONG SPIRAL WAVEGUIDE LINK UNDER A 50/125 MM MMF LAUNCH WITH THE USE OF A MM USING PULSE GENERATION SYSTEM 1 AT $\lambda = 850$ NM AND (C) 19.2 CM LONG REFERENCE WAVEGUIDE LINK UNDER A 10 \times MICROSCOPE OBJECTIVE LAUNCH USING PULSE GENERATION SYSTEM 2 AT $\lambda = 787$ NM.	110
FIGURE 4-20 NEAR FIELD IMAGES OF INPUT FIBRE AND LENS UNDER THE DIFFERENT LAUNCH CONDITIONS STUDIED: (A) A 50/125 MM MMF; (B) A 50/125 MM MMF WITH A MM AND (C) A 10 \times MICROSCOPE OBJECTIVE.	111
FIGURE 4-21 EXAMPLES OF CURVE FITTING: (A) ORIGINAL PULSE OF THE LASER SOURCE WITH SECH ² SHAPE, AND THE STRUCTURED PULSES AFTER PROPAGATION OVER THE WAVEGUIDES WITH (B) GAUSSIAN AND (C) LORIENTZIAN SHAPES.	112
FIGURE 4-22 ILLUSTRATIONS OF BANDWIDTH ESTIMATION USING PULSE BROADENING METHOD: (A) TIME-DOMAIN AND (B) FREQUENCY-DOMAIN.	112
FIGURE 4-23 EXPERIMENTAL RESULTS OF THE -3 DB BANDWIDTH FOR THE 105.5 CM LONG SPIRAL POLYMER MULTIMODE WAVEGUIDES AND RESPECTIVE NORMALISED RECEIVED POWER FOR A 50/125 μ M MMF INPUT WITH AND WITHOUT THE MM: (A) SI WAVEGUIDE WITH NO MM, (B) SI WAVEGUIDE WITH MM, (C) GI WAVEGUIDE WITH NO MM AND (D) GI WAVEGUIDE WITH MM ($\lambda = 850$ NM).	113
FIGURE 4-24 NEAR FIELD IMAGES OF THE (A) SI AND (B) GI REFERENCE WAVEGUIDE UNDER A RESTRICTED LAUNCH; AND THE (C) SI AND (D) GI SPIRAL WAVEGUIDE UNDER A 50/125 μ M MMF LAUNCH.	114
FIGURE 4-25 EXPERIMENTAL RESULTS OF BLPs (GHZ \times M) OF THE 19.2 CM LONG (A) SI AND (B) GI UNDER A 10 \times MICROSCOPE OBJECTIVE LAUNCH AT $\lambda = 787$ NM (HIGH BLP REGION NOTED IN RED DASHED LINE).	115
FIGURE 4-26 NORMALISED MEASURED COUPLING LOSS (UNITS IN dB) OF THE 19.2 CM LONG SI AND GI REFERENCE WAVEGUIDE UNDER A 10 \times MICROSCOPE OBJECTIVE LAUNCH AT $\lambda = 787$ NM (RED DASHED LINE INDICATES THE HIGH BLP REGION SHOWN IN FIGURE 4-25).	116
FIGURE 4-27 ASSUMED MODE POWER DISTRIBUTION INSIDE THE INPUT 50/125 MM MMF PATCHCORD FOR CONDITION: (A) A 50/125 MM MMF WITH NO MM ($PMN \leq 15$) AND (B) A 50/125 MM MMF WITH MM ($PMN \leq 22$).	117

FIGURE 4-28 THE CURVES OF MODE SELECTIVE LOSS ASSUMED FOR THE (A) SI AND (B) GI WAVEGUIDE.	117
FIGURE 4-29 NORMALISED RECEIVED POWER VERSUS POSITION OF INPUT 50/125 MM MMF: (A) SI WAVEGUIDE WITH NO MM ($PMN \leq 15$), (B) SI WAVEGUIDE WITH MM ($PMN \leq 22$), (C) GI WAVEGUIDE WITH NO MM ($PMN \leq 15$) AND (D) GI WAVEGUIDE WITH MM ($PMN \leq 22$).	118
FIGURE 4-30 SIMULATION AND EXPERIMENTAL RESULTS OF THE -3 dB BLP (UNIT IN GHz×M) FOR THE 105.5 CM LONG SPIRAL POLYMER MULTIMODE WAVEGUIDES FOR A 50/125 μM MMF INPUT WITH AND WITHOUT MM: (A) SI WAVEGUIDE WITH NO MM, (B) SI WAVEGUIDE WITH MM, (C) GI WAVEGUIDE WITH NO MM AND (D) GI WAVEGUIDE WITH MM ($\lambda = 850$ NM).	119
FIGURE 4-31 SIMULATION RESULTS OF THE -3 dB BLP (UNIT IN GHz×M) OF THE 19.2 CM LONG REFERENCE POLYMER MULTIMODE WAVEGUIDE FOR A 10× MICROSCOPE OBJECTIVE LAUNCH ($\lambda = 787$ NM): (A) SI WAVEGUIDE AND (B) GI WAVEGUIDE.	119
FIGURE 4-32 MODE PROFILES OF THE SI WAVEGUIDE (FIRST 5 MODES).	120
FIGURE 4-33 (A) REFRACTIVE INDEX PROFILE OF THE SI WAVEGUIDE AT 678 NM AND (B) MODE POWER DISTRIBUTION OF THE SI WAVEGUIDE AT VARYING LOCATIONS UNDER RESTRICTED LAUNCH.	120
FIGURE 4-34 MODE PROFILES OF THE GI WAVEGUIDE (FIRST 5 MODES).	121
FIGURE 4-35 (A) REFRACTIVE INDEX PROFILE OF THE GI WAVEGUIDE AT 678 NM AND (B) MODE POWER DISTRIBUTION OF THE GI WAVEGUIDE AT VARYING LOCATIONS UNDER RESTRICTED LAUNCH.	121
FIGURE 4-36 (A) MEASURED REFRACTIVE INDEX PROFILE OF WG01 AT 678 NM AND (B) EXPERIMENTAL RESULT OF BLPs (GHz×M) OF WG01 WITH THE RECORDED NEAR FIELD IMAGES AT DIFFERENT INPUT POSITIONS INSET.	124
FIGURE 4-37 (A) MEASURED REFRACTIVE INDEX PROFILE OF WG02 AT 678 NM AND (B) EXPERIMENTAL RESULT OF BLPs (GHz×M) OF WG02 WITH THE RECORDED NEAR FIELD IMAGES AT DIFFERENT INPUT POSITIONS INSET.	125
FIGURE 4-38 (A) MEASURED REFRACTIVE INDEX PROFILE OF WG03 AT 678 NM AND (B) EXPERIMENTAL RESULT OF BLPs (GHz×M) OF WG03 WITH THE RECORDED NEAR FIELD IMAGES AT DIFFERENT INPUT POSITIONS INSET.	125

FIGURE 5-1 EXAMPLE TECHNIQUES FOR WAVEGUIDE CROSSINGS: (A) MULTIPLE WAVEGUIDE LAYERS WITH FLIP-CHIP BONDED [1], (B) MULTIPLE WAVEGUIDE LAYERS WITH DIRECTIONAL COUPLER AND (C) SINGLE WAVEGUIDE LAYER [2].....	130
FIGURE 5-2 SCHEMATICS OF THE (A) 90° WAVEGUIDE BENDS AND (B) 90° WAVEGUIDE MIRRORS.	130
FIGURE 5-3 SCHEMATIC OF SHUFFLE INTERCONNECTIONS: (A) BASIC SHUFFLE INTERCONNECTION CONCEPT AND (B) RECONFIGURED TO UTILISE THE BASIC ELEMENTS (90° BENDS AND CROSSINGS) REQUIRED FOR COMPLEX BACKPLANE TOPOLOGIES [8].	131
FIGURE 5-4 SCHEMATICS OF THE WAVEGUIDE COMPONENTS USED FOR THE REFRACTIVE INDEX STUDIES: (A) 90° WAVEGUIDE BENDS, (B) 90° AND 45° WAVEGUIDE CROSSINGS, (C) REFERENCE WAVEGUIDES AND (D) SPIRAL WAVEGUIDES.	133
FIGURE 5-5 PHOTOGRAPHS OF (A) 90° WAVEGUIDE BEND ($R = 8$ MM), (B) 90° WAVEGUIDE CROSSING (SINGLE CROSSING), (C) REFERENCE WAVEGUIDE AND (D) SPIRAL WAVEGUIDE ILLUMINATED WITH RED LIGHT.	134
FIGURE 5-6 MEASURED RI PROFILE OF THE 3 WAVEGUIDE SAMPLES AT 678 NM.....	134
FIGURE 5-7 EXPERIMENTAL SETUP OF THE POWER TRANSMISSION MEASUREMENTS.....	135
FIGURE 5-8 FAR FIELD INTENSITY OF DIFFERENT LAUNCH CONDITIONS: (A) A 9/125 MM SMF, A 50/125 MM MMF AND A 100/140 MM MMF + MM; AND NEAR FIELD IMAGES OF INPUT FIBRE FOR DIFFERENT LAUNCH CONDITIONS: (B) A 9/125 MM SMF, (C) 50/125 MM MMF AND (D) 100/140 MM MMF + MM.	136
FIGURE 5-9 EXPERIMENTAL SETUPS FOR SHORT PULSE MEASUREMENT: (A) 10× MICROSCOPE OBJECTIVE LAUNCH AND (B) 50/125 MM OR 100 MM + MM LAUNCH.....	137
FIGURE 5-10 NEAR FIELD IMAGES OF THE INPUTS FOR DIFFERENT LAUNCH CONDITIONS: (A) 10× MICROSCOPE OBJECTIVE, (B) A 50/125 MM MMF AND (C) A 100/140 MM MMF + MM..	137
FIGURE 5-11 (A) GEOMETRY OF A WAVEGUIDE BEND AND A TYPICAL RAY IN THE CORE OF A BENT STEP-INDEX GUIDE AND (B) ILLUSTRATIONS OF RADIATION CAUSTIC (RED DASHES), CONSTANT PHASE (DOTTED BLACK ARROW) AND MODE PROFILE OF THE LOWEST ORDER MODE (BLUE).	139

FIGURE 5-12 (A) INDUCED LOSS FOR A 90° WAVEGUIDE BEND WITH WIDTH OF 50 MM FOR DIFFERENT INDEX STEPS Δn AND (B) INDUCED LOSS FOR A 90° WAVEGUIDE BEND WITH STEP INDEX $\Delta n = 0.02$ FOR DIFFERENT WAVEGUIDE WIDTHS.	141
FIGURE 5-13 (A) INSERTION LOSS OF THE 90° BENDS VERSUS BENDING RADIUS, AND (B) NORMALISED BENDING LOSS VERSUS BENDING RADIUS OF 3 DIFFERENT WAVEGUIDES UNDER A 9/125 MM SMF, A 50/125 MM MMF AND A 100/140 MM MMF + MM LAUNCH.	142
FIGURE 5-14 ILLUSTRATION OF THEORETICAL MODELLING METHODS: (A) ELECTROMAGNETIC APPROACH BASED ON THE FREE-SPACE FIELD EXPANSION AND (B) RAY TRACING TECHNIQUE BASED ON THE RAY TRAJECTORIES IN THE WAVEGUIDE (RAY 1: SOLID LINE, RAY 2: DASHED LINE).	144
FIGURE 5-15 (A) INPUT POWER DISTRIBUTIONS USED IN THE RAY TRACING MODEL, (B) EXCESS LOSS OF WAVEGUIDE CROSSINGS FOR A 50 MM WIDE WAVEGUIDE, $\Delta n = 0.02$ FOR VARYING INPUT POWER DISTRIBUTION AND (C) EXCESS LOSS OF WAVEGUIDE CROSSINGS FOR A 50 MM WIDE WAVEGUIDE FOR VARYING INDEX DIFFERENT Δn WHEN THE INPUT POWER IS “INF”.	144
FIGURE 5-16 (A) INSERTION LOSS OF THE 90° CROSSING VERSUS THE NUMBER OF CROSSINGS, AND (B) NORMALISED INSERTION LOSS VERSUS THE NUMBER OF CROSSINGS OF 3 WAVEGUIDES UNDER A 9/125 MM SMF, A 50/125 MM MMF AND A 100/125 MM MMF + MM LAUNCH.	145
FIGURE 5-17 (A) INSERTION LOSS OF THE 45° CROSSING VERSUS THE NUMBER OF CROSSINGS, AND (B) NORMALISED INSERTION LOSS VERSUS THE NUMBER OF CROSSINGS OF 3 WAVEGUIDES UNDER A 9/125 MM SMF, A 50/125 MM MMF AND A 100/125 MM MMF + MM LAUNCH.	146
FIGURE 5-18 LOSS/CROSSING OF (A) 90° AND (B) 45° DEGREE CROSSINGS FOR 3 WAVEGUIDES UNDER A 9/125 MM SMF, A 50/125 MM MMF AND A 100/140 MM MMF + MM LAUNCH.	147
FIGURE 5-19 INSERTION LOSSES OF (A) REFERENCE WAVEGUIDES AND (B) SPIRAL WAVEGUIDES UNDER A 9/125 MM SMF, A 50/125 MM MMF AND A 100/140 MM MMF + MM LAUNCH.	148

FIGURE 5-20 BANDWIDTH-LENGTH PRODUCTS OF THE 3 REFERENCE WAVEGUIDES UNDER A 10× MICROSCOPE OBJECTIVE, A 50/125 MM MMF AND A 100/140 MM MMF + MM LAUNCH.	149
FIGURE 5-21 FAR FIELD INTENSITY OF THE 3 REFERENCE WAVEGUIDES IN THE HORIZONTAL DIRECTION UNDER (A) A 10× MICROSCOPE OBJECTIVE, (B) A 50/125 MM MMF AND (C) A 100/140 MM MMF + MM LAUNCH.	150
FIGURE 5-22 BANDWIDTH-LENGTH PRODUCTS OF (A) 90° BENDS VERSUS RADIUS OF CURVATURE AND (B) 90° CROSSINGS VERSUS THE NUMBER OF CROSSINGS OF 3 WAVEGUIDES UNDER THE 50/125 MM MMF LAUNCH.	151
FIGURE 6-1 ILLUSTRATION OF (A) NRZ AND (B) PAM-4 SIGNALS.	158
FIGURE 6-2 BLOCK DIAGRAM OF THE SIMULATION MODEL USED FOR THE SYSTEM EVALUATION.	160
FIGURE 6-3 ILLUSTRATION OF PRE-CURSOR ISI AND POST-CURSOR ISI IN A DISPERSIVE CHANNEL.	163
FIGURE 6-4 SCHEMATIC DIAGRAM OF AN FIR T-SPACED N-TAP FFE.	163
FIGURE 6-5 SCHEMATIC DIAGRAM OF AN IIR T-SPACED M-TAP DFE.	164
FIGURE 6-6 SCHEMATIC DIAGRAM OF A T-SPACED N-TAP FFE AND T-SPACED M-TAP DFE EQUALISER.	165
FIGURE 6-7 LINK POWER BUDGET MODEL FOR MULTILEVEL MODULATION SCHEMES IN WAVEGUIDE BASED TRANSMISSION SYSTEMS.	166
FIGURE 6-8 (A) IDEAL LASER OUTPUT POWER WITH DC BIAS AND (B) REAL LASER OUTPUT POWER WITH INTENSITY NOISE [24].	168
FIGURE 6-9 PLOT OF EYE DIAGRAM AT THE OPTICAL RECEIVER.	169
FIGURE 6-10 GAUSSIAN PROBABILITY DENSITY FUNCTIONS OF BINARY 1s AND 0s WITH THE FLUCTUATING SIGNAL ILLUSTRATED AT THE RECEIVER (THE COLOUR REGIONS REPRESENT THE PROBABILITY OF ERROR).	171
FIGURE 6-11 GAUSSIAN PROBABILITY DENSITY FUNCTIONS OF MULTILEVEL SIGNALS.	173
FIGURE 6-12 EYE DIAGRAMS OF THE IDEAL SIGNALS: (A) NRZ AT 40 GB/S, (B) NRZ AT 56 GB/S AND (C) PAM-4 AT 56 GB/S.	177

FIGURE 6-13 EYE DIAGRAMS OF THE TRANSMITTED SIGNALS AFTER VCSEL: (A) NRZ AT 40 GB/s, (B) NRZ AT 56 GB/s AND (C) PAM-4 AT 56 GB/s.	178
FIGURE 6-14 EYE DIAGRAMS OF SIGNALS AFTER PROPAGATION OF WAVEGUIDE LENGTHS OF 0.5M, 1 M AND 1.5 M FOR (A) NRZ AT 40 GB/s, (B) NRZ AT 56 GB/s AND (C) PAM-4 AT 56 GB/s.....	179
FIGURE 6-15 EYE DIAGRAMS OF THE SIGNALS AFTER THE RECEIVER AFTER PROPAGATION OF WAVEGUIDE LENGTHS OF 0.5M, 1 M AND 1.5 M FOR (A) NRZ AT 40 GB/s, (B) NRZ AT 56 GB/s AND (C) PAM-4 AT 56 GB/s WITHOUT THE USE OF EQUALISERS.	180
FIGURE 6-16 EYE DIAGRAMS OF THE SIGNALS AFTER THE RECEIVER AFTER PROPAGATION OF WAVEGUIDE LENGTHS OF 0.5M, 1 M AND 1.5 M FOR (A) NRZ AT 40 GB/s, (B) NRZ AT 56 GB/s AND (C) PAM-4 AT 56 GB/s WITH THE USE OF A 7-TAP FFE AND 5-TAP DFE EQUALISER.	181
FIGURE 6-17 POWER BUDGET FOR NRZ SIGNALS AT (A) 40 GB/s AND (B) 56 GB/s FOR WAVEGUIDE LENGTHS OF 0.5 M, 1 M AND 1.5 M, RESPECTIVELY.	182
FIGURE 6-18 POWER BUDGET FOR PAM-4 SIGNALS AT 56 GB/s WITH THE USE OF (A) FEC(10^{-5} , 10^{-15}) AND (B) FEC(10^{-3} , 10^{-12}) FOR WAVEGUIDE LENGTHS OF 0.5 M, 1 M AND 1.5 M, RESPECTIVELY.	182
FIGURE 6-19 EXPERIMENTAL SETUP FOR (A) THE WAVEGUIDE LINK AND (B) THE BACK-TO-BACK OPTICAL LINK.	185
FIGURE 6-20 RECEIVED EYE DIAGRAMS FOR OPTICAL BACK-TO-BACK AND THE WAVEGUIDE LINKS AT 25 GB/s, 36 GB/s AND 40 GB/s. AVERAGE RECEIVED OPTICAL POWER NOTED FOR EACH DATA RATE AS WELL AS THE RESPECTIVE VOLTAGE AND TIME SCALES OF THE RECORDED WAVEFORMS.	186
FIGURE 6-21 BER CURVES FOR THE OPTICAL BACK-TO-BACK (B2B) LINK AND THE LINK WITH THE 1 M LONG SPIRAL WAVEGUIDE (WG) OBTAINED AT 25, 36 AND 40 GB/s.....	187
FIGURE 6-22 RECEIVED EYE DIAGRAMS FOR OPTICAL BACK-TO-BACK AND THE WAVEGUIDE LINKS AT 25 GB/s FOR DIFFERENT HORIZONTAL OFFSETS. AVERAGE RECEIVED OPTICAL POWER AS WELL AS THE RESPECTIVE VOLTAGE AND TIME SCALES OF THE RECORDED WAVEFORMS NOTED.....	188
FIGURE 6-23 (A) BER CURVES FOR THE OPTICAL BACK-TO-BACK (B2B) LINK AND THE LINK WITH THE 1 M LONG SPIRAL WAVEGUIDE (WG) AT DIFFERENT HORIZONTAL OFFSETS, AND	

(B) NORMALISED RECEIVED POWER AND POWER PENALTIES FOR A BER OF 10^{-9} AS FUNCTION OF INPUT OFFSETS OBTAINED AT 25 Gb/s.	188
FIGURE 6-24 RECEIVED EYE DIAGRAMS FOR OPTICAL BACK-TO-BACK AND THE WAVEGUIDE LINKS AT 40 Gb/s FOR DIFFERENT SPATIAL OFFSETS. AVERAGE RECEIVED OPTICAL POWER AS WELL AS THE RESPECTIVE VOLTAGE AND TIME SCALES OF THE RECORDED WAVEFORMS NOTED.....	189
FIGURE 6-25 (A) BER CURVES FOR THE OPTICAL BACK-TO-BACK (B2B) LINK AND THE LINK WITH THE 1 M LONG SPIRAL WAVEGUIDE (WG) AT DIFFERENT HORIZONTAL OFFSETS, AND (B) NORMALISED RECEIVED POWER AND POWER PENALTIES FOR A BER OF 10^{-9} AS FUNCTION OF INPUT OFFSETS OBTAINED AT 40 Gb/s.	189
FIGURE 6-26 EXPERIMENTAL SETUP OF (A) THE BACK-TO-BACK AND (B) THE WAVEGUIDE LINK.	191
FIGURE 6-27 RECORDED 28 GBAUD (56 Gb/s) EYE DIAGRAMS FOR THE (A) BACK-TO-BACK AND (B) THE WAVEGUIDE LINK [36].....	192
FIGURE 6-28 ESTIMATED BER USING Q-FACTOR ANALYSIS [36].....	192
FIGURE 7-1 SCHEMATIC DIAGRAM OF (A) TWIN-SPOT LAUNCH, (B) HERMITE-GAUSSIAN (5, 0) LINE LAUNCH AND (C) HERMITE-GAUSSIAN (3, 3) SQUARE LAUNCH. THE TWO DIFFERENT COLOURS IN (B) AND (C) REPRESENT TWO PHASES WITH A DIFFERENCE OF 180°	202
FIGURE 7-2 SCHEMATIC DIAGRAMS OF THE WAVEGUIDE LINK CONFIGURATIONS: (A) AN “RX-FFE/DFE” LINK AND (B) A “TX-FFE/DFE” LINK.	203
FIGURE 7-3 SCHEMATIC DIAGRAMS OF THE TRANSMISSION SYSTEMS: (A) PAM-4 AND (B) CAP-16 OR CAP-64 [11].	204
FIGURE 7-4 SYSTEM DIAGRAM OF WAVELENGTH-DIVISION MULTIPLEXING.	205
FIGURE 7-5 2DIO DEMULTIPLEXER DEVICES (A) DEVICE OPERATION AND (B) DEVICE COMPONENTS [15].....	206
FIGURE 7-6 (A) CROSS-SECTIONAL OF 2-DEMENSIONAL 4×12 WAVEGUIDE ARRAY, (B) TWO-LAYER OUT-OF-PLANE COUPLING CONFIGURATION AND (C) TWO-LAYER INTER-PLANE COUPLING CONFIGURATION [16], [17].....	207

FIGURE 7-7 (A) AN INTEGRATED OLED WITH POLYMER WAVEGUIDE AND (B) SCHEMATIC OF PROPOSED OPTICAL PLASTIC INTEGRATED DEVICES: OLED AND OPD FORMED DIRECTLY ON A POLYMER SUBSTRATE [19], [20].	208
FIGURE A-1 UV MASK DESIGN.....	211

LIST OF TABLES

TABLE 2-1 ATTRIBUTES OF INTEREST FOR POLYMER MATERIALS FOR OPTICAL WAVEGUIDES [19].....	21
TABLE 2-2 SUMMARY OF COMMON POLYMER MATERIALS CHARACTERISED AT 800-850 NM WAVELENGTH.	22
TABLE 2-3 DEMONSTRATED BOARD-LEVEL OPTICAL INTERCONNECTIONS BASED ON MULTIMODE POLYMER WAVEGUIDES FROM BOTH ACADEMIA AND INDUSTRY.....	38
TABLE 3-1 COMPARISON OF DIFFERENT METHODS.....	64
TABLE 4-1 RELATIONSHIP BETWEEN THE AUTOCORRELATION WIDTH AND PULSE WIDTH FOR COMMONLY USED PULSE SHAPES.....	108
TABLE 5-1 SUMMARY OF THE CHARACTERISTICS OF 3 WAVEGUIDE SAMPLES AT 678 NM.	134
TABLE 5-2 FAR FIELD NA (5% INTENSITY) OF THE VARIOUS INPUT FIBRES EMPLOYED IN THE POWER TRANSMISSION EXPERIMENTS.....	136
TABLE 5-3 THE REQUIRED RADIUS FOR BENDING LOSS BELOW 1 dB OF 3 WAVEGUIDES WITH DIFFERENT RI PROFILES UNDER DIFFERENT LAUNCH CONDITIONS STUDIED.	142
TABLE 5-4 LOSS PER CROSSING OF 90° CROSSINGS FOR 3 WAVEGUIDES UNDER A 9/125 MM SMF, 50/125 MM MMF AND 100/140 MM MMF + MM LAUNCH.	147
TABLE 5-5 LOSS PER CROSSING OF 45° CROSSINGS FOR 3 WAVEGUIDES UNDER A 9/125 MM SMF, 50/125 MM MMF AND 100/140 MM MMF + MM LAUNCH.	147
TABLE 5-6 INSERTION LOSSES (dB) OF (A) REFERENCE WAVEGUIDES AND (B) SPIRAL WAVEGUIDES UNDER A 9/125 MM SMF, A 50/125 MM MMF AND A 100/140 MM MMF + MM LAUNCH.	148
TABLE 5-7 FAR FIELD NA (5% INTENSITY) OF 3 DIFFERENT WAVEGUIDES UNDER DIFFERENT LAUNCH CONDITIONS EMPLOYED.	150
TABLE 6-1 NATURAL AND GRAY CODES FOR PAM-4.	159
TABLE 6-2 LIST OF PARAMETERS FOR EACH COMPONENT USED IN THE SIMULATION MODEL...	177
TABLE 7-1 100 GB/S SYSTEM PARAMETERS FOR VARIOUS MODULATION SCHEMES.....	204

LIST OF ACRONYMS AND ABBREVIATIONS

1-D/2-D/3-D	1-Dimensional/2-Dimensional/3-Dimensional
2DIO	Two Dimensional Integrated Optics
APD	Avalanche Photodiode
BER	Bit-Error-Ratio
BERT	Bit Error Rate Tester
BLP	Bandwidth-Length Product
BPM	Beam Propagation Method
BT	Bessel Thomson
CAP	Carrierless Amplitude and Phase
CAPE	Centre of Advanced Photonics and Electronics
CCD	Charge-Coupled Device
CMOS	Complementary-Metal-Oxide-Semiconductor
dB	Decibel
dBm	Decibel Power Ratio (Referenced to a milliwatt)
dBo	Decibel Optical Power Ratio
DFE	Decision-Feedback Equalisation
EIM	Effective Index Method
EMI	Electromagnetic Interference
eV	Electron-Volts
FDM	Finite Difference Method
FEC	Forward Error Correction
FEM	Finite Element Method
FFE	Feed-Forward Equalisation
FIR	Finite Impulse Response
FMM	Film Mode Matching
FR4	Flame Retardant 4
FWHM	Full-Width-At-Half-Maximum
Gb/s	Gigabit Per Second
GbE	Gigabit Ethernet
GI	Graded-Index
HPC	High Performance Computer
IIR	Infinite Impulse Response
iNEMI	International Electronics Manufacturing Initiative
ISI	Intersymbol Interference
ITRS	International Technology Roadmap for Semiconductors
LAN	Local-Area Network
LC	Inductive-Capacitive
LED	Light Emitting Diode
LP	Linear Polarised
MEMS	Micro-Electro-Mechanical Systems
MIMIC	Micromoulding In Capillaries
MM	Mode Mixer
MMF	Multimode Fibre
MMSE	Minimum-Mean-Square-Error
MSM	Metal-Semiconductor-Metal
MT	Mechanical Transfer
NA	Numerical Aperture
NRZ	Non-Return-To-Zero

OLED	Organic Light Emitting Diode
OPD	Organic Photodiode
PAM	Pulse Amplitude Modulation
PCB	Printed Circuit Board
PD	Photodiode
PDF	Probability Density Function
PDL	Polarisation Dependent Loss
PDMS	Polydimethylsiloxane
PLC	Planar Lightwave Circuit
PMD	Polarisation Mode Dispersion
PMMA	Polymethylmethacrylate
PMN	Principal Mode Number
PMT	Photomultiplier Tube
POF	Plastic Optical Fibre
PRBS	Pseudo-Random Bit Sequence
QPM	Quasi-Phase Matching
RC	Resistive-Capacitive
RF	Radio Frequency
RI	Refractive Index
RIE	Reactive Ion Etching
RIN	Relative Intensity Noise
RMS	Root Mean Square
RMSE	Root-Mean-Square-Error
RZ	Return-To-Zero
SER	Symbol-Error-Ratio
SHG	Second Harmonic Generation
SI	Step-Index
SMF	Single-Mode Fibre
SOI	Silicon-On-Insulator
TIA	Transimpedance Amplifier
TIR	Total Internal Reflection
UV	Ultra-Violet
VCSEL	Vertical-Cavity Surface-Emitting Laser
VOA	Variable Optical Attenuator
WDM	Wavelength-Division Multiplexing
WG	Waveguide
μTM	Microtransfer Moulding

1 INTRODUCTION

This chapter explains the motivation behind the research described in this dissertation and introduces the bandwidth limitations faced by electrical interconnections in computing systems. The cost and performance demands of board-level links suggest the need for high-performance optical interconnections based on polymer waveguides. The chapter finally sets out the objectives of the dissertation and presents the main contributions of this work.

1.1 Motivation and Rationale

In recent years, there has been a rapidly growing demand for interconnection bandwidth for home users due to the expansion of internet applications and also for enterprise organisations owing to the increasing data generation and access requirements. Global internet traffic is growing aggressively each year for example due to high-definition video applications, which alone account for over half of the bandwidth used on the Internet [1]. New technologies such as smart devices, social networks, 3D content, cloud computing are also driving internet traffic levels [2] (Figure 1-1). These trends have been made possible by consistent advances in computing power with the development of ever more advanced data centres and high performance computers (HPC) [3] (Figure 1-2).

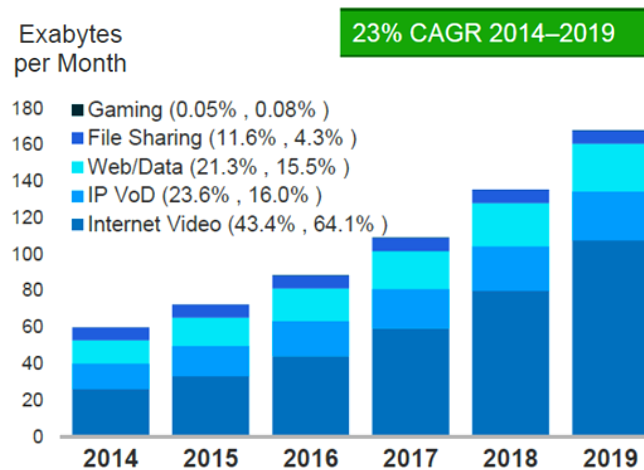


Figure 1-1 Cisco global IP traffic forecast, 2014-2019 (by application category) [2].

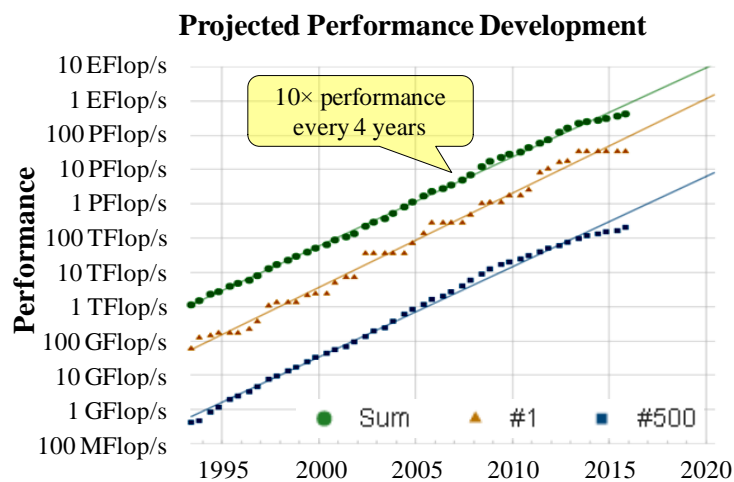


Figure 1-2 Increase in computing power in supercomputer applications [4].

In data centre environments, the operators are quickly adopting 100 Gb/s Ethernet (GbE) from the current 10 GbE driven by the increased bandwidth demands of multi-core and multithreaded CPUs as well as server and storage upgrades and greater inter-processor communication requirements [3], [5]. In the HPC environments, the performance growth evidenced by the top 500 supercomputers have continued to follow Moore's law [4]. Processors are becoming increasingly fast due to the constant scaling of size and density of the transistors, which enlarges the gap between the devices and interconnections. The International Technology Roadmap for Semiconductors (ITRS) has highlighted the increasing importance of on-chip and off-chip interconnections [6]. It has been realised that the high-performance semiconductor integrated circuits will be limited by the electrical interconnects within and between them in the coming years. Various electrical schemes have been developed to maintain the increasing data rates. However, to accommodate the on-going

increase in speed, printed circuit board electrical links are becoming increasingly sophisticated resulting in increased costs. Even more importantly, electrical cables are still facing the fundamental “communication bottleneck” which comes from their inherent drawbacks such as:

- High frequency loss: skin effect losses increase in proportion with the square-root of frequency while dielectric loss increases linearly with frequency;
- Impedance discontinuities: contribute significantly to signal degradation due to the signal paths through vias, connectors, etc.;
- Crosstalk: electromagnetic interference (EMI) from the neighbouring signals which limits the density of metal wirings.

Much work has been done to overcome the disadvantages of electrical interconnections and extend the useful lifetime of well-established copper cables by using various techniques. For example, manufacturers are trying to make copper with lower surface roughness to reduce the skin effects [7], [8]. However substantial loss still remains even for the finest copper lines. Advanced board materials such as Flame Retardant 4+ (FR4+), Rogers 4000 and GETEK have been also developed to increase bandwidth. However, they can significantly add to the total cost [9], [10]. Sophisticated signal processing techniques such as pre-emphasis, equalisation techniques, multilevel techniques and coding can be used at the transmitter and/or receivers to increase data rates but at an increased circuit complexity and hence cost and power dissipation. Various analyses tend to agree that the saturation of data rates on electrical links will occur at approximately 20 Gb/s (Figure 1-3) [3], [11].

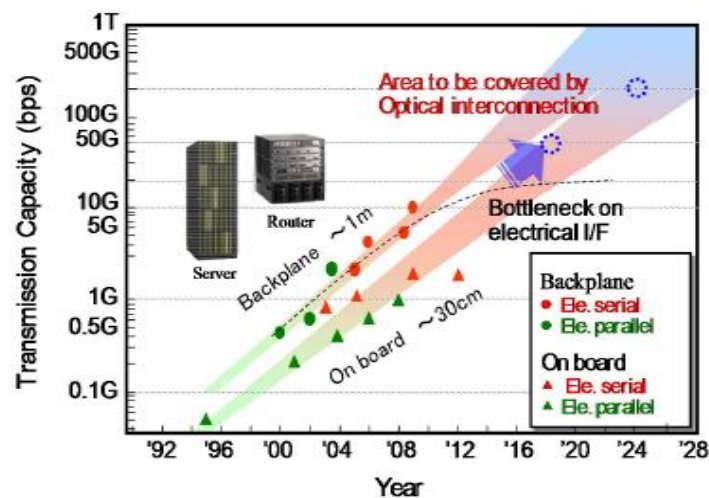




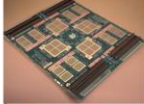
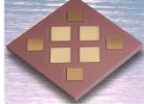
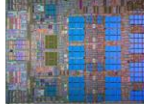


Figure 1-3 Comparison of transmission capacity of electrical and optical interconnections [11].

Therefore, researchers have considered fundamentally changing the physical means of interconnection to overcome the obstacles that conventional electrical interconnections face. Optics can provide an alternative solution to address most of the problems mentioned above. Indeed, optical communications have become a dominant technology in long-haul telecommunications due to the development of optical fibre technologies and the invention of lasers in the last fifty years. A clear trend can be seen in the use of optics for interconnections over shorter distances (Figure 1-4) [12]. Nowadays, optical links are commonly used over rack-to-rack and intra-cabinet routes. The reasons for this are that optics offers important advantages over its electric counterpart:

- Larger bandwidth;
- Lower power consumption;
- Good immunity to EMI;
- Higher density;
- Scalability.

Physical link types	MAN/WAN	Cables-long	Cables-short	Card-to-card	Intra-card	Intra-module	Intra-chip
Features							
Distance	Multi-km	10-300 m	1-10 m	0.3-1 m	0.1-0.3 m	5-100 mm	0-20 mm
No of lines per link	1	1-10s	1-10s	1-100s	1-100s	1-100s	1-100s
Use of optics	Since 80s	Since 90s	Since late 00's	Since 2010-2011	2012-2015	After 2015	Later

Single-mode Optics
 Mixed multi-mode optics & copper
 Copper

Figure 1-4 Historical timeline and predicted trends in the deployment of optical technology for various interconnection hierarchies [12].

The consideration of using optics as an alternative interconnection technology to chips inside computers was first proposed by Goodman in 1984 [13], and since then many publications in the literature have proposed that optical interconnections will be deployed within existing electronic circuits [14]–[19]. Optical interconnections in such small scales can be divided into two categories according to the link length (Figure 1-5):

- On-chip interconnections (<1 cm);

- On-board interconnections: chip-to-chip (<30 cm), card-to-card (<1 m).

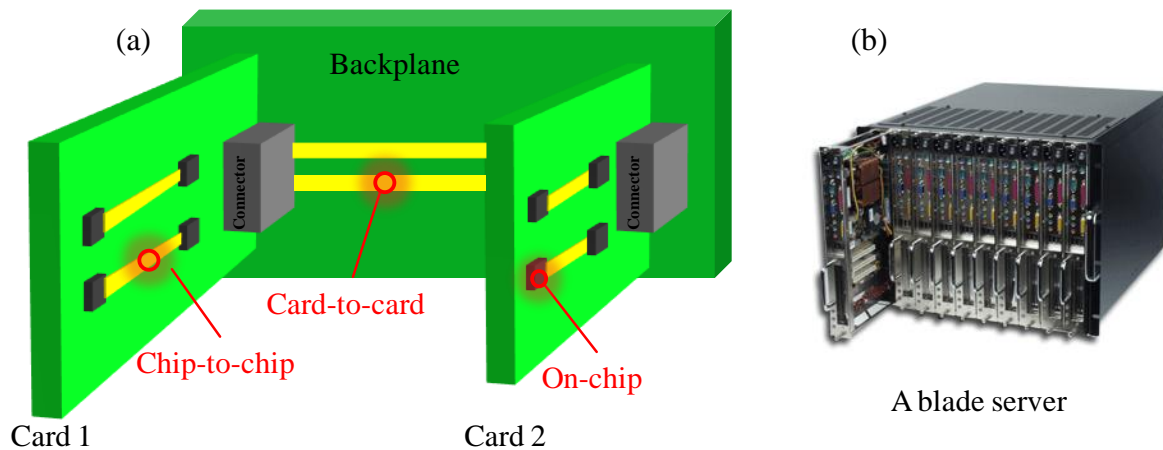


Figure 1-5 (a) Schematic of optical interconnections: on-chip, chip-to-chip and card-to-card interconnections and (b) a blade server [20].

Optical links for card-to-card and chip-to-chip interconnects are expected to enjoy a commercial exploitation soon while on-chip optical interconnections will be next (Figure 1-6) [21]. While on-board interconnects has been an active area of research for many years, the transition from electrical to optical interconnection is going gradually as cost plays a significant role in any technological shift. As printed circuit board (PCB) manufacturing becomes a cheaper and more mature technology, optical interconnects need to be compatible with existing electronic manufacturing processes and have the ability to be efficiently integrated into existing architectures. This results in significant research interests on integrated optical technologies. In particular, polymer-based optical waveguides have drawn a considerable amount of attention as they can be directly implemented to conventional PCBs in a cost-effective way.

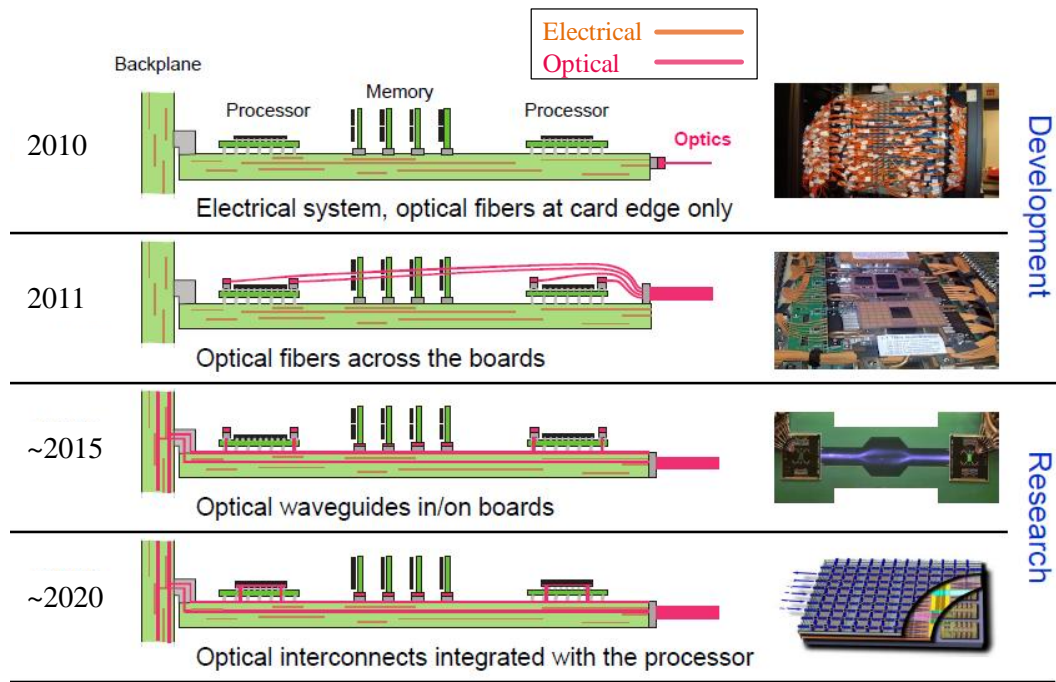


Figure 1-6 Photonic roadmap for optical interconnects in supercomputing [21].

1.2 Comparisons between Electrical and Optical Interconnects

It is important to understand the nature of the challenges that traditional electrical interconnects face in order to justify the advantages of optical interconnects. Therefore, technical comparisons between electrical and optical interconnections are presented in the following sections from two main aspects in information processing systems: (i) bandwidth limitation and (ii) power consumption [19], [22]–[25].

1.2.1 Bandwidth Limitation

The capacity of electrical wires has a fundamental scaling limitation known as “aspect ratio” given by (for on-off keying scheme):

$$B \leq B_0 \frac{A}{L^2} \text{ (bits/s)} \quad (1-1)$$

where B is the maximum data rate, A and L are the cross-sectional area and the length of the electrical wire respectively, and B_0 is a constant. $B_0 \sim 10^{15}$ b/s for a typical off-chip inductive-capacitive (LC) lines, $B_0 \sim 10^{16}$ b/s for the on-chip resistive-capacitive (RC) lines, and $B_0 \sim 10^{17}$ b/s for off-chip equalised inductive–capacitive lines with typical resistive loss (RLC) lines [24]. In the gigahertz frequency regime, nearly all electrical interconnect lines on-chip are

RC-type, whereas off-chip lines are primarily LC transmission lines. It should be noted that this simple approximation does not take account of additional loss from surface scattering in wires or dielectric loss, both of which reduce the bandwidth of electrical wires.

It can be noticed that the ratio A/L^2 is dimensionless which means that the capacity of the wire cannot be simply increased by making the wires smaller or bigger. Current electrical wires are experiencing this bandwidth limitation at all levels from global wires on board to backplanes between boards. As mentioned earlier, skin effect and dielectric losses can also significantly limit the bandwidth of copper links on FR4 and the dielectric losses start to dominate at higher frequencies. For example, a recent analysis shows that a 1 m long electrical cable on standard FR4 is limited to 5 Gb/s [26]. The use of advanced materials can increase the bandwidth. For example, Rogers substrates can increase this limit to ~15 Gb/s, but they are 5 times more expensive than FR4 and difficult to process [9]. A further increase to 20 Gb/s may be possible with the deployment of modulation schemes and equalisations aforementioned [26]–[28]. However, all of these techniques increase the system complexity and often overall power dissipation. In addition, it is possible to break a long link into several shorter links in series with repeaters. Although this can be feasible on-chip, it is less desirable for off-chip interconnections due to the additional number of repeaters chips. This can also increase power consumption [19].

In contrast, optics does not suffer from many of the problems seen in scaling the electrical interconnections as the physics of optics is fundamentally different. Optics is not subject to the physical scaling invariant limits of the capacity encountered by the electrical interconnections. Single-mode fibres (SMFs), for example, can in principle carry tens of terabits per second. Even multimode fibres (MMFs) can carry high information capacity, potentially orders of magnitude higher than can be achieved on copper cables. To achieve such high-speed data transmission over fibres certainly is not an easy task, and would require high-performance transmitters and receivers. Nevertheless, the fibre itself is not likely to limit the bandwidth for on-board and on-chip interconnections in the foreseeable future.

Fibre-based approaches however cannot be easily laminated into PCBs, thus preventing a high level of integration with boards. Therefore, polymer waveguide based approaches have been considered. However, this technology will not be adopted until it can offer a significant improvement in bandwidth over existing electrical wires. Therefore, the understanding of the bandwidth limitations of polymer waveguides is essential, and hence the design of high-bandwidth polymer waveguides is a major goal of this thesis.

1.2.2 Power Consumption

As power consumption is also becoming of greater concern for electrical interconnections, it is critical that optical interconnections consume less power irrespective of their high bandwidth. For electrical links, the energy required is at least that needed to charge the whole line (or at least the section of line whose length corresponds to the electrical pulse length) to the signalling voltage. The total energy can be expressed as:

$$E_s \geq C_l V_r^2 \quad (1-2)$$

where C_l is the capacitance of the line and V_r is the signalling voltage. In order to reduce the total energy consumption, it is typically desirable to reduce the voltage rather than the capacitance of electrical lines as all well-designed lines have similar capacitance.

On the contrary, this energy can be avoided in optical systems as there is no need to “charge” the line to signal voltage. This physics is a quantum-mechanical phenomenon, which makes the classical voltage in the light beam not directly relevant to the voltage that can be generated [29]. The relevant energy for comparison is given by:

$$E_p \geq C_d V_r \frac{h\omega}{e} \quad (1-3)$$

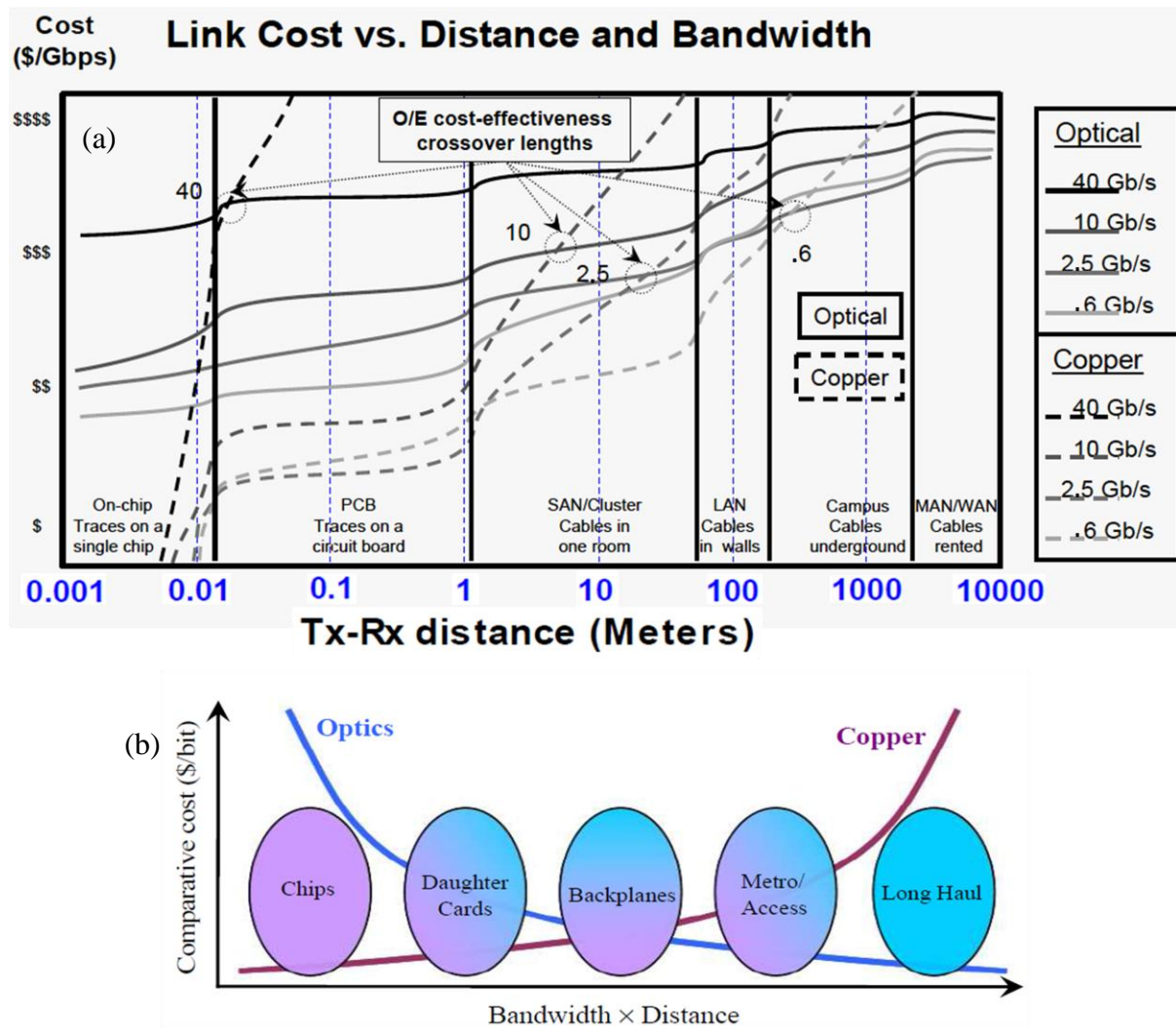
where C_d is the total capacitance of the photodetector, and voltage $h\omega/e$ is numerically equal to the photon energy in unit of electron-volts (eV) (quantum efficiency is assumed to be 1 here for simplicity).

From Equations (1-2) and (1-3), it can be seen that the power consumption of optical links is less than electrical ones if $C_d \cdot h\omega/e < C_l V_r$. Since $h\omega/e$ (e.g. $\sim 1\text{V}$) might be bigger than the electrical signalling voltage V_r (e.g. 100mV or less), optics has lower energy consumption only if $C_d \ll C_l$. This general relationship indicates that optics can become beneficial for longer guide lengths and lower detector capacitances. In comparing energy consumption, care should be taken to note the total power needed to convert from electrical signals to optical signals or vice versa in addition to transmission losses. Comprehensive theoretical work has been done to estimate the crossover length beyond which optical interconnections dissipate less power than electrical counterparts [9], [10], [27], [30]–[43]. For instance, Cho [10] compared the power consumption of optical and electrical interconnections, and found that

optical links become more power efficient beyond a critical length of 43 cm at data rate of 6 Gb/s and this length reduces for higher bit rates. Therefore, there is an opportunity to optics for use in board-level interconnections as it can not only solve the bandwidth challenges that electrical interconnects have but also potentially consume less power at higher data rates or longer lengths.

1.3 Challenges for Optical Interconnects

It is generally recognised that optical interconnects for use in board-level links is an exciting and on-going research topic. However, the technology roadmaps and the predictions made over recent years have proven to be overly optimistic as the adoption of board-level optical interconnects has fallen behind predictions. Perhaps the biggest challenge is the cost related to the existing optical solutions as well as the continuous improvements made in the electrical interconnect systems. The cheapest on-board optical interconnects are estimated to be at least twice as expensive as the traditional electrical interconnects which do not justify their improved performance [44]. Hence, the proposed optical interconnects have not yet been fully adopted on large-scale commercial levels despite the excellent performance of these high-capacity optical links. The successful adoption of on-board optical interconnects will only occur when the bandwidth is really only met by optical links with an overall system cost and power consumption that are competitive with the alternative electrical solutions [45], [46]. As the data rate increases, a crossover point will appear where optics will be able to offer a more cost-effective solution and electrical links will exponentially become more expensive. Although the point at which optical interconnects become superior to electrical interconnects is not fixed, as the available sources and receivers continuously evolve, bandwidth-length analyses comparing electrical and optical systems tend to agree that the crossover point is estimated to be ~2-3 m at 25 Gb/s and this crossover is expected to occur at an even lower data rate if the price of optics goes down [Figure 1-7(a)] [47]. The transition from electrical to optical interconnects is highly cost-driven and application specific. The international Electronics Manufacturing Initiative (iNEMI) has suggested that this transition may first occur at the backplane level at which optics may have a better cost performance over electrical interconnects (beyond this length optics has completely replaced electronics) [Figure 1-7(b)] [48].



Therefore, board-level optical interconnects is believed to be the next step for a clear commercial application of next-generation optical technology. In order to push the electrical-to-optical boundary further, the study of high-bandwidth polymer waveguides based interconnects inevitably becomes the direction of this work.

1.4 Aim and Contribution of the Dissertation

Multimode polymer waveguides have drawn intense interest for use in board-level optical interconnections. Considerable research worldwide has sought to develop cost-effective polymer waveguides and demonstrate their engineering feasibility for applications such as optical backplanes [49]–[57]. However, few demonstrators have been reported with a

convincing level of high-speed data transmission to compete with existing electrical on-board solutions for future data centres and supercomputers. Therefore, the objective of this dissertation is to tackle the “interconnection bottleneck” for board-level communication links through a focussed study of developing low-loss and high-bandwidth polymer waveguides and using advanced modulation schemes to enable higher data transmission rates. The author has sought to advance the on-going development of optical integrated circuits and optical backplanes by making the meaningful contributions below:

- Investigating the high-speed performance of multimode polymer waveguides using both frequency-domain measurements (S_{21}) and short-pulse measurements under different launch conditions in the presence of input spatial offsets. Bandwidth-length products of $>70 \text{ GHz}\times\text{m}$ for a $50 \text{ }\mu\text{m}$ MMF launch and $>100 \text{ GHz}\times\text{m}$ for a restricted launch are presented over a large range of offsets ($>\pm 10 \text{ }\mu\text{m}$) for the first time, indicating the capability of data transmission rates of 100 Gb/s and beyond over such waveguides using launch conditioning schemes. A theoretical model is developed using real measured refractive index profiles, and a good agreement has been found between the simulation and experimental results.
- Identifying the effects of refractive index profiles and waveguide layouts (bends, crossing) on the optical transmission properties and dynamic performance of multimode polymer waveguides, and demonstrating that the waveguide performance can be enhanced by appropriate refractive index engineering and intelligent waveguide layout design. The results demonstrate that low loss interconnection (waveguide bends with excess loss below 1 dB for a radius $>6 \text{ mm}$, crossings with crossing loss less than 0.02 dB/crossing) while exhibiting adequate link bandwidth ($>47 \text{ GHz}\times\text{m}$) can be achieved for a $50 \text{ }\mu\text{m}$ MMF launch using appropriate refractive index engineering. In addition, 1.55 times bandwidth improvement ($\text{BLP}>60 \text{ GHz}\times\text{m}$) over the straight waveguides is achieved using a waveguide bend with a radius of 5 mm and with a loss penalty of $\sim 1.9 \text{ dB}$ under a $50 \text{ }\mu\text{m}$ MMF launch. To the best of author’s knowledge, this is the first detailed study on the impact of refractive index profiles and waveguide layouts on the loss and bandwidth performance of highly-multimoded polymer waveguide components.
- Investigating the high-speed data transmission over these waveguides using advanced modulation formats for board-level optical interconnects, and demonstrating for the first time that such polymer multimode waveguides can support non-return-to-zero (NRZ)-based 40 Gb/s and 4-level pulse-amplitude-modulation (PAM-4)-based 56 Gb/s data transmission rates

over a 1 m long multimode polymer waveguide. A system simulation model is developed and the simulation results agree well with the experiments. These are the highest data rates for a polymer-based optical interconnects at the time of writing.

1.5 Outline of Dissertation

Each chapter in this dissertation undertakes to focus on a particular topic concerned with the development of high-performance multimode polymer waveguides for board-level optical interconnects for next-generation data centres and supercomputers. Figure 1-8 depicts the general outline of the dissertation with the focus of each chapter indicated. The focus of each chapter is briefly provided as follows:

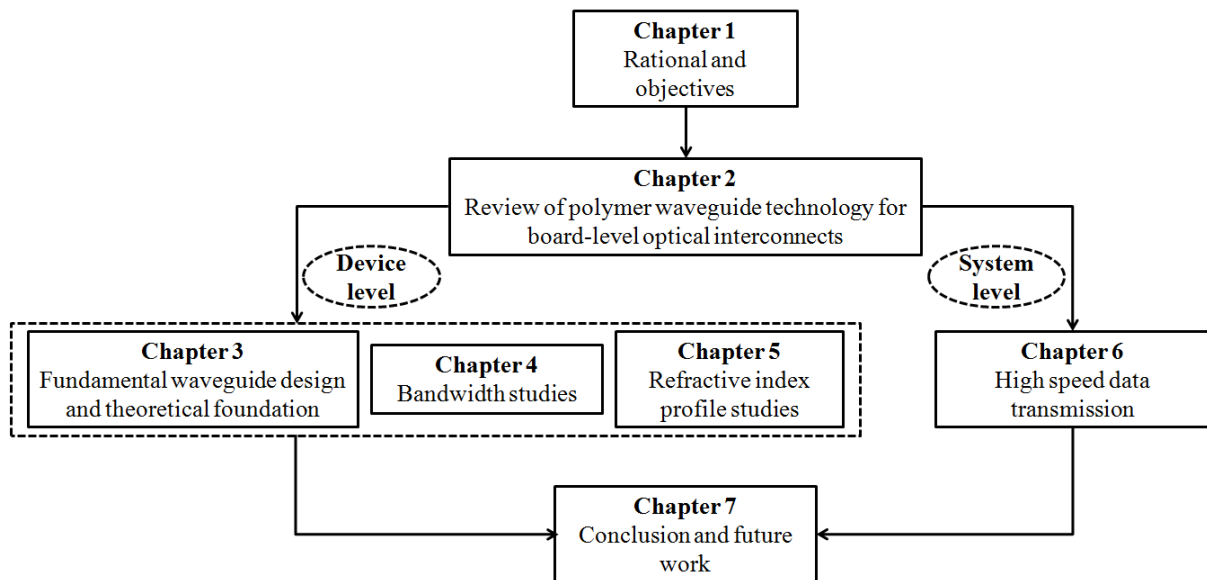


Figure 1-8 Structure of the dissertation with indicated focus of each chapter.

Chapter 1 – identifies the on-going demand for higher interconnection bandwidth and the predicted transition from electrical to optical interconnects. The comparisons between the electrical and optical interconnects for on-board communication links are presented from the perspectives of bandwidth and power consumption. It is concluded that optical interconnects, although facing serious engineering challenges, can potentially offer both higher bandwidth and lower power consumption for future applications.

Chapter 2 – reviews the polymer waveguide systems for board-level optical interconnections focusing on the major optical components used. Various materials suitable for integration on PCBs are reviewed, and siloxane polymers are identified as the choice of this thesis. Active devices (e.g. sources and receivers) as well as different coupling schemes

suitable for on-board optical interconnects are reviewed. State-of-the-art demonstrators based on polymer waveguides are presented, and possible areas of improvements are identified.

Chapter 3 – presents the waveguide design parameters and the fundamental optical transmission studies of the waveguide samples in this thesis. Coupling efficiency and available bandwidth-length product are theoretically investigated for different waveguide parameters under low-cost coupling schemes typically employed in real-world applications. It is shown that optimum waveguide design parameters can be chosen to ensure low coupling loss and sufficient link bandwidth for many applications.

Chapter 4 – reports the experimental bandwidth results of various multimode polymer waveguides under different launch conditions and in the presence of input offsets. Both frequency-domain and ultra-short pulse measurements are conducted. Simulation results show good agreement with the experiments. The results indicate the possibility of transmitting data rates of >100 Gb/s over a single waveguide channel without introducing significant performance impairments in the link with the use of launch conditioning schemes and appropriate refractive index engineering.

Chapter 5 – examines the effects of refractive index profiles and waveguide layouts on the loss and bandwidth performance of passive waveguide components such as bends and crossings for use in optical backplanes. The characterisation of waveguide samples with different refractive index profiles are carried out. The experimental results indicate that low loss interconnection and adequate link bandwidth can be achieved using appropriate refractive index engineering and intelligent waveguide layout.

Chapter 6 – investigates high-speed data transmission over multimode polymer waveguides using advanced modulation formats. A system simulation is developed to show the feasibility of transmitting very high data rates (>40 Gb/s) over these waveguides. Record high data transmission of 40 Gb/s NRZ and 56 Gb/s PAM-4 over a 1 m long multimode polymer waveguide are demonstrated experimentally.

Chapter 7 – summarises all the work conducted in this dissertation. The major conclusions are highlighted and future work that can be carried out to further advance the development of high-speed optical interconnects integrated at the board level is identified.

1.6 References

- [1] “Cisco Visual Networking Index: Forecast and Methodology, 2014-2019.” [Online].

- Available: http://www.cisco.com/c/en/us/solutions/collateral/service-provider/ip-ngn-ip-next-generation-network/white_paper_c11-481360.html.
- [2] Cisco, *The Zettabyte Era: Trends and Analysis*. White paper, 2015.
 - [3] P. Pepeljugoski, F. Doany, D. Kuchta, L. Schares, C. Schow, M. Ritter, and J. Kash, "Data Center and High Performance Computing Interconnects for 100 Gb/s and Beyond," *OFC/NFOEC 2007*, p. OMR4, 2007.
 - [4] "Top500 Supercomputer Sites." [Online]. Available: <http://www.top500.org>.
 - [5] C. Kachris, K. Kanonakis, and I. Tomkos, "Optical Interconnection Networks in Data Centers : Recent Trends and Future Challenges," *IEEE Commun. Mag.*, vol. 51, no. 9, pp. 39–45, 2013.
 - [6] "International technology roadmap for semiconductors." [Online]. Available: <http://www.itrs2.net/>.
 - [7] T. Okubo, T. Sudo, T. Hosoi, H. Tsuyoshi, and F. Kuwako, "Signal Transmission Loss on Printed Circuit Board in GHz Frequency Region," *2013 IEEE Electr. Des. Adv. Packag. Syst. Symp.*, pp. 112–115, 2013.
 - [8] S. Hinaga, M. Koledintseva, and P. Anmula, "Effect of Conductor Surface Roughness upon Measured Loss and Extracted Values of PCB Laminate Material Dissipation Factor," *Proc. Tech. Conf. IPC Expo/APEX*, pp. S20–2, 2009.
 - [9] D. Huang, T. Sze, A. Landin, R. Lytel, and H. L. Davidson, "Optical interconnects: Out of the box forever?," *IEEE J. Sel. Topics Quantum Electron.*, vol. 9, no. 2, pp. 614–623, 2003.
 - [10] H. Cho, P. Kapur, and K. C. Saraswat, "Power comparison between high-speed electrical and optical interconnects for interchip communication," *J. Light. Technol.*, vol. 22, no. 9, pp. 2021–2033, 2004.
 - [11] K. Hiramoto, T. Takemoto, and K. Adachi, "Multichannel 1.3-um Lens-Integrated Surface-Emitting DFB Laser (LISEL) Arrays for High-speed Optical Interconnects at 100Gbps and beyond," *Eur. Conf. Opt. Commun.*, 2013.
 - [12] A. F. Benner, M. Ignatowski, J. A. Kash, D. M. Kuchta, and M. B. Ritter, "Exploitation of Optical Interconnects in Future Server Architectures," *IBM J. Res. Dev.*, vol. 49, no. 4, pp. 755–775, 2005.
 - [13] J. W. Goodman, F. I. Leonberger, S.-Y. Kung, and R. A. Athalea, "Optical Interconnections for VLSI Systems," *Proc. IEEE*, vol. 72, pp. 850–866, 1984.
 - [14] R. T. Chen, L. Lin, C. Choi, Y. J. Liu, B. Bihari, L. Wu, S. Tang, R. Wickman, B. Picor, M. K. Hibbs-Brenner, J. Bristow, and Y. S. Liu, "Fully Embedded Board-Level Guided-Wave Optoelectronic Interconnects," *Proc. IEEE*, vol. 88, no. 6, pp. 780–793, 2000.
 - [15] F. E. Doany, C. L. Schow, R. Budd, C. Baks, D. M. Kuchta, P. Pepeljugoski, J. A. Kash, and F. Libsch, "Chip-to-chip Board-level Optical Data Buses Optocard," *OFC/NFOEC*, 2008.
 - [16] P. Kapur and K. C. Saraswat, "Optical Interconnects for Future High Performance Integrated Circuits," *Phys. E*, vol. 16, pp. 620–627, 2003.
 - [17] A. F. J. Levi, "Optical interconnects in systems," *Proc. IEEE*, vol. 88, no. 6, pp. 750–757, 2000.
 - [18] D. A. B. Miller, "Optical Interconnects to Silicon," *IEEE J. Sel. Topics Quantum Electron.*, vol. 6, no. 6, pp. 1312–1317, 2000.
 - [19] D. A. B. Miller, "Rationale and Challenges for Optical Interconnects to Electronic Chips," *Proc. IEEE*, vol. 88, no. 6, pp. 728–749, 2000.
 - [20] "Maxi-Pedia." [Online]. Available: <http://www.maxi-pedia.com/blade+server+what+is>.
 - [21] B. J. Offrein, "Optical Interconnects for Computing Applications," *Swisslasernet Work.*, 2010.
 - [22] D. A. B. Miller, "Optical Interconnects to Electronic Chips," *Appl. Opt.*, vol. 49, no. 25, pp.

- 59–70, 2010.
- [23] D. A. B. Miller, “Device Requirement for Optical Interconnects to Silicon Chips,” *IEEE Spec. Issue Silicon Photonics*, vol. 97, no. 7, pp. 1166–1185, 2009.
 - [24] D. A. B. Miller, “Limit to the Bit-Rate Capacity of Electrical Interconnects from the Aspect Ratio of the System Architecture,” *J. Parallel Distrib. Comput.*, vol. 41, no. 1, pp. 42–52, 1997.
 - [25] D. A. B. Miller, “Physical Reasons for Optical Interconnection,” *Int. J. Optoelectron.*, vol. 11, pp. 155–168, 1997.
 - [26] C. Berger, M. Kossel, C. Menolfi, T. Morf, T. Toifl, and M. Schmatz, “High-density Optical Interconnects Within Large-scale Systems,” *Proc. SPIE*, vol. 4942, pp. 222–235, 2003.
 - [27] E. Yuceturk, S. Esener, H. Dawei, and T. Sze, “Comparative Study of Very Short Distance Electrical and Optical Interconnects Based on Channel Characteristics,” *Opt. Comput.*, vol. 90, pp. 7–9, 2003.
 - [28] H. Braunisch, J. E. Jaussi, J. A. Mix, M. B. Trobough, B. D. Horine, V. Prokofiev, S. Member, D. Lu, S. Member, R. Baskaran, P. C. H. Meier, D. Han, K. E. Mallory, and M. W. Leddige, “High-Speed Flex-Circuit Chip-to-Chip Interconnects,” *IEEE Trans. Adv. Packag.*, vol. 31, no. 1, pp. 82–90, 2008.
 - [29] D. A. B. Miller, “Optics for Low-energy Communication Inside Digital Processors: Quantum Detectors, Sources, and Modulators as Efficient Impedance Converters,” *Opt. Lett.*, vol. 14, no. 2, pp. 146–148, 1989.
 - [30] M. Haurylau, G. Chen, H. Chen, J. Zhang, N. a. Nelson, D. H. Albonesi, E. G. Friedman, and P. M. Fauchet, “On-chip Optical Interconnect Roadmap: Challenges and Critical Directions,” *IEEE J. Sel. Topics Quantum Electron.*, vol. 12, no. 6, pp. 1699–1704, 2006.
 - [31] K. Koo, H. Cho, P. Kapur, and K. C. Saraswat, “Performance Comparisons Between Carbon Nanotubes, Optical, and Cu for Future High-Performance On-Chip Interconnect Applications,” *IEEE Trans. Electron Devices*, vol. 54, no. 12, pp. 3206–3215, 2007.
 - [32] J. H. Collet, F. Caignet, F. Sellaye, and D. Litaize, “Performance Constraints for Onchip Optical Interconnects,” *IEEE J. Sel. Topics Quantum Electron.*, vol. 9, no. 2, pp. 425–432, 2003.
 - [33] O. Kibar, D. A. Van Blerkom, C. Fan, and S. C. Esener, “Power Minimization and Technology Comparisons for Digital Free-space Optoelectronic Interconnections,” *J. Light. Technol.*, vol. 17, no. 4, pp. 546–555, 1999.
 - [34] E. Berglind, E. Berglind, C. Svensson, and C. Svensson, “A Comparison of Dissipated Power and Signal-to-Noise Ratios in Electrical and Optical Interconnects,” *J. Light. Technol.*, vol. 17, no. 1, pp. 68–73, 1999.
 - [35] P. Kapur and K. C. Saraswat, “Comparisons Between Electrical and Optical Interconnects for On-chip Signaling,” *Int. Interconnect Technol. Conf.*, pp. 89–91, 2002.
 - [36] S. Rakheja and V. Kumar, “Comparison of electrical, optical and plasmonic on-chip interconnects based on delay and energy considerations,” *Int. Symp. Qual. Electron. Des.*, pp. 732–739, 2012.
 - [37] G. I. Yayla, P. J. Marchand, and S. C. Esener, “Speed and Energy Analysis of Digital Interconnections: Comparison of On-Chip, Off-Chip, and Free-Space Technologies,” *Appl. Opt.*, vol. 37, no. 2, pp. 205–227, 1998.
 - [38] M. W. Haney and M. P. Christensen, “Performance Scaling Comparison for Free-space Optical and Electrical Interconnection Approaches,” *Appl. Opt.*, vol. 37, no. 14, pp. 2886–2894, 1998.
 - [39] E. D. Kyriakis-Bitzaros, N. Haralabidis, M. Lagadas, A. Georgakilas, Y. Moisiadis, and G. Halkias, “Realistic End-to-End Simulation of the Optoelectronic Links and Comparison with

- the Electrical Interconnections for System-on-Chip Applications,” *J. Light. Technol.*, vol. 19, no. 10, pp. 1532–1542, 2001.
- [40] M. R. Feldman, S. C. Esener, C. C. Guest, and S. H. Lee, “Comparison Between Optical and Electrical Interconnects Based on Power and Speed Considerations,” *Appl. Opt.*, vol. 27, no. 9, pp. 1742–1751, 1988.
- [41] A. Naeemi, J. Xu, A. V. Mule, T. K. Gaylord, and J. D. Meindl, “Optical and Electrical Interconnect Partition Length Based on Chip-to-Chip Bandwidth Maximization,” *IEEE Photon. Technol. Lett.*, vol. 16, no. 4, pp. 1221–1223, 2004.
- [42] C. Svensson, “Electrical interconnects revitalized,” *IEEE Trans. Very Large Scale Integr. (VLSI) Syst.*, vol. 10, no. 6, pp. 777–788, 2002.
- [43] H. Cho, K.-H. Koo, P. Kapur, and K. C. Saraswat, “Performance Comparisons Between Cu/Low- κ Carbon-Nanotube, and Optics for Future On-Chip Interconnects,” *IEEE Electron Device Lett.*, vol. 29, no. 1, pp. 122–124, 2008.
- [44] “Enabling Technologies for Board-level Optical Interconnects,” *Commun. Ind. Res.*, 2010.
- [45] J. Bautista, “The Potential Benefits of Photonics In The Computing Platform,” *Optoelectron. Integr. Circuits VIII*, vol. 5729, pp. 1–8, 2005.
- [46] S. Uhlig and M. Robertsson, “Limitations to and Solutions for Optical Loss in Optical Backplanes,” *J. Light. Technol.*, vol. 24, no. 4, pp. 1710–1724, 2006.
- [47] A. Benner, “Optical Interconnect Opportunities in Supercomputers and High End Computing,” *OFC 2012 Tutor. - Datacom, Comput. Short Range Exp. Opt. Networks*, 2012.
- [48] J. W. Trubini, L.J. Stafford, “iNEMI Optoelectronics Technology Roadmap,” 2006. [Online]. Available: <http://www.inemi.org>.
- [49] L. Schares, *et al.*, “Terabus: Terabit / Second-Class Card-Level Optical Interconnect Technologies,” *IEEE J. Sel. Topics Quantum Electron.*, vol. 12, no. 5, pp. 1032–1044, 2006.
- [50] N. Bamiedakis, A. Hashim, R. V. Penty, and I. H. White, “Regenerative Polymeric Bus Architecture for Board-level Optical Interconnects,” *Opt. Exp.*, vol. 20, no. 11, pp. 11625–11636, 2012.
- [51] J. Beals, N. Bamiedakis, A. Wonfor, R. V. Penty, I. H. White, J. V. DeGroot, K. Hueston, T. V. Clapp, and M. Glick, “A Terabit Capacity Passive Polymer Optical Backplane Based on a Novel Meshed Waveguide Architecture,” *Appl. Phys. A*, vol. 95, no. 4, pp. 983–988, 2009.
- [52] N. Bamiedakis, J. Beals, R. V. Penty, I. H. White, J. V. DeGroot, and T. V. Clapp, “Cost-effective Multimode Polymer Waveguides for High-speed On-board Optical Interconnects,” *IEEE J. Quantum Electron.*, vol. 45, no. 4, pp. 415–424, 2009.
- [53] R. Pitwon, M. Immonen, K. Wang, H. Itoh, T. Shioda, J. Wu, L. X. Zhu, H. J. Yan, and A. Worrall, “International standards for optical circuit board fabrication, assembly and measurement,” *Opt. Commun.*, vol. 362, pp. 22–32, 2016.
- [54] R. C. A. Pitwon, K. Hopkins, K. Wang, D. R. Selviah, H. Baghsiahi, B. J. Offrein, R. Dangel, F. Horst, M. Halter, and M. Gmür, “Design and Implementation of an Electro-optical Backplane with Pluggable In-plane Connectors,” *Proc. SPIE*, vol. 44, no. 0, p. 76070J–76070J–12, 2010.
- [55] A. Hashim and N. Bamiedakis, “Multimode 90°-Crossings, Combiners and Splitters for a Polymer-Based On-Board Optical Bus,” *Conf. Lasers Electro-optics*, p. CM2A.5, 2012.
- [56] A. Hashim, N. Bamiedakis, J. Beals, R. V. Penty, and I. H. White, “Cost-effective 10 Gb/s Polymer-based Chip-to-Chip Optical Interconnect,” *IET Optoelectron.*, vol. 6, no. 3, p. 140, 2012.
- [57] N. Bamiedakis, A. Hashim, J. Beals, R. V. Penty, and I. H. White, “Low-cost PCB-integrated 10-Gb/s Optical Transceiver Built with a Novel Integration Method,” *IEEE Trans. Compon. Packag. Manuf. Technol.*, vol. 3, no. 4, pp. 592–600, 2013.

2 TECHNOLOGY

CONSIDERATIONS FOR BOARD-LEVEL OPTICAL INTERCONNECTS

This chapter provides a brief introduction to board-level optical interconnection technologies and reviews their major constituent optical components. Suitable materials technologies for integration with conventional PCBs are discussed with particular focus on the characteristics of siloxane polymers. Active optoelectronic components used to take advantage the development of on-board optical interconnects including VCSELs and PDs are introduced and a review of different coupling schemes between polymer waveguides and such devices is provided. The main research conducted in the field is presented along with a review of the state-of-the-art demonstrators in polymer waveguide technology for on-board optical interconnections. The direction of this thesis is finally discussed.

2.1 Introduction

As seen in Chapter 1, the ever increasing interconnection bandwidth for short-reach links is pushing traditional electrical links to the limits. Optics can offer a solution to solve the bandwidth bottleneck problem; however a technology appropriate for cost-effective board-level interconnects is required. As the coexistence of optics and electronics in future

electronic systems is inevitable, it is necessary to integrate optics readily into existing system architectures using compatible manufacturing processes with conventional PCBs. Therefore, this chapter provides an overview of board-level optical interconnection technologies with a discussion of appropriate polymer materials, optical components and sub-system architectures that are suitable for on-board integration.

In summary, a complete board-level optical link consists of the following parts: (a) transmission media, (b) a transmitter, (c) a receiver and if necessary (d) coupling optics. These different areas are reviewed separately in this chapter. Section 2.2 introduces and compares the advantages and disadvantages of different transmission media employed in integrated optical circuits. Section 2.3 focuses on polymer materials compatible with standard PCBs while some common waveguide fabrication techniques are discussed in section 2.4. High-speed active optical devices such as vertical-cavity surface-emitting lasers (VCSELs) and photodiodes (PDs) used in board-level optical interconnection systems are discussed in section 2.5. Section 2.6 reviews different coupling schemes that enable cost-effective system integration. The chapter closes by highlighting state-of-the-art demonstrators from major academic and industrial research groups in the field as discussed in section 2.7. The strengths and weaknesses of recently demonstrated board-level optical interconnect technologies are shown to influence the direction of this thesis. Finally, section 2.8 concludes the chapter.

2.2 Transmission Medium

There are many approaches to implementing optical interconnects and a wide range of materials can be utilised to develop integrated optical devices. These range from free-space systems to guided systems based on silica, silicon and polymer. It is valuable briefly to discuss the most common techniques used in optical interconnects. Each technology area is broad and thus it is not feasible to describe all thoroughly here. Rather, a brief overview will be given in order to summarise their suitability for use in board-level optical interconnections.

A number of free-space optical interconnects have been successfully demonstrated. It is perhaps the most straightforward method for short-distance point-to-point optical links as it utilises air [1], [2] or a substrate as medium for light propagation [3]. Point-to-multipoint free-space systems such as a shared-bus topology are also demonstrated [4], [5]. Free-space interconnects have been developed employing active routing by means of holographic beam

steering [6] or using micro-electro-mechanical systems (MEMS) devices [7] while passive routing has also been employed and implemented using for example beam-steering diffraction gratings [8]. The need for light steering is disadvantageous given its complexity and hence increased system assembly cost. In addition, the main challenge that all free-space optics face is the need for good alignment which necessitates excellent packaging design in order to maintain the tight alignment tolerances over the life-time of the system. Although some solutions exist to the alignment problems such as the use of active alignment [9], the fundamental issues of maintaining the alignment of delicate components is challenging. Moreover, any dust on the free-space element surfaces may introduce extra link loss or even system failure.

The use of waveguide structures can eliminate many problems found in free-space systems. Mature optical fibre technologies have led to studies concerning their possible use in board-level optical interconnects for the following reasons: (i) very low loss; (ii) compatibility with many readily available optoelectronic components; and (iii) known optical transmission properties. However, a major drawback of fibre-based technologies for interconnect applications is that they need to be assembled as discrete elements and a straightforward method of integrating fibres onto the conventional PCBs is not yet available. Moreover, glass fibre is difficult to manufacture and install over short lengths in addition to being expensive, fragile and having high bending losses [10]. Although perfluorinated plastic optical fibre (POF) is gaining popularity as an alternative low-cost solution to glass fibre for short-reach optical links [11], its low-loss transmission wavelength is the visible light spectrum which limits the data rates due to the availability of high-speed sources at these wavelengths although sources in the 800 nm range may be suitable for very short links [12].

The use of integrated waveguide technology has been proposed as an alternative to using optical fibres or other discrete elements. Monolithic interconnect structures allow the formation of functional components such as splitters, couplers and filters directly in the waveguides, and thus offer more cost-effective and efficient optical systems. There are different ways of implementing integrated planar lightwave circuits (PLCs). Silicon-on-insulator (SOI) technologies are enjoying a growing interest in part due to the success of silicon photonics. The high index step between silicon and silicon dioxide allows strong confinement, tight bend structures and high waveguide packing density. In addition, it becomes possible to integrate active devices such as lasers, photodiodes and modulators on chip directly using SOI technology [13], [14]. Moreover, the compatibility with standard

complementary-metal-oxide-semiconductor (CMOS) platforms makes silicon photonics very appealing at a commercial level [15], [16]. However, the high propagation loss (0.1–3 dB/cm) depending on the dimensions and processing conditions [17] and large mismatch with low-cost multimode fibre and VCSEL technology make it an unsuitable candidate for large-scale board-level optical interconnects such as backplanes. As a result, SOI technology is believed to be a promising candidate for use in on-chip interconnections [18].

Polymers are another class of materials that are attractive for use in integrated optical devices. They are sufficiently low-cost, flexible (mechanical flexibility shown in Figure 2-1), possess favourable thermal, mechanical and optical properties and can be fabricated on any type of substrate practically. The selection of polymers is typically application-specific to ensure best performance without experiencing severe environmental degradation. Polymer structures can be patterned using a variety of techniques including but not limited to photolithography, moulding, embossing and direct printing [19], [20]. Importantly, there are a variety of polymers that exhibit low transmission loss at the datacommunication wavelength of 850 nm. In particular, they can be integrated with existing PCB technology in the way that other aforementioned materials do not. This makes polymer technology very appealing for use in short-reach optical links.

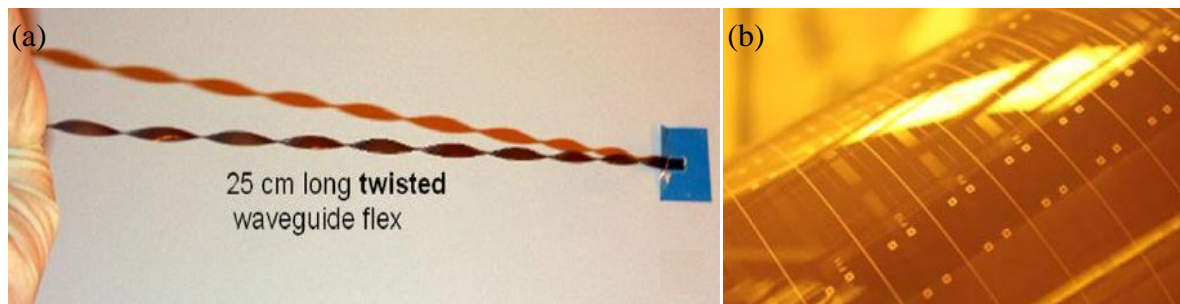


Figure 2-1 (a) No visible cracking shown in twisted polymer waveguides during the twist and (b) large-area flexible polymer waveguide demonstrators [21], [22].

Owing to its perceived compatibility with conventional PCB manufacturing processes and the potential of fabricating polymer waveguides on a large-scale in a cost-effective manner, this thesis focuses on polymer waveguide elements exclusively as the base for future board-level interconnection applications. However, it should be emphasised that an awareness of on-going research based on other materials is required for any future technology development. The hybrid integration of different material platforms such as silicon and polymers may ultimately offer optimised system performance.

2.3 Polymer Materials

It is worth reviewing key characteristics of polymers such as their thermal, mechanical and optical properties to appreciate why a particular Dow Corning siloxane polymer is chosen for use in this thesis.

Common polymer materials used for polymer waveguides are SU-8 (from MicroChem) [23], fluorinated polyimide [24], polymethylmethacrylate (PMMA) [25] and some commercial polymers such as Ormocer® (from Fraunhofer ISC) and Truemode™ (from Exxelis). However, the majority of polymers used in photosensitive patterning can be classed as epoxies, acrylates, polyimides and siloxanes. Many factors must be considered while choosing a certain type of polymer for a particular application. Some of the most important properties that polymers need to possess for the applications of optical waveguides are listed below.

Table 2-1 Attributes of interest for polymer materials for optical waveguides [19].

Low absorption loss
Low birefringence
Low polarisation dependent loss (PDL)
Low polarisation mode dispersion (PMD)
Variable refractive index difference (Δn)
Ability to vary refractive index profile
Low refractive index dispersion ($dn/d\lambda$)
Thermal stability
Stability with humidity
Adhesion (to substrates, self, electrodes)
Machinability (cleaving, dicing, polishing)
Large thermo-optic coefficient (dn/dT)
Optimal thermal conductivity
Manufacturability with repeatable properties

As mentioned earlier, the wavelength range used for short-reach datacommunication links is around 850 nm due to the availability of cost-effective and high-speed active optical

devices (will be explained in more details shortly). Therefore, a variety of polymer materials have been appropriately engineered to exhibit low losses at short wavelengths (800–850 nm). These are reviewed and summarised in Table 2-2.

Table 2-2 Summary of common polymer materials characterised at 800-850 nm wavelength.

Manufacturer	Polymer Type [Trade Name]	Patterning Techniques	Propagation Loss, dB/cm [wavelength, nm]
Corning [19]	Acrylate	Photoexposure / wet etch, RIE, laser ablation	0.02 [840]
Dow Corning [26]	Polysiloxane	Photoexposure/wet etch	0.04 [850]
General Electric [27]	Polyetherimide	RIE, laser ablation	0.24 [830]
NTT [28]	Halogenated acrylate	RIE	0.02 [830]
Optical Crosslinks [29]	Acrylate	Diffusion	0.18 [800]
Telephotronics [30]	[OASIC TM]	Photoexposure / wet etch, RIE, laser ablation	<0.01 [840]

Siloxane polymers possess a number of desirable characteristics that have been of particular interest for use in optical waveguides. Alternating oxygen and silicon atoms composes the backbone of a siloxane polymer without carbon in the backbone chain as is the case for many other polymers, making it an unusual “inorganic” polymer with great stability at high temperatures and resistance to water and oxidation [31]. The siloxane molecule can rotate freely around the Si-O bond, resulting in low birefringence (3.0×10^{-5}) [20]. Meanwhile by engineering its chemistry the thermo-optic coefficient of the siloxane material may be tuned from ~ -2 to $-5 \times 10^{-4}/^{\circ}\text{C}$ [32].

Compared with carbon-based polymers, siloxane polymers have demonstrated excellent reliability and are less susceptible than many polymers to long-term degradation when subjected to high temperature, humidity and high optical flux owing to their stronger and more stable Si-O bonds. This makes them very appealing for use in harsh environments for applications requiring long-term reliability and particularly for use in PCBs where solder-

reflow and lamination may occur. The negligible effect of temperatures on the optical loss of bulk polydimethylsiloxane (PDMS) can be observed in Figure 2-2.

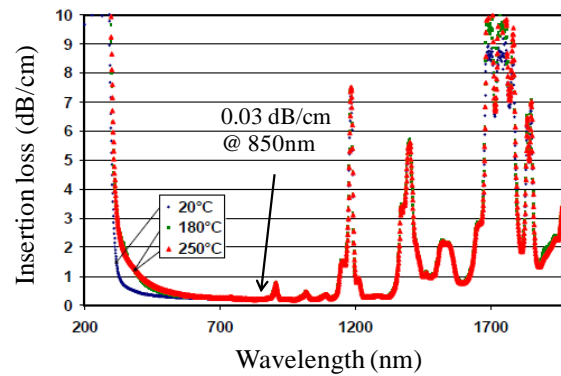


Figure 2-2 Negligible effect of temperature on the optical transmission of bulk generic PDMS [33].

Figure 2-3(a) shows the temperature and optical loss comparison of different polymer families while the optical propagation loss of the Dow Corning siloxane material over a range of wavelengths is shown in Figure 2-3(b). It can be seen that acrylates have superior performance of low optical loss at 850 nm than polyimides, while polyimides exhibit much better thermal robustness compared with acrylates [34]. The PDMS polymer developed by Dow Corning Corporation (labelled as DC silicon) possesses both good optical and thermal properties.

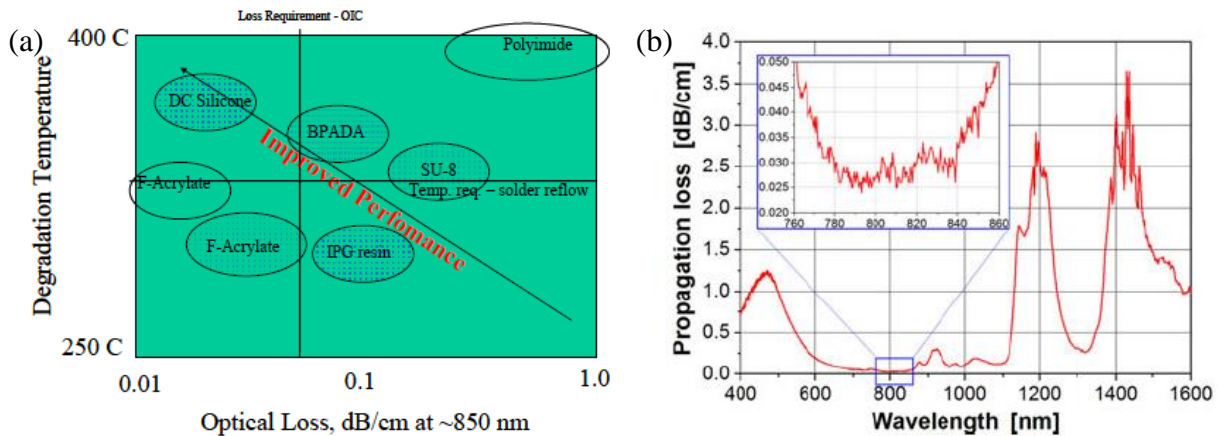


Figure 2-3 (a) Degradation temperature and optical loss comparison of different polymer families [34] and (b) measured propagation loss of Dow Corning siloxane material [21].

The siloxane materials employed in this work have been developed by Dow Corning. Over the years, these materials have been gradually improved from previous ones known as OE-4140 Optical Elastomer core and OE-4141 Optical Elastomer cladding to the latest ones

named as WG-1020 Optical Waveguide Core and XX-1023 Optical Waveguide Clad. They have been appropriately engineered to offer superior material performance for use in board-level optical interconnections. The materials can be directly spun onto a variety of substrates such as FR4, silicon or glass which allows the direct integration onto conventional PCBs. These materials have successfully passed the solder reflow and environmental stability tests, and shown the ability of withstanding temperatures up to 350°C [34]. This attribute is very important due to the lead-free solder technologies such as Sn-Ag-Cu used in the electronics industry which have high melting points (around 200–230°C) [35].

In addition, the Dow Corning siloxane materials exhibit very low intrinsic attenuation at datacommunication wavelengths (~ 0.03 dB/cm at 850 nm). This value is below the recommended loss (0.05 dB/cm at 850 nm) typically required for board-level optical links (~ 1 m in length) to achieve a sufficient system power margin [36]. Moreover, they have been successfully tested to Telecordia GR-1209/GR-1221-CORE standards [37], [38]. No measureable changes in intrinsic losses have been found after over 2000 hours under 85°C and 85% relative humidity environment. The materials have also been subjected to 500 thermal cycles from -40°C to +120°C, after which stable optical properties have been observed [22], [34]. Finally, the refractive index of the bulk materials can be tuned accordingly so as to meet the required index differences between the core and the cladding for different applications.

In summary, the Dow Corning siloxane materials employed in this thesis exhibit excellent properties to satisfy all important technological requirements associated with the applications of board-level optical interconnections:

- Sufficiently low-cost;
- Very low loss around the datacommunication wavelengths (0.03–0.05 dB/cm);
- Very low birefringence ($< 5 \times 10^{-5}$);
- Optical stability or resistance to high optical flux;
- High thermal and environmental stability (up to 350 °C);
- Large refractive index tunability (1.49–1.52);
- High processability (adhesion, coating, etching, dicing, etc.);
- Flexible.

2.4 Waveguide Fabrication

There are a variety of methods of fabricating polymer waveguides. Depending on the type of polymer, production cost and the ease of fabrication required, an appropriate fabrication technique should be chosen. Common techniques for casting polymer films include spin coating, doctor-blading, extrusion and lamination. Ensuring that a film is free of bubbles and striations and is of uniform thickness with good attachment to the substrate are the major issues in the process of film fabrication. There are advantages and disadvantages for each casting technique. For instance, spin coating provides good control of uniformity and thickness but has difficulty in removing striations. Primary methods for the fabrication of polymer waveguides are photoresist-based patterning, direct lithograph patterning, laser direct writing and soft lithography. Figure 2-4 illustrates the fabrication procedure for photoresist-based patterning, direct lithographic patterning and laser direct writing respectively, while Figure 2-5 shows two examples of microtransfer moulding (μ TM) and micromoulding in capillaries (MIMIC) used in the soft lithography.

- Photoresist-based Patterning

In general, this fabrication method of polymer waveguides is similar to a standard semiconductor processing technology, for instance where one would use spin-coating, baking and reactive ion etching (RIE). A solvent is typically applied to the sample to remove the photoresist in any unwanted areas. The problem is that conventional RIE can introduce large surface roughness and thus induce large scattering losses. Therefore, significant efforts have been made to improve this fabrication process to minimise the roughness-induced scattering losses by optimising the process in areas of deep, smooth and vertical sidewall etching [30]. However this approach, using large-area photolithography, has higher cost not least due to the requirement of large-size masks.

- Direct Lithographic Patterning

Direct lithographic patterning is often used to fabricate waveguides made from photosensitive polymers. The waveguide structure is fabricated by wet etching of the polymer films selectively exposed to light through a mask [39]. This method offers a simplified process with faster turnaround times and typically induces less surface roughness than RIE processes.

- Laser Direct Writing

Laser direct writing is another way of forming waveguide structures in polymer films. A laser beam spot is used to define the desired waveguide patterns. This method is more rapid and cost-effective because it requires no mask as opposed to the traditional mask-based photolithographic approaches in which masks need to be designed and fabricated before the waveguides can be made. Also, this technique has the potential to be adopted in the large-scale fabrication where masks cannot be easily produced [29].

- Soft Lithography

Soft lithography or moulding is a non-photolithographic technique used in microfabrication pioneered by Xia and Whitesides [40]. This process includes casting, embossing, and moulding or stamping techniques. Using this technique, the micro-structures of the polymer can be replicated on a given substrate by using the PDMS mould, which can be prepared by casting PDMS on a silicon master with the desired micro-structures. Microtransfer moulding (μ TM) and micromoulding in capillaries (MIMIC) are two examples. Soft lithography is a cost-efficient technique and is suitable for large-scale manufacturing. However, the drawback of this approach is that it also induces additional surface roughness which results in larger scattering loss.

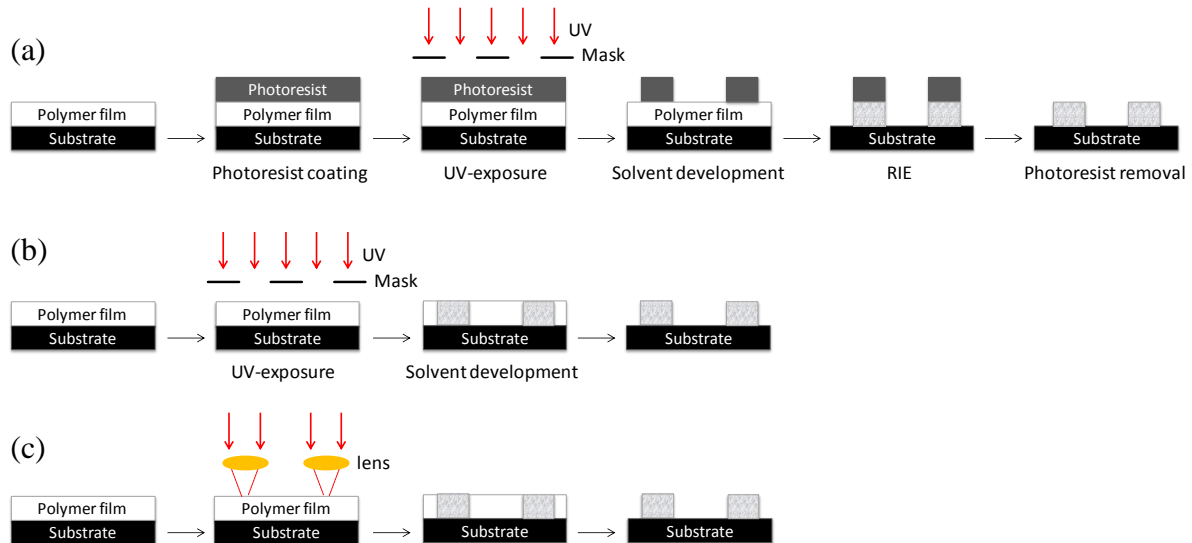


Figure 2-4 Schematic illustration of procedures for (a) photoresist-based patterning, (b) direct lithographic patterning and (c) laser direct writing [30].

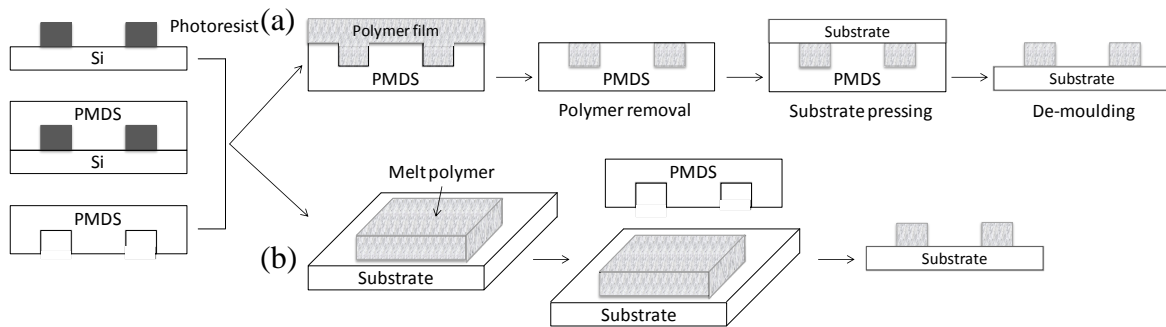


Figure 2-5 Schematic illustration of procedures for (a) microtransfer moulding (μ TM) and (b) micromoulding in capillaries (MIMIC) [30], [40].

Other fabrication processes include but are not limited to laser ablation [41], [42], ink jet printing [43], [44] and direct dispensing [45], [46]. Despite the range of fabrication techniques, this work mainly results from conventional photolithography for the following reasons. Firstly, it is straightforward and relatively fast to fabricate waveguides using fabrication facilities in the clean room at Centre of Advanced Photonics and Electronics (CAPE) laboratory. Secondly, the siloxane polymers are photosensitive under ultra-violet (UV) irradiation. Thirdly, the waveguides have planar structures and hence there is no need for use other complex fabrication techniques.

Figure 2-6 illustrates the fabrication process used for the optical waveguides employed in this work. The bottom layer is first coated on a substrate (FR4, silicon or glass) for the purpose of masking the substrate surface roughness and ensuring sufficient waveguide isolation from the substrate. A core polymer layer is deposited on top of the bottom cladding layer, and subsequently is exposed under UV irradiation via a mask. The exposed polymer core material remains as it is negative photoresist while the unwanted areas of polymers are washed away by the properly designed solvent. Finally the top cladding layer is added. The top cladding serves as a protective layer for the waveguide core to avoid any damage from the ambient environment and also from the dicing process. More details about the waveguide design parameters will be discussed in section 3.2 in Chapter 3.

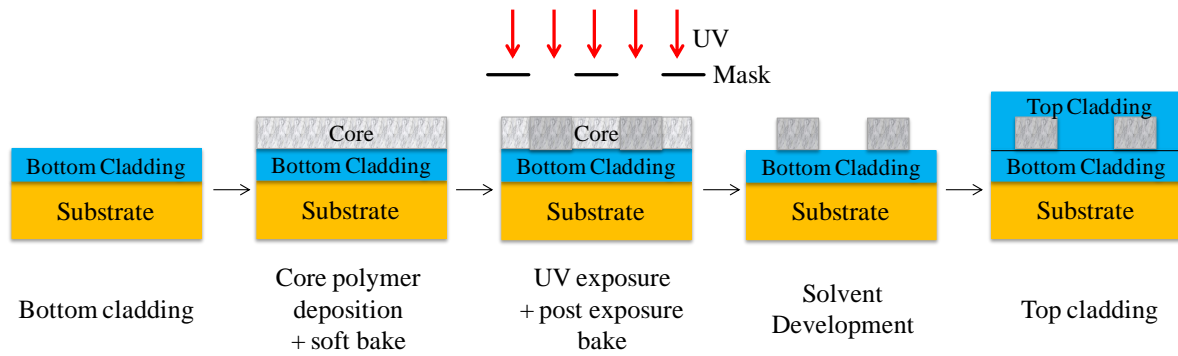


Figure 2-6 Fabrication procedure for the siloxane polymer waveguides employed in this thesis.

2.5 Active Components

To ensure the successful deployment of polymer waveguides, the use of active optoelectronic components needs to satisfy requirements such as low cost, high bandwidth, low power consumption and easy integration on PCBs. In the following sections, the suitable technologies of active devices for on-board optical interconnects are briefly reviewed.

2.5.1 Optical Sources

Light emitting diodes (LEDs) and semiconductor lasers are the two commonly used optical transmitters for optical communications. LEDs have much lower costs than lasers. However they have limited bandwidth, typically of the order of 250 MHz [47]. So in order to achieve the targeted on-board data rates (e.g. ≥ 25 Gb/s), lasers need be considered due to their much higher bandwidth. There are two types of lasers for board-level optical interconnections, which are edge-emitting diode lasers and surface-emitting diode lasers. The latter, particularly vertical-cavity surface-emitting lasers (VCSELs), are generally agreed to be the preferred optical sources due to a number of appealing characteristics: low cost, low current density, low power consumption, high modulation bandwidth and availability in an array configuration [48]. In addition, their apertures are typically smaller than the cross-sectional area of multimode polymer waveguides ($< 15 \mu\text{m}$) and their numerical apertures are small enough to enable easy and efficient coupling into these waveguides ($\text{NA}_{\text{wg}} \leq 0.25$) [49].

Since VCSELs were invented by Prof. Kenichi Iga in 1977 [50], they have attracted worldwide research interest and have become the major optical sources in the Gigabit Ethernet and high-speed local-area networks (LANs) [51]. Although VCSELs operating at

1310 nm and 1550 nm have been demonstrated for use in long distance telecommunications, VCSELs have been mostly used in short reach data communications at 850 nm [52]. They are ideal for use with polymer waveguides also as the polymer materials have low loss at similar wavelengths. As VCSEL-based optical interconnects with speed of 25 Gb/s over each channel are becoming available commercially, the next-generation is likely to be 40 Gb/s or even higher for applications in high-performance computing and data centres [53], [54]. Figure 2-7(a) summarises bit rate and temperature records for 850 nm VCSELs in the past 15 years while Figure 2-7(b) shows their improvement in speed in recent years [54]–[69]. It is clear that the VCSEL devices have been rapidly developed over the past decade with consistently increasing speeds while the market for VCSELs is still continuously growing [70].

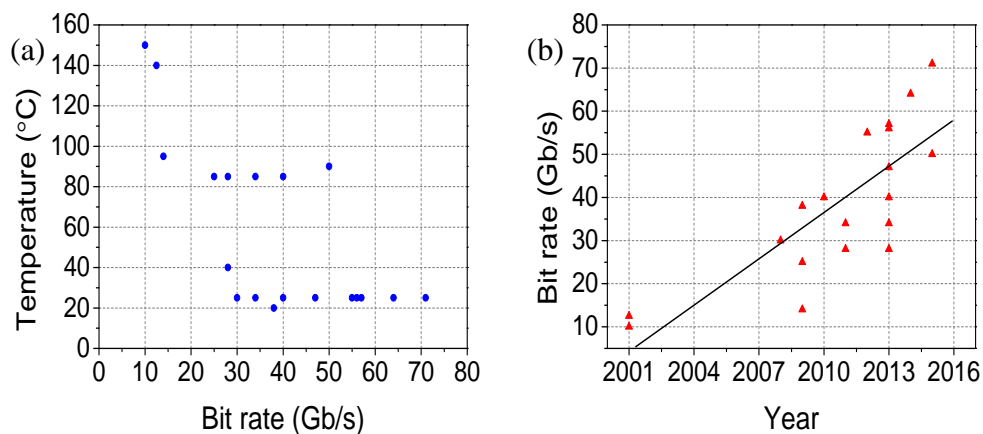


Figure 2-7 (a) VCSEL speed records versus temperature and (b) speed records versus year of development since 2001 [57].

On-going research in both academia and industry have focused on VCSEL-based high-speed optical interconnects. For example, the feasibility of a robust VCSEL array based system with 24 channels operating at 15 Gb/s each (aggregate 360 Gb/s) has been demonstrated using polymer waveguides [71]. In addition, structures such as micro-lenses [72] or output rods [73] integrated with VCSEL devices have been shown to improve the coupling efficiency with polymer waveguides. Therefore, it is widely recognised that VCSELs are appropriate optical sources that complement the characteristics of polymer waveguides used in board-level optical interconnects.

2.5.2 Optical Receivers

A high-bandwidth optical receiver is equally important for high speed on-board optical interconnections to convert the light at the waveguide output to electrical signals. There are three main types of commercially available photodetectors: PIN PDs, metal-semiconductor-metal photodiodes (MSM) PDs and avalanche photodiodes (APDs). To date, most of the optical interconnections based on multimode polymer waveguides employ PIN PDs as they require low reverse bias voltages of 2-5V (comparable to the on-board electronic components), have high conversion efficiency (~98%) [74], [75] and are also available in array configurations. For example, 1×12 high-speed photodiode arrays with each operating up to 40 Gb/s are commercially available at 850 nm [76]. It should be noted that smaller size photodiodes are used to minimise device capacitance and increase the bandwidth [77]. However, these can potentially cause reduced coupling efficiency. Therefore, it is important that the PD's aperture is larger than that of the polymer waveguides to prevent excessive coupling losses.

Despite PIN PDs being the most commonly used receivers, other PDs are worthy of investigating for future board-level optical interconnects. For instance, APDs may be considered when the link loss is very high as they have much higher responsivity due to their internal gain. However, the drawback of APDs is their high reverse bias voltage [47], [75]. In addition, MSM PDs have been demonstrated as fully embedded with polymer waveguides [78], [79]. MSM PDs have low-capacitance and a larger active area than PINs but their responsivity is typically lower than of PINs.

2.6 Coupling Schemes

Having discussed a variety of materials and fabrication processes of polymer waveguides as well as the suitable active devices for low-cost polymer based interconnects, it is of great importance to develop cost-effective assembly and packaging techniques for the whole optical interconnection system. In this context, the development of low-loss coupling schemes for coupling the light in and out of the polymer waveguides is briefly reviewed. There are essentially two coupling schemes that are being explored by different research groups: out-of-plane and butt-coupling (see Figure 2-8). There are numerous approaches to realising these schemes, and a short overview of the advantages and disadvantages of different coupling schemes is given in the following sections.

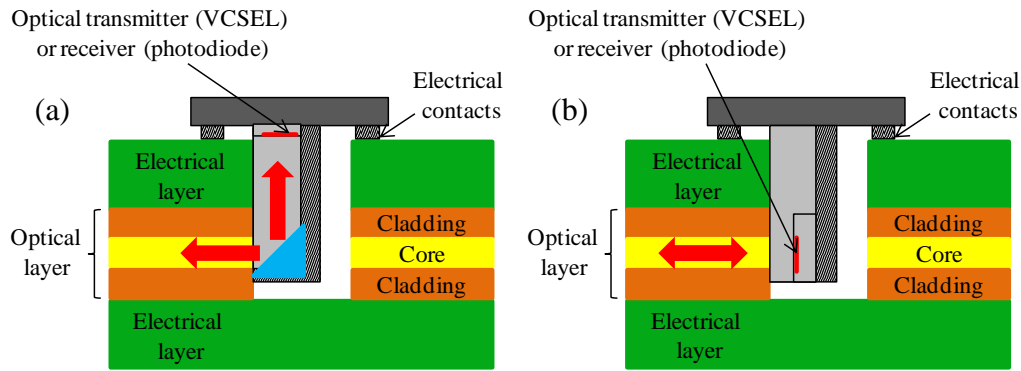


Figure 2-8 Illustration of coupling schemes: (a) out-of-plane and (b) butt-coupling [80].

2.6.1 Out-of-plane Coupling

Out-of-plane coupling scheme is very appealing as it allows simple implementation. The optoelectronic modules can be placed on the surface of the board in close proximity to the driving circuits, therefore enabling short electrical wire connections to the electronic chips. However, the use of 90° beam-turning elements is required at the both waveguide ends to couple the light in and out of the optical transmission layer, which results in the complexity in the optical domain. A number of techniques to achieve beam-turning have been employed and are reviewed below.

- Integrated 45° Mirror

A substantial amount of work has been conducted for the study of out-of-plane waveguide mirrors alone. Numerous approaches for forming these 45° mirrors have been demonstrated including laser ablation [81], [82], laser direct writing [83], dicing [28], [84], [85], v-blade cut waveguides [86], [87], wedge-shaped end-blocks [88], reactive ion etching [89], micro-milling [33], moulding [90], [91], embossing [92], UV photolithography [93], X-ray lithography [94] and grey-scale lithography [95]. Waveguide integrated 45° mirrors with excess loss below 1 dB have been fabricated using many of the above methods [84], [90], [91], [94]. Figure 2-9 depicts some examples of the integrated 45° mirrors fabricated.

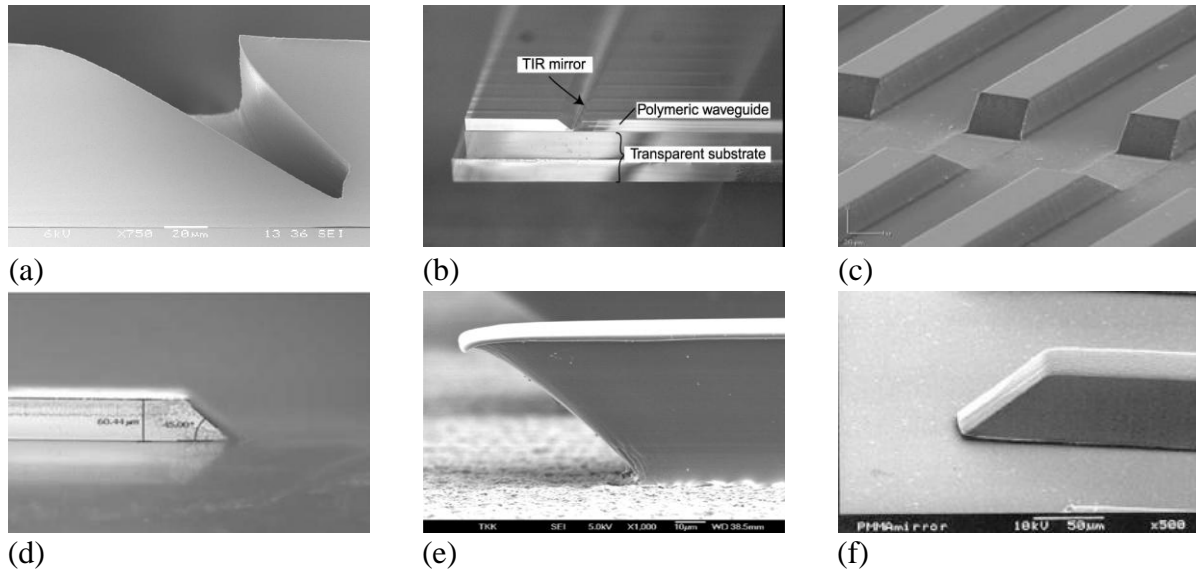


Figure 2-9 Examples of waveguide integrated 45° mirrors using fabrication methods of (a) laser ablation [82], (b) dicing [28], (c) micro-milling [33], (d) embossing [92] (e) UV photolithography [93] and (f) X-ray lithography [94].

It is important to note that the integration of mirrors in board-level interconnections imposes strict requirements on the fabrication process of the hybrid optoelectronic board. The performance of the mirrors, whether metalised or operating on a total internal reflection (TIR) principle, can be severely impaired by the surface roughness and non-optimum angles. In addition, the TIR mirrors can be contaminated in real-world applications so that their reflectivity can be affected [88]. Moreover, the metalised mirrors increase the fabrication complexity as additional post processing steps are required. Therefore, it is necessary that highly-reflective mirrors are cost-effectively formed in order to meet the performance and low cost requirements.

A suitable beam delivery scheme is also required in such out-of-plane coupling configurations in order to reduce the losses owing to the beam divergence along the free-space optical path. Various configurations for beam delivery have been proposed, including direct coupling, micro-lens coupling (single or a pair) and vertical waveguide coupling using optical pillars (Figure 2-10) [96]. Direct coupling is the most cost-effective scheme. However, it is only suitable when the VCSEL output beam has low light divergence and/or the separation distance between the waveguide and VCSEL is short. Although the use of micro-lenses or optical pillars can improve the system performance, the main disadvantage is that additional fabrication and assembly steps are required which result in increased costs [97]. Overall, numerous board-level interconnection systems employing these integrated 45° mirrors have been demonstrated as shown in Figure 2-11 [28], [98], [99].

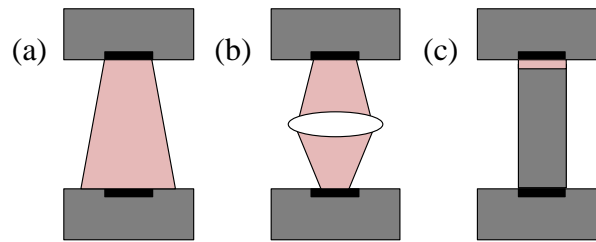


Figure 2-10 Beam delivery techniques: (a) directly coupling, (b) with micro-lenses and (c) with optical pillars [96].

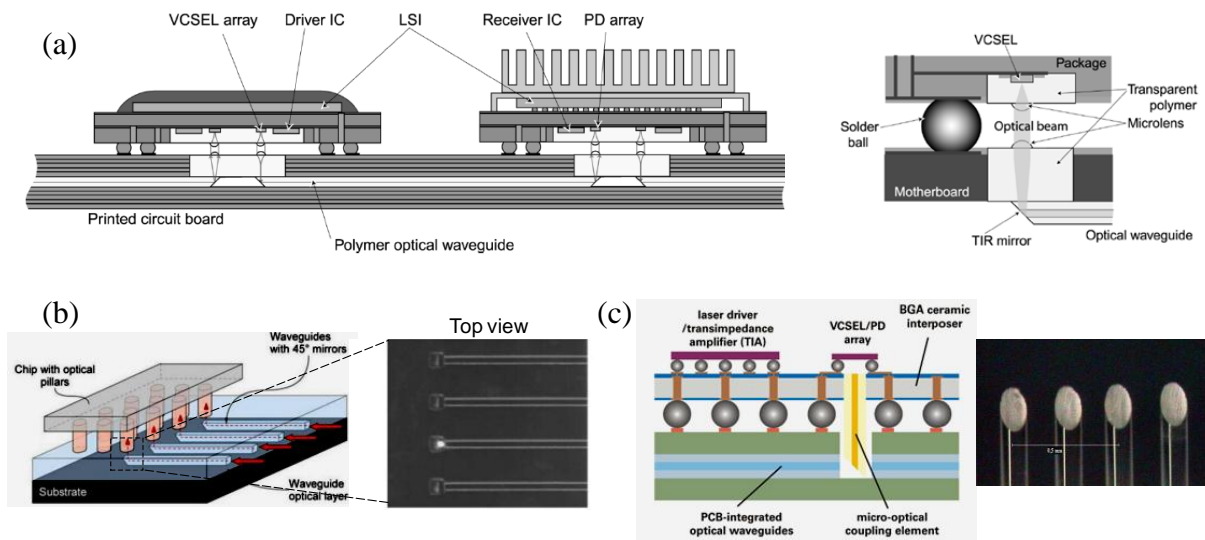


Figure 2-11 Examples of interconnection systems employing integrated 45° mirrors and various beam delivery schemes employing (a) dual-lens [28], (b) and (c) optical pillars [98], [99].

- Other Schemes

Alternative schemes include the use of 90°-bent multimode fibre arrays [100]–[102], evanescent couplers [103] and diffraction gratings [104], [105]. The concept of 90° micro-bends is illustrated in Figure 2-12. This scheme enables the deployment of conventional two-dimensional multimode arrays with a sufficiently low loss of 0.6 dB for a 1 mm fibre bending radius. In addition, Figure 2-13 shows the configuration for the evanescent fibre ribbon couplers. The optical evanescent coupling scheme is based on the concept of a waveguide directional coupler and achieved by putting pressure on polymer waveguide ribbons. The scheme is low-cost but sensitive to pressure change. Finally, the implementation of surface grating structures is illustrated in Figure 2-14. This scheme is wavelength-sensitive and requires careful design of waveguide parameters. The accurate fabrication of such grating structures also raises concerns on the potential of use in low-cost interconnection systems.

Nevertheless, the latter two schemes are not very appealing from a manufacturing perspective as their high coupling losses (>3 dB) do not justify their complexity.

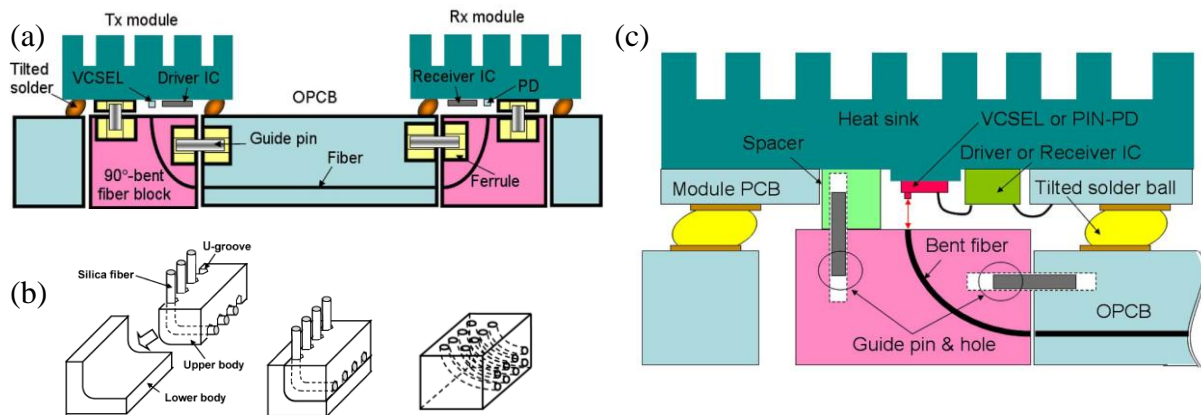


Figure 2-12 Illustration of coupling scheme employing conventional fibre ribbon arrays: (a) system schematic, (b) schematics for single-layer and multi-layer connection and (c) detailed coupling configuration [100]–[102].

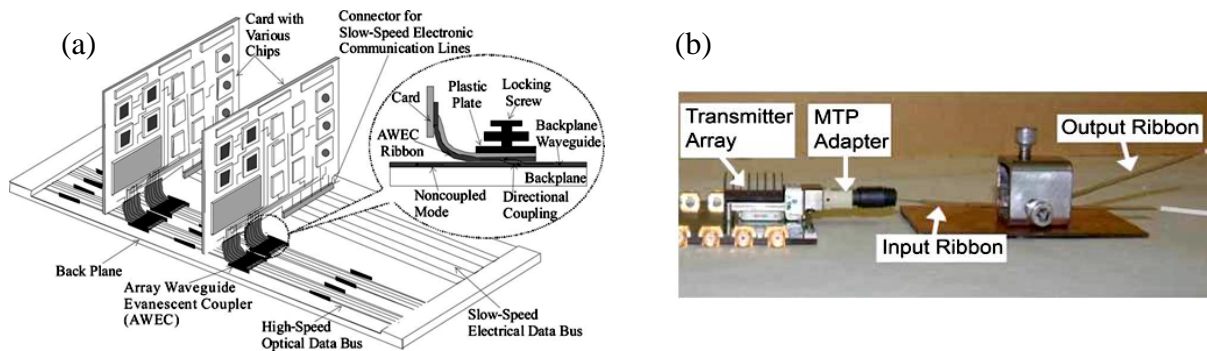


Figure 2-13 Illustration of coupling scheme employing an evanescent fibre ribbon coupler: (a) system schematic and (b) actual implementation [103].

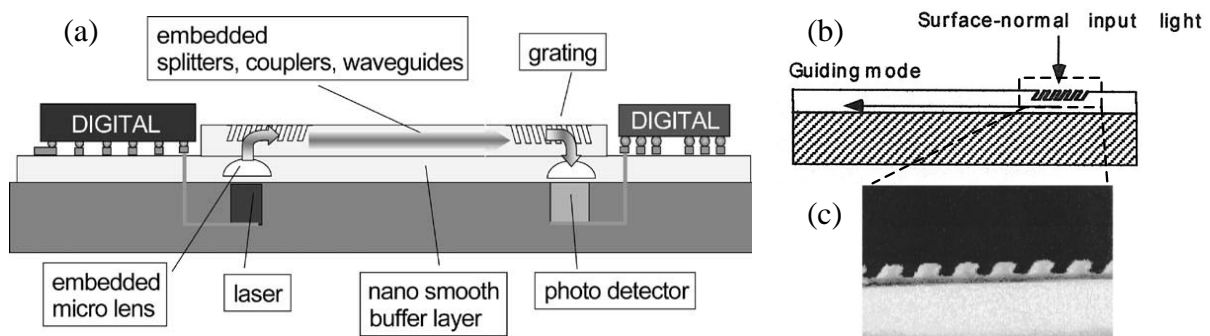


Figure 2-14 Illustration of coupling scheme employing a tilted surface grating: (a) system schematic, (b) schematic of coupling a surface-normal input light into waveguide and (c) a tilted grating structure [104], [105].

2.6.2 Butt-coupling

Butt-coupling (or end-fire/in-plane coupling) have primarily leveraged either the existing connector types such as mechanical transfer (MT)-ferrule [106]–[109] or stripped optical fibres and then accommodate directly in the locating slots that are integrated in the polymer layer itself [110]–[112]. This scheme couples output light from the VCSEL or fibre input into the polymer waveguides and onto the PD or output fibre directly. The need for additional beam turning elements can be eliminated, and therefore the cost can be reduced. Butt-coupling is an attractive candidate for low-cost optical interconnections as it requires less optical components to be formed and aligned. Although the complexity in the optical domain is reduced, careful design is required in the electrical domain. For instance, impedance matching connectors are needed to route the high-speed electrical signal from the surface of the board by 90° to the optical sources and detectors positioned near the waveguide facets.

Ribbon fibre connectors (e.g. MT-type) appear to be an appealing method as they offer manual plug-and-play assembly and good repeatability, enabling the low-cost implementation. This has been demonstrated by IBM as illustrated in Figure 2-15 [106], [107], while another similar design demonstrated by Xyratex and UCL is shown in Figure 2-16 [108], [109]. However, such schemes are typically used at the edge of the board due to the required large area to place the pins and ferrules, therefore imposing strict layout requirements and limiting them for use mostly in card-to-card rather than chip-to-chip interconnections.

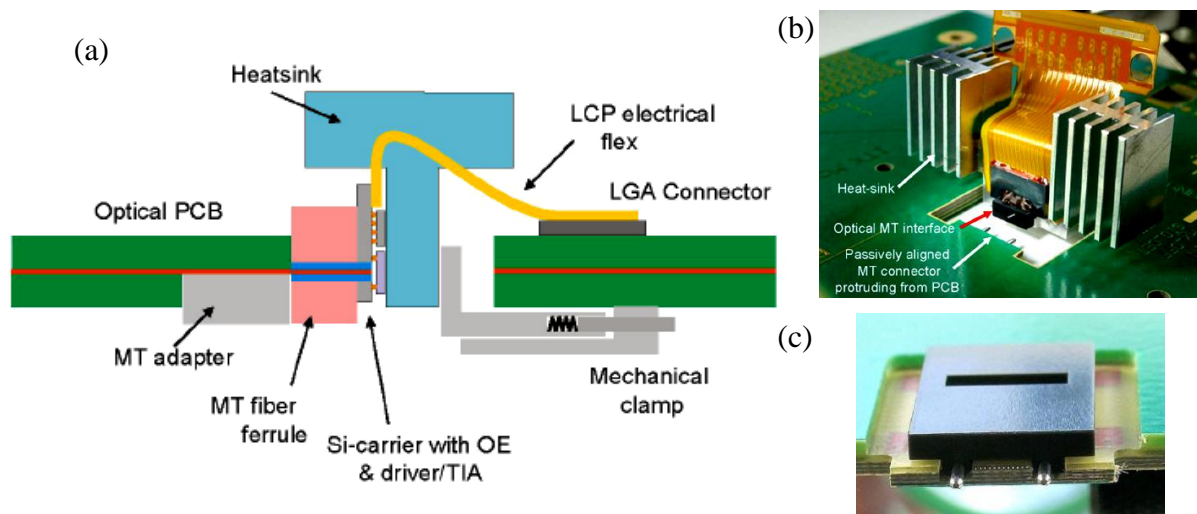


Figure 2-15 Illustration of a butt-coupled scheme employing an MT-compatible ribbon fibre connector proposed by IBM Zurich: (a) schematic, (b) actual implementation and (c) the MT connector [106], [107].

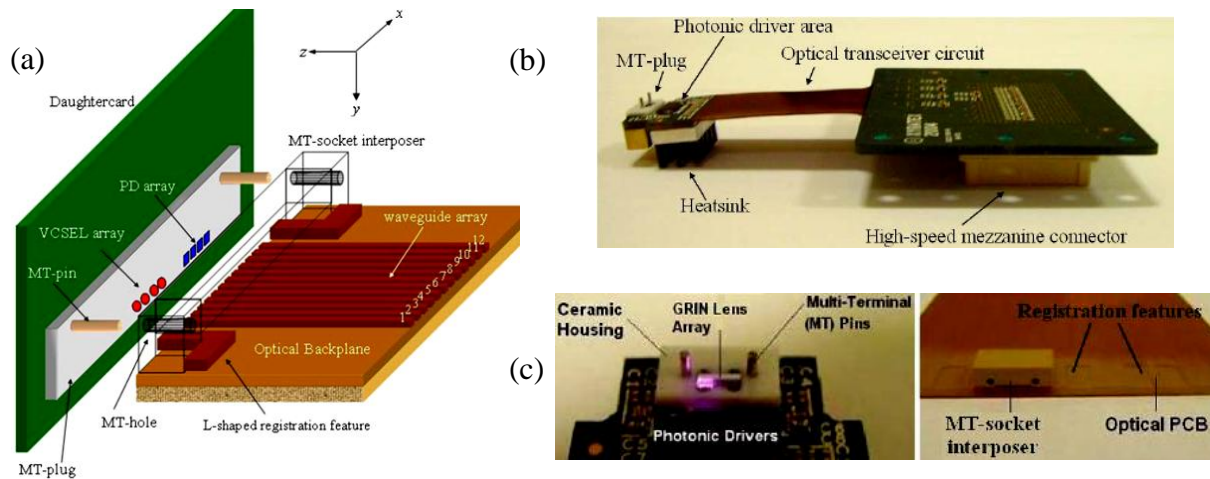


Figure 2-16 Illustration of a butt-coupled scheme employing an MT-compatible ribbon fibre connector and VCSEL/PD array proposed by Xyratex and UCL: (a) schematic, (b) actual implementation of a line-card and (c) the MT-plug and MT-socket interposer [108], [109].

Mid-board coupling can eliminate the layout restrictions and allow the optical-electrical interfaces anywhere on the board. A novel design demonstrated by researchers in University of Cambridge utilises an L-shape connector where VCSELs and PDs are mounted in order to directly couple the light to the polymer waveguides [113]. This approach allows the pick-and-place technique commonly used in the electronic industries, and thereby provides a simple low-cost solution. However, the drawback of this method is the requirement of opening holes or gaps in the board.

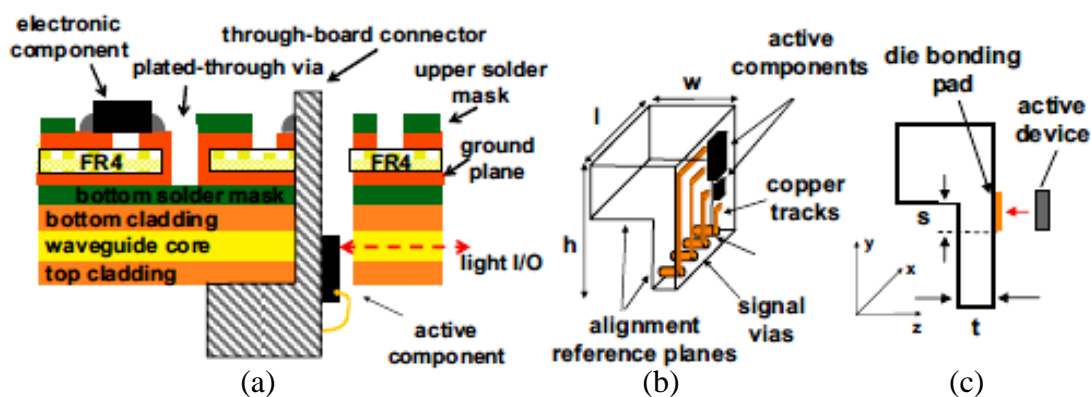


Figure 2-17 Illustration of a butt-coupled scheme employing an L-shaped connector: (a) cross section of an OE PCB with L-shaped connector, (b) and (c) schematics of the L-shaped connector [113].

Alternatively, monolithically formed channels integrated with polymer layers can be employed to hold and align fibres without the need for additional connectors. A number of

approaches have been proposed, including U-grooved or V-grooved channels and UV photolithography patterning (Figure 2-18) [110]–[112]. However, the use of a fibre channel typically requires fibre cleaving and thus raises concerns on the robustness of connectivity.

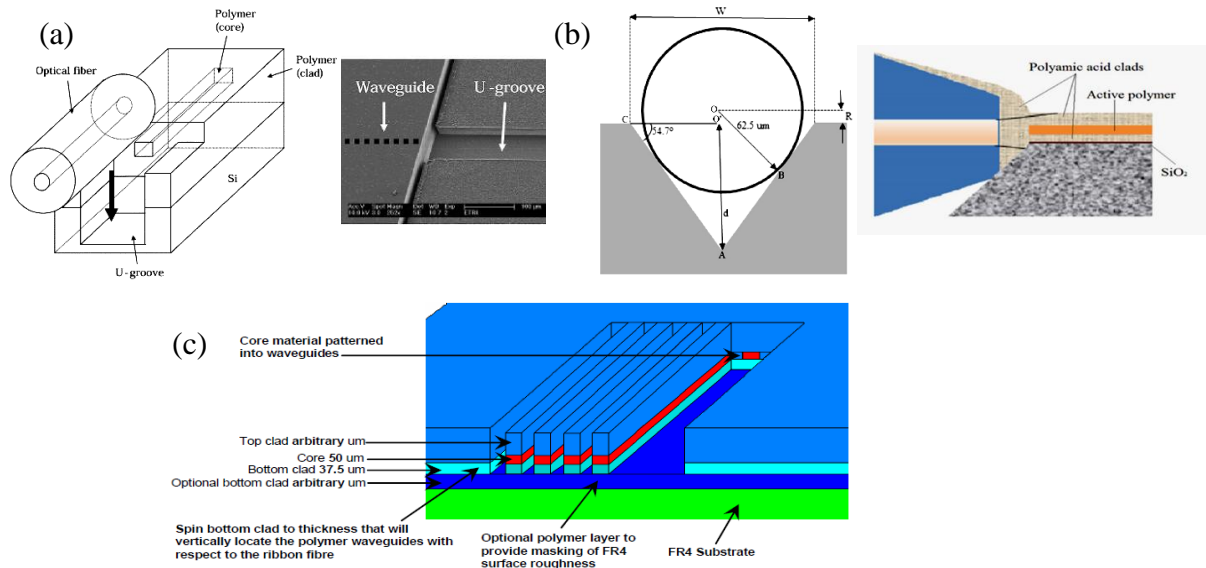
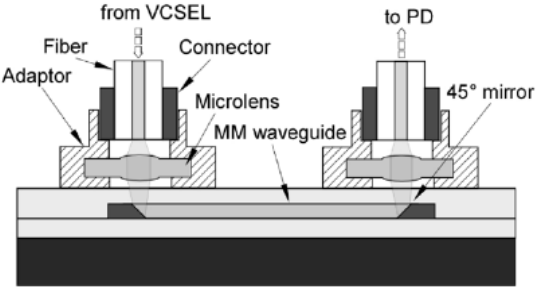
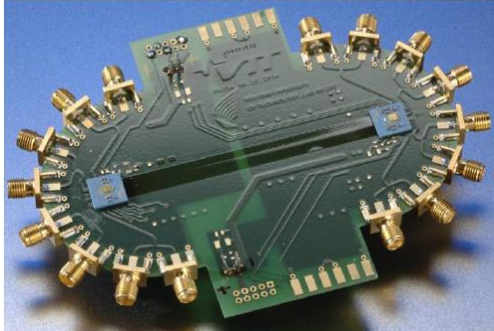
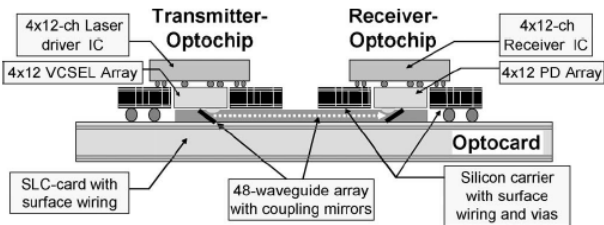
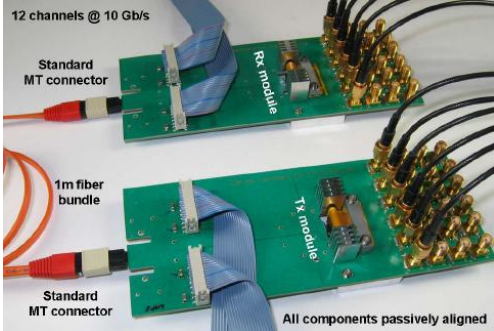


Figure 2-18 Illustration of a butt-coupled scheme employing channels formed in the polymer layer: (a) a U-groove formed in polymer, (b) a cleaved fibre placed in a V-groove in substrate and (c) spin-coating and UV photolithographic patterning [110]–[112].

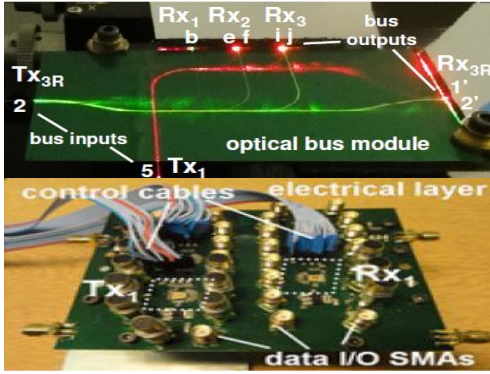

2.7 State-of-the-art Demonstrators

The numerous methods of coupling light in and out of the waveguide have been addressed in the previous section. In this section, several polymer waveguide-based on-board optical interconnections demonstrated recently from major research groups and industries are summarised (Table 2-3). Related information regarding the achieved data rates, coupling schemes, waveguide parameters (length, shape, size and index step) and loss at wavelengths of interest are presented. It should be noted that many particular aspects such as materials, waveguide components or fabrication methods are omitted in the table, and can be found for example in papers [26], [83], [114]–[126] and the reviews provided by the thesis of Papakonstantinou [127] and Bamiedakis [128]. This is by no means an exhaustive list of polymer waveguide-based links but provides a clear image of the nature of the research done to-date in this field.

Table 2-3 Demonstrated board-level optical interconnections based on multimode polymer waveguides from both academia and industry.

	<p>Group: Fujitsu, 2005 [88], [129]</p> <p>Data rate: 10.7 Gb/s</p> <p>Waveguide: 25 cm straight</p> <p>Coupling scheme: Out-of-plane</p> <p>Metrics: core = $30 \times 30 \mu\text{m}^2$, $\Delta n = 0.024$, loss = 0.05 dB @850 nm.</p>
	<p>Group: VTT, 2006 [130]</p> <p>Data rate: 10 Gb/s</p> <p>Waveguide: 10 cm straight</p> <p>Coupling scheme: Out-of-plane</p> <p>Metrics: core = 50×40 and $75 \times 40 \mu\text{m}^2$, $\Delta n = 0.014$, loss = 0.55 dB @850 nm.</p>
	<p>Group: IBM Terabus, 2006 [131]</p> <p>Data rate: Tx=20 Gb/s, Rx=14 Gb/s (4×12 channels)</p> <p>Waveguide: 30 cm bend</p> <p>Coupling scheme: Out-of-plane</p> <p>Metrics: core = $35 \times 35 \mu\text{m}^2$, $\Delta n = 0.028\text{--}0.038$, loss = 0.1–0.16 dB/cm @985nm.</p>
	<p>Group: IBM, 2007 [106], [132]</p> <p>Data rate: 12×10 Gb/s</p> <p>Waveguide: 2×15 cm straight</p> <p>Coupling scheme: In-plane</p> <p>Metrics: core = 50×50 and $35 \times 35 \mu\text{m}^2$, $\Delta n = 0.028\text{--}0.038$, loss = 0.04–0.05 dB/cm @850nm [133].</p>

	<p>Group: Xyratex and University College London, 2008 [108]</p> <p>Data rate: 10 Gb/s</p> <p>Waveguide: 10 cm straight</p> <p>Coupling scheme: In-plane</p> <p>Metrics: core = $70 \times 70 \mu\text{m}^2$, $\Delta n = 0.03$, loss = 0.07–0.09 dB @850 nm.</p>
	<p>Group: IBM, 2009 [134], [135]</p> <p>Data rate: 16×10 Gb/s</p> <p>Waveguide: 15 cm straight</p> <p>Coupling scheme: Out-of-plane</p> <p>Metrics: core = $35 \times 35 \mu\text{m}^2$, $\Delta n = 0.028\text{--}0.038$, loss = 0.1–0.16 dB/cm @985 nm.</p>
	<p>Group: Xyratex and University College London, 2010 [136], [137]</p> <p>Data rate: 10 Gb/s</p> <p>Waveguide: ~13–20 cm straight, bend</p> <p>Coupling scheme: In-plane</p> <p>Metrics: core = $70 \times 70 \mu\text{m}^2$, $\Delta n = 0.036$, loss = 0.03–0.04 dB @850 nm.</p>
	<p>Group: IBM, 2012 [71], [138]</p> <p>Data rate: 24×15 Gb/s</p> <p>Waveguide: 15 cm straight</p> <p>Coupling scheme: Out-of-plane</p> <p>Metrics: core = $35 \times 35 \mu\text{m}^2$, $\Delta n = 0.028\text{--}0.038$, loss = 0.067–0.1 dB @850 nm.</p>

	<p>Group: University of Cambridge, 2014 [139], [140]</p> <p>Data rate: 4×10 Gb/s</p> <p>Waveguide: ~10 cm bend</p> <p>Coupling scheme: In-plane</p> <p>Metrics: core = 50×50 μm^2, $\Delta n = 0.02$, loss = 0.03–0.05 dB/cm @850 nm.</p>
	<p>Group: Finisar, 2014 [141]</p> <p>Data rate: 24×25 Gb/s</p> <p>Waveguide: Bend (length not available)</p> <p>Coupling scheme: Out-of-plane</p> <p>Metrics: core = 50×50 μm^2, $\Delta n \sim 0.018$, loss ≤ 0.05 dB/cm @850 nm.</p>

A distinct focus on waveguide coupling schemes such as the development of out-of-plane mirrors and fibre-to-waveguide connectors can be found; however, the understanding of the behaviour and performance of multimode polymer waveguides itself for high-speed optical interconnects is equally important as the coupling technology. By reviewing the backplane demonstrators and various waveguide components, a few important points that need to be further studied can be made:

- Waveguide parameters: the majority of the waveguides employed have dimensions varying from 20×20 μm^2 to 70×70 μm^2 with index steps from 0.01 to 0.04. It is well believed that the use of large core multimode waveguides is desired as they offer relaxed alignment tolerances and allow system assembly with common pick-and-place tools used in the existing electronics industry. However, no single reference exists regarding to the choice of waveguide parameters. Therefore, the investigation of optimised waveguide design (e.g. minimum coupling loss, maximum alignment tolerances, maximum bandwidth) is required to achieve high-performance optical interconnects for specific interconnection structures and launch conditions.

- Link bandwidth: important concerns have been raised regarding the capability of these waveguides to support very high on-board data rates due to their highly-multimoded nature as

the speed of VCSEL devices is continuously increasing. Although some preliminary experimental studies of dispersion have been presented in [126] and [142], the studies were conducted under restricted launch in most cases where the waveguides are underfilled. The dependence of the bandwidth performance has not been examined under various launch conditions and in the presence of input misalignments, which are likely to be encountered in real-world applications. In addition, the effects of interconnection layout (bends or crossing structures) on the bandwidth performance of these multimode polymer waveguides have yet been studied.

- Refractive index engineering: the polymer waveguides studied to date are primarily step-indexed while limited work has been carried out to study the effects of refractive index profiles on the optical transmission properties (e.g. coupling loss, bending loss, crossing loss, dispersion, etc.) of these guides. Some interest in graded-index waveguides has been reported. However, most of these studies only focus on the performance improvement in one particular aspect (e.g. waveguides with low crossing loss only) [143]–[147]. Various design trade-offs with regard to the waveguide performances employing refractive index engineering have not been studied thoroughly. Moreover, the fabrication process of the graded-index waveguides presented in [145] utilizes a microdispenser to dispense a viscous monomer directly onto the substrates and thus raises concerns on its compatibility with the conventional electronic manufacturing process. Therefore, its feasibility for large-scale low-cost implementation has yet to be proven.

- Modulation schemes: it can be noticed that optical interconnects operating at data rates of 25 Gb/s per waveguide channel are becoming available. However, most of the demonstrators employ fairly short waveguides (<20 cm) and are only limited to on-off keying modulation scheme. With the recent developments of VCSELs operating at higher speed, data rates of ≥ 40 Gb/s over a single channel is believed to be the next target. The employment of modulation formats with higher spectral efficiency is a potential way of achieving such high data rates over each waveguide channel [148]. Very limited work has been reported on the use of advanced modulation schemes on board-level optical interconnects.

Therefore, the aim of this thesis is to address these issues so as to determine design principles for low-loss and high-bandwidth multimode polymer waveguides for use in next-generation board-level optical interconnections.

2.8 Summary

Multimode polymer waveguides constitute an attractive approach for use in board-level interconnections. Particular polymer materials, such as siloxanes, are chosen as they possess excellent optical properties and also exhibit robust material characteristics which allow direct integration onto PCBs using conventional manufacturing methods employed by the electronics industry. In addition, multimode waveguide structures are preferred as they enjoy a straightforward fabrication process and offer relaxed alignment tolerances, enabling cost-effective system assembly using standard pick-and-place tools.

Bearing in mind the intended applications, different transmission media, various polymer materials, fabrication processes, active optoelectronic devices (sources and receivers) and coupling schemes are reviewed and compared with regard to their suitability for implementing low-cost board-level optical interconnections. Finally, in this chapter state-of-the-art polymer based optical interconnect demonstrators are reviewed. It can be seen that a considerable amount of work has been put into the demonstration of the feasibility of this technology using simple polymer waveguide links. However, the fundamental waveguide behaviours have not been studied thoroughly and more is yet to explore.

Therefore, there is a need to investigate the relations between the waveguide performance (e.g. loss and bandwidth) and the choice of waveguide parameters, launch conditioning, interconnection layouts and refractive index profiles. In pursuit of the vision of designing low-loss and high-bandwidth polymer waveguides for high-performance board-level optical interconnections, studies also need to be taken to demonstrate the capability of this technology to support even higher on-board data rates (e.g. ≥ 40 Gb/s). Achieving these aims is the focus of this thesis which intends to lay the groundwork for the design and demonstration of low-loss and high-bandwidth multimode polymer waveguides for use in on-board optical interconnections by employing launch conditioning, refractive index engineering and interconnection layout as well as advanced modulation formats.

2.9 References

- [1] H. P. Kuo, P. Rosenberg, R. Walmsley, S. Mathai, L. Kiyama, J. Straznicky, M. McLaren, M. Tan, and S. Y. Wang, "Free-space Optical Links for Board-to-board Interconnects," *Appl. Phys. A Mater. Sci. Process.*, vol. 95, no. 4, pp. 955–965, 2009.
- [2] B. Ciftcioglu, R. Berman, S. Wang, J. Hu, I. Savidis, M. Jain, D. Moore, M. Huang, E. G. Friedman, G. Wicks, and H. Wu, "3-D Integrated Heterogeneous Intra-chip Free-space Optical Interconnect," *Opt. Exp.*, vol. 20, no. 4, pp. 4331, 2012.

- [3] M. Jarczyński, T. Seiler, and J. Jahns, "Integrated Three-dimensional Optical Multilayer using Free-space Optics," *Appl. Opt.*, vol. 45, no. 25, pp. 6335, 2006.
- [4] J. H. Yeh, R. K. Kostuk, and K. Y. Tu, "Hybrid Free-space Optical Bus System for Board-to-board Interconnections," *Appl. Opt.*, vol. 35, no. 32, pp. 6354–6364, 1996.
- [5] K. Wang, A. Nirmalathas, C. Lim, E. Skafidas, and K. Alameh, "High-speed Free-space Based Reconfigurable Card-to-card Optical Interconnects with Broadcast Capability," *Opt. Exp.*, vol. 21, no. 13, pp. 15395–15400, 2013.
- [6] T. D. Wilkinson, B. Crossland, N. Collings, F. Zhang, and M. Fan, "Reconfigurable Free-Space Optical Cores for Storage Area Networks," *IEEE Commun. Mag.*, vol. 43, no. 3, pp. 93–99, 2005.
- [7] J. Chou, "MEMS Lens Scanners for Free-Space Optical Interconnects," University of California at Berkeley, 2011.
- [8] M. P. Christensen, P. Milojkovic, and M. W. Haney, "Low-distortion Hybrid Optical Shuffle Concept," *Opt. Lett.*, vol. 24, no. 3, pp. 169–171, 1999.
- [9] F. Lacroix, E. Bernier, M. H. Ayliffe, F. A. P. Tooley, D. V. Plant, and A. G. Kirk, "Implementation of a Compact, Four-stage, Scalable Optical Interconnect for Photonic Backplane Applications," *Appl. Opt.*, vol. 41, no. 8, pp. 1541–55, 2002.
- [10] L. Eldada, R. Blomquist, L. W. Shacklette, and M. J. McFarland, "High-performance Polymeric Componentry for Telecom and Datacom Applications," *Opt. Eng.*, vol. 39, no. 3, pp. 596–609, 2000.
- [11] I. T. Monroy, H. P. A. vd Boom, A. M. J. Koonen, G. D. Khoe, Y. Watanabe, Y. Koike, and T. Ishigure, "Data Transmission Over Polymer Optical Fibers," *Opt. Fiber Technol.*, vol. 9, no. 3, pp. 159–171, 2003.
- [12] T. Wipiejewski, G. Duggan, D. Barrow, B. McGarvey, V. Hung, T. Calvert, M. Maute, and J. Lambkin, "Red VCSELs for POF Data Transmission and Optical Sensing Applications," *Proc. - Electron. Components Technol. Conf.*, pp. 717–721, 2007.
- [13] F. Boeuf, L. Fulbert, C. Baudot, J. M. Fedeli, L. Vivien, B. Ben Bakir, L. Viot, B. Caire-Remonnay, A. Le Liepvre, C. Kopp, P. Grosse, S. Bernabe, and S. Menezo, "Silicon Photonics Research for CMOS Compatible Optical Interconnects at 40Gb/s and beyond," *IEEE 2012 Int. Semicond. Conf. Dresden-Grenoble, ISCDG 2012*, pp. 87–91, 2012.
- [14] W. M. Green, M. J. Rooks, L. Sekaric, and Y. a Vlasov, "Ultra-compact, Low RF power, 10 Gb/s Silicon Mach-Zehnder Modulator," *Opt. Exp.*, vol. 15, no. 25, pp. 17106–17113, 2007.
- [15] B. G. Lee, X. Chen, A. Biberman, X. Liu, I. Hsieh, C. Chou, J. I. F. Xia, W. M. J. Green, L. Sekaric, Y. a Vlasov, and R. M. Osgood, "Ultrahigh-Bandwidth Silicon Photonic Nanowire Waveguides for On-Chip Networks," *IEEE Photon. Technol. Lett.*, vol. 20, no. 6, pp. 398–400, 2008.
- [16] R. Dangel, J. Hofrichter, F. Horst, D. Jubin, A. La Porta, N. Meier, I. M. Soganci, J. Weiss, and B. J. Offrein, "Polymer waveguides for electro-optical integration in data centers and high-performance computers," *Opt. Exp.*, vol. 23, no. 4, pp. 4736–4750, 2015.
- [17] J. Bahram and S. Fathpour, "Silicon Photonics," *J. Light. Technol.*, vol. 24, no. 12, pp. 4600–4615, 2006.
- [18] R. Soref, L. Fellow, and I. Paper, "The Past, Present, and Future of Silicon Photonics," *IEEE J. Sel. Topics Quantum Electron.*, vol. 12, no. 6, pp. 1678–1687, 2006.
- [19] L. Eldada, "Polymer Integrated Optics: Promise vs. Practicality," *Proc. SPIE, Org. Photonic Mater. Devices IV*, vol. 4642, pp. 11–22, 2002.
- [20] M. Zhou, "Low-loss Polymeric Materials for Passive Waveguide Components in Fiber Optical Telecommunication," *Opt. Eng.*, vol. 41, no. 7, pp. 1631–1643, 2002.
- [21] R. Dangel, F. Horst, D. Jubin, N. Meier, J. Weiss, B. J. Offrein, B. W. Swatowski, C. M. Amb,

- D. J. Deshazer, and W. K. Weidner, "Development of Versatile Polymer Waveguide Flex Technology for Use in Optical Interconnects," *J. Light. Technol.*, vol. 31, no. 24, pp. 3915–3926, 2013.
- [22] B. Swatowski, C. Amb, S. K. Breed, D. J. Deshazer, W. K. Weidner, R. F. Dangel, N. Meier, and B. J. Offrein, "Flexible, Stable, and Easily Processable Optical Silicones for Low Loss Polymer Waveguides," *Proc. SPIE*, vol. 8622, p. 862205, 2013.
- [23] M. Immonen, M. Karppinen, and J. K. Kivilahti, "Investigation of Environmental Reliability of Optical Polymer Waveguides Embedded on Printed Circuit Boards," *Microelectron. Reliab.*, vol. 47, pp. 363–371, 2005.
- [24] J. Kobayashi, T. Matsuura, Y. Hida, S. Sasaki, and T. Maruno, "Fluorinated Polyimide Waveguides with Low Polarization-Dependent Loss and Their Applications to Thermo-optic Switches," *J. Light. Technol.*, vol. 16, no. 6, pp. 1024–1029, 1998.
- [25] D. Bosc, A. Maalouf, F. Henrio, and S. Haesaert, "Strengthened Poly(methacrylate) Materials for Optical Waveguides and Integrated Functions," *Opt. Mater. (Amst.)*, vol. 30, no. 10, pp. 1514–1520, 2008.
- [26] N. Bamiedakis, J. Beals, R. V. Penty, I. H. White, J. V. DeGroot, and T. V. Clapp, "Cost-effective Multimode Polymer Waveguides for High-speed On-board Optical Interconnects," *IEEE J. Quantum Electron.*, vol. 45, no. 4, pp. 415–424, 2009.
- [27] Y. S. Liu, H. S. Cole, R. Guida, T. Sitnik, E. W. Balch, P. O. Box, J. Bristow, Y. Liu, and T. Marta, "Optoelectronic Packaging and Polymer Waveguides for Multichip Module and Board-Level Optical Interconnect Applications," *IEEE Electron. Components Technol. Conf.*, pp. 185–188, 1995.
- [28] Y. Ishii, S. Koike, Y. Arai, and Y. Ando, "SMT-Compatible Large-Tolerance 'OptoBump' Interface for Interchip Optical Interconnections," *IEEE Trans. Adv. Packag.*, vol. 26, no. 2, pp. 122–127, 2003.
- [29] L. Eldada and L. W. Shacklette, "Advances in Polymer Integrated Optics," *IEEE J Sel Top Quant.*, vol. 6, no. 1, pp. 54–68, 2000.
- [30] B. H. Ma, A. K. Jen, and L. R. Dalton, "Polymer-Based Optical Waveguides: Materials, Processing, and Devices," *Sci. Technol. Adv. Mater. Adv. Mater.*, vol. 14, no. 19, pp. 1339–1365, 2002.
- [31] A. Norris, J. Degroot, T. Ogawa, T. Watanabe, T. Kowalczyk, A. Baugher, R. Blum, and G. Corporation, "High Reliability of Silicone Materials for Use as Polymer Waveguides," *Linear Nonlinear Opt. Org. Mater. III*, vol. 5212, pp. 76–82, 2003.
- [32] T. V. Clapp, R. Paquet, A. Norris, and B. Pettersen, "Dow Corning photonics: the silicon advantage in automotive photonics," *Proc. SPIE*, vol. 5663, pp. 208–215, 2005.
- [33] A. Neyer, S. Kopetz, E. Rabe, W. J. Kang, and S. Tombrink, "Electrical-Optical Circuit Board using Polysiloxane Optical Waveguide Layer," *Electron. Components Technol.*, pp. 246–250, 2005.
- [34] J. V. DeGroot, Jr., "Cost Effective Optical Waveguide Components for Printed Circuit Applications," *Proc. SPIE*, vol. 6781d, pp. 678116–1–12, 2007.
- [35] M. Abtew and G. Selvaduray, "Lead-free Solders in Microelectronics," *Mater. Sci. Eng.*, vol. 27, pp. 95–141, 2000.
- [36] D. M. Kuchta, Y. Taira, C. Baks, G. McVicker, L. Schares, and H. Numata, "Optical Interconnects for Servers," *Jpn. J. Appl. Phys.*, vol. 47, no. 8, pp. 6642–6645, 2008.
- [37] S. Kopetz, D. Cai, E. Rabe, and A. Neyer, "PDMS-based Optical Waveguide Layer for Integration in Electrical-optical Circuit Boards," *Int. J. Electron. Commun.*, vol. 61, no. 3, pp. 163–167, 2007.
- [38] D. Zhu, D. Cai, S. Kopetz, and A. Neyer, "Environmental Stability of PDMS-Waveguides for

- Electrical-optical Circuit Boards,” *Electron. Lett.*, vol. 43, no. 11, pp. 627–629, 2007.
- [39] L. Merhari, *Hybrid Nanocomposites for Nanotechnology*. Springer, 2009.
 - [40] Y. Xia and G. M. Whitesides, “Soft Lithography,” *Annu. Rev. Mater. Sci.*, vol. 28, pp. 153–184, 1998.
 - [41] G. Van Steenberge, P. Geerinck, S. Van Put, J. Van Koetsem, H. Ottevaere, D. Morlion, H. Thienpont, and P. Van Daele, “MT-Compatible Laser-Ablated Interconnections for Optical Printed Circuit Boards,” *J. Light. Technol.*, vol. 22, no. 9, pp. 2083–2090, 2004.
 - [42] G. V. S. G. Van Steenberge, N. H. N. Hendrickx, E. B. E. Bosman, J. V. E. J. Van Erps, H. T. H. Thienpont, and P. V. D. P. Van Daele, “Laser Ablation of Parallel Optical Interconnect Waveguides,” *IEEE Photon. Technol. Lett.*, vol. 18, no. 9, pp. 1106–1108, 2006.
 - [43] P. Calvert, “Inkjet Printing for Materials and Devices,” *Chem. Mater.*, vol. 13, pp. 3299–3305, 2001.
 - [44] B.-J. de Gans, P. C. Duineveld, and U. S. Schubert, “Inkjet Printing of Polymers: State of the Art and Future Developments,” *Adv. Mater.*, vol. 16, no. 3, pp. 203–213, 2004.
 - [45] M. Hajj-Hassan, T. Gonzalez, E. Ghafar-Zadeh, H. Djeghelian, V. Chodavarapu, M. Andrews, and D. Theriault, “Direct-Dispense Polymeric Waveguides Platform for Optical Chemical Sensors,” *Sensors*, vol. 8, no. 12, pp. 7636–7648, 2008.
 - [46] B. P. Keyworth, R. Narendra, J. N. McMullin, and R. I. Macdonald, “Direct Dispensing of Polymer Waveguides,” *LEOS 1993 Summer Top. Meet.*, pp. H41 – H42, 1993.
 - [47] C. DeCusatis, *Handbook of Fiber Optic Data Communication*, 4th Editio. 2013.
 - [48] A. Larsson, “Advances in VCSELs for Communication and Sensing,” *IEEE J. Sel. Topics Quantum Electron.*, vol. 17, no. 6, pp. 1552–1567, 2011.
 - [49] T. L. Koch, *Optical Fiber Telecommunications IIIB*. Academic Press, 1997.
 - [50] K. Iga, “Surface-Emitting Laser — Its Birth and Generation of New Optoelectronics Field,” *IEEE J. Sel. Topics Quantum Electron.*, vol. 6, no. 6, pp. 1201–1215, 2000.
 - [51] K. Iga, “Vertical-Cavity Surface-Emitting Laser: Its Conception and Evolution,” *Jpn. J. Appl. Phys.*, vol. 47, no. 1, pp. 1–10, 2008.
 - [52] F. Koyama, “Recent Advances of VCSEL Photonics,” *J. Light. Technol.*, vol. 24, no. 12, pp. 4502–4513, 2006.
 - [53] A. Benner, “Optical Interconnect Opportunities in Supercomputers and High End Computing,” *Opt. Fiber Commun. Conf. Expo.*, pp. 1–60, 2012.
 - [54] D. M. Kuchta, A. V. Rylyakov, C. L. Schow, J. E. Proesel, C. Baks, P. Westbergh, J. S. Gustavsson, and A. Larsson, “64Gb/s transmission over 57m MMF using an NRZ modulated 850nm VCSEL,” *Conf. Opt. Fiber Commun.*, p. Th3C.2, 2014.
 - [55] J. Wang, M. Keever, Z. Feng, T. Fanning, C. Chu, A. Sridhara, F. Hopfer, T. Sale, A. Cheng, B. Shao, L. Ding, and P. Wen, “28 Gb/s 850 nm Oxide VCSEL Development at Avago,” *Proc. SPIE*, vol. 8639, pp. 86390K–1–6, 2013.
 - [56] P. Westbergh, J. S. Gustavsson, B. Kögel, A. Haglund, A. Larsson, A. Mutig, A. Nadtochiy, D. Bimberg, and A. Joel, “40 Gbit/s Error-Free Operation of Oxide-Confined 850 nm VCSEL,” *Electron. Lett.*, vol. 46, no. 14, pp. 1014–1016, 2010.
 - [57] D. M. Kuchta, A. V. Rylyakov, C. L. Schow, J. E. Proesel, C. W. Baks, P. Westbergh, J. S. Gustavsson, and A. Larsson, “A 50 Gb/s NRZ Modulated 850 nm VCSEL Transmitter Operating Error Free to 90 °C,” *J. Light. Technol.*, vol. 33, no. 4, pp. 802–810, 2015.
 - [58] D. M. Kuchta, A. V. Rylyakov, C. L. Schow, J. E. Proesel, and C. Baks, “A 55Gb/s Directly Modulated 850nm VCSEL-Based Optical Link,” *IEEE Photonics Conf.*, pp. 1 – 2, 2012.
 - [59] D. M. Kuchta, C. L. Schow, A. V. Rylyakov, J. E. Proesel, F. E. Doany, and C. Baks, “A

- 56.1Gb/s NRZ Modulated 850nm VCSEL-Based Optical Link,” *OFC/NFOEC Tech. Dig.*, p. OW1B.5, 2013.
- [60] N. Li, C. Xie, W. Luo, C. J. Helms, L. Wang, C. Liu, Q. Sun, S. Huang, C. Lei, K. P. Jackson, and R. F. Carson, “Emcore’s 1 Gb/s to 25 Gb/s VCSELs,” *Proc. SPIE*, vol. 8276, p. 827603, 2012.
- [61] Y.-C. Chang, C. S. Wang, and L. A. Coldren, “High-efficiency, high-speed VCSELs with 35 Gbit/s error-free operation,” *Electron. Lett.*, vol. 43, pp. 1022–1023, 2007.
- [62] P. Westbergh, E. P. Haglund, E. Haglund, R. Safaisini, J. S. Gustavsson, and A. Larsson, “High-speed 850 nm VCSELs Operating Error Free up to 57 Gbit/s,” *Electron. Lett.*, vol. 49, no. 16, pp. 1021–1023, 2013.
- [63] F. H. Peters and M. H. Macdougall, “High-Speed High-Temperature Operation of Vertical-Cavity Surface-Emitting Lasers,” *IEEE Photon. Technol. Lett.*, vol. 13, no. 7, pp. 645–647, 2001.
- [64] P. Westbergh, R. Safaisini, E. Haglund, J. S. Gustavsson, A. Larsson, M. Geen, R. Lawrence, and A. Joel, “High-speed Oxide Confined 850-nm VCSELs Operating Error-Free at 40 Gb/s up to 85°C,” *IEEE Photon. Technol. Lett.*, vol. 25, no. 8, pp. 768–771, 2013.
- [65] S. A. Blokhin, J. A. Lott, A. Mutig, G. Fiol, N. N. Ledentsov, M. V. Maximov, A. M. Nadtochiy, V. A. Shchukin, and D. Bimberg, “Oxide-confined 850 nm VCSELs operating at bit rates up to 40 Gbit/s,” *Electron. Lett.*, vol. 45, no. 10, pp. 501–503, 2009.
- [66] J. Shi, W. Weng, F. Kuo, and J. Chyi, “Oxide-Relief Vertical-Cavity Surface-Emitting Lasers with Extremely High Data-Rate/Power-Dissipation Ratios,” *OSA/OFC/NFOEC*, p. OThG2, 2011.
- [67] J. W. Shi, J. C. Yan, J. M. Wun, J. Chen, and Y. J. Yang, “Oxide-Relief and Zn-diffusion 850-nm Vertical-Cavity Surface-Emitting Lasers With Extremely Low Energy-to-Data-Rate Ratios for 40 Gbit/s Operations,” *IEEE J. Sel. Topics Quantum Electron.*, vol. 19, no. 2, p. 7900208, 2013.
- [68] L. A. Graham, H. Chen, D. Gazula, T. Gray, J. K. Guenter, B. Hawkins, R. Johnson, C. Kocot, A. N. MacInnes, G. D. Landry, and J. a. Tatum, “The Next Generation of High Speed VCSELs at Finisar,” *Proc. SPIE*, vol. 8276, p. 827602, 2012.
- [69] D. M. Kuchta, A. V. Rylyakov, F. E. Doany, C. L. Schow, J. E. Proesel, C. W. Baks, P. Westbergh, J. S. Gustavsson, and A. Larsson, “A 71-Gb/s NRZ Modulated 850-nm VCSEL-Based Optical Link,” *IEEE Photon. Technol. Lett.*, vol. 27, no. 6, pp. 577–580, 2015.
- [70] R. Michalzik, *VCSELs: Fundamentals, Technology and Applications of Vertical-Cavity Surface-Emitting Lasers*. Springer-Verlag Berlin Heidelberg, 2013.
- [71] F. E. Doany, *et al.*, “Terabit/s-Class Optical PCB Links Incorporating 360-Gb/s Bidirectional 850 nm Parallel Optical Transceivers,” *J. Light. Technol.*, vol. 30, no. 4, pp. 560–571, 2012.
- [72] H. S. Lee, S. An, Y. Kim, D. K. Kim, J. K. Kang, Y. W. Choi, S. G. Lee, B. H. O, and E. H. Lee, “Fabrication of a 2.5 Gbps \times 4 Channel Optical Micro-Module for O-PCB Application,” *Microelectron. Eng.*, vol. 83, pp. 1347–1351, 2006.
- [73] A. Kanda, T. Ogawa, and O. Mikami, “VCSEL Module With Polymer Optical Output Rods to Enable High Efficiency Coupling for Optical Interconnection,” *IEEE Photon. Technol. Lett.*, vol. 21, no. 11, pp. 685–687, 2009.
- [74] G. Keiser, *Optical Fiber Communications*, 4th Editio. McGraw-Hill Higher Education, 2010.
- [75] G. P. Agrawal, *Fibre-optic Communication Systems*, Third Edit. John Wiley & Sons, Inc., 2002.
- [76] VI Systems, “2015 Product Catalog.”
- [77] J. A. Lott, A. S. Payusov, S. A. Blokhin, P. Moser, N. N. Ledentsov, and D. Bimberg, “Arrays of 850 nm Photodiodes and Vertical Cavity Surface Emitting Lasers for 25 to 40 Gbit/s

- Optical Interconnects,” *Phys. Status Solidi Curr. Top. Solid State Phys.*, vol. 9, no. 2, pp. 290–293, 2012.
- [78] S. Y. Cho, M. A. Brooke, and N. M. Jokerst, “Optical Interconnections on Electrical Boards using Embedded Active Optoelectronic Components,” *IEEE J. Sel. Topics Quantum Electron.*, vol. 9, no. 2, pp. 465–476, 2003.
 - [79] Y. Liu, L. Lin, C. Choi, B. Bihari, R. T. Chen, and S. Member, “Optoelectronic Integration of Polymer Waveguide Array and Metal – Semiconductor – Metal Photodetector Through Micromirror Couplers,” *IEEE Photon. Technol. Lett.*, vol. 13, no. 4, pp. 355–357, 2001.
 - [80] E. Griese, “A High-Performance Hybrid Electrical – Optical Interconnection Technology for High-Speed,” *IEEE Trans. Adv. Packag.*, vol. 24, no. 3, pp. 375–383, 2001.
 - [81] N. Hendrickx, J. Van Erps, G. Van Steenberge, H. Thienpont, and P. Van Daele, “Tolerance Analysis for Multilayer Optical Interconnections Integrated on a Printed Circuit Board,” *J. Light. Technol.*, vol. 25, no. 9, pp. 2395–2401, 2007.
 - [82] G. Van Steenberge, P. Geerinck, M. Riester, S. Pongratz, and P. Van Daele, “Laser Ablated Coupling Structures for Optical Printed Circuit Boards,” *Proc. SPIE*, vol. 5956, p. 59561A–59561A–7, 2005.
 - [83] A. McCarthy, H. Suyal, and A. C. Walker, “Fabrication and Characterisation of Direct Laser-Written Multimode Polymer Waveguides with Out-of-Plane Turning Mirrors,” *Conf. Lasers Electro-Optics Eur.*, p. 477, 2005.
 - [84] S. Nakagawa, Y. Taira, H. Numata, K. Kobayashi, K. Terada, and Y. Tsukada, “High-Density Optical Interconnect Exploiting Build-up Waveguide-on-SLC Board,” *Electron. Components Technol. Conf.*, pp. 256–260, 2008.
 - [85] Z. Zhang, D. Felipe, V. Katopodis, P. Groumas, C. Kouloumentas, H. Avramopoulos, J.-Y. Dupuy, A. Konczykowska, A. Dede, A. Beretta, A. Vannucci, G. Cangini, R. Dinu, D. Schmidt, M. Moehrle, P. Runge, J.-H. Choi, H.-G. Bach, N. Grote, N. Keil, and M. Schell, “Hybrid Photonic Integration on a Polymer Platform,” *Photonics*, vol. 2, pp. 1005–1026, 2015.
 - [86] R. Yoshimura, M. Hikita, M. Usui, S. Tomaru, and S. Imamura, “Polymeric Optical Waveguide Films with 45° Mirrors Formed with a 90° V-Shaped Diamond Blade,” *Electron. Lett.*, vol. 33, no. 15, pp. 1311–1312, 1997.
 - [87] C. Choi, L. Lin, Y. Liu, J. Choi, L. Wang, D. Haas, J. Magera, and R. T. Chen, “Flexible Optical Waveguide Film Fabrications and Optoelectronic Devices Integration for Fully Embedded Board-Level Optical Interconnects,” *J. Light. Technol.*, vol. 22, no. 9, pp. 2168–2176, 2004.
 - [88] A. L. Glebov, J. Roman, M. G. Lee, and K. Yokouchi, “Optical Interconnect Modules With Fully Integrated Reflector Mirrors,” *IEEE Photon. Technol. Lett.*, vol. 17, no. 7, pp. 1540–1542, 2005.
 - [89] M. Kagami, A. Kawasaki, and H. Ito, “A Polymer Optical Waveguide With Out-of-Plane Branching Mirrors for Surface-Normal Optical Interconnections,” *J. Light. Technol.*, vol. 19, no. 12, pp. 1949–1955, 2001.
 - [90] J. V. DeGroot, S. O. Glover, M. J. Dyer, and W. K. Bischel, “Polymeric Optical Interconnect for Chip-to-Chip Communication,” *OFC/NFOEC Tech. Dig. Opt. Fiber Commun. Conf.*, vol. 5, p. OFD6, 2005.
 - [91] L. Wang, X. Wang, W. Jiang, J. Choi, H. Bi, and R. Chen, “45° Polymer-Based Total Internal Reflection Coupling Mirrors for Fully Embedded Intraboard Guided Wave Optical Interconnects,” *Appl. Phys. Lett.*, vol. 87, no. 14, pp. 141110–141110–3, 2005.
 - [92] I. Cho, W. Lee, M. Jeong, and H. Park, “Optical Module Using Polymer Waveguide With Integrated Reflector Mirrors,” *IEEE Photon. Technol. Lett.*, vol. 20, no. 6, pp. 410–412, 2008.
 - [93] M. Immonen, M. Karppinen, and J. K. Kivilahti, “Fabrication and Characterization of Polymer

- Optical Waveguides With Integrated Micromirrors for Optical Interconnects,” *IEEE Trans. Electron. Packag. Manuf.*, vol. 28, no. 4, pp. 304–311, 2005.
- [94] J.-S. Kim and J.-J. Kim, “Fabrication of Multimode Polymeric Waveguides and Micromirrors Using Deep X-Ray Lithography,” *IEEE Photon. Technol. Lett.*, vol. 16, no. 3, pp. 798–800, 2003.
 - [95] V. Kudryashov, X. C. Yuan, W. C. Cheong, and K. Radhakrishnan, “Grey Scale Structures Formation in SU-8 with e-beam and UV,” *Microelectron. Eng.*, vol. 67–68, pp. 306–311, 2003.
 - [96] A. L. Glebov and M. G. Lee, “Vertical Light Coupling in Optical Interconnect Systems,” *19th Annu. Meet. IEEE Lasers Electro-Optics Soc.*, pp. 577–578, 2006.
 - [97] R. C. A. Pitwon, K. Hopkins, K. Wang, D. R. Selviah, H. Baghsiahi, B. J. Offrein, R. Dangel, F. Horst, M. Halter, and M. Gmür, “Design and Implementation of an Electro-optical Backplane with Pluggable In-plane Connectors,” *Proc. SPIE*, vol. 44, no. 0, p. 76070J–76070J–12, 2010.
 - [98] A. L. Glebov, C. J. Uchibori, and M. G. Lee, “Direct Attach of Photonic Components on Substrates With Optical Interconnects,” *IEEE Photon. Technol. Lett.*, vol. 19, no. 8, pp. 547–549, 2007.
 - [99] K. Nieweglowski, P. Galardziak, and K. J. Wolter, “Ceramic Interposer for Optoelectronic Array Devices,” *29th Int. Spring Semin. Electron. Technol.*, pp. 68–73, 2006.
 - [100] D.-W. Kim, T.-W. Lee, M. H. Cho, and H.-H. Park, “High-Efficiency and Stable Optical Transmitter using VCSEL-Direct-Bonded Connector for Optical Interconnection,” *Opt. Exp.*, vol. 15, no. 24, pp. 15767–75, 2007.
 - [101] S. H. Hwang, M. H. Cho, S. Kang, H. Park, H. S. Cho, and S. Kim, “Passively Assembled Optical Interconnection System Based on an Optical Printed-Circuit Board,” *IEEE Photon. Technol. Lett.*, vol. 18, no. 5, pp. 652–654, 2006.
 - [102] M. H. Cho, S. H. Hwang, H. S. Cho, and H. Park, “High-Coupling-Efficiency Optical Interconnection Using a 90-Bent Fiber Array Connector in Optical Printed Circuit Boards,” *IEEE Photon. Technol. Lett.*, vol. 17, no. 3, pp. 690–692, 2005.
 - [103] J. J. Yang, A. S. Flores, and M. R. Wang, “Array Waveguide Evanescent Ribbon Coupler for Card-to-Backplane Optical Interconnects,” *Opt. Lett.*, vol. 32, no. 1, pp. 14–16, 2007.
 - [104] R. T. Chen, L. Lin, C. Choi, Y. J. Liu, B. Bihari, L. Wu, S. Tang, R. Wickman, B. Picor, M. K. Hibbs-Brenner, J. Bristow, and Y. S. Liu, “Fully Embedded Board-Level Guided-Wave Optoelectronic Interconnects,” *Proc. IEEE*, vol. 88, no. 6, pp. 780–793, 2000.
 - [105] G. K. Chang, D. Guidotti, F. Liu, Y. J. Chang, Z. Huang, V. Sundaram, D. Balaraman, S. Hegde, and R. R. Tummala, “Chip-to-Chip Optoelectronics SOP on Organic Boards or Packages,” *IEEE Trans. Adv. Packag.*, vol. 27, no. 2, pp. 386–397, 2004.
 - [106] L. Dellmann, C. Berger, R. Beyeler, R. Dangel, M. Gmür, R. Hamelin, F. Horst, T. Lamprecht, N. Meier, T. Morf, S. Oggioni, M. Spreafico, R. Stevens, and B. J. Offrein, “120 Gb/s Optical Card-to-Card Interconnect Link Demonstrator with Embedded Waveguides,” *Electron. Components Technol. Conf.*, pp. 1288–1293, 2007.
 - [107] T. Lamprecht, F. Horst, R. Dangel, R. Beyeler, N. Meier, L. Dellmann, M. Gmür, C. Berger, and B. J. Offrein, “Passive Alignment of Optical Elements in a Printed Circuit Board,” *Electron. Components Technol. Conf.*, pp. 761–767, 2006.
 - [108] I. Papakonstantinou, D. R. Selviah, K. Wang, R. A. Pitwon, K. Hopkins, and D. Milward, “Optical 8-Channel, 10 Gb/s MT Pluggable Connector Alignment Technology for Precision Coupling of Laser and Photodiode Arrays to Polymer Waveguide Arrays for Optical Board-to-Board Interconnects,” *Electron. Components Technol. Conf.*, pp. 1769–1775, 2008.
 - [109] I. Papakonstantinou, D. R. Selviah, R. C. A. Pitwon, and D. Milward, “Low-Cost, Precision,

- Self-Alignment Technique for Coupling Laser and Photodiode Arrays to Polymer Waveguide Arrays on Multilayer PCBs,” *IEEE Trans. Adv. Packag.*, vol. 31, no. 3, pp. 502–511, 2008.
- [110] A. Rashidi, R. Gharavi, and A. Gharavi, “Fiber to Polymer-Waveguide Coupling with Low Insertion Loss,” *J. Opt.*, vol. 17, no. 4, pp. 1–5, 2015.
 - [111] S. Park, J. M. Lee, and S. C. Ko, “Fabrication Method for Passive Alignment in Polymer PLCs With U-Grooves,” *IEEE Photon. Technol. Lett.*, vol. 17, no. 7, pp. 1444–1446, 2005.
 - [112] J. Beals IV, “Polymer Waveguide Technology Enabling High-Bandwidth Optical Backplane Architectures,” University of Cambridge, 2009.
 - [113] N. Bamiedakis, A. Hashim, J. Beals, R. V. Penty, and I. H. White, “Low-Cost PCB-Integrated 10-Gb/s Optical Transceiver Built With a Novel Integration Method,” *IEEE Trans. Compon. Packag. Manuf. Technol.*, vol. 3, no. 4, pp. 592–600, 2013.
 - [114] G. L. Bona, B. J. Offrein, U. Bapst, C. Berger, R. Beyeler, R. Budd, R. Dangel, L. Dellmann, and F. Horst, “Characterization of Parallel Optical-Interconnect Waveguides Integrated on a Printed Circuit Board,” *Micro-Optics, VCSELs, and Photonic Interconnects*, vol. 5453, pp. 134–141, 2004.
 - [115] J. Moisel, J. Guttman, H.-P. Huber, O. Krumpholz, M. Rode, R. Bogenberger, and K.-P. Kuhn, “Optical Backplanes with Integrated Polymer Waveguides,” *Opt. Eng.*, vol. 39, no. 3, pp. 673–679, 2000.
 - [116] F. Mederer, R. Michalzik, J. Guttman, H. P. Huber, B. Lunitz, J. Moisel, and D. Wiedenmann, “10 Gb/s Data Transmission with TO-Packaged Multimode GaAs VCSELs Over 1 m Long Polymer Waveguides for Optical Backplane Applications,” *Opt. Commun.*, vol. 206, pp. 309–312, 2002.
 - [117] A. Borreman, S. Musa, A. A. M. Kok, M. B. J. Diemeer, and A. Driessen, “Fabrication of Polymeric Multimode Waveguides and Devices in SU-8 Photoresist Using Selective Polymerization,” *Symp. IEEE/LEOS Benelux*, pp. 83–86, 2002.
 - [118] A. Hashim, N. Bamiedakis, R. V. Penty, and I. H. White, “Multimode 90°-Crossings, Combiners and Splitters for a Polymer-Based On-Board Optical Bus,” *Conf. Lasers Electro-optics*, p. CM2A.5, 2012.
 - [119] J. D. Ingham, N. Bamiedakis, R. V. Penty, I. H. White, J. V. DeGroot, and T. V. Clapp, “Multimode Siloxane Polymer Waveguides for Robust High-Speed Interconnects,” *Conf. Lasers Electro-Optics*, p. CThS4, 2006.
 - [120] N. Bamiedakis, J. Beals, R. V. Penty, I. H. White, J. V. DeGroot, and T. V. Clapp, “Low Loss and Low Crosstalk Multimode Polymer Waveguide Crossings for High-Speed Optical Interconnects,” *Conf. Lasers Electro-Optics*, p. CMG1, 2007.
 - [121] N. Bamiedakis, J. Beals, F. Yang, A. Wonfor, R. V. Penty, I. H. W. J. V. D. Jr, and T. V. Clapp, “Low-Loss, High-Uniformity 1x2, 1x4 and 1x8 Polymer Multimode Y-Splitters Enabling Radio-over-Fibre Multicasting Applications,” *Eur. Conf. Integr. Opt.*, p. ThG04, 2007.
 - [122] R. Dangel, J. Hofrichter, F. Horst, D. Jubin, A. La Porta, N. Meier, I. M. Soganci, J. Weiss, and B. J. Offrein, “Polymer Waveguides for Electro-optical Integration in Data Centers and High-performance Computers,” *Opt. Exp.*, vol. 23, no. 4, p. 4736, 2015.
 - [123] T. Ishigure, K. Shitanda, T. Kudo, S. Takayama, T. Mori, K. Moriya, and K. Choki, “Low-Loss Design and Fabrication of Multimode Polymer Optical Waveguide Circuit with Crossings for High-Density Optical PCB,” *Electron. Components Technol. Conf.*, pp. 297–304, 2013.
 - [124] A. Hashim, N. Bamiedakis, R. V. Penty, and I. H. White, “Multimode Polymer Waveguide Components for Complex On-Board Optical Topologies,” *J. Light. Technol.*, vol. 31, no. 24, pp. 3962–3969, 2013.

- [125] I. Papakonstantinou, K. Wang, D. R. Selviah, and F. A. Fernández, “Transition, Radiation and Propagation Loss in Polymer Multimode Waveguide Bends,” *Opt. Exp.*, vol. 15, no. 2, pp. 669–679, 2007.
- [126] X. Wang, L. Wang, W. Jiang, and R. Chen, “Hard-Molded 51 cm Long Waveguide Array with a 150 GHz Bandwidth for Board-Level Optical Interconnects,” *Opt. Lett.*, vol. 32, no. 6, pp. 677–679, 2007.
- [127] I. Papakonstantinou, “Analysis, Design and Measurement of Guided Wave Optical Backplane Interconnection Systems,” University College London, 2008.
- [128] N. Bamiedakis, “Multimode Polymer Waveguides for High-speed On-board Optical Interconnects,” University of Cambridge, 2008.
- [129] A. L. Glebov, M. G. Lee, and K. Yokouchi, “Integration Technologies for Pluggable Backplane Optical Interconnect Systems,” *Opt. Eng.*, vol. 46, no. 1, pp. 015403–1–10, 2007.
- [130] M. Karppinen, T. Alajoki, A. Tanskanen, K. Kataja, J. T. Mäkinen, K. Kautio, P. Karioja, M. Immonen, and J. Kivilahti, “Parallel Optical Interconnect between Ceramic BGA Packages on FR4 Board using Embedded Waveguides and Passive Optical Alignments,” *Electron. Components Technol. Conf.*, pp. 799–805, 2006.
- [131] L. Schares, *et al.*, “Terabus: Terabit/Second-Class Card-Level Optical Interconnect Technologies,” *IEEE J. Sel. Topics Quantum Electron.*, vol. 12, no. 5, pp. 1032–1044, 2006.
- [132] R. Dangel, C. Berger, R. Beyeler, L. Dellmann, F. Horst, T. Lamprecht, N. Meier, and B. J. Offrein, “Prospects of a Polymer-Waveguide-Based Board-Level Optical Interconnect Technology,” *11th IEEE Work. Signal Propag. Interconnects*, pp. 131–134, 2007.
- [133] R. Dangel, U. Bapst, C. Berger, R. Beyeler, L. Dellmann, F. Horst, B. Offrein, and G.-L. Bona, “Development of a Low-Cost Low-Loss Polymer Waveguide Technology for Parallel Optical Interconnect Applications,” *Dig. LEOS Summer Top. Meet.*, p. MB4.3, 2004.
- [134] F. E. Doany, C. L. Schow, C. W. Baks, D. M. Kuchta, P. Pepeljugoski, L. Schares, R. Budd, F. Libsch, R. Dangel, and F. Horst, “160 Gb/s Bidirectional Polymer-Waveguide Board-Level Optical Interconnects Using CMOS-Based Transceivers,” *IEEE Trans. Adv. Packag.*, vol. 32, no. 2, pp. 345–359, 2009.
- [135] F. E. Doany, C. L. Schow, J. A. Kash, C. Baks, R. Budd, P. Pepeljugoski, D. Kuchta, R. Dangel, F. Horst, and B. Offrein, “Terabus: A 160-Gb/s Bidirectional Board-Level Optical Data Bus,” *Lasers Electro-Optics Soc. Annu. Meet.*, pp. 545–546, 2007.
- [136] R. C. A. Pitwon, K. Wang, J. Graham-Jones, I. Papakonstantinou, H. Baghsiahi, B. J. Offrein, R. Dangel, D. Milward, and D. R. Selviah, “FirstLight: Pluggable Optical Interconnect Technologies for Polymeric Electro-Optical Printed Circuit Boards in Data Centers,” *J. Light. Technol.*, vol. 30, no. 21, pp. 3316–3329, 2012.
- [137] R. C. A. Pitwon, K. Hopkins, K. Wang, D. R. Selviah, H. Baghsiahi, B. J. Offrein, R. Dangel, F. Horst, M. Halter, and M. Gmür, “Design and Implementation of an Electro-optical Backplane with Pluggable In-plane Connectors,” *Proc. SPIE*, vol. 44, no. 0, pp. 76070J–1–12, 2010.
- [138] C. L. Schow, F. E. Doany, B. G. Lee, R. Budd, C. Baks, R. Dangel, R. A. John, F. Libsch, and J. a Kash, “225 Gb/s Bi-Directional Integrated Optical PCB Link,” *OSA/OFC/NFOEC*, p. PDPA2, 2011.
- [139] N. Bamiedakis, A. Hashim, R. V. Penty, and I. H. White, “A 40 Gb/s Optical Bus for Optical Backplane Interconnections,” *J. Light. Technol.*, vol. 32, no. 8, pp. 1526–1537, 2014.
- [140] N. Bamiedakis, A. Hashim, R. V. Penty, and I. H. White, “Regenerative Polymeric Bus Architecture for Board-level Optical Interconnects,” *Opt. Exp.*, vol. 20, no. 11, pp. 11625–11636, 2012.
- [141] K. Schmidtke, F. Flens, A. Worrall, R. Pitwon, F. Betschon, T. Lamprecht, and R. Krähenbühl,

- “960 Gb/s Optical Backplane Ecosystem Using Embedded Polymer Waveguides and Demonstration in a 12G SAS Storage Array,” *J. Light. Technol.*, vol. 31, no. 24, pp. 3970–3974, 2013.
- [142] F. E. Doany, P. K. Pepeljugoski, A. C. Lehmanl, J. A. Kash, and R. Dangel, “Measurement of Optical Dispersion in Multimode Polymer Waveguides,” *LEOS Summer Top. Meet.*, p. MB4.4, 2004.
- [143] T. Mori, K. Moriya, K. Kitazoe, S. Takayama, S. Terada, M. Fujiwara, K. Takahama, K. Choki, and T. Ishigure, “Polymer Optical Waveguide having Unique Refractive Index Profiles for Ultra High-Density Interconnection,” *Opt. Fiber Commun. Conf.*, p. OTu1I.6, 2012.
- [144] T. Ishigure, “Graded-Index Core Polymer Optical Waveguide for High-Speed and High-Density On-Board Interconnects,” *2nd IEEE CPMT Symp. Japan*, pp. 1–4, 2012.
- [145] K. Soma and T. Ishigure, “Fabrication of a Graded-Index Circular-Core Polymer Parallel Optical Waveguide Using a Microdispenser for a High-Density Optical Printed Circuit Board,” *IEEE J. Sel. Topics Quantum Electron.*, vol. 19, no. 2, 2013.
- [146] T. Ishigure, K. Shitanda, T. Kudo, S. Takayama, T. Mori, K. Moriya, and K. Choki, “Low-loss design and fabrication of multimode polymer optical waveguide circuit with crossings for high-density optical PCB,” *Electron. Components Technol. Conf.*, pp. 297–304, 2013.
- [147] T. Ishigure, K. Shitanda, and Y. Oizmi, “Index-Profile Design for Low-Loss Crossed Multimode Waveguide for Optical Printed Circuit Board,” *Opt. Exp.*, vol. 23, no. 17, pp. 22262–22273, 2015.
- [148] S. Walklin and J. Conradi, “Multilevel Signaling for Increasing the Reach of 10 Gb/s Lightwave Systems,” *J. Light. Technol.*, vol. 17, no. 11, pp. 2235–2248, 1999.

3 FUNDAMENTAL STUDIES OF MULTIMODE POLYMER WAVEGUIDES

This chapter introduces the multimode polymer waveguides used in this thesis along with key design issues and their optical transmission properties. The chapter continues by describing the theoretical work carried out to investigate the coupling efficiency and waveguide bandwidth. The coupling losses, alignment tolerances and bandwidth of links using the waveguides are theoretically estimated for a wide range of waveguide parameters. The results of this study not only highlight the potential for designing waveguides with high alignment tolerance and high bandwidth, but also provide a theoretical foundation for the experimental work on dispersion studies presented in the next chapter.

3.1 Introduction

Chapters 1 and 2 have described the increasing demand for datacommunication link capacity within data centres and supercomputers this, in turn, necessitating the development of high-speed short-reach optical interconnects. Multimode polymer waveguides, in particular, are attractive as they offer significant advantages over their electrical counterparts as discussed previously. However, the successful development of high performance optical interconnects requires a thorough study of the key technological parameters involved in the

waveguide design. Therefore, this chapter presents studies of the fundamental optical transmission properties and important waveguide parameters for high bandwidth operation.

Three properties are of particular importance:

- Low loss transmission at wavelengths of interest;
- High coupling efficiency and misalignment tolerances to ensure low system penalties and low-cost assembly employing conventional fibres and optical components;
- High available link bandwidth.

The structure of this chapter is as follows. Sections 3.2 and 3.3 introduce the fabricated multimode waveguide with different refractive index profiles and describe some design issues resulting from the waveguide fabrication. Section 3.4 briefly discusses the two methods used to understand light propagation through the waveguides. In section 3.5, the methodology employed to estimate the coupling efficiency is described first. The section continues by studying the coupling loss and misalignment tolerances on a wide range of waveguide parameters employing different launch schemes. Section 3.6 introduces the measurement of insertion loss and the investigation of the alignment tolerances of butt-coupled schemes using standard optical fibres. Section 3.7 discusses the theoretical approaches of dispersion studies employed in the thesis, while section 3.8 presents the estimated bandwidth limitations of the multimode waveguides for various launch conditions. Finally, section 3.9 summarises the results presented in this chapter.

3.2 Waveguide Geometry

The multimode polymer waveguides studied in this thesis mainly have rectangular shapes and are all fabricated in a similar manner by Dow Corning. A typical $50 \times 50 \mu\text{m}^2$ waveguide sample with separation distance of $250 \mu\text{m}$, the typical optical fibre pitch, is illustrated in Figure 3-1. It consists of three layers: a uniform bottom cladding, a patterned core and a top cladding. The facet of the waveguide array is plotted in Figure 3-1(a) with the cross section of the waveguide highlighted in Figure 3-1(b).

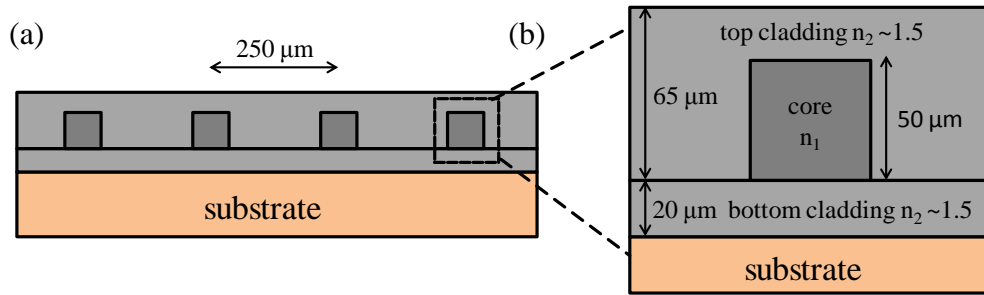


Figure 3-1 Schematic of polymer waveguides: (a) array of waveguide facets and (b) cross section of a $50 \times 50 \mu\text{m}^2$ waveguide.

A symmetric waveguide geometry in both horizontal and vertical direction is often desired in order to match the symmetry of conventional optical fibres and some lasers and detectors so that similar behaviour will be expected in both transverse directions. It is worth noting that the profiles of the guided modes can be affected by the asymmetry in the vertical direction of the waveguide structure induced by the air and substrate regions at the top and bottom of the waveguide core. Hence, sufficiently large top and bottom cladding thicknesses are often used to minimise the induced effects on the waveguide modes. The confinement factor (Γ_m , defined as the fraction of the mode energy density confined in the waveguide core) of the waveguide mode is calculated for a varying cladding thickness for a waveguide with cross section of $50 \times 50 \mu\text{m}^2$ and index step $\Delta n = 0.005$ (better light confinement expected for higher index step). Figure 3-2 plots the confinement factor of the fundamental mode ($m=1$) and the higher-order mode close to cut-off ($m \approx N_{tot}$, where N_{tot} is the total number of guided modes in the waveguide) for different thicknesses. It can be seen that the mode confinement decreases with increasing top cladding thickness due to the lower refractive index of the cladding region. The mode confinement varies for each waveguide mode and the value of higher-order modes can provide an estimation of the required cladding thickness. It can be noticed that Γ_m remains constant when the thickness becomes larger than a characteristic value of $\sim 5 \mu\text{m}$ for the waveguide parameters studied.

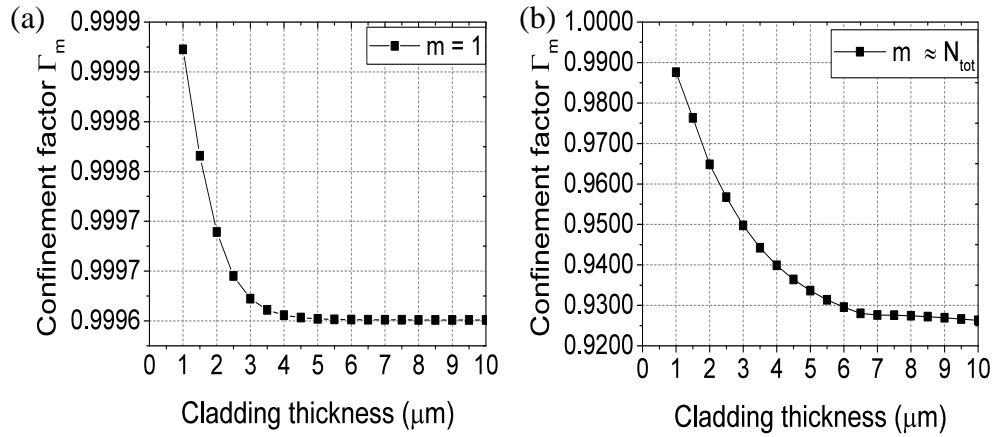


Figure 3-2 Confinement factor of (a) the fundamental mode and (b) a higher order mode for index step $\Delta n = 0.005$, waveguide width $w = 50 \mu\text{m}$.

However, in practice, the top and bottom cladding thicknesses are usually larger than 10 μm to protect the buried waveguide and ensure good waveguide isolation. Figure 3-3(a) shows a fabricated sample consisting of an array of $50 \times 50 \mu\text{m}^2$ waveguides, while Figure 3-3(b) presents the images of the waveguide facet illuminated under white light. The waveguide facets studied in this thesis are diced with a saw blade and not polished although they can be mechanically polished in order to obtain a smoother facet surface. The polishing procedure brings additional costs and complexity during the manufacturing process which is highly unlikely to be used in the industry, and thus is not employed in this work.

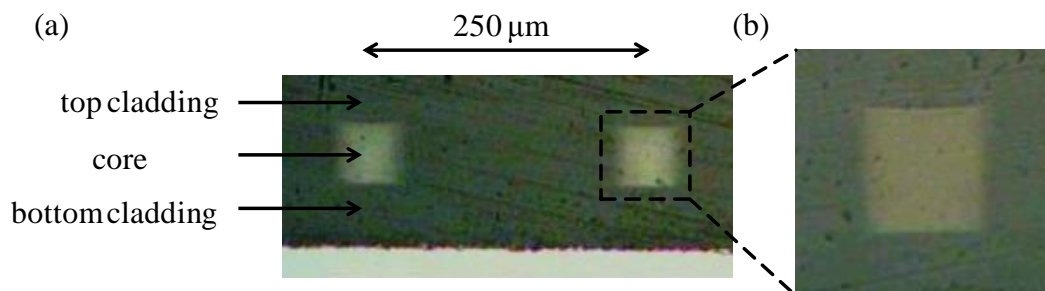


Figure 3-3 (a) Waveguide sample fabricated on a silicon substrate comprising of $50 \times 50 \mu\text{m}^2$ waveguides with separation distance of 250 μm and (b) $50 \times 50 \mu\text{m}^2$ waveguide illuminated with white light.

3.3 Step-index and Graded-index Waveguides

Based on the refractive index profile of the core, waveguides can be categorised into two types: step-index and graded-index. The refractive index profile in a step-index waveguide

has a uniform refractive index within the core and has an abrupt decrease at the boundary of core and cladding. In contrast, the graded-index waveguides have a gradual decreasing refractive index with increasing distance from the centre axis within the core. The most commonly used graded-index variation in the core follows a power law relationship typically seen in graded-index fibres. The refractive index profile in the rectangular waveguide can be modified from the power-law form as expressed in Equation (3-1) [1].

$$n(x, y) = \begin{cases} n_{co} \cdot \sqrt{1 - \Delta \cdot [f(x) + g(y)]}, & 0 \leq f(x) + g(y) \leq 2 \\ n_{co} \cdot \sqrt{1 - 2\Delta} = n_{cl}, & f(x) + g(y) \geq 2 \end{cases} \quad (3-1)$$

$$\text{where } f(x) = \left(\frac{x}{a_x}\right)^s, \quad g(y) = \left(\frac{y}{a_y}\right)^t \text{ and } \Delta = \frac{n_{co}^2 - n_{cl}^2}{2n_{co}^2}.$$

Here, n_{co} and n_{cl} are the refractive indices at the centre axis of the core and cladding, respectively. a_x and a_y are the half-width and half-height of the rectangular core, respectively. The dimensionless parameters s and t define the shape of the index profile in the horizontal and vertical directions in the core, respectively. For $s = t = \infty$, $n(x, y)$ reduces to the step-index profile, i.e. $n(x, y) = n_{co}$ (Figure 3-4).

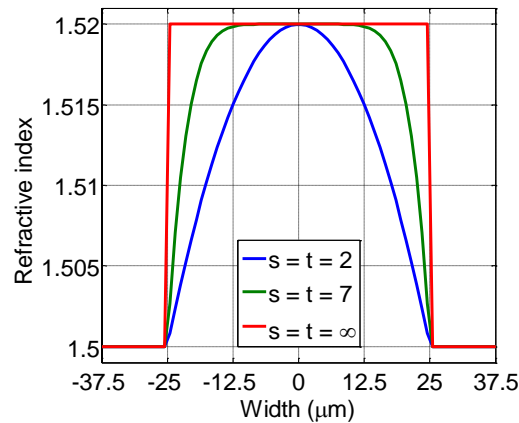


Figure 3-4 Refractive index profiles with different index exponent values for a waveguide with core width of 50 μm .

The multimode waveguides allow light to travel in many propagation paths (or modes in mode theory) due to the large core size. Figure 3-5(a) depicts the examples of refractive index profiles of step-index ($s = t = \infty$) and graded-index waveguides ($s = t = 2$), while Figure 3-5(b) illustrates the difference between the light propagation paths inside step-index

waveguides and graded-index waveguides from the perspective of ray optics. In simplest terms, light travels based on the total internal reflection in the step-index waveguides, whereas the light paths are close to sinusoidal shapes in the graded-index waveguides. Unlike the rays in the step-index waveguides, the rays with larger launch angles travel further but also travel faster at the edges than the rays propagating along the waveguide axis due to a lower edge refractive index in the graded-index waveguides. Therefore, the graded-index waveguides can in principle greatly reduce the intermodal dispersion as it is possible for different rays to arrive at the waveguide end together. More details on the effects of refractive index profiles on the performance of the waveguides and waveguide components will be further discussed in Chapters 4 and 5.

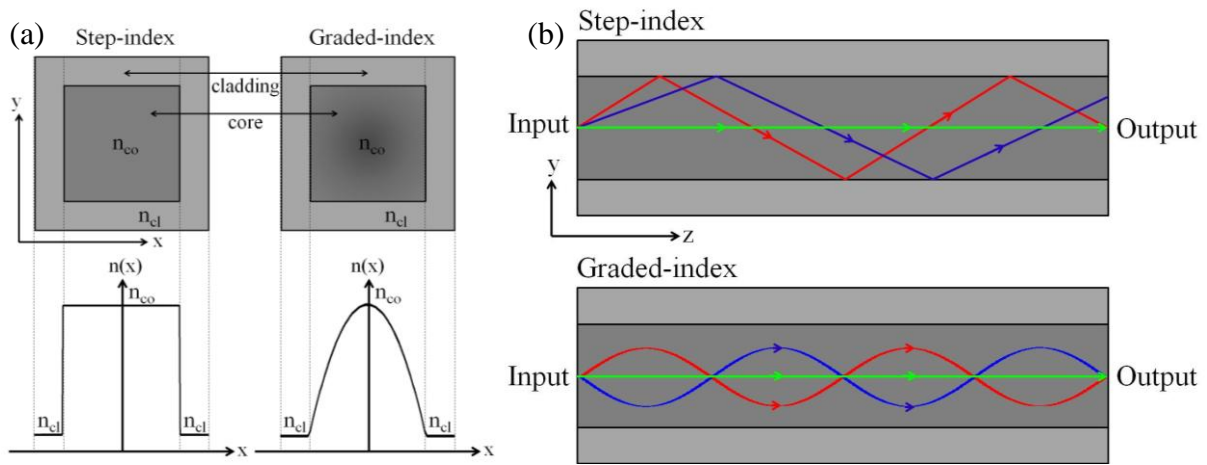


Figure 3-5 (a) Cross section and refractive index profiles for step-index ($s = t = \infty$) and graded-index ($s = t = 2$) waveguides and (b) light propagations inside the step-index and graded-index waveguides.

For the purpose of an investigation of the waveguide parameters (i.e. width w and index step Δn) that need to be taken into account for the study of coupling efficiency and waveguide bandwidth, the simulation only employs waveguides with square geometries and step-index profiles in the remainder of this chapter. The core sizes of the waveguide are chosen to be from $20\ \mu\text{m}$ to $60\ \mu\text{m}$. The refractive index differences are chosen to be from 0.005 to 0.03 while the cladding refractive index is fixed to 1.5 for the simplicity of the analysis. These values can be readily obtained with the polymer materials employed elsewhere in this thesis. Although arbitrary index profiles can also be modelled, the simulation utilises step-index profiles to provide a general description of the change of waveguide behaviour with varying dimensions and index differences.

3.4 Methodology

Appropriate methods of understanding light propagation should be determined as it is essential for any further studies such as the evaluation of coupling loss and waveguide dispersion. In this section, two major approaches employed in this thesis are introduced briefly, namely the ray tracing analysis and the electromagnetic treatment. Each method is compared in terms of accuracy, speed and versatility.

3.4.1 Ray Tracing Analysis

Ray tracing, based on the laws of geometric optics, is the simplest and most straightforward method to analyse light propagation in a dielectric medium [2]. Ray tracing analysis can be used when the waveguide dimension is much larger than the operating wavelength [3]. In early days, the ray tracing method was widely used for designing multimode fibres and other optical components owing to the lack of simulation and design tools. Even nowadays, this method is still extensively being used as it provides an intuitive description of the waveguide operation especially for very large size of waveguides which typically requires long computational time.

For a waveguide with larger core refractive index n_{co} surrounded by lower cladding refractive index n_{cl} , the light coupled into the core can be viewed as light rays propagating inside the waveguide. These light rays can be categorised into guided rays and radiated rays depending on the incident angle θ at the core-cladding interface. Bounded rays travel inside the waveguide core via total TIR without losing power along the waveguide, whereas leaky rays lose power while travelling inside the waveguide as they are only transmitted partially at every reflection at the interface of core and cladding. Light propagation in the core is illustrated in Figure 3-6.

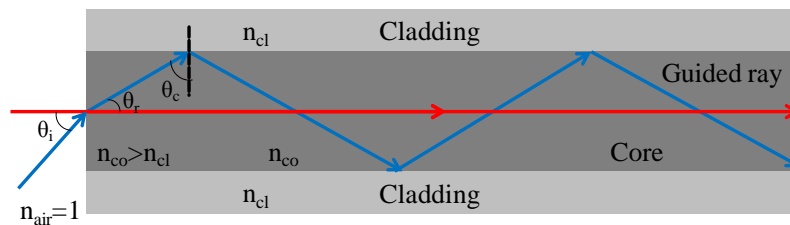


Figure 3-6 Illustration of total internal reflection (TIR).

When a ray with θ_i is incident at the centre of the core, refraction occurs at the air-core interface. The refractive angle θ_r is given by Snell's Law:

$$n_{air} \sin \theta_i = n_{co} \sin \theta_r \quad (3-2)$$

where n_{air} and n_{co} are the refractive indices of the air and waveguide core, respectively.

When the ray reaches the core-cladding interface, it is refracted again only for an angle of incidence such that $\sin \theta < n_{cl} / n_{co}$. The ray experiences TIR when the angle of incidence $\theta > \theta_c$, and θ_c is called critical angle, defined as:

$$\sin \theta_c = n_{cl} / n_{co} \quad (3-3)$$

where n_{co} and n_{cl} are the refractive indices of the waveguide core and cladding, respectively.

Combining Equation (3-2) and Equation (3-3), the maximum angle of incident ray that remains confined inside the core can be calculated.

$$n_{air} \sin \theta_i = n_{co} \cos \theta_c = \sqrt{n_{co}^2 - n_{cl}^2} \quad (3-4)$$

$n_{air} \sin \theta_i$ is known as the numerical aperture (NA) of the waveguide, which represents the light gathering capacity of a waveguide.

The ray tracing method can provide a very intuitive picture for highly-multimoded structures such as waveguide crossings and bends, the applications of which will be further discussed in section 5.4 and 5.5 in Chapter 5. However, this approach has many limitations. Therefore, rigorous analyses using electromagnetic treatment are required for a complete description of the waveguide fields.

3.4.2 Electromagnetic Treatment

Electromagnetic analysis is based on solving Maxwell's equations. Since Marcatili and Marcuse's thorough studies on rectangular dielectric waveguides in the late 1960s, various numerical and analytical methods have been developed to compute the electromagnetic fields in waveguides. Some important numerical methods include the finite difference method (FDM), film mode matching method (FMM) and beam propagation method (BPM); some analytical methods include Marcatili's approximation method and effective index method

(EIM) [4]. Each method has its own advantages and disadvantages in terms of computational speed, accuracy and complexity. It is worth introducing mode theory before comparing different methods.

3.4.2.1 Mode Theory

A waveguide mode corresponds to a specific solution of the Maxwell equations that satisfies appropriate boundary conditions and its spatial distribution remains the same with propagation [5]. The electric and magnetic field of a mode in the channel waveguide can be written as:

$$E_m(x, y, z, t) = \mathcal{E}_m(x, y) e^{i(\omega t - \beta_m z)} \quad (3-5)$$

$$H_m(x, y, z, t) = \mathcal{H}_m(x, y) e^{i(\omega t - \beta_m z)} \quad (3-6)$$

where m is mode index (an integer), $\mathcal{E}_m(x, y)$ and $\mathcal{H}_m(x, y)$ are mode field profiles, β_m is the propagation constant of the mode m , and ω is the angular frequency.

The propagation constant β_m can be expressed by the following normalised guide index b_m , and all the parameters are shown in Figure 3-6.

$$b_m = \frac{\beta_m^2 - k_{cl}^2}{k_{co}^2 - k_{cl}^2} = \frac{n_{eff,m}^2 - n_{cl}^2}{n_{co}^2 - n_{cl}^2} \quad (3-7)$$

where $k = 2\pi / \lambda$, is the free-space wavenumber (also called free-space propagation constant), and $n_{eff,m} = \beta_m / k = \beta_m \lambda / 2\pi$, is the effective refractive index of the waveguide mode that has a propagation constant β_m .

The number of guided modes in a waveguide depends on the waveguide dimensions and refractive index differences between the core and cladding. For instance, the smaller waveguide dimension w and lower index step Δn ($w = 20 \mu\text{m}$, $\Delta n = 0.005$) may have less than 100 modes, whereas for larger waveguides with bigger index steps ($w = 60 \mu\text{m}$, $\Delta n = 0.03$) the number of modes can increase to around 3000 at 850 nm. Therefore, it is very important to choose a method that has sufficient accuracy, and yet is fast to compute. In this chapter, the EIM is preferred as it generates results that have good accuracy for guided modes that are far from the cut-off for waveguides with symmetric waveguide geometries and refractive index profiles [6]. However, for waveguides with asymmetric index profiles such as the graded-

index waveguide discussed in the next chapter, greater calculation accuracy is desired and therefore the FMM is employed. A brief description of each major method is given below.

3.4.2.2 Simulation Methods

- Effective index method (EIM)

The basic principle of EIM is to approximate a channel waveguide into two planar waveguides, that is to say, to convert a two-dimensional problem into a one-dimensional one as illustrated in Figure 3-7 [7]. The two planar waveguides are solved separately while the results obtained from one are employed to derive the mode profiles of the other one. This method is based on the assumption that the electromagnetic field in the two transverse directions in the waveguide is independent.

The effective index is mode dependent, determining different TE_{mn} or TM_{mn} modes separately. The waveguide structure is first divided into three vertical regions I, II and III, each of which is then treated as a planar waveguide to find the propagation constants β_m for mode m and effective indices for a vertical planar waveguide with width w . For “quasi-TE” mode, the x dependence of the y component of the electric mode field $\mathcal{E}_{m,y}(x)$ for central waveguide region I is first found. Then the structure is treated as a planar waveguide to calculate the propagation constant β_{mn} and the y dependence of the y component of the electric mode field $\mathcal{E}_{n,y}(y)$. It should be noted that the \mathcal{E}_y component of the TM_n field of the effective vertical planar waveguide is used to obtain $\mathcal{E}_{n,y}(y)$ of the original waveguide. Therefore, for the case of a TE_{mn} mode, the y component of the overall mode field for the original waveguide $\mathcal{E}_{mn,y}(x, y) = \mathcal{E}_{m,y}(x) \times \mathcal{E}_{n,y}(y)$. The EIM method is straightforward and performs adequately for waveguides with small refractive index contrast and simple geometrical cross-section profiles [8].

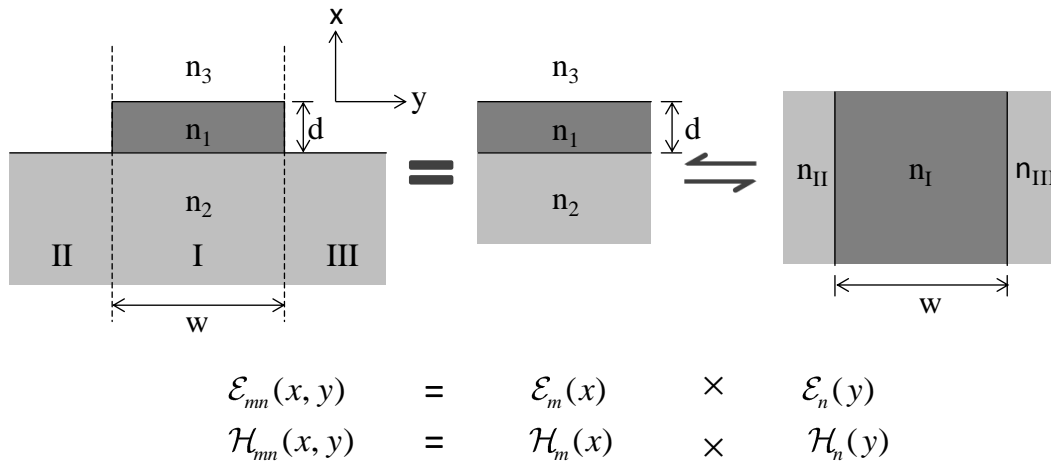


Figure 3-7 Basic concept of effective index method (EIM): dividing the 2-D problem into two 1-D problems in each transverse direction [7].

- Film mode matching method (FMM)

The FMM is a useful numerical method to analyse waveguide structures consisting of a small number of homogeneous rectangles [9]. The cross section of the waveguide can be considered to be a sandwich of M slices, each of which is cut from the N-layer film waveguide. The slices and layers are perpendicular to each other as shown in Figure 3-8. This method involves finding the TE and TM modes of each film, collecting the modes that have the same propagation constant in the z-direction, and matching the field distributions at the interfaces of the slice by adjusting the modal amplitudes in each film.

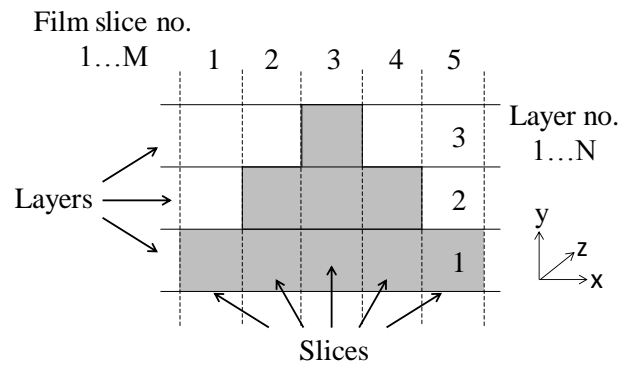


Figure 3-8 Illustration of film mode matching method (FMM) on the cross section of a ridge waveguide.

The algorithm is as follows. For each 1-dimensional (1-D) slice, the TE and TM modes are solved analytically assuming the slice to be infinitely wide. In a given slice, the field profile in the waveguide can be expressed as a linear combination of the 1-D TE and TM modes of the slice expressed as:

$$F(x, y) = \sum_{m=1}^{\infty} \left[u_m^{TE} \exp(ik_{xm}^{TE} x) \phi_m^{TE}(y) + u_m^{TM} \exp(ik_{xm}^{TM} x) \phi_m^{TM}(y) \right] \quad (3-8)$$

where u_m^{TE} and u_m^{TM} are mode amplitudes of the 1-D modes m , $\phi_m^{TE}(y)$ and $\phi_m^{TM}(y)$ are the 1-D field profiles (either electric or magnetic field), k_m^{TE} and k_m^{TM} are the wavevectors.

The overlap integrals of the modes at the interface between the slices are formed into matrices. The solver tries to find the amplitude for each 1-D mode. Using the matrices, the 2-D modes are found by “propagating” the vertical 1-D modes in the x-direction based on a guessed propagation constant β . Then β is scanned through a range of values until the mode matching occurs at the interface using the continuity of the transverse E and H fields at the slice interfaces and the boundary conditions (electric and magnetic walls). This method is full-vectorial and offers very high accuracy but also requires large computation power for the cases of highly-multimoded waveguides.

3.4.3 Method Comparison

For a $50 \times 50 \mu\text{m}^2$ waveguide with index step of 0.02, the number of guided modes is 1325 and 1293 for EIM and FMM method respectively. Similar values of effective index (n_{eff}) for all guided modes are obtained and plotted in Figure 3-9. It can be seen that the differences are negligible for modes far away from the cut-off ($n < 850$) while they become larger for higher-order modes close to cut-off (of the order of 10^{-4}).

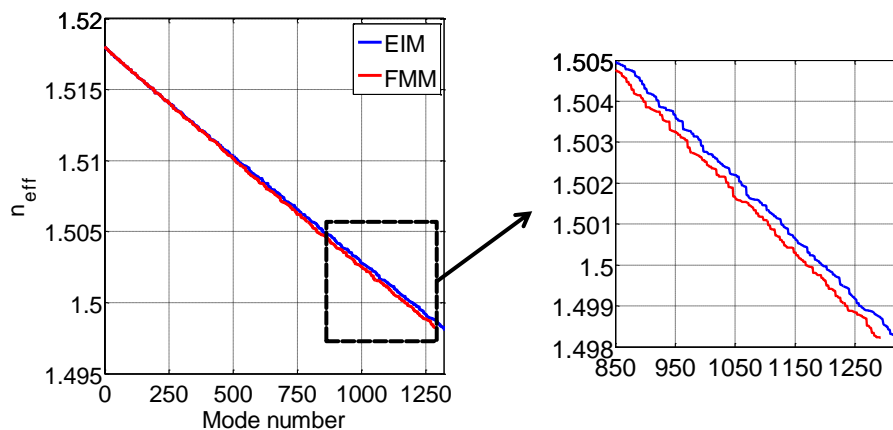


Figure 3-9 Effective index for guided modes computed with EIM and FMM methods for a $50 \times 50 \mu\text{m}^2$ waveguide with index step of 0.02.

In summary, Table 3-1 compares different methods of analysing light propagation in waveguides. Appropriate methods should be chosen depending on the accuracy and speed needed. EIM is usually preferred for initial calculations to provide a general guideline of the properties of the waveguides as it requires less computational time and gives relatively good approximation compared to the other aforementioned methods. FMM is required when high accuracy of field calculations is desired. In this thesis, ray tracing is implemented using MATLAB software while both EIM and FMM methods are supported by the commercially available software FIMMWAVE [10].

Table 3-1 Comparison of different methods.

Method	Speed	Accuracy	Advantage
Ray Tracing	Fast	Poor	Simple
EIM	Fast	Medium	Speed
FMM	Slow	High	Accuracy

3.5 Coupling Efficiency Calculation

Input and output coupling coefficients determine the total coupling efficiency as expressed in Equation (3-9). The input coupling coefficient describes the percentage of the input power coupled into the waveguide, and output coupling coefficient describes the percentage of the output power coupled into the output (e.g. a fibre).

$$C_{total} = \frac{P_{out}}{P_{in}} = \frac{P_{wg}}{P_{in}} \cdot \frac{P_{out}}{P_{wg}} = c_{in} \cdot c_{out} \quad (3-9)$$

In logarithmic scale, the total coupling loss is the summation of input and output coupling losses:

$$C_{total} = -10 \log c_{total} = -(10 \log c_{in} + 10 \log c_{out}) = C_{in} + C_{out} \text{ (dB)} \quad (3-10)$$

As mentioned earlier, most of the experiments conducted in this thesis utilises a lens at the waveguide output to receive the optical signal. Since the numerical aperture of the lens is larger than that of the waveguide ($NA_{lens} > NA_{wg}$), all output light can be collected when a

large area detector is employed. Therefore, the induced output coupling loss can be assumed to be zero when the Fresnel loss is not taken into account.

The summation of the power P_m of all the excited modes inside the waveguide is equal to the total power P_{wg} coupled into the guide. The power P_m of each excited mode is found by calculating the mode coupling coefficients a_m , which is computed using the overlap integrals of the field distribution E_t and H_t incident on the waveguide facet and the waveguide mode profiles $\mathcal{E}_{t,m}$ and $\mathcal{H}_{t,m}$ as shown in Equation (3-11) and Equation (3-12) [2], [11].

$$P_{wg} = \sum_m P_m = \sum_m |a_m|^2 \quad (3-11)$$

$$a_m = \frac{1}{2} \int_{A_o} \hat{z} \cdot (E_t \times \mathcal{H}_{t,m}^*) dA = \frac{1}{2} \int_{A_o} \hat{z} \cdot (\mathcal{E}_{t,m}^* \times H_t) dA \quad (3-12)$$

Assuming mode profiles $\mathcal{E}_{t,m}$ and $\mathcal{H}_{t,m}$ are orthonormal:

$$\frac{1}{2} \int_{A_o} \hat{z} \cdot (\mathcal{E}_{t,n} \times \mathcal{H}_{t,m}^*) dA = \frac{1}{2} \int_{A_o} \hat{z} \cdot (\mathcal{E}_{t,m}^* \times \mathcal{H}_{t,n}) dA = \begin{cases} 1 & \text{if } m = n \\ 0 & \text{if } m \neq n \end{cases} \quad (3-13)$$

The mode profiles of the waveguides are computed using EIM in FIMMWAVE. It should be noted that both polarisations are treated equally in the simulation model and Fresnel losses are not included in the results presented in the following sections.

3.5.1 SMF Launch

The use of SMF at the waveguide input results in high coupling efficiency due to the larger number of modes of the waveguides studied. It is worth mentioning that a standard 9 μm SMF is no longer strictly single-mode at 850 nm as normalised frequency (V number) > 2.405 [12]. However, it can still be viewed as a restricted launch as the second order mode is near cut off. The study of this launch also indicates the type of behaviour that might occur if light is injected from single mode VCSELs, though their beam properties will be different quantitatively.

According to [8], the fundamental mode of a SMF can be modelled effectively using a Gaussian field profile. Figure 3-10(a) illustrates the input coupling configuration under a

SMF launch while the free-space expansion of a Gaussian beam is plotted in Figure 3-10(b). Equation (3-14) represents the electrical field of the emitted light of a SMF in Cartesian coordinates:

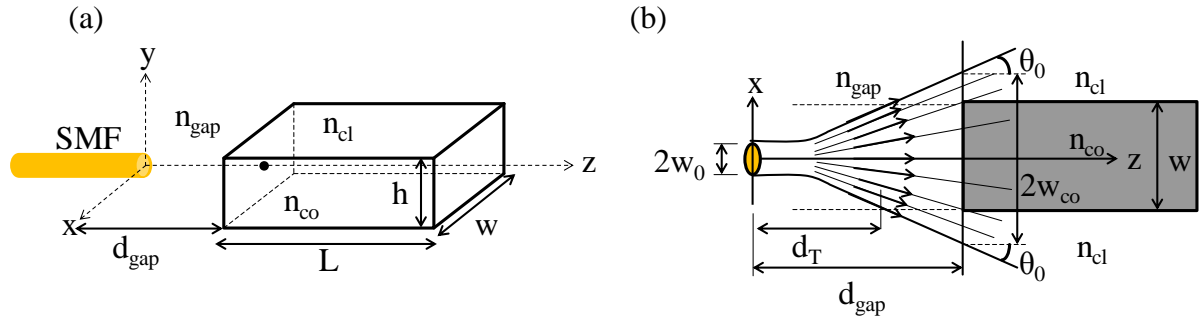


Figure 3-10 (a) Schematic of the coupling configuration for a SMF input at a distance d_{gap} from the waveguide facet and (b) illustration of the free-space expansion of Gaussian beam.

$$e_{x,y}^{SMF}(x, y, z) = A \frac{w_0}{W(z)} \exp[-((x - x_0)^2 + (y - y_0)^2) \cdot (\frac{1}{W^2(z)} + j \frac{kn_{gap}}{2R(z)}) - jkn_{gap}z + j\theta(z)] \quad (3-14)$$

$$W(z) = w_0 \cdot \sqrt{1 + (\frac{\lambda z}{\pi n_{gap} w_0^2})^2} \quad (3-15)$$

$$R(z) = z \cdot [1 + (\frac{\pi n_{gap} w_0^2}{\lambda z})^2] \quad (3-16)$$

$$\theta(z) = \tan^{-1}(\frac{\lambda z}{\pi n_{gap} w_0^2}) \quad (3-17)$$

where k and n_{gap} are the free-space wavenumber and the refractive index of the free-space gap respectively, (x_0, y_0) are the coordinates of the beam centre, parameters w_0 and $W(z)$ represent the beam radius (location of $1/e$ electrical field value) at positions $z = 0$ and z respectively, $R(z)$ is the curvature of the phase front and $\theta(z)$ is the phase shift between the Gaussian beam and ideal local plane wave. The constant A is employed to normalize the power over the SMF cross section. From Equation (3-14), the value of constant A can be obtained.

$$\int_{-\infty}^{\infty} \int_{-\infty}^{\infty} |e_{x,y}^{SMF}(x, y, 0)|^2 dx dy = 1 \rightarrow A = \frac{1}{w_0} \sqrt{\frac{2}{\pi}} \quad (3-18)$$

The full-width-at-half-maximum (FWHM) of the fundamental mode of a standard SMF is typically in the range of 6–8 μm . Thus, a FWHM of 7 μm is used in the simulation, i.e. $w_0 = 4.2 \mu\text{m}$.

3.5.1.1 Coupling Loss

For a well-aligned butt-coupled SMF ($z = 0$), perfect coupling is expected due to its small input spot and small numerical aperture. The coupling loss is calculated for the interface between a perfectly aligned butt-coupled SMF and square waveguides with varying parameters studied ($0.005 \leq \Delta n \leq 0.03$, $20 \mu\text{m} \leq w \leq 60 \mu\text{m}$) using Equation (3-12):

$$C_{in}^{SMF} |_{(x,y,z)=(0,0,0)} = 0 \text{ dB, for } \begin{cases} 0.005 \leq \Delta n \leq 0.03 \\ 20 \mu\text{m} \leq w \leq 60 \mu\text{m} \end{cases} \quad (3-19)$$

Thus, only Fresnel loss contributes to the input coupling loss in this case. In the next section, the effect of transverse input misalignments is studied.

3.5.1.2 Transverse Misalignment

A perfectly butt-coupled fibre is assumed (no longitudinal gap) when evaluating the input offset in x-y plane (transverse misalignment). The -3 dB alignment tolerances for the x-axis offset for all waveguide parameters under consideration are plotted in Figure 3-11(a). It can be noticed that the -3 dB transverse misalignment is independent of the index step Δn of the waveguide. Figure 3-11(b) shows the input coupling loss across different input positions for a $50 \times 50 \mu\text{m}^2$ waveguide with an index step Δn of 0.02. Note that only one quarter of the waveguide facet is shown in Figure 3-11(b) as both waveguide and input fibre have symmetric geometries in the horizontal and vertical directions. Similar plots are expected to be obtained for the misalignments in both directions. It can be noticed that -3 dB transverse alignment tolerances are of the order of the half width of the waveguide core: $\Delta x_{-3dB} = \Delta y_{-3dB} \approx \pm w/2$.

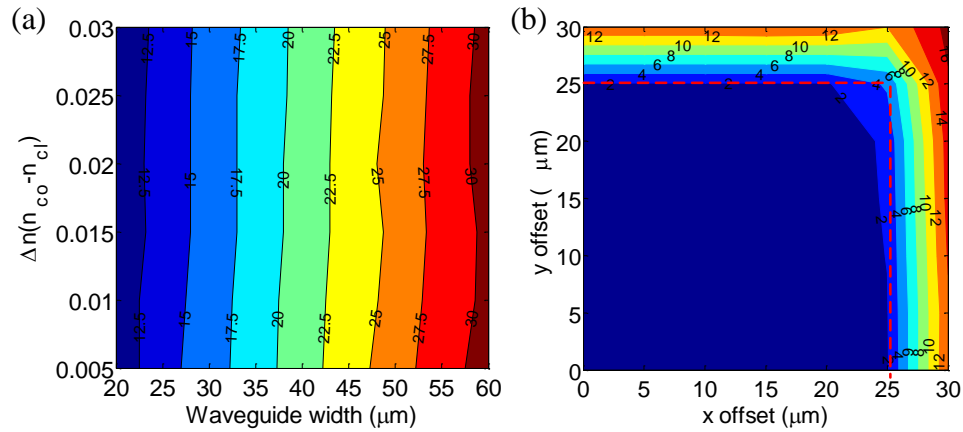


Figure 3-11 (a) -3 dB alignment tolerance (unit in μm) as a function of waveguide parameters for horizontal offsets for a SMF input, (b) input coupling loss as a function of input SMF positions on a $50 \times 50 \mu\text{m}^2$ waveguide with $\Delta n = 0.02$ (-3 dB alignment tolerances indicated in red dashed line) at $\lambda = 850 \text{ nm}$.

3.5.2 50 μm GI MMF Launch

Multimode fibre inputs constitute a very attractive way of coupling light into the waveguides due to the low-cost technologies available such as packaged active devices with ribbon fibres. However, it is non-trivial to compute the input coupling efficiency mainly owing to the large number of guided modes in both the input fibre and waveguide. The exact knowledge of the power distribution and relative phase difference of the fibre is required to calculate the coupling loss at the fibre-waveguide interface. In practice, many factors such as microbends and mode mixing can vary the parameters of the guided modes inside the fibre substantially. Therefore, a uniform input is defined here so as to provide a common reference to investigate the MMF-waveguide systems. The uniform input is based on the assumptions that all guided modes are uniformly excited in the input fibre. In addition, a perfect alignment (no longitudinal or angular offsets) between the fibre and waveguide is assumed as illustrated in Figure 3-12(a).

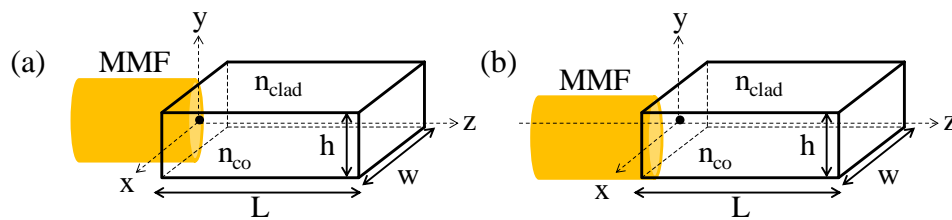


Figure 3-12 Schematic of the coupling configuration for a 50 μm GI MMF input: (a) well-alignment and (b) transverse misalignment with no longitudinal offsets.

A uniform mode power distribution assumed in this chapter, despite being not true in real systems, can provide a “worst-case” input condition and this constitutes a reference employed in the multimode systems. In this section, the electromagnetic treatment is employed to compute the dependency of the coupling efficiency on the waveguide parameters and input misalignment. It should be noted that the employed graded-index (GI) MMFs are assumed to have a square power-law profile without any defects as shown in Figure 3-13. The refractive index of these fibres is expressed as:

$$n(r) = \begin{cases} n_{co} \cdot \sqrt{1 - 2\Delta \cdot \left(\frac{r}{R}\right)^\alpha}, & 0 \leq r \leq R \\ n_{co} \cdot \sqrt{1 - 2\Delta}, & r \geq R \end{cases} \quad (3-20)$$

where R and α are the radius of the fibre and the coefficient of the square-law profile respectively. The parameters are chosen to match the conventional GI MMFs used in the experiments: $R = 25 \mu\text{m}$, $\Delta = 0.018$ and $\alpha = 2$.

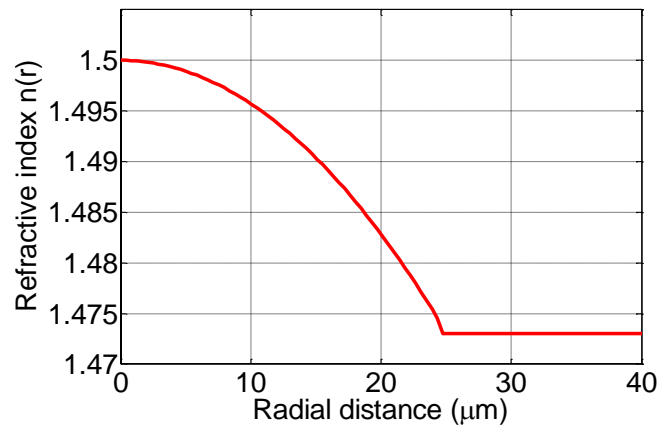


Figure 3-13 Refractive index profile the 50 μm GI MMF employed.

3.5.2.1 Coupling Loss

The linear polarised (LP) modes with indices m (cylindrical order) and n (radial order) of the input MMF are computed using an analytic mode solver [13] while the waveguide modes are obtained using EIM. The refractive index profile of the MMF and the operating wavelength are the input parameters of the calculation. The modes can be divided into degenerate groups indexed by the principal mode number (PMN) defined as $m + 2n + 1$. The power coupling coefficient c_{ij} (i.e. the power coupled into each waveguide mode i from each

fibre mode j) can be calculated using overlap integrals of the mode profiles of both input fibre and waveguide and is expressed as (in polar coordinates) [2], [12]:

$$c_{ij} = \frac{\left| \iint E_i^w E_j^f r dr d\phi \right|^2}{\left(\iint |E_i^w|^2 r dr d\phi \right) \cdot \left(\iint |E_j^f|^2 r dr d\phi \right)} \quad (3-21)$$

where E_i^w, E_j^f are the electric fields of the waveguide mode i and fibre mode j respectively. The relative phase between the different fibre modes is neglected and thus no interference effects are considered for the purpose of this study. This assumption is common in the analysis of highly-multimoded waveguides so as to simplify the calculation as the relative phases of different fibre modes are unknown in practice [14], [15].

The power p_i^w coupled into each waveguide mode i ($i = 1, \dots, N$ where N is the number of waveguide modes) can be expressed as the multiplication of the coefficient c_{ij} and the power p_j^f of the fibre modes ($j = 1, \dots, M$ where M is the number of fibre modes): $p_i^w = \sum_{j=1}^M c_{ij} p_j^f$.

Thus, the following matrix can be developed:

$$\begin{bmatrix} p_1^w \\ p_2^w \\ \dots \\ p_N^w \end{bmatrix} = \begin{bmatrix} c_{11} & c_{12} & \dots & c_{1M} \\ c_{21} & c_{22} & \dots & c_{2M} \\ \dots & \dots & \dots & \dots \\ c_{N1} & c_{N2} & \dots & c_{NM} \end{bmatrix} \cdot \begin{bmatrix} p_1^f \\ p_2^f \\ \dots \\ p_M^f \end{bmatrix} \quad (3-22)$$

The total power P_{in}^w coupled into the waveguide can be calculated from the summation of the power of all waveguide modes:

$$P_{in}^w = \sum_{i=1}^N p_i^w = \sum_{i=1}^N \sum_{j=1}^M c_{ij} p_j^f \quad (3-23)$$

If a uniform power distribution is assumed inside the input fibre, then $p_j^f = 1/M$.

The calculated coupling loss of a 50 μm GI MMF input for the waveguide parameters w and Δn under consideration is plotted in Figure 3-14. It shows that the larger waveguide dimensions and index steps can improve the input coupling efficiency. For example, the coupling loss is <0.25 dB when the waveguide width $w \geq 45 \mu\text{m}$ and index step $\Delta n \geq 0.02$. It

should be noted that the 50 μm GI MMF in principle should provide lower coupling loss than the 50 μm SI MMF due to its more confined field profiles [11]. In all the experiments presented in this thesis, the employed MMF input is a standard 50 μm GI MMF fibre.

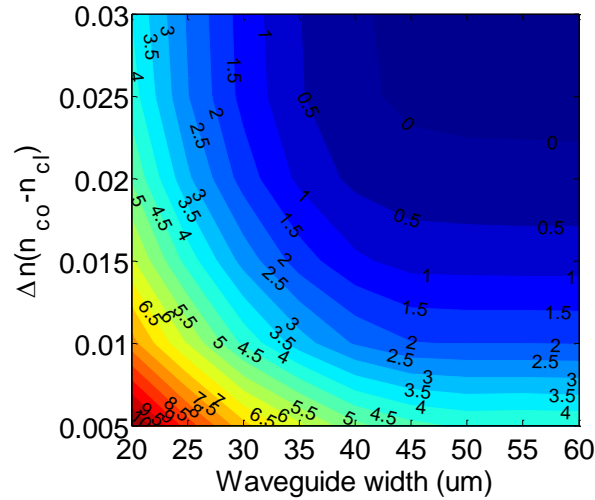


Figure 3-14 Input coupling loss for a 50 μm GI MMF as a function of waveguide width w and index step Δn at $\lambda = 850 \text{ nm}$.

3.5.2.2 Transverse Misalignment

The alignment tolerances for the butt-coupled MMFs with the waveguides are evaluated in this section. The input fibre is assumed to be perfectly coupled to the waveguide (no longitudinal offsets) as illustrated in Figure 3-12(b).

The alignment tolerances allowed are calculated using overlap integrals between the fibre and waveguide modes by offsetting the input fibre in both horizontal and vertical directions. As mentioned before, the symmetric properties of the input fibre and waveguide should result in a similar behaviour in both directions. Figure 3-15 shows the coupling loss for a quarter facet of a $50 \times 50 \mu\text{m}^2$ waveguide with index step Δn of 0.02 for a 50 μm GI MMF input. The -1 dB and -3 dB alignment tolerances as a function of waveguide width w and index step Δn for the horizontal offsets are also shown in Figure 3-16.

It is encouraging to see that the -1 dB alignment tolerances are $> \pm 10 \mu\text{m}$ even for the worst cases among the waveguides under study ($25 \mu\text{m} \leq w \leq 35 \mu\text{m}$, $\Delta n \geq 0.02$). It can also be seen that the -3 dB alignment tolerances are at nearly half waveguide width and do not strongly depend on the index step Δn only when the waveguide dimensions are comparable to the input fibre sizes (i.e. $w \geq 45 \mu\text{m}$). If the input fibre is much larger than the waveguide size

(i.e. $w \leq 30 \mu\text{m}$), the alignment tolerances are larger than the half width of the waveguide and also strongly affected by the index step Δn . For example, for a waveguide with width $w = 20 \mu\text{m}$, a $5 \mu\text{m}$ difference of -3 dB alignment tolerance can be observed between index steps $\Delta n = 0.005$ and $\Delta n = 0.03$.

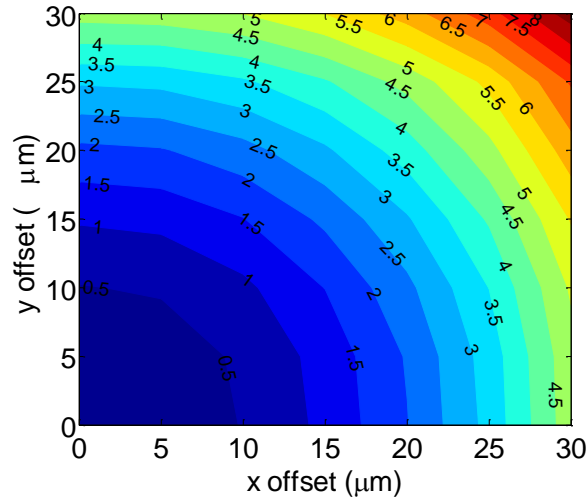


Figure 3-15 Input coupling loss as a function of the input positions for a $50 \times 50 \mu\text{m}^2$ waveguide with an index step $\Delta n = 0.02$ for a $50 \mu\text{m}$ GI MMF input at $\lambda = 850 \text{ nm}$.

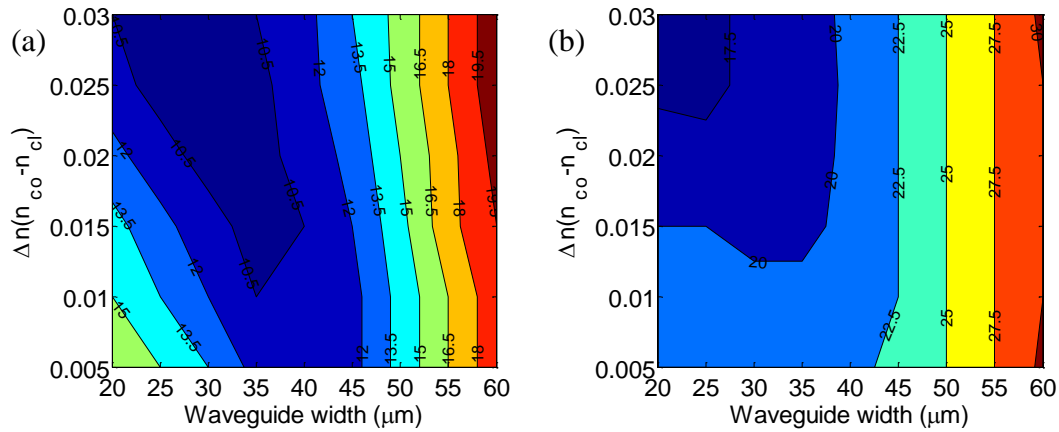


Figure 3-16 (a) -1 dB and (b) -3 dB alignment tolerances (unit in μm) as a function of waveguide parameters for horizontal offsets for a $50 \mu\text{m}$ GI MMF input at $\lambda = 850 \text{ nm}$.

3.6 Experimental Approach

3.6.1 Insertion Loss

Insertion loss is a very important parameter used in the characterisation of the waveguide devices employed. It measures the loss of the system due to the insertion of the device under test to the system without the device as shown in Figure 3-17. Thus, insertion loss comprises of coupling losses, propagation loss and excess loss as defined below. For the passive components investigated in this thesis, the excess loss is defined as the difference between the insertion loss of the test sample which might have features such as bends or splitters and a reference waveguide (e.g. a straight waveguide) with a similar length as the test sample. Therefore, the excess loss is induced by the geometry of the device such as bending loss of a bent waveguide.

(a) *Insertion loss = Coupling losses + Propagation loss + Excess Loss*

(b) *Excess loss = Insertion loss of the device under test -*

Insertion loss of a reference waveguide

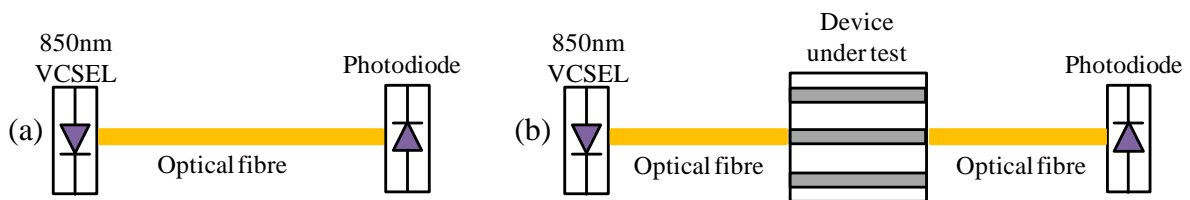


Figure 3-17 Illustration of the definition of insertion loss: (a) back-to-back optical link and (b) optical link with the device under test.

- Coupling Loss

Fresnel loss is an inevitable loss due to the light coupling in and out of the waveguide and occurs at the interfaces of waveguides or fibres and air. Assuming the near-normal incidence of the light, the Fresnel reflection (R) and transmission (T) coefficients are given by:

$$R = \left(\frac{n_{air} - n_{co}}{n_{air} + n_{co}} \right)^2, \quad T = 1 - R = \frac{4n_{air}n_{co}}{(n_{air} + n_{co})^2} \quad (3-24)$$

where n_{air} and n_{co} are the refractive indices of the air and waveguide core (this value being accurate for multimode devices). For example, as both fibres and waveguides employed in

this work have indices of ~ 1.5 , and air has index of ~ 1.0 , the Fresnel loss at each waveguide facet is estimated as:

$$\text{For } n_{\text{air}} = 1.0, n_{\text{co}} = 1.5, T = 10 \log \frac{4 \times 1.0 \times 1.5}{(1.0 + 1.5)^2} \approx -0.18 \text{ dB (in dB)}$$

In practice, index matching gel can be employed to eliminate the Fresnel losses at the interfaces between the fibres or waveguides and air.

In addition, the coupling loss can be substantially affected by the quality of the waveguide facets. As mentioned earlier, the samples employed in this work are diced rather than polished, the background scattered light in the cladding can be increased due to the facet roughness and additional coupling loss may be induced.

- Propagation Loss

Propagation loss includes both absorption loss and scattering loss. Absorption loss is the main cause for the intrinsic material loss which is due to the absorption of optical energy by the atomic bonds and conversion to other energy forms such as vibrations. The optical absorption spectrum generally depends on the chemical composition of each polymer material, and can be reduced by appropriate material engineering [16]. Scattering losses are caused by the material inhomogeneities and irregular waveguide boundaries. Any imperfections in a waveguide due to the sidewall roughness and variation of the irregularities along the waveguide can result in radiation loss. The improvement of the material properties and fabrication technology can directly reduce the scattering loss [16], [17]. The particular polymer materials used in this work have been optimised for low-loss operation at short data communications wavelengths (0.8–1 μm). For example, the propagation loss is measured to ~ 0.04 dB/cm at 0.85 μm and ~ 0.1 dB/cm at 1 μm [18].

- Experimental Setup

A basic experimental setup for insertion loss measurement is illustrated in Figure 3-18. An 850 nm multimode VCSEL is collimated and focused into an optical fibre using a pair of microscope objectives. From time to time, a free-space launch is desirable, in which case the input fibre is replaced by a lens with approximate numerical aperture and magnification. For measuring output power or imaging a waveguide output facet, a 16 \times microscope objective (NA = 0.32) is used at the waveguide output to avoid any mode selective loss due to its larger NA compared with the waveguides studied. For the consistency of the work, the majority of the measurements conducted in this thesis utilise a butt-coupled cleaved fibre patchcord to

launch the light into the waveguide and a lens to collect the light at the waveguide output unless otherwise mentioned. In all cases, the input fibres are mounted on a 3D translation stage and a displacement sensor to control the input offsets with sub-micron accuracy.

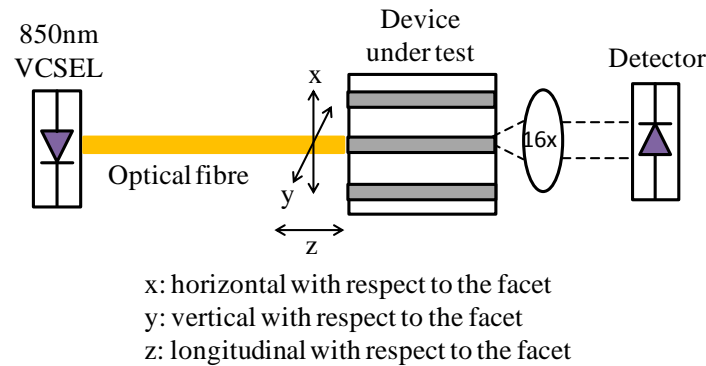


Figure 3-18 Experimental setup employed for measurement of insertion loss with axis definition noted.

The accuracy of all the measurements in this work depends on the stability of the launch power and the precision of the power meter. The power meter employed is a HP 81525A with a precision of 0.01 dB. All the measurements are conducted on an optical bench to minimise the bench vibration. Air-conditioning and ambient lights are also turned off during all the experiments to avoid any air-currents and inaccuracy due to the ambient lighting. In addition, the stages are re-visited after their alignments in order to evaluate the degree of stage shift. Therefore, the experiment conditions are optimised as far as possible. The experimental values of the insertion loss presented in this thesis are subject to an error of ± 0.2 dB.

3.6.2 Alignment Tolerances

The evaluation of acceptable alignment tolerances of the multimode waveguides is important as it determines the potential of the deployment of low-cost packaging modules. Coupling loss increases in the presence of misalignment due to the decrease of the percentage of incident power on the waveguide facet as well as the increase of the mode mismatch between the input field and waveguide modes. In this section, the coupling efficiency is examined employing the butt-coupled SMF and 50 μm GI MMF inputs on a sample 50 \times 50 μm^2 straight waveguide. The experimental results are in good agreement with the theoretical estimation while the transverse alignment tolerances are also assessed.

The experimental setup is the same as illustrated in Figure 3-18. For the measurement of input coupling efficiency, the output lens is fixed at the position where the power

transmission is maximised while the received power is recorded as the input fibre moves laterally (horizontally and vertically). It should be noted that the longitudinal offset is minimised as far as possible throughout the experiments presented in this thesis. It has been shown that the longitudinal offset has a less significant effect on the coupling performance compared to the transverse misalignments [11]. Therefore, any possible subtle longitudinal offsets introduced in the experiments can be practically neglected. Figure 3-19 plots the normalised received power as a function of input offsets for both SMF and 50 μm GI MMF launches. The theoretical calculations are also shown for comparison.

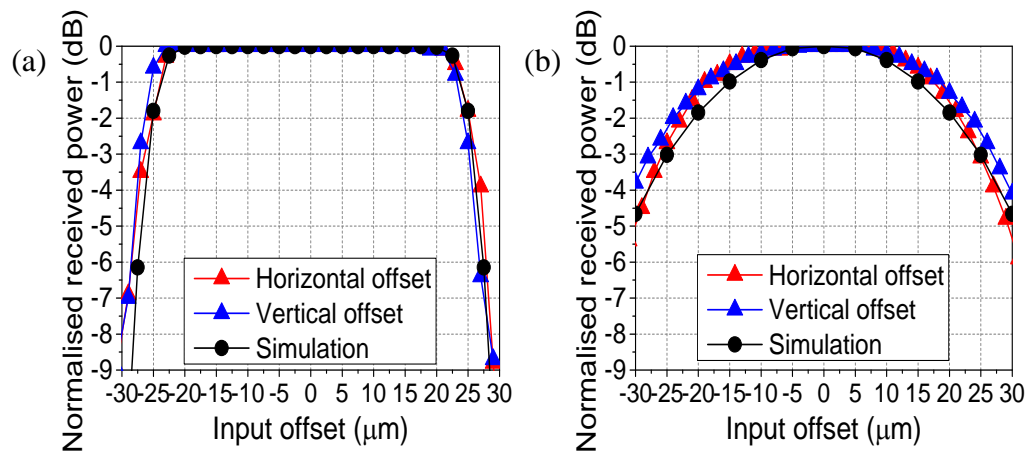


Figure 3-19 Normalised received power as a function of input offsets for a $50 \times 50 \mu\text{m}^2$ waveguide for (a) a SMF and (b) a 50 μm GI MMF launch. Index matching gel is employed.

A notable difference in the coupling efficiency between a SMF launch and a MMF launch can be found. It can be observed that the SMF launch results in a better coupling efficiency than the MMF input due to the smaller spot size and lower numerical aperture of the SMF. The coupling loss under a SMF launch remains relatively constant over a large range of input offset of $\sim \pm 20 \mu\text{m}$. The -3 dB alignment tolerances are indicated in the plots, and are found to be $\sim \pm 25 \mu\text{m}$ (on the order of half of the waveguide width) for both launches. In addition, the -1 dB alignment tolerance is well above $\pm 10 \mu\text{m}$ even under the worse-case MMF launch. It can also be seen that similar behaviours are observed in the both horizontal and vertical direction, which is due to x-y symmetry of both the waveguides and input fibres. It is encouraging that similar results have been obtained by other colleagues in the group [11], [19]. Finally, the simulation results agree very well with the experimental results verifying the validity of the model employed.

3.7 Dispersion Studies

Dispersion is an important issue as it limits the maximum data rates and the link length in optical communication systems. Therefore, dispersion investigation is essential for the multimode polymer waveguides to ensure they have sufficient bandwidth for the applications of on-board optical interconnects. There are generally two major types of dispersion: chromatic dispersion and multimode dispersion.

- Chromatic dispersion:

Chromatic dispersion (including both waveguide and material dispersion) is due to the wavelength-dependent nature of the refractive indices of the core and cladding materials, and can be expressed as $n_{eff}^i(\lambda)$ for each waveguide mode.

- Multimode dispersion:

Multimode dispersion is caused by the different propagation velocities for different waveguide modes.

Two theoretical approaches for the evaluation of dispersion in multimode polymer waveguides are presented in the following sections.

3.7.1 Ray Tracing Approach

The model bandwidth of a waveguide depends on the difference of the propagation times of different modes. A simple ray tracing model is used here considering all guided rays and computing their propagation velocity according to the angle θ_i (between the ray trajectory and the waveguide axis).

The angle θ_i of all guided rays must meet the law of total internal reflection, i.e. $-\bar{\theta}_c \leq \theta_i \leq \bar{\theta}_c$, where $\bar{\theta}_c$ is the complement of the critical angle θ_c as illustrated in Figure 3-6:

$$\bar{\theta}_c = \cos^{-1}(n_{cl} / n_{co}) \quad (3-25)$$

The propagation time t_i of each ray for a given waveguide length L is given by:

$$t_i = \frac{L}{c} \cdot \frac{n_{co}}{\cos \theta_i} \quad (3-26)$$

So the maximum time delay (difference between the maximum propagation time t_{\max} and minimum propagation time t_{\min}) is:

$$t_d = t_{\max} - t_{\min} = \frac{L}{c} n_{co} \left(\frac{n_{co}}{n_{cl}} - 1 \right) \quad (3-27)$$

We assume that the ray power distribution is uniform:

$$\int_{-\theta_c}^{\theta_c} p(\theta_i) \cdot d\theta_i = 1 \Rightarrow p(\theta) = \frac{1}{2\theta_c} \quad (3-28)$$

Then the impulse response $h(t)$ can be expressed as [shown in Figure 3-20(a)]:

$$h(t) = \frac{1}{2\theta_c}, \quad t_{\min} \leq t \leq t_{\max} \quad (3-29)$$

Thus, the corresponding transfer function is a sinc function given by:

$$|H(f)| = \frac{1}{2\theta_c} t_d \frac{\sin(\pi f t_d)}{\pi f t_d} \quad (3-30)$$

The -3 dB bandwidth-length product (BLP) $f_{-3dB} \times L$ and dispersion per unit of length t_d / L as a function of the index step Δn (assuming $n_{cl} = 1.5$) are plotted in Figure 3-20(b). It can be seen that the BLPs range from 5 to 35 GHz×m for the respective $\Delta n = 0.03$ to $\Delta n = 0.005$. Despite the simplicity of the model, it reveals that the dispersion depends on the waveguide length linearly and also the index difference between the core and cladding. A larger index step results in a larger critical angle which represents the higher-order modes. Therefore, the dispersion can be reduced by decreasing the core and cladding index step Δn due to the smaller number of guided modes. However, $f_{-3dB} \times L$ is only a function of the index step Δn and the waveguide dimensions have not been taken into account in this ray tracing model. Therefore, a more accurate model based on electromagnetic approach is needed to better investigate the dispersion in the multimode waveguides.

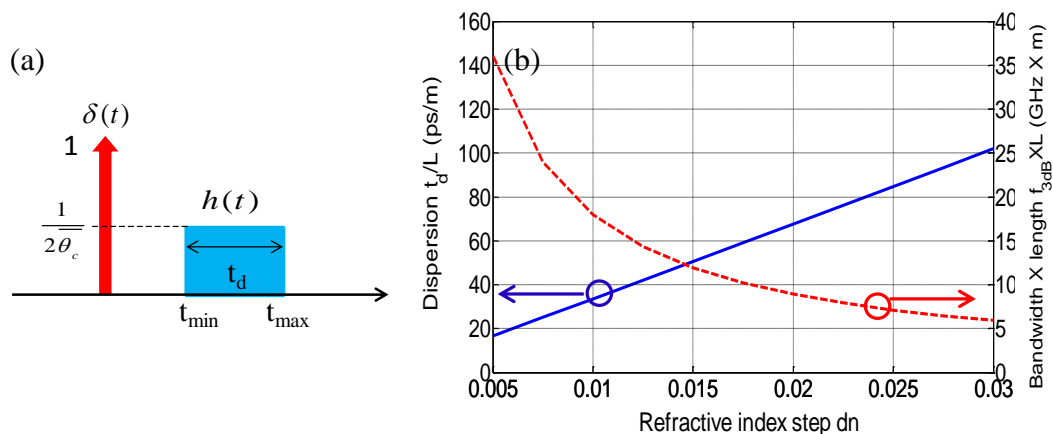


Figure 3-20 (a) A uniform ray power distribution (in red) and impulse response due to multimode dispersion (in blue), (b) BLP and dispersion per unit of length as a function of index step Δn .

Moreover, the maximum modal delay calculated using Equation (3-27) is ~ 95 ps for a 1.4 m long waveguide ($\Delta n = 0.02$), which is the longest length available for measurement in this thesis. It is worth mentioning that the 90% of the power resides in the first 100 waveguide modes under an overfilled MMF launch according to a mode coupling analysis and thus the delay between the 1st and 100th modes is only ~ 7 ps [19]. This is very useful value as it indicates that short pulses on a picoseconds timescale or even less are necessary to directly measure the modal dispersion of these waveguides; therefore such measurements typically require the use of ultra-short laser source and autocorrelation techniques. This will be further illustrated in the next chapter.

3.7.2 Electromagnetic Analysis

Electromagnetic analysis computes the dispersion in the waveguides by taking into account the propagation of the waveguide modes in various waveguide dimensions, and thus provides a more accurate estimation compared with the ray tracing approach. The two types of dispersion are studied separately below.

- Chromatic Dispersion

The standard approach to compute chromatic dispersion can be found in [20]. Assuming that the source centre wavelength λ_0 is much larger than the root mean square (RMS) source spectral width and the first order dispersion dominates, the impulse response of every

waveguide mode can be expressed as the form of a normalised Gaussian function, given by [20]:

$$h_i(t) = \frac{1}{\sigma_\lambda D_i L \sqrt{2\pi}} \cdot \exp\left(-\frac{(t-t_i)^2}{2(\sigma_\lambda D_i L)^2}\right) \quad (3-31)$$

where t_i is the mean propagation delay for waveguide mode i , and D_i is the first order chromatic dispersion at $\lambda = \lambda_0$ for waveguide mode i , and L is the link length:

$$D_i^{\lambda_0} = -\frac{\lambda_0}{c} \cdot \left. \frac{d^2 n_{eff}^i(\lambda)}{d\lambda^2} \right|_{\lambda=\lambda_0} \quad (3-32)$$

The core and cladding bulk refractive indices depend on wavelength that is based on a first-order Sellmeier formula (see Appendix C in [11]), and the material dispersion $dn/d\lambda$ is found to be on the order of -20×10^{-6} [11]. The effective index $n_{eff}^i(\lambda)$ of each waveguide mode can be computed using EIM. The second term in Equation (3-32) can be approximately calculated using the expression in Equation (3-33) assuming $\Delta\lambda$ is sufficiently small:

$$\left. \frac{d^2 n_{eff}^i(\lambda)}{d\lambda^2} \right|_{\lambda=\lambda_n} \approx \frac{n_{eff}^i(\lambda_{n+1}) - 2n_{eff}^i(\lambda_n) + n_{eff}^i(\lambda_{n-1}))}{\Delta\lambda^2} \quad (3-33)$$

The chromatic dispersion can subsequently be calculated, and D_i at $\lambda_0 = 850$ nm for a $50 \times 50 \mu\text{m}^2$ waveguide with $\Delta n = 0.02$ is found to be of the order of $-0.25 \text{ ps} \times \text{nm}^{-1} \times \text{m}^{-1}$. Considering that the waveguide length for such applications is approximately 1 m, it can be concluded that chromatic dispersion is very low for a wavelength of 850 nm and less significant compared with multimode dispersion [11].

- Multimode Dispersion

In order to evaluate the multimode dispersion, the core and cladding material indices are considered to be wavelength independent and the source is assumed to be monochromatic operating at $\lambda = \lambda_0$. The EIM is employed to calculate the effective indices $n_{eff}^i(\lambda_0)$ of each waveguide mode and subsequently the group refractive indices $n_{group}^i(\lambda_0)$ of each waveguide mode are calculated using:

$$n_{group}^i(\lambda_0) = n_{eff}^i(\lambda_0) - \lambda_0 \cdot \left. \frac{dn_{eff}^i}{d\lambda} \right|_{\lambda=\lambda_0} \quad (3-34)$$

The propagation delay time t_i of each waveguide mode for a length of L is given by:

$$t_i = \frac{L \cdot n_{group}^i}{c} \quad (3-35)$$

Then the impulse response $h(t)$ of the link can be expressed as:

$$h(t) = \sum_i p_i a_L \cdot \delta(t - t_i) \quad (3-36)$$

where p_i is the mode power distribution ($\sum_{i=1}^N p_i = 1$, where N is the total number of guided modes), and a_L is the power attenuation of all modes. In order to simplify the calculation in this chapter, all modes are assumed to have the same mode attenuation. In practice, this can be found by fitting a calculated coupling loss to the experimental data, which will be further illustrated in the next chapter. The -3 dB frequency can be readily obtained by taking the Fourier transform $H(f)$ of the impulse response $h(t)$.

It should be noted that no mode mixing is assumed in this model. However, mode mixing can significantly affect the multimode dispersion induced. Nevertheless, the assumption of no mode mixing can be employed to gain an initial description of the waveguide bandwidth for link lengths much shorter than the equilibrium length of the guides.

3.8 Bandwidth Evaluation

It has been determined that multimode dispersion is the prevalent dispersion component in such multimode waveguides, which also agrees well with the studies conducted previously in multimode fibres [12], [15], [21]. However, the modal dispersion depends strongly on the mode power distribution at the waveguide input. Therefore, in this section, the waveguide bandwidth is investigated for different input coupling schemes using the electromagnetic treatment.

The waveguides with varying sizes and index steps (same parameters employed in the coupling loss calculation) are used to evaluate the available link bandwidth. The input

schemes studied in this section includes: an overfilled waveguide, a SMF input and an overfilled MMF input.

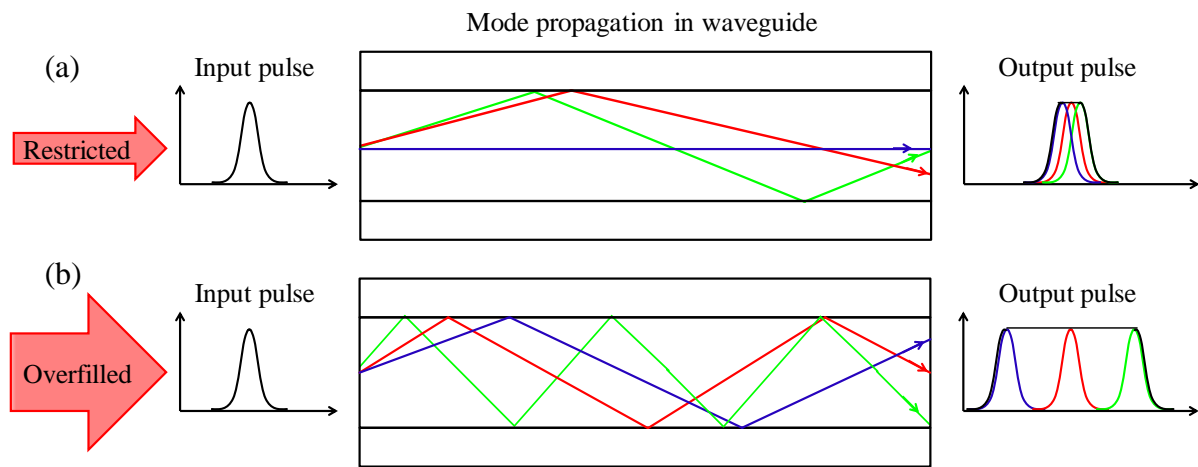


Figure 3-21 Illustration of (a) the restricted centre launch and (b) overfilled launch.

In a basic waveguide, the overfilled waveguide offers an important reference for the waveguide-based system design as it represents the worst-case scenario. The other input launches can be summarised into two categories: restricted launch (SMF input) and overfilled launch (overfilled MMF input). The SMF input provides a restricted launch which results in the largest BLP due to the selective mode excitation. In contrast, the overfilled MMF input offers an overfilled launch which couples power to a much larger number of modes, therefore generating a more uniform mode power distribution inside the waveguide. This can also be understood using ray optics intuitively. As illustrated in Figure 3-21(a), for a centre restricted launch, a small number of lower-order modes are excited and a smaller differential modal delay (the difference in time delays among the propagating modes in the waveguide) can be obtained, therefore a larger bandwidth performance is expected. On the contrary, an overfilled launch results in the excitation of larger number of higher-order modes and thus a larger differential modal delay as illustrated in Figure 3-21(b). As expected, such a launch provides worse link bandwidth compared to the restricted centre launch. Overall, useful conclusions are derived regarding the deployment of these multimode waveguides for board-level optical links in the following sections.

3.8.1 Overfilled Waveguide

As explained earlier, the induced multimode dispersion is the largest for an overfilled waveguide with a uniform mode power distribution. The BLPs are computed and plotted in Figure 3-22 for different waveguide widths w and index steps Δn under consideration.

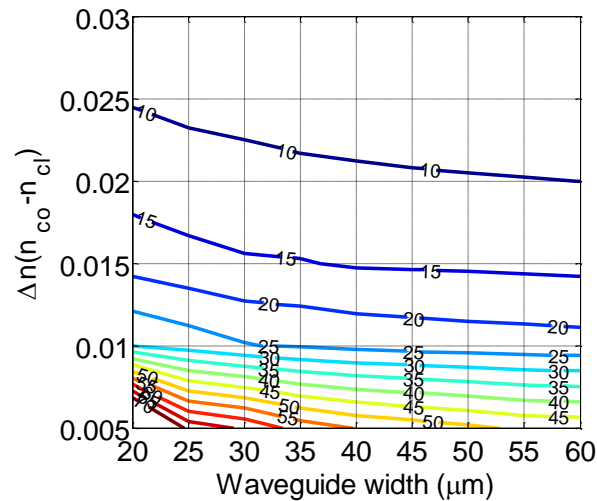


Figure 3-22 BLPs (GHz×m) as a function of waveguide width w and index step Δn assuming a uniform mode power distribution.

It can be observed that the available bandwidth for an overfilled waveguide increases as the waveguide widths and refractive index steps decrease. Moreover, the effect of the index step on the waveguide bandwidth is much larger than that of the waveguide width on the link bandwidth. The calculated BLP values range from 7 to 50 GHz×m, which is in general agreement with the values obtained using ray tracing approach. The difference resides in the consideration of waveguide dispersion of each mode using the electromagnetic treatment.

This result indicates the worst-case scenario in terms of the available link bandwidth in such waveguide systems. It constitutes a useful design rule as parameters such as the waveguide width and index step can be chosen appropriately to ensure robust data transmission depending on the required link length and data rates.

3.8.2 SMF Launch

The bandwidth estimation is obtained using a well-aligned SMF launch [Figure 3-23(a)] that is modelled with a Gaussian electric field profile with a beam width w_0 of 4.2 μm as explained in section 3.5.1. Such a launch couples a large amount of input power into the

lower-order modes [Figure 3-23(b)] and therefore large BLP values ($>100 \text{ GHz}\times\text{m}$) are obtained. The BLP as a function of waveguide width w and index step Δn is plotted in Figure 3-23(c). It can be seen that larger values are generally obtained on waveguides with smaller widths and index steps with a maximum BLP value of $\sim 150 \text{ GHz}\times\text{m}$ observed, stemming from the smaller number of modes guided inside the waveguides. However, some variations of BLP values can be observed. For instance, slightly larger values for waveguides with width of approximately $35 \mu\text{m}$ are found at index step of ~ 0.02 owing to the maximisation of power coupled into the lower-order modes.

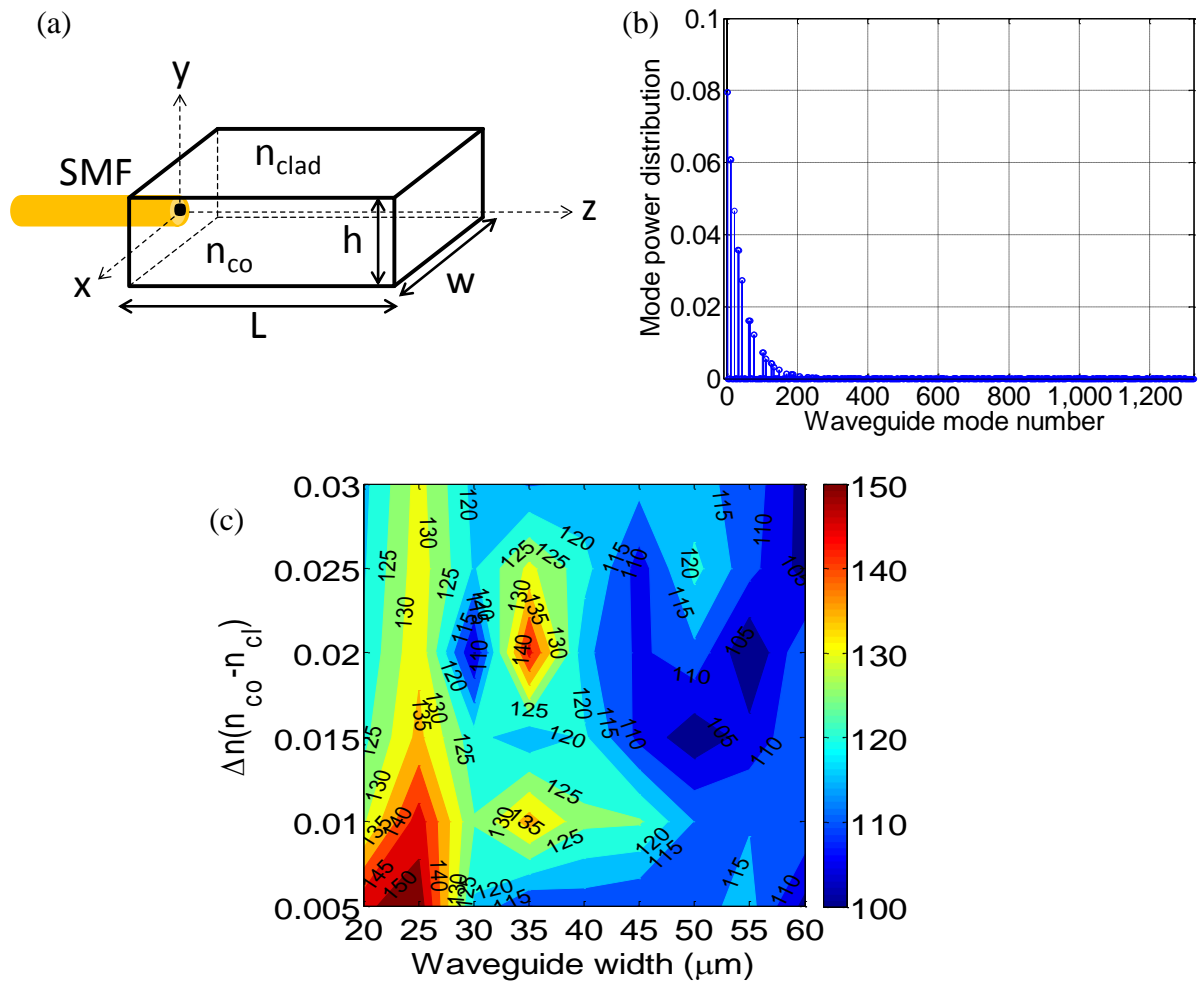


Figure 3-23 (a) Schematic of a well-aligned SMF input, (b) example of a generated mode power distribution for a $50\times 50 \mu\text{m}^2$ waveguide with $\Delta n = 0.02$ and (c) calculated BLPs ($\text{GHz}\times\text{m}$) as a function of waveguide width w and index step Δn for a SMF input.

3.8.3 50 μm GI MMF Launch

For the case shown in Figure 3-24(a), all fibre modes in a 50 μm GI MMF input are assumed to be excited uniformly as illustrated in Figure 3-24(b). Figure 3-24(d) plots the BLPs for a perfectly-aligned 50 μm GI MMF input as a function of waveguide width w and step index Δn . The values obtained under such a launch are of the same magnitude as those calculated in the case of an overfilled waveguide. This is due to the fact that the overfilled MMF input has a large number of modes excited inside the fibre which resembles the case of an overfilled waveguide that has a uniform mode power distribution inside the guide. This can be seen from the generated waveguide mode power distribution illustrated in Figure 3-24(c).

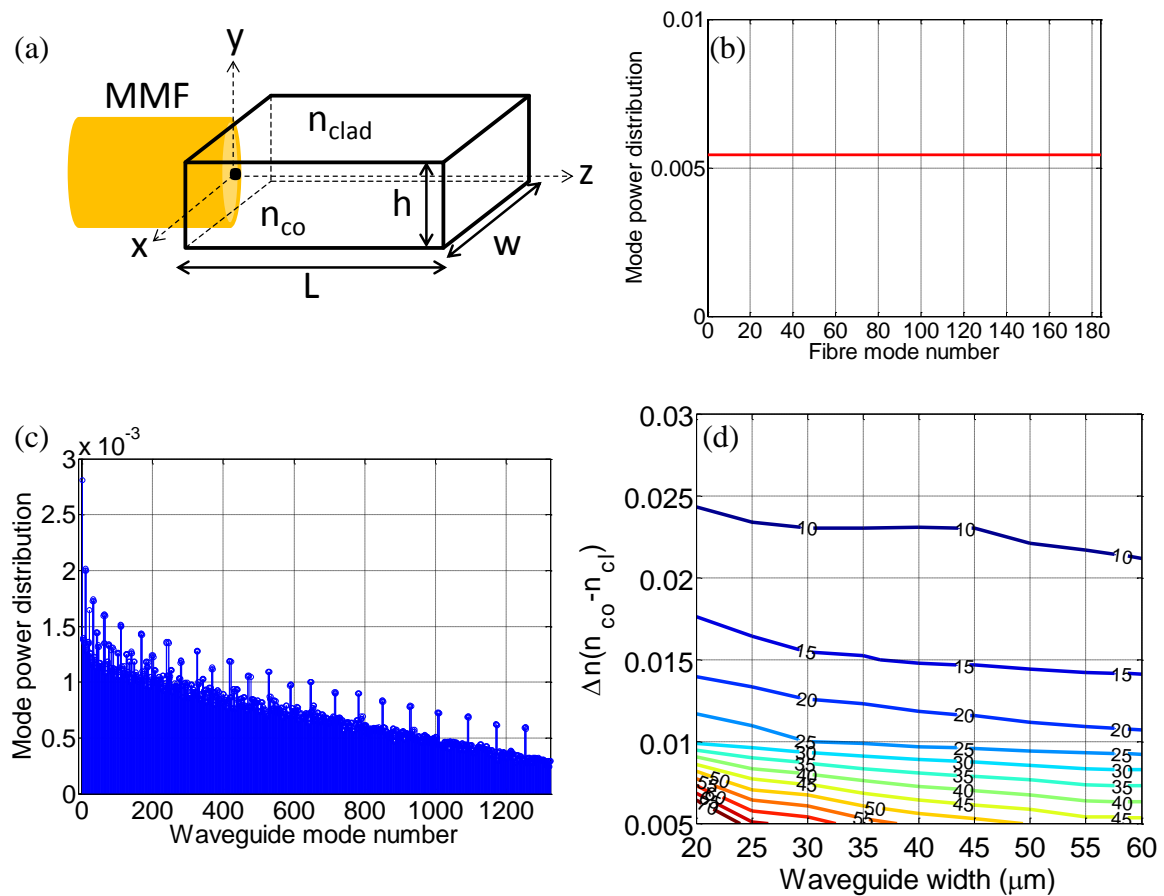


Figure 3-24 (a) Schematic of a well-aligned 50 μm GI MMF input, (b) uniform mode power distribution in a 50 μm GI MMF, (c) example of a generated mode power distribution for a 50 \times 50 μm^2 waveguide with $\Delta n = 0.02$ and (d) calculated BLPs (GHz \times m) as a function of waveguide width w and index step Δn for an overfilled 50 μm GI MMF input.

In addition, Figure 3-25 plots the obtained BLP values of a $50 \times 50 \mu\text{m}^2$ waveguide with a step index Δn of 0.02 as a function of the input positions under a $50 \mu\text{m}$ GI MMF launch. As expected, the presence of spatial input offsets has minimal effect on the waveguide bandwidth due to the large input spot size and overfilled input fibre. This indicates that BLP values of $>10 \text{ GHz}\times\text{m}$ can be obtained even under an overfilled launch and the link bandwidth remain relatively consistent for different input offsets under such a launch.

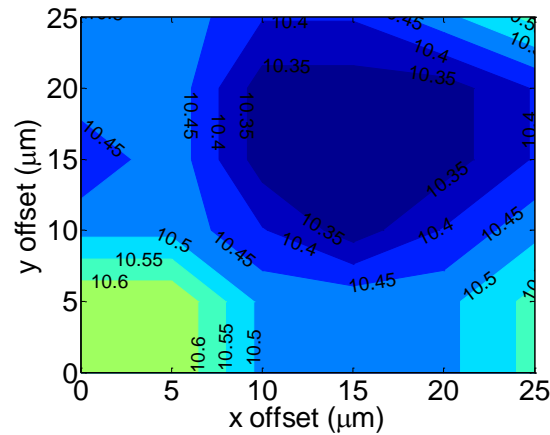


Figure 3-25 Estimated BLPs ($\text{GHz}\times\text{m}$) as a function of input position for a $50 \times 50 \mu\text{m}^2$ with an index step Δn of 0.02 for a $50 \mu\text{m}$ GI MMF input.

3.8.4 Discussion

It should be noted, however, that the multimode fibres in practice are far from overfilled as assumed in this simulation and therefore much higher BLP values may be obtained in real-world applications. As indicated earlier, the use of graded-index profiles can also improve the waveguide bandwidth performance substantially as opposed to the step-index profiles employed in the simulation throughout this chapter. Interestingly, it is often seen that light is not uniformly distributed throughout the cross-section of the core in some waveguide samples. These guiding behaviours have been observed by colleagues from the group previously [19]. This is related to the nature of the core and cladding index of the waveguide, which is likely a function of the fabrication process. The precise reasons for this particular power distribution remained unknown until the refractive index profiles of these waveguides are revealed in this thesis. More details on the refractive index profiles will be discussed in Chapters 4 and 5. Nevertheless, with the “worst-case” bandwidth of in excess of 10 GHz for a 1 m long multimode waveguide, there should not be severe bandwidth limitations for the

applications of short-reach on-board optical interconnects with typical link lengths of tens of centimetres.

In summary, it has been shown that the SMF input can provide significant advantages over a MMF input, including:

- Larger input misalignment tolerances and better coupling efficiency due to the small spot size of the SMF;
- Larger bandwidth performance due to the selective mode excitation.

However, there have been concerns on the link susceptibility to modal noise using such a highly mode selective launch on multimode fibres as all essential conditions for modal noise to occur in such links are met [22], [23]:

- Multiple modes interfere to create a speckle pattern;
- Mode selective loss due to bends;
- Modal interference vary over time that causes the speckle pattern to change.

Detailed studies investigating the effects of modal noise on these multimode waveguides have been carried out in [19]. Both theoretical and experimental studies have confirmed that the modal noise power penalties are sufficiently small even with a single mode VCSEL source, indicating that modal noises do not pose a serious impediment to high-speed link operations of these multimode waveguides.

In the next chapter, the bandwidth performance of these multimode waveguides will be examined experimentally under different launch conditions so as to verify the validity of the theoretical model using real-measured refractive index profiles.

3.9 Summary

This chapter first presents the multimode polymer waveguide samples employed in this thesis and introduces the step-index and graded-index waveguides. The two major theoretical methods employed (ray tracing and electromagnetic treatment) are subsequently discussed briefly. Coupling efficiency and input alignment tolerances using different launch schemes employed are also investigated theoretically for a wide range of waveguide parameters (waveguide widths $20\text{ }\mu\text{m} \leq w \leq 60\text{ }\mu\text{m}$, and index steps $0.005 \leq \Delta n \leq 0.03$). The SMF launch results in negligible input coupling losses for the various waveguide parameters considered

while the MMF inputs exhibit higher input coupling loss depending on the waveguide dimensions as well as the index steps of the waveguide. For both launches, the half power alignment tolerances are in the order of the waveguide half width. Useful design rules can be derived accordingly depending on the launch schemes. The fundamental transmission properties of the waveguides are also studied, including insertion loss, coupling efficiency and related input alignment tolerances for both SMF and MMF inputs. The experimental observations are in good agreement with the simulation results.

Furthermore, a theoretical investigation on the dispersion in the multimode polymer waveguides is conducted in order to evaluate the link bandwidth for different launch conditions that are likely employed in practice. The results obtained clearly show that the multimode dispersion of the waveguides highly depend on the input launch conditions. The overfilled waveguides exhibit BLP values ranging from 7 to 50 GHz×m for the different waveguide parameters under consideration. Restricted launch offers a significantly larger bandwidth compared to the overfilled launch. BLPs of larger than 100 GHz×m are obtained using a SMF launch. Moreover, the overfilled MMF launch provides similar bandwidth performance as the worst-case scenario of an overfilled waveguide. Overall, this chapter provides a concrete basis for the understanding of the light propagation inside the waveguides and particularly their modal dispersion needed to proceed with the development of low-loss and high-bandwidth multimode polymer waveguides for use in board-level optical interconnections.

3.10 References

- [1] T. Ishigure, K. Shitanda, and Y. Oizumi, "Index-Profile Design for Low-Loss Crossed Multimode Waveguide for Optical Printed Circuit Board," *Opt. Exp.*, vol. 23, no. 17, pp. 22262–22273, 2015.
- [2] A. W. Snyder and J. D. Love, *Optical Waveguide Theory*. London: Chapman & Hall, 1983.
- [3] T. Bierhoff, A. Wallrabenstein, A. Himmler, E. Griesse, and G. Mrozynski, "Ray Tracing Technique and Its Verification for the Analysis of Highly Multimode Optical Waveguides with Rough Surfaces," *IEEE Trans. Magn.*, vol. 37, no. 5, pp. 3307–3310, 2001.
- [4] R. Scarmozzino, A. Gopinath, R. Pregla, and S. Helfert, "Numerical Techniques for Modeling Guided-Wave Photonic Devices," *IEEE J. Sel. Topics Quantum Electron.*, vol. 6, no. 1, pp. 150–162, Jan. 2000.
- [5] G. P. Agrawal, *Fiber-Optic Communications Systems*, Third Edit. John Wiley & Sons, Inc., 2002.
- [6] F. Ladouceur and J. D. Love, *Silica-Based Buried Channel Waveguides and Devices*. Chapman & Hall, 1996.
- [7] J. Liu, *Photonic Devices*. Cambridge University Press, 2005.

- [8] K. Okamoto, *Fundamentals of Optical Waveguides*. Academic Press, 2010.
- [9] A. S. Sudbo, "Film Mode Matching: A Versatile Numerical Method for Vector Mode Field Calculations in Dielectric Waveguides," *Pure Appl. Opt.*, vol. 2, pp. 211–233, 1993.
- [10] *FIMMWAVE*, Version 6. Photon Design.
- [11] N. Bamiedakis, "Multimode Polymer Waveguides for High-speed On-board Optical Interconnects," University of Cambridge, 2008.
- [12] L. Raddatz, I. White, D. G. Cunningham, and M. C. Nowell, "An Experimental and Theoretical Study of the Offset Launch Technique for the Enhancement of the Bandwidth of Multimode Fiber Links," *J. Light. Technol.*, vol. 16, no. 3, pp. 324–331, 1998.
- [13] H. S. Mackenzie, "Evanescent Field Devices for Non-Linear Optical Applications," University of Cambridge, 1987.
- [14] P. Pepeljugoski, S. Golowich, A. J. Ritger, P. Kolesar, and A. Risteski, "Modeling and Simulation of Next-Generation Multimode Fiber Links," *J. Light. Technol.*, vol. 21, no. 5, pp. 1242–1255, 2003.
- [15] M. S. Lans, P. Pepeljugoski, S. Member, M. J. Hackert, J. S. Abbott, S. E. Swanson, S. E. Golowich, A. J. Ritger, P. Kolesar, Y. C. Chen, and P. Pleunis, "Development of System Specification for Laser-Optimized 50- μ m Multimode Fiber for Multigigabit Short-Wavelength LANs," *J. Light. Technol.*, vol. 21, no. 5, pp. 1256–1275, 2003.
- [16] H. Ma, A. K.-Y. Jen, and L. R. Dalton, "Polymer-Based Optical Waveguides: Materials, Processing, and Devices," *Adv. Mater.*, vol. 14, no. 19, pp. 1339–1365, Oct. 2002.
- [17] T. Barwicz and H. A. Haus, "Three-Dimensional Analysis of Scattering Losses Due to Sidewall Roughness in Microphotonic Waveguides," *J. Light. Technol.*, vol. 23, no. 9, pp. 2719–2732, 2005.
- [18] B. Swatoski, C. Amb, S. K. Breed, D. J. Deshazer, W. K. Weidner, R. F. Dangel, N. Meier, and B. J. Offrein, "Flexible, Stable, and Easily Processable Optical Silicones for Low Loss Polymer Waveguides," *Proc. SPIE*, vol. 8622, p. 862205, 2013.
- [19] J. Beals IV, "Polymer Waveguide Technology Enabling High-Bandwidth Optical Backplane Architectures," University of Cambridge, 2009.
- [20] G. D. Brown, "Bandwidth and rise time calculations for digital multimode fiber-optic data links," *J. Light. Technol.*, vol. 10, no. 5, pp. 672–678, May 1992.
- [21] M. Webster, L. Raddatz, I. H. White, and D. G. Cunningham, "A Statistical Analysis of Conditioned Launch for Gigabit Ethernet Links Using Multimode Fiber," *J. Light. Technol.*, vol. 17, no. 9, pp. 1532–1541, 1999.
- [22] P. Pepeljugoski, D. Kuchta, and A. Risteski, "Modal Noise BER Calculations in 10-Gb/s Multimode Fiber LAN Links," *IEEE Photon. Technol. Lett.*, vol. 17, no. 12, pp. 2586–2588, 2005.
- [23] G. C. Papen and G. M. Murphy, "Modal Noise in Multimode Fibers under Restricted Launch Conditions," *J. Light. Technol.*, vol. 17, no. 5, pp. 817–822, 1999.

4 BANDWIDTH STUDIES ON MULTIMODE POLYMER WAVEGUIDES

This chapter reports dispersion studies of multimode polymer waveguides under different launch conditions and for varying input offsets using frequency-domain and time-domain measurements. It is experimentally shown that the multimode polymer waveguides can exhibit high-bandwidth performance without introducing significant impairments in the performance of the properties of the system link. A theoretical model based on the measured refractive index profiles agrees well with the experiments. The results indicate the feasibility of using these multimode polymer waveguides to transmit data rates of 100 Gb/s over a single wavelength channel with the use of appropriate refractive index engineering and launch conditioning.

4.1 Introduction

Following the theoretical studies concerning the coupling loss and bandwidth performance of waveguides discussed in Chapter 3, this chapter presents experimental work to evaluate the dispersion of the fabricated polymer multimode waveguides. The characterisation of the dynamic performance of such multimode waveguides is essential if the potential of the technology for use in high-speed applications is to be verified. High speed operation is important as the bandwidth performance of VCSELs has improved substantially

in recent years. For example, recent results have demonstrated links using VCSELs operating with error-free transmission at bit rates up to 57 Gb/s without the use of equalisation, and 71 Gb/s with equalisation [1]–[5]. However, important concerns have been raised concerning the potential of the bandwidth of multimode polymer waveguides to match that of VCSELs and support very high on-board data rates. Moreover, the requirement for relaxed alignment tolerances in the system assembly and the need for operation with different launches make the challenge of achieving adequate channel bandwidths more difficult.

Research on the dispersion of multimode polymer waveguides has been reported by different groups. For instance, the estimated -3 dB bandwidth and bandwidth-length product (BLP) of the guides reported has been found to be 23 GHz (BLP: 57.5 GHz×m) for a 2.55 m long waveguide [6] and 150 GHz (BLP: 75 GHz×m) for a 51 cm long waveguide [7] under a SMF launch. A larger value of 1.03 GHz (BLP: 90 GHz×m) for a 90 m long graded-index waveguide has been found under restricted launch [8]. However, these measurements have been conducted only under a centre launch and no information is provided on alignment tolerance. Therefore, in this chapter, the bandwidth performance of these multimode waveguides is thoroughly investigated both experimentally and theoretically for various launch conditions and in the presence of input spatial offsets. Frequency-domain (S_{21}) measurements are first carried out on these multimode polymer waveguides. However, these measurements are limited by the capability of the instruments (up to 40 GHz) and the bandwidth of the active devices (up to 30 GHz) used in the experiments. As a result, time-domain (pulse broadening) measurements are further employed so as to measure the actual bandwidth of these guides in the presence of input spatial offsets and for various launch conditions.

The chapter is structured as follows. Section 4.2 presents the bandwidth studies using frequency-domain measurements (S_{21} measurement) under various launch conditions with spatial input offsets. Section 4.3 introduces the femtosecond laser source and autocorrelator employed in the time-domain measurements. Section 4.4 reveals the actual bandwidth of these multimode waveguides using the pulse broadening measurements for different launch conditions and across different input offsets. The simulation model is found to agree well with the experiments. The experimental results on the bandwidth performance of the straight waveguides are further discussed in section 4.5 to provide more insight into the influence of refractive index design on the dynamic performance of these guides while section 4.6 summarises the chapter.

4.2 Frequency Response Measurement

4.2.1 1.4 m Long Spiral Waveguide

The 1.4 m long spiral waveguide is fabricated on a 6-inch glass substrate using siloxane polymer materials (Core: Dow Corning OE-4140 Cured Optical Elastomers; cladding: OE-4141 Cured Optical Elastomer) that exhibit excellent optical properties to allow direct integration onto PCBs [9], [10]. The core and cladding materials have bulk refractive indices of approximately 1.52 and 1.50 at 850 nm respectively. The waveguide core has a cross section of $50 \times 20 \mu\text{m}^2$ and is sandwiched between the top and cladding layers while the waveguide facets are exposed with a dicing saw. Figure 4-1 shows the images of the 1.4 m long spiral waveguide and its input facet.

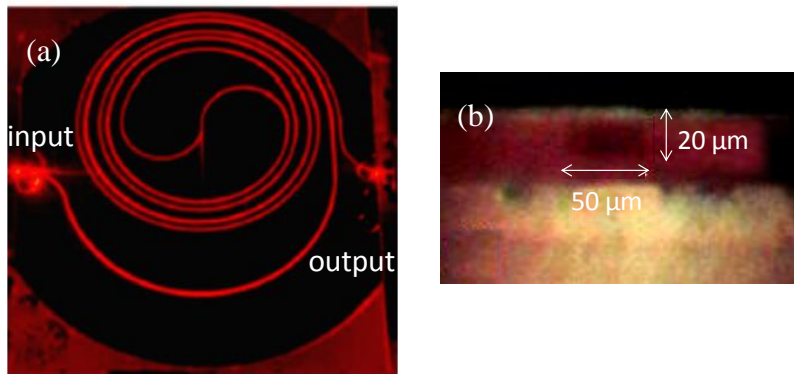


Figure 4-1 Photographs of (a) the 1.4 m long spiral waveguide illuminated with red light and (b) input facet of the waveguide [10].

4.2.1.1 S_{21} Measurement

- Experimental Setup

The experimental setup is illustrated in Figure 4-2. An 850 nm VCSEL (bandwidth of ~ 25 GHz) is used as the transmitter which is connected to a vector network analyser (Agilent 8722ET) via a 40 GHz radio frequency (RF) probe, while a photodiode (VIS D30-850M) with bandwidth of 30 GHz is employed as the receiver. The VCSEL is butt-coupled to the cleaved input fibre patchcord (SMF, 50/125 μm MMF or 100/140 μm MMF), and the cleaved end of the same type of fibre is used to couple the light into the spiral waveguide. A cleaved 50/125 μm MMF (NA = 0.2) is employed to couple the light output from the waveguide to the photodiode while a 38 GHz RF amplifier (SHF 806E) is used to amplify the received electrical signals. Index-matching gel is used at the waveguide input and output facets to

reduce the Fresnel losses and the scattering losses due to surface roughness. For the 50 μm MMF launch, a mode mixer (MM: Newport FM-1) is used to generate a quasi-overfilled launch condition that provides a more uniform power distribution at the fibre input. The near field images of different fibre inputs are captured via a microscope objective and a charge-coupled device (CCD) camera and are shown in Figure 4-3. It should be noted that all near field images are captured with a neutral density attenuator used in order to lower the optical power into the camera to avoid any saturation in the rest of this thesis. These are strictly qualitative approximations and do not account for the mode angles. It can be seen that the quasi-overfilled 50 μm MMF and 100 μm MMF launches offer a relatively uniform power distribution over the fibre cross section.

For the back-to-back link, an Agilent NA7766A multimode mode variable optical attenuator (VOA) is employed to adjust the optical power received by the photodiode to the levels similar to those obtained in the respective waveguide link. For all measurements, the cleaved end of the input fibre is placed on a precision translation stage to introduce the input offsets while a displacement sensor is employed to monitor accurately the induced spatial offsets.

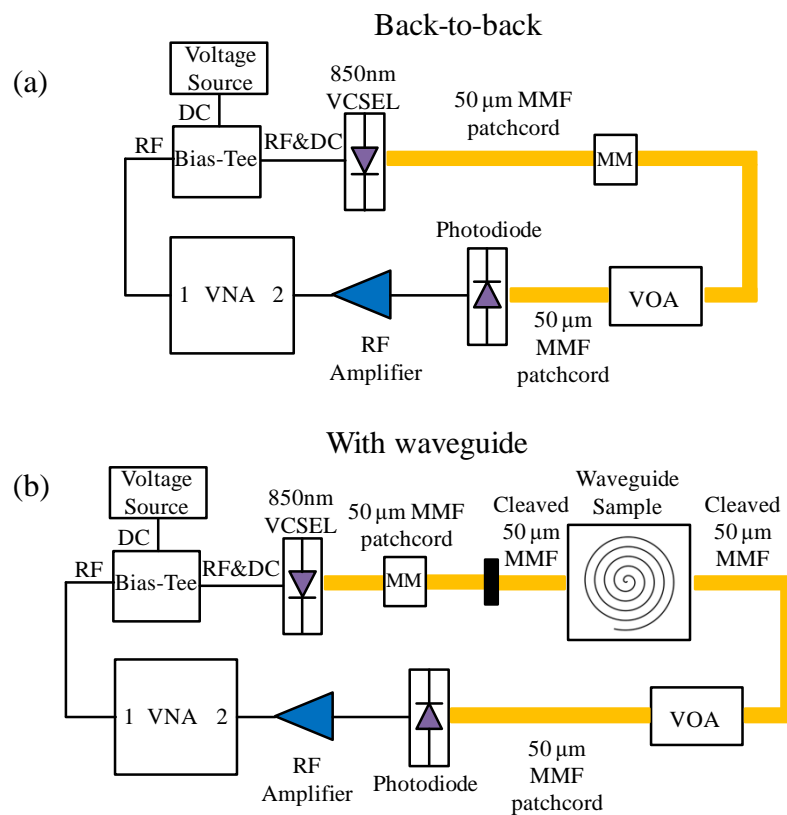


Figure 4-2 Experimental setup for the S_{21} measurement for (a) the back-to-back link and (b) the waveguide link under a quasi-overfilled 50/125 μm launch condition.

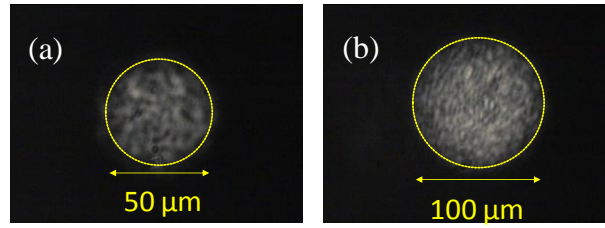


Figure 4-3 Near field images of the output facet of the fibres employed: (a) a quasi-overfilled 50/125 μm MMF and (b) a 100/140 μm MMF.

- Experimental Results

The measurement is conducted under different launch conditions: (i) 9/125 μm SMF launch, (ii) a quasi-overfilled 50/125 μm MMF launch ($\text{NA} = 0.2$) and (iii) a 100/140 μm MMF launch ($\text{NA} = 0.29$). Launch conditions (i), (ii) and (iii) provide increased uniform mode power distributions at the waveguide input and hence, causing increasing levels of multimode dispersion in the waveguide. A SMF is used to emulate a restricted launch while a quasi-overfilled 50/125 μm MMF launch and a 100/140 μm MMF launch are used to investigate the waveguide performance with a broader mode power distribution. Although these launches are not strictly-speaking “worst-case”, they provide a wide range of input conditions that can be encountered in practice, therefore providing a useful insight in the bandwidth performance normally encountered. In addition, the measurement is carried out for different input positions so as to examine the waveguide bandwidth performance owing to the induced spatial offsets. Different launch offsets also result in different mode power distributions at the waveguide input, and therefore different levels of multimode dispersion in the guides.

The insertion loss (including coupling loss and propagation loss) of the spiral waveguide is 11.5 dB, 23.5 dB and 26.3 dB under the 9/125 μm SMF, quasi-overfilled 50/125 μm MMF and 100/140 μm MMF launch respectively. The S_{21} parameter of the optical link with and without (back-to-back) the spiral waveguide is measured, and the frequency response of the waveguide can be obtained from the difference between the recorded frequency response of the waveguide link and the back-to-back link. Figure 4-4 shows the measured normalised frequency responses of the waveguide for the 9/125 μm SMF, the quasi-overfilled 50/125 μm MMF input and 100/140 μm MMF launch with different horizontal input offsets. It can be seen that all frequency responses are flat up to at least the 25 GHz instrumental limit for all types of input launch conditions. No significant bandwidth degradation can be observed even under the 100/140 μm MMF launch. The results demonstrate that the specific waveguide has

BLP of at least 35 GHz×m, indicating that it is possible to achieve data transmission of beyond 25 Gb/s over such waveguide structures.

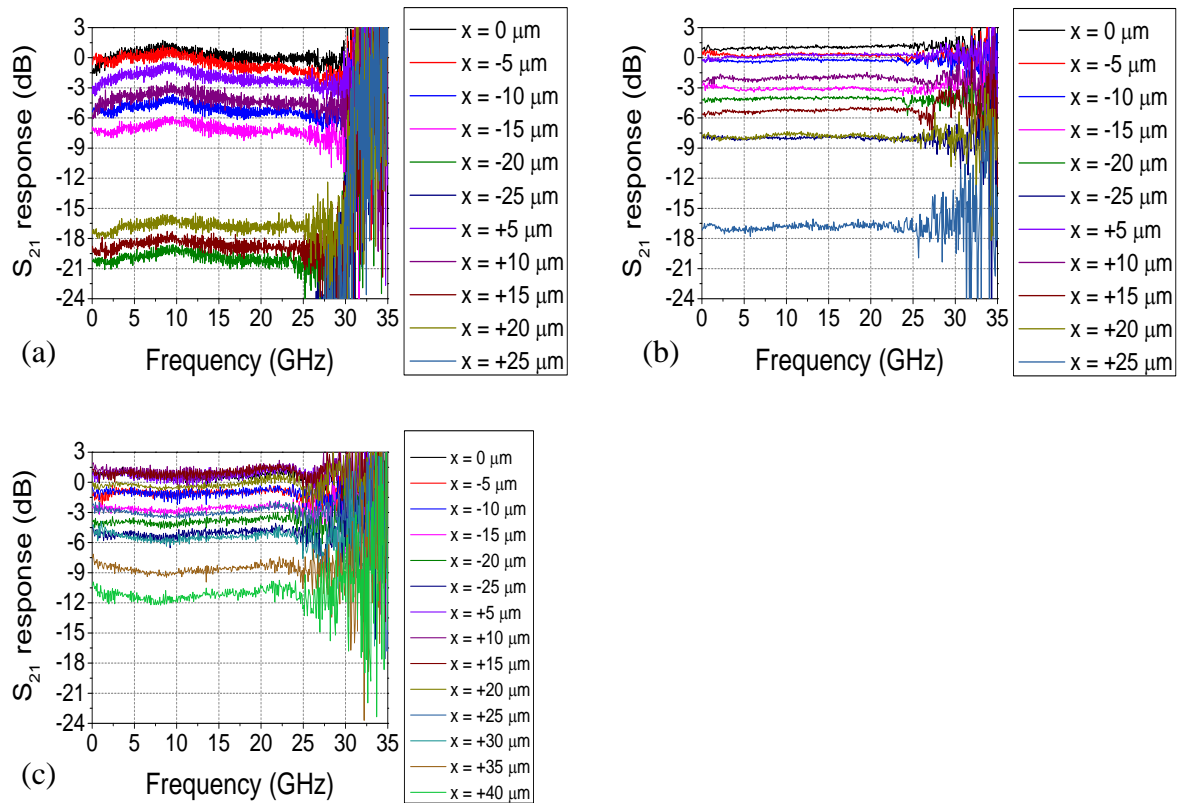


Figure 4-4 Normalised frequency response of the 1.4 m long spiral waveguide for different input horizontal offsets under (a) a 9/125 μm SMF, (b) a quasi-overfilled 50/125 μm MMF and (c) a 100/140 μm MMF launch.

4.2.1.2 Offset Launch Studies

- Experimental Setup

A similar setup is used to assess the dynamic performance of the 1.4 m long spiral waveguide (Figure 4-5). The VCSEL is directly modulated using a pattern generator (Anritsu MP1800A) of 256 bits with a pattern of “000...010...000” so as to emulate a single pulse transmission in the waveguide. A single pulse is generated with a repetition rate ~ 172 MHz. The optical pulse is launched into the spiral waveguide using the same launch conditions as employed in the S_{21} measurement with different spatial input offsets introduced and is collected with a 50/125 μm MMF. The received electrical signal is amplified by a 38 GHz amplifier (SHF 806E), and the FWHM of the received pulse is measured with a digital communication analyser (Agilent 86100A) for the different input positions.

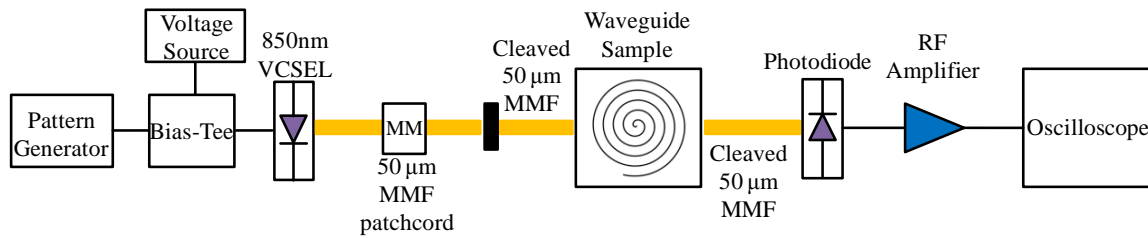


Figure 4-5 Experimental setup for the offset launch measurement for the 1.4 m long spiral waveguide under a quasi-overfilled 50/125 μm launch condition.

- Experimental Results

The FWHM of the received pulse for the back-to-back link is ~ 29 ps. The FWHM of the received pulse in the waveguide link is measured under different launch conditions for each input position and is plotted in Figure 4-6. As expected from the S_{21} measurement, the FWHM of the received pulse for the waveguide link remains relatively constant for the different input positions, with no significant pulse broadening observed. The power received at the waveguide output is also measured for the different input positions. Increasing offsets result in larger power coupled into higher-order modes which suffer from higher bending losses in the spiral waveguide. The results show that the pulse width for different input offsets under different launch conditions does not change significantly (less than ± 1 ps across input offsets of ± 22 μm), indicating that the waveguide dispersion is very small.

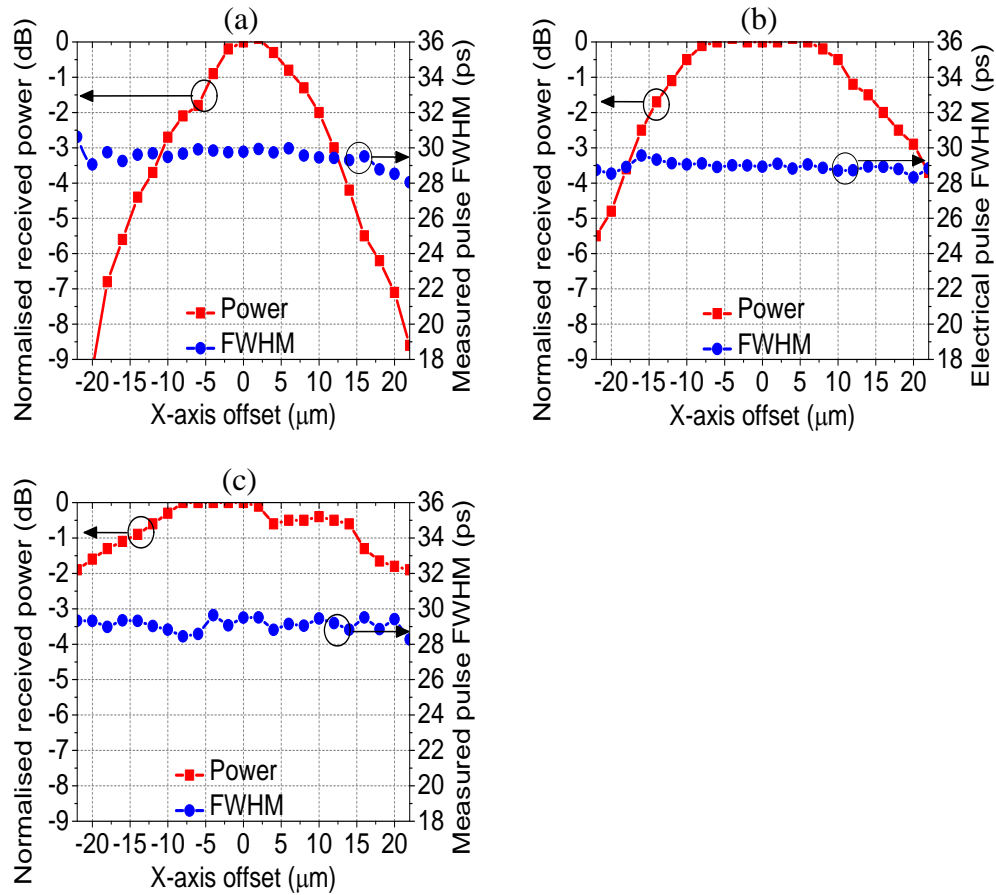


Figure 4-6 The FWHM of received signal and the normalised received optical power over the 1.4 m long spiral waveguide for different horizontal offsets under (a) a 9/125 μm SMF, (b) a quasi-overfilled 50/125 μm MMF and (c) a 100/140 μm MMF launch.

In fact, error-free ($\text{BER} < 10^{-12}$) data transmission of 25 Gb/s with a small power penalty of ~0.5 dB has been successfully demonstrated on this 1.4 m long spiral waveguide [10]. The high bandwidth performance observed on this particular waveguide can be attributed to the long bending structure as the complex bends may suppress the higher-order modes and therefore result in a reduced multimode dispersion at the waveguide output. Moreover, the refractive index profile of this waveguide may not have strict step index due to the diffusion of the cladding material during the fabrication process, resulting in a smaller NA and reduced multimode dispersion as well. More detailed studies on the effects of refractive index profile and bending structure are required and will be discussed in the next chapter.

4.2.2 1 m Long Spiral Waveguide

The 1 m long spiral waveguide is fabricated on an 8-inch silicon wafer from silicone polymer materials (core: WG-1020 Optical Waveguide Core and cladding: Dow Corning OE-4141 Cured Optical Elastomer) using conventional photolithography [11], [12]. The refractive index of the core and cladding is ~ 1.52 and 1.50 respectively at a wavelength of 850 nm . The waveguide has a length of 105.5 cm and core size of approximately $32 \times 50\text{ }\mu\text{m}^2$. Figure 4-7 shows the images of the 1 m long spiral waveguide illuminated with red light and the output facet of the waveguide.

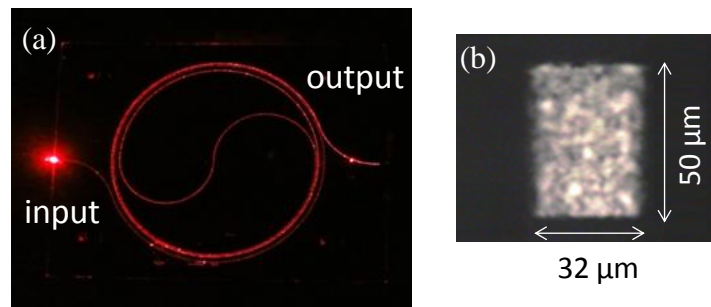


Figure 4-7 Photographs of (a) the 1 m long spiral waveguide illuminate with red light and (b) the waveguide output facet illuminated with 850 nm light.

4.2.2.1 Experimental Setup

The S_{21} measurement setup is the same as the one shown in Figure 4-2. A slightly higher bandwidth of 40 GHz RF amplifier (SHF 807) is used in this experiment. The main difference is that more launch conditions are employed in order to allow a more detailed study. This particular experiment is done in collaboration with Dr. Nikos Bamiedakis. It should be noted that the use of the $50/125\text{ }\mu\text{m}$ MMF at the waveguide output is not ideal as its NA is slightly smaller than that of the waveguide which may result in the suppression of the power from higher-order modes at the waveguide output. However, it cannot be avoided as both the high-speed photodiode and the VOA have $50\text{ }\mu\text{m}$ fibre-coupled inputs. In order to examine any effect this may cause on the measurements, the received optical power collected using the $50/125\text{ }\mu\text{m}$ MMF ($\text{NA} = 0.2$) and the $100/140\text{ }\mu\text{m}$ ($\text{NA} = 0.29$) at the waveguide output are compared under both quasi-overfilled $50/125\text{ }\mu\text{m}$ MMF and the $100/140\text{ }\mu\text{m}$ MMF input launches respectively. No obvious difference is observed between the two types of fibres used at the waveguide output, indicating that the mode-selective loss is very low and therefore the use of the $50/125\text{ }\mu\text{m}$ MMF should not have a significant effect on the measurements conducted.

4.2.2.2 Launch Conditions

The bandwidth performance of the waveguide is assessed for different input offsets under a wide range of launch conditions, ranging from restricted to relatively overfilled launch: (i) 4/125 μm SMF, (ii) typical 50/125 μm MMF (NA = 0.2), (iii) a quasi-overfilled 50/125 μm MMF and (iv) a 100/140 μm MMF (NA = 0.29). The 4/125 μm SMF is chosen here as it generates a restricted launch condition at the waveguide input. Unlike the 9/125 μm SMF in which a few modes can exist at 850 nm, the 4/125 μm SMF guarantees single-mode operation at 850 nm due to its small core size. The quasi-overfilled 50/125 μm launch condition is generated using a MM so that a more uniform mode power distribution can be achieved inside the fibre input, whereas the typical 50/125 μm MMF launch is achieved without the use of a MM. The typical 50/125 μm MMF launch is often encountered in system use. The 100/140 μm MMF launch provides an overfilled launch at the waveguide input equivalent to a “worst-case” scenario compared with the other launches employed here. Figure 4-8 shows the near field images of the input fibre end.

In general, a restricted launch excites a small number of modes inside the waveguide and therefore leads to a higher bandwidth. However this launch condition may result in a larger variation of bandwidth performance for different spatial input offsets [13]. An overfilled launch is expected to increase the multimode dispersion of the waveguide and hence results in a smaller bandwidth as it couples a larger percentage of power into higher-order modes at the input of the waveguide. In addition, different spatial offsets are introduced at the waveguide input as different mode groups can be excited and hence varying levels of multimode dispersion can be induced at the waveguide output. Therefore, the frequency response of the waveguide is investigated under different launch conditions as well as different input positions so as to assess the robustness of the waveguide bandwidth performance.

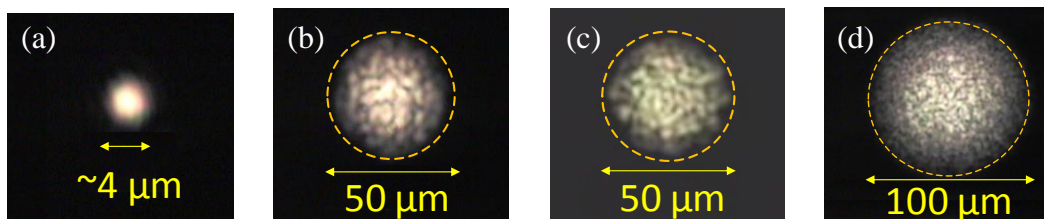


Figure 4-8 Near field images at the input fibre end under the different launch conditions studied: (a) a 4/125 μm SMF, (b) a typical 50/125 μm MMF, (c) a quasi-overfilled 50/125 μm MMF and (d) a 100/140 μm MMF.

4.2.2.3 Experimental Results

The insertion loss (including coupling loss and propagation loss) of the 1 m long spiral waveguide is measured to be 8.2 dB, 9.3 dB, 10 dB and 12.5 dB for a 4/125 μm SMF, typical 50/125 μm MMF, quasi-overfilled 50/125 μm MMF and 100/140 μm MMF input respectively. A significant improvement of ~ 6 dB on the loss performance is achieved compared with the 1.4 m long spiral waveguide employed previously. This newer 1 m long spiral is designed to exhibit better bending structure and is fabricated using improved process. Figure 4-9 shows the normalised waveguide frequency response under different launch conditions in the presence of spatial input offsets. For the SMF launch, flat frequency response can be seen up to the 35 GHz instrumental limit with no significant transmission impairments observed across spatial input offsets although some slight degradation of the bandwidth performance can be noticed with larger input offsets due to the excitation of higher-order modes at the waveguide input. As expected, the more overfilled launches result in less flat frequency responses owing to the coupling of more power into the higher-order modes at the input of the waveguide and hence the increased multimode dispersion induced. However, the frequency response is flat up to the instrumental limit of 35 GHz, yielding a BLP of at least 35 GHz \times m under all launch conditions studied and in the presence of input spatial offsets. These results indicate that it is possible to transmit beyond 40 Gb/s over such long waveguides without any significant transmission impairments. Successful demonstration of 40 Gb/s data transmission over such 1 m long spiral waveguide will be discussed in Chapter 6 [12].

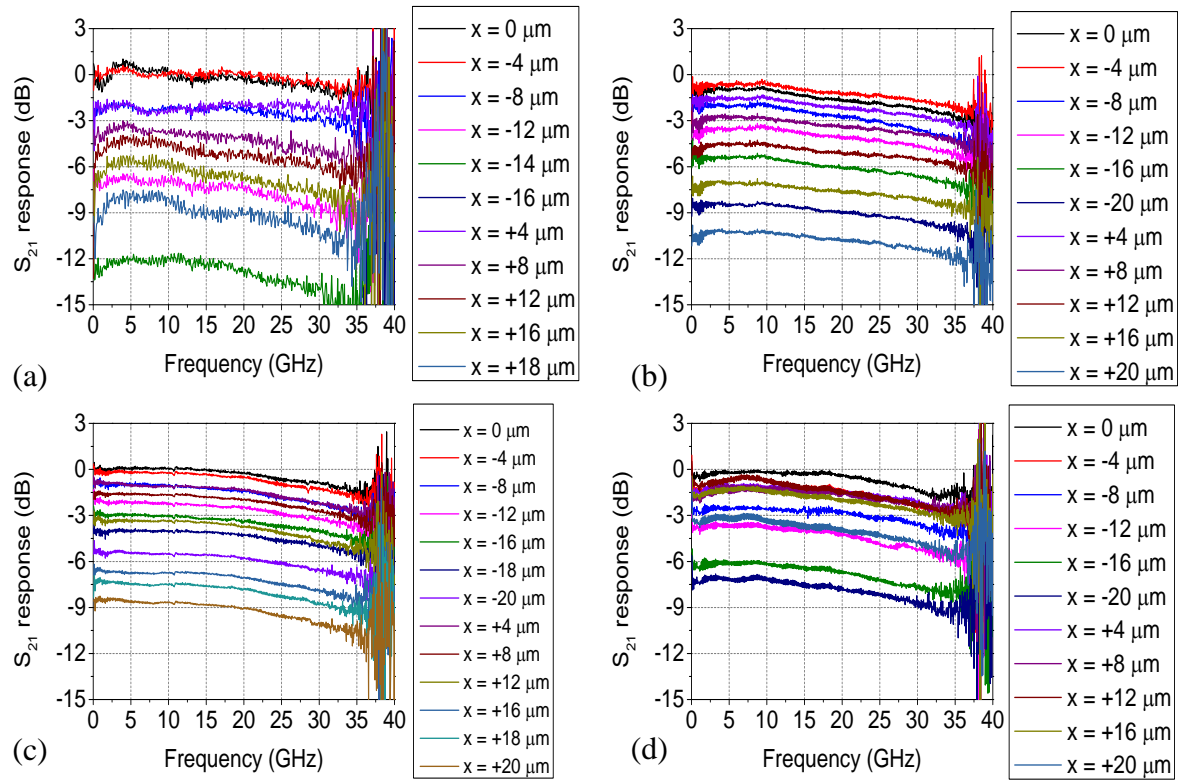


Figure 4-9 Normalised frequency response of the 1 m long spiral waveguide for different input horizontal offsets under (a) a 4/125 μm SMF, (b) a typical 50/125 μm MMF, (c) a quasi-overfilled 50/125 μm MMF and (d) a 100/140 μm MMF launch.

Moreover, in order to gain more insight into the mode propagation within the waveguide, the near field images of the waveguide output are also recorded under different launch conditions for different input offsets as shown in Figure 4-10. For the 4/125 μm SMF input, strong mode filling can be observed despite using a highly-restricted launch condition. This can be attributed to the mode mixing inside the waveguide due to the surface roughness and local imperfections as well as due to the long spiral structure of the waveguide. As expected, more uniform power distribution at the waveguide output can be seen under more overfilled launch conditions. In all cases, no significant changes can be observed from the near field images across different spatial offsets, although some power redistribution at the waveguide output can be noticed.

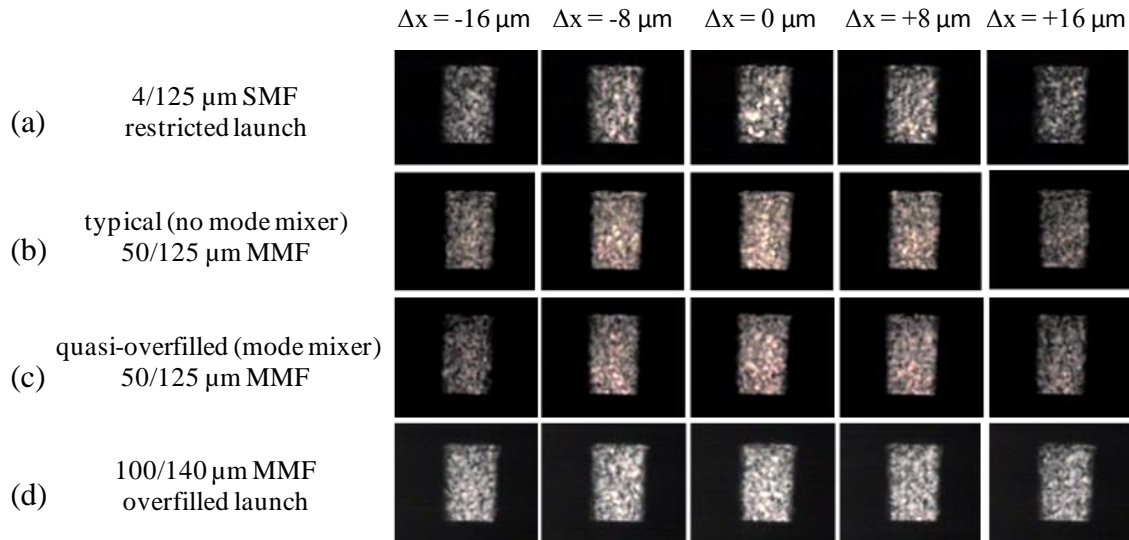


Figure 4-10 Near field images of the waveguide output under (a) a 4/125 μm SMF, (b) a typical 50/125 μm MMF, (c) a quasi-overfilled 50/125 μm MMF and (d) a 100/140 μm MMF launch across different input offsets.

In addition, it can be noted that the frequency response of this 1 m long spiral waveguide is less flat than that obtained on the 1.4 m long spiral previously discussed in section 4.2.1, which indicates that the 1 m long spiral waveguide sample exhibits larger multimode dispersion. Due to the optimised spiral structure and improved loss performance compared with the older 1.4 m long waveguide, higher-order modes may be suppressed less as they propagate along the bending structure in the newer 1 m long waveguide sample. As a result, the difference observed between the obtained frequency responses of the two waveguides can be justified as the newer sample is expected to have slightly increased multimode dispersion. This observation indicates that waveguide bends with more loss might provide improved bandwidth performance owing to the mode filtering properties, illustrating an important trade-off in the waveguide layout design. More details on the waveguide bending loss versus bandwidth performance will be discussed in the next chapter.

4.3 Pulse Broadening Measurement

We have previously presented bandwidth studies on the 1.4 and 1 m long spiral multimode polymer waveguide using frequency-domain (S_{21}) measurements and reported an instrumentation-limited BLP of at least 35 GHz \times m even in the presence of input spatial offsets and for various launch conditions. As a result, we have undertaken time-domain (pulse broadening) measurements in order to measure the actual bandwidth of these guides.

The following sections briefly introduce the femtosecond laser and autocorrelator employed in the pulse broadening measurements.

4.3.1 Femtosecond Laser

The dispersion induced by the waveguide samples presented from this section onward are measured using two short pulse generation systems in order to allow more detailed studies with a range of launch conditions. A femtosecond Ti:Sapphire laser (Coherent Chameleon [14]) operating at a wavelength of 850 nm is employed as the source in the short pulse generation system 1. In the short pulse generation system 2, a femtosecond erbium-doped mode-locked fibre laser source (TOPTICA FemtoFiber Scientific [15]) operating at a wavelength of 1574 ± 0.5 nm and a frequency-doubling crystal (MSHG1550-0.5-1) are employed in order to generate short pulses at the wavelength of 787 ± 0.5 nm. The autocorrelation traces of the pulses from the two short pulse generation systems are shown in Figure 4-11. The author acknowledges the contribution of Dr. Tom Edwards and Dr. C Tom A Brown from University of St Andrews and Dr. Nikos Bamiedakis for the experimental work enabled by the short pulse generation system 1.

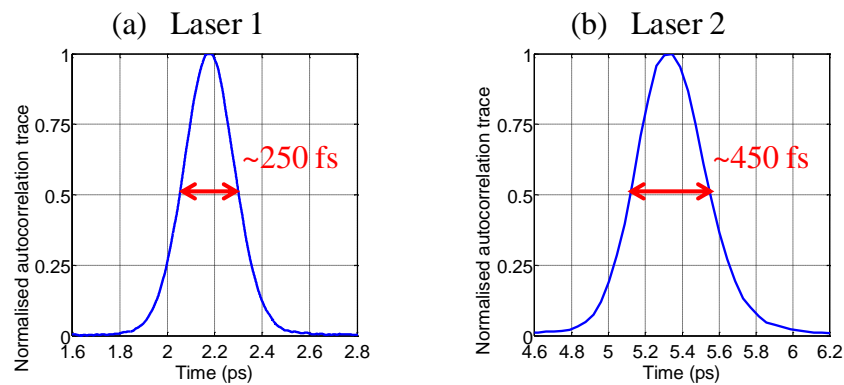


Figure 4-11 Autocorrelation traces of the pulses from the two short pulse generation systems: (a) FWHM = ~250 fs at $\lambda = 850$ nm and (b) FWHM = ~450 fs at $\lambda = 787$ nm.

For the short pulse generation system 2, a 1 mm long nonlinear crystal (MSHG1550-0.5-1, Covesion Ltd.) is employed to achieve second harmonic generation (SHG). The crystal is an MgO doped LiNbO_3 with periodically poled gratings [16]. It can yield higher conversion efficiency compared with traditional nonlinear crystals such as $\beta\text{-BaB}_2\text{O}_4$ (BBO) and LiB_3O_5 (LBO) by choosing the appropriate periodicity of the crystal [17]. In order to access a high nonlinear coefficient, the input light must have polarisation aligned with the dipole moment of the crystal. This is accomplished by aligning the polarisation axis of the light parallel to

the thickness of the crystal using a polarisation controller. By choosing the correct grating period, the optimum conversion efficiency can be achieved when the quasi-phase matching (QPM) is ensured [18]. It has been found that the optimum efficiency can be achieved when the ratio of the crystal length to the confocal parameter is 2.84 [19]. The confocal parameter is defined as the distance between the two points at $z = \pm z_R$ (definition of parameters shown in Figure 4-12). The spot size of the input beam can be then calculated as follows:

$$\left. \begin{aligned} \frac{L}{b} &= 2.84 \\ b &= \frac{2\pi n w_0^2}{\lambda} \end{aligned} \right\} w_0 = \sqrt{\frac{b \lambda_0}{2\pi n}} = 6.5 \mu m \quad (1/e^2 \text{ radius}) \quad (4-1)$$

where $n = 2.15$, $L = 1\text{mm}$, $\lambda_0 = 1574\text{ nm}$ (n is the refractive index of the crystal, L is the length of the crystal).

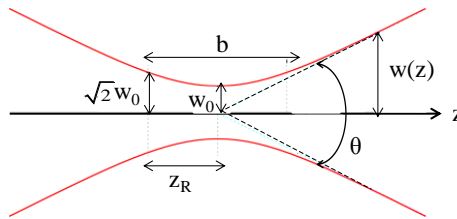


Figure 4-12 Gaussian beam width $w(z)$ as a function of the distance z along the beam (w_0 : beam waist; b : depth of focus; z_R : Rayleigh range; θ : total angular spread).

As the calculated spot size is similar to that of a SMF, a pair of 10 \times microscope objectives (NA = 0.25) are chosen to focus the vertically polarised fundamental pulses into the crystal in order to achieve high conversion efficiency (~10% conversion efficiency achieved in our case). Figure 4-13 illustrates the experimental setup for the SHG used in the short pulse generation system 2, while the spectrums of the original pulse and second harmonic pulse are measured using optical spectrum analyzer (Agilent 86140A) and are plotted in Figure 4-14.

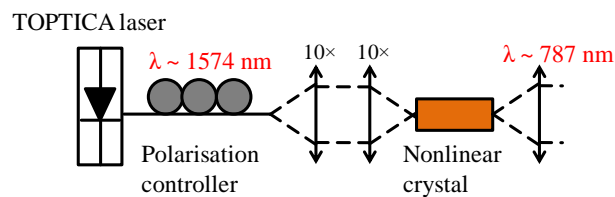


Figure 4-13 Experimental setup for second harmonic generation in the short pulse generation system 2.

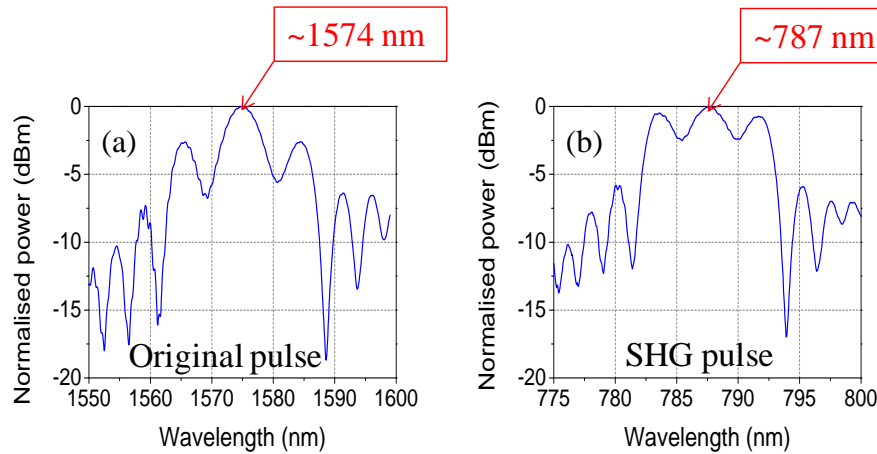


Figure 4-14 Spectrums of the (a) original pulse (peak at ~1574 nm) and (b) generated second harmonic pulse (peak at ~787 nm).

4.3.2 Autocorrelator

In this section, ultra-short laser pulsewidth measurement based in the time domain is introduced. The simplest and more direct way of measuring the duration of a laser pulse is to use fast digital sampling oscilloscopes. However, this approach is typically only feasible to record pulse widths down to tens of picoseconds (>10 ps). Autocorrelators are the most commonly used technique to characterise ultra-short pulses as they can measure pulse duration down to sub-picosecond accuracy without the bandwidth limitation.

In the measurements presented in this chapter, two different autocorrelators are used: for the short pulse generation system 1, a commercially-available Rapid Scanning Autocorrelator (Model FR-103MN) provided by University of St Andrews is employed; a home-made autocorrelator is used for the short pulse generation system 2 (in collaboration with Prof. Peter Vasil'ev). The former utilises background-free (non-collinear) second harmonic generation for the autocorrelation measurement of the repetitive ultra-short laser pulses, while the latter is based on the principle of collinear intensity autocorrelation. Figure 4-15 shows a schematic diagram of the standard commercial FR-103MN autocorrelator while Figure 4-16 plots a diagram of the home-made autocorrelator used [20].

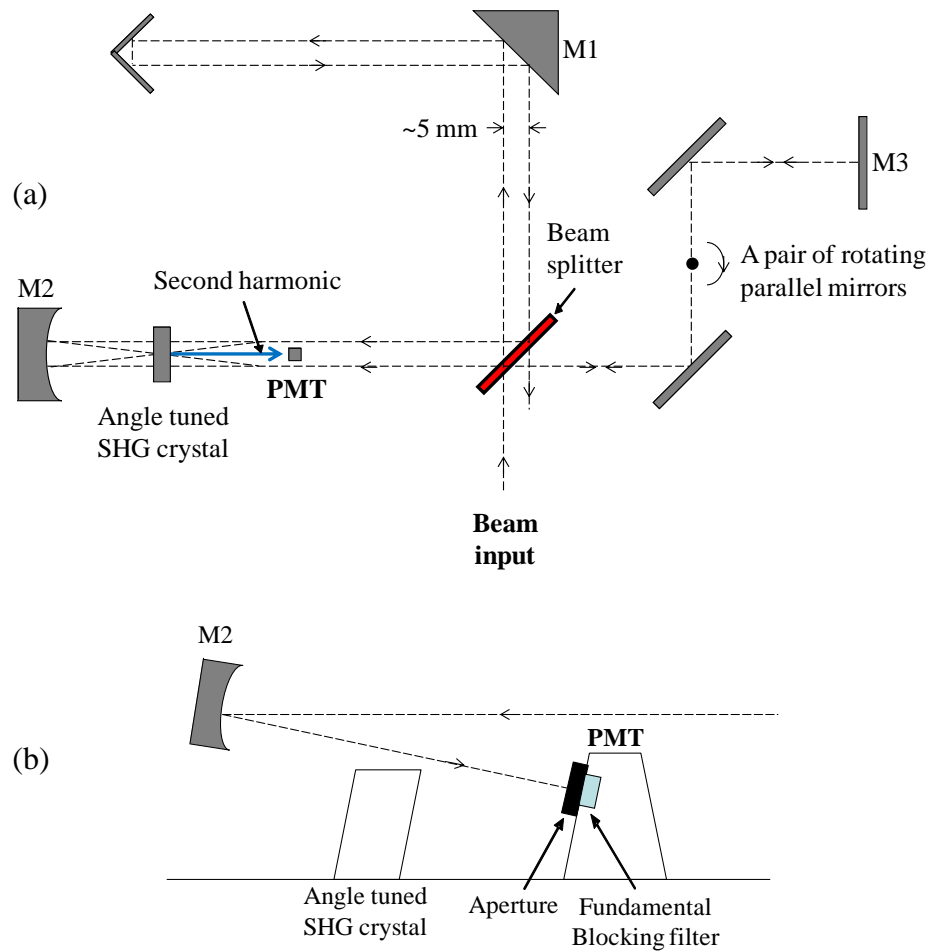


Figure 4-15 (a) Top view schematic and (b) side view schematic of the FR-103MN for the SHG autocorrelation measurement with non-collinear beam used in the short pulse generation system 1 [20].

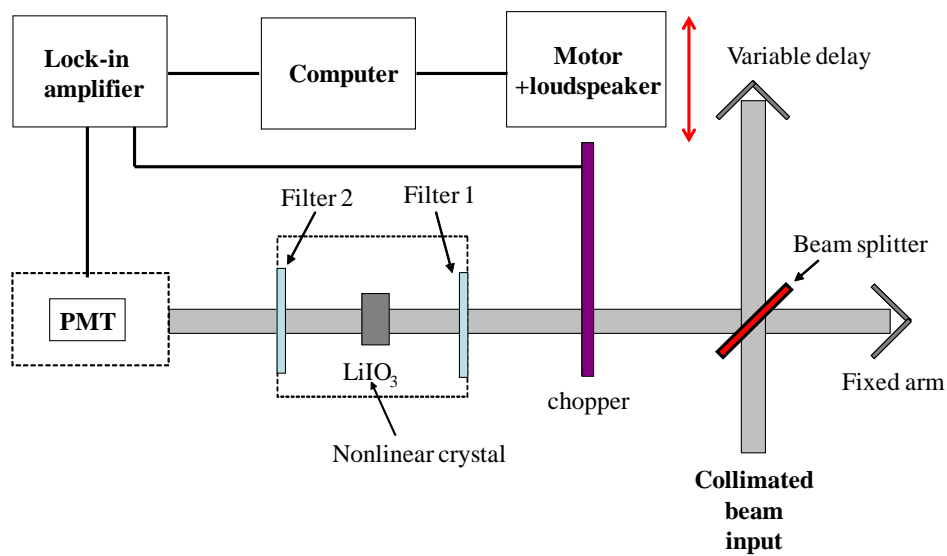


Figure 4-16 Experimental setup for the SHG autocorrelation measurement with two collinear beams used in the short pulse generation system 2.

The basic principle of an autocorrelator is explained as follows. A beam splitter is used to split the incoming laser pulse into two beams, and the two beams are then recombined after one has encountered a fixed and adjustable optical delay. Different kinds of delay methods can be used. For example, the standard FR-103MN utilises rotating mirrors whereas the home-made one uses mirrors mounted on loudspeakers. A nonlinear crystal (e.g. lithium iodate) is used to generate the second harmonic of the fundamental frequency of the laser beam. The SHG signal is detected and amplified by a highly-sensitive photomultiplier tube (PMT). A chopper and a lock-in amplifier are often used in order to increase the signal-to-noise ratio. The recorded function can be expressed as a function of the variable delay in the interferometer and is proportional to:

$$\int \left| [E(t) + E(t - \tau)]^2 \right|^2 dt \quad (4-2)$$

where $E(t)$ is the electric field of the laser pulse and τ is the relative delay in the interferometer arms. If the interference fringes in the recombined beam are averaged out, it can be shown that the recorded signal is given by the following expression for a collinear intensity autocorrelation (the case for short pulse generation system 2 shown in Figure 4-16):

$$f(\tau) = 1 + 2 \frac{\int I(t)I(t - \tau)dt}{\int I(t)^2 dt} \quad (4-3)$$

where $I(t)$ is the intensity of the laser pulse. The intensity autocorrelation function is a symmetrical function even for asymmetric $I(t)$ by definition. In some experimental arrangements, the background-free autocorrelation function $f_c(\tau)$ is measured (the case for short pulse generation system 1 shown in Figure 4-15) [21]:

$$f_c(\tau) = \frac{\int I(t)I(t - \tau)dt}{\int I(t)^2 dt} \quad (4-4)$$

The conversion from the FWHM autocorrelation trace width (ΔT) to the FWHM pulse width (Δt) depends on the assumed pulse shapes. Table 4-1 shows the commonly used pulse shapes, while more pulse shapes that are widely used in the short pulse measurements can be found in [22].

Table 4-1 Relationship between the autocorrelation width and pulse width for commonly used pulse shapes.

Pulse shape	$\Delta t/\Delta T$
Hyperbolic secant	0.648
Gaussian	0.707
Lorentzian	0.5

4.4 Short Pulse Measurement on Spiral Waveguides

4.4.1 Waveguide Samples

The waveguide samples employed for the short pulse measurements are fabricated from siloxane materials developed by Dow Corning on 8-inch silicon substrates using standard photolithography [23]. The core and cladding materials are Dow Corning WG-1020 Optical Waveguide Core and XX-1023 Optical Waveguide Clad respectively. Two types of waveguide components are fabricated on the same substrate: long spiral and shorter reference waveguides. The spiral waveguides have a length of 105.5 cm and the reference waveguides have a length of 19.2 cm. The cross section of the waveguides is approximately $35 \times 35 \mu\text{m}^2$. In order to gain more insight into the effects of refractive index profiles on the bandwidth performance of the waveguide, two samples are fabricated with slightly different fabrication parameters so as to exhibit different refractive index profiles: one has a step-like index profile while the other exhibits a more graded index profile. Figure 4-17 shows photographs of the spiral and the reference waveguide employed in this work illuminated with red light.

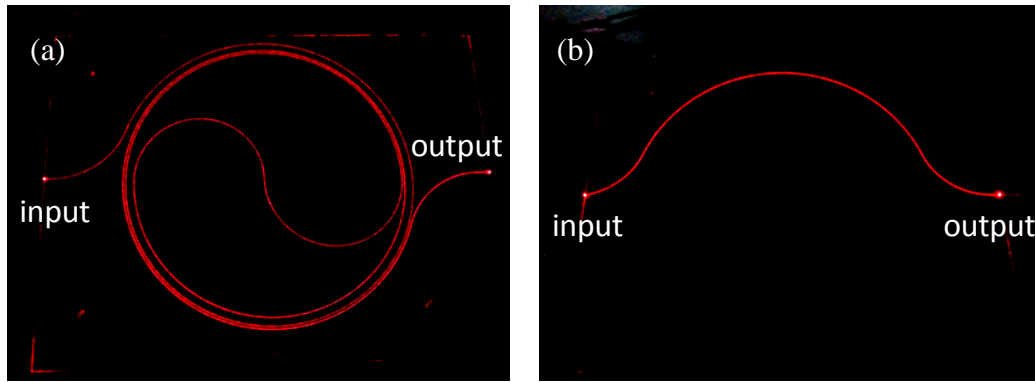


Figure 4-17 Photograph of (a) the 105.5 cm long spiral and (b) the 19.2 cm long reference waveguide illuminated with a red laser source.

The refractive index profile of the waveguide samples is measured using the refractive near field method and is shown in Figure 4-18 [24]. The waveguides shown in Figure 4-18(a) and (b) are named as “step-index” (SI) and “graded-index” (GI) in the rest of this chapter, although neither of them has a strictly-speaking proper SI or GI index profile as the ones typically seen in optical fibres. The SI waveguide has a larger index difference between the core and cladding ($\max \Delta n \sim 0.017$) compared to the GI waveguide ($\max \Delta n \sim 0.01$). The SI waveguide also exhibits a more uniform index distribution with a slight index dip near the middle of the core, whereas the refractive index of the GI waveguide shows a triangle-like shape toward the upper side of the core. It should be noted that the index variation of the cladding seen in the plot is due to measurement artifacts. Dow Corning has carried out detailed studies which determine that these index profiles can be varied with fabrication conditions and material formulations, and can also be produced reliably with low variability.

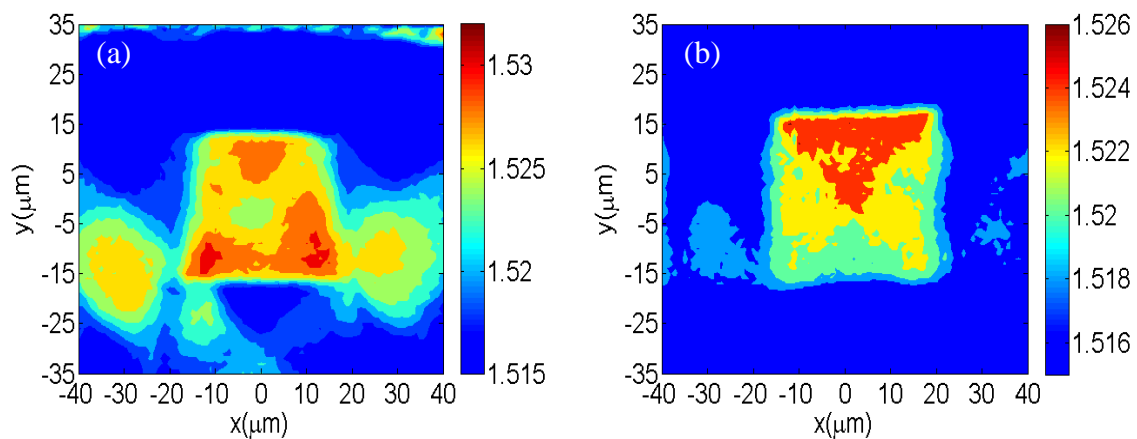


Figure 4-18 Measured refractive index profile of the (a) SI and (b) GI waveguide at the wavelength of 678 nm.

4.4.2 Experimental Setups

The dispersion induced by the two waveguide samples is studied using the two short pulse generation systems aforementioned in section 4.3. Figure 4-19 illustrates the experimental setups of the pulse broadening measurements carried out on the link with and without (back-to-back) the waveguide using the two systems.

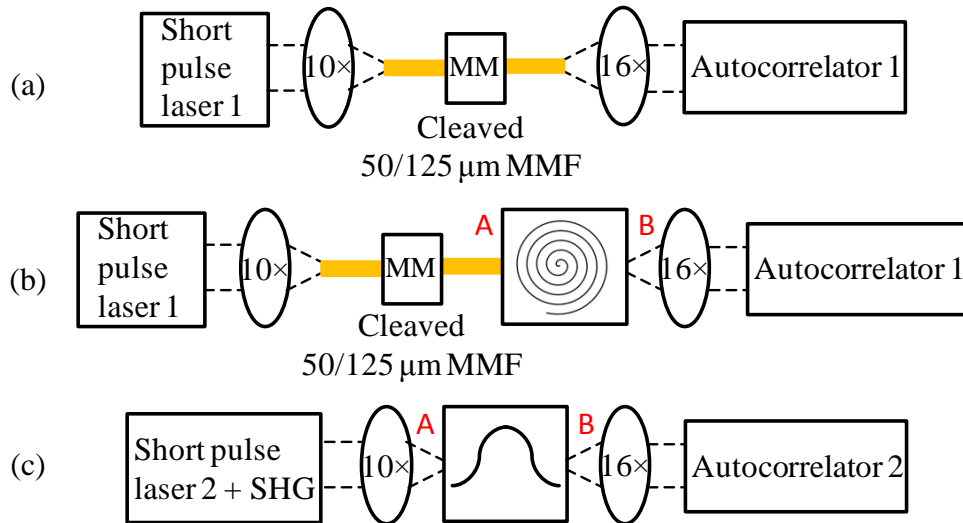


Figure 4-19 Experimental setup used for the (a) back-to-back link; (b) 105.5 cm long spiral waveguide link under a 50/125 μm MMF launch with the use of a MM using pulse generation system 1 at $\lambda = 850$ nm and (c) 19.2 cm long reference waveguide link under a 10× microscope objective launch using pulse generation system 2 at $\lambda = 787$ nm.

The short pulse measurements are conducted for three launch conditions: (i) a 50/125 μm MMF, (ii) a 50/125 μm MMF with the use of a MM (Newport FM-1) and (iii) a 10× microscope objective (NA = 0.25) launch. The measurements of the spiral waveguides are conducted under launch condition (i) and (ii) while the measurement on the reference waveguides are done under launch condition (iii). For launch conditions (i) and (ii), the light is coupled to a 50/125 μm MMF patchcord (<1 m) via a 10× microscope objective (NA = 0.25). Figure 4-20 shows the near field images of the input for each launch condition studied. As it can be seen in Figure 4-20(a), only a small number of mode groups are excited inside the MMF patchcord input under a centre lens launch for launch condition (i). For launch condition (ii), a greater percentage of power is distributed to higher-order modes inside the input fibre with the use of the MM, and hence this launch produces a “worst-case” condition with respect to dispersion among the launches studied on these waveguides [Figure 4-20(b)]. The 10× lens launch provides a restricted launch which results in a Gaussian input with a spot size of 5 ± 1 μm (FWHM) [Figure 4-20(c)].

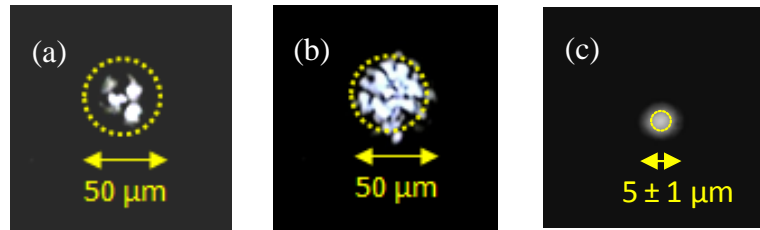


Figure 4-20 Near field images of input fibre and lens under the different launch conditions studied: (a) a 50/125 μm MMF; (b) a 50/125 μm MMF with a MM and (c) a 10 \times microscope objective.

The cleaved end of the input MMF or the 10 \times microscope objective is mounted on a precision translation stage, while a precision displacement sensor is used to control the introduced spatial offsets. At the waveguide output, a 16 \times microscope objective (NA = 0.32) is used to collect the light and deliver it to a power meter or an autocorrelator. The 16 \times lens with a NA larger than that of the waveguide is chosen in order to prevent any mode selective loss at the waveguide output. A broad area optical head (HP 81525A) is used to measure the optical power received at the waveguide output while the autocorrelation trace of the transmitted pulses is recorded for each launch condition and input position.

4.4.3 Experimental Results

The pulse width at the waveguide output is estimated from the recorded autocorrelation traces using curve fitting with common pulse shapes (i.e. sech^2 , Gaussian or Lorentzian) to approximate the shape of the output pulses for each measurement. The best-matching shape for each pulse is determined by choosing the one with minimum root-mean-square-error (RMSE) compared with the actual pulse. The output pulses after propagation through the multimode waveguides are strongly structured due to the waveguide dispersion, although the output pulses of the femtosecond laser used in the experiments have a sech^2 shape. As a result, the pulse shapes which have analytic solutions are fitted to the correlation equation using the standard approach to estimate the waveguide bandwidth. The examples of curve fitting are illustrated in Figure 4-21. The pulse broadening resulting from the light propagation over the waveguide is estimated by comparing the received pulse with that obtained for the respective back-to-back link. By taking the Fourier transform of the respective received optical pulses, the frequency responses of the back-to-back and the waveguide link for each launch condition studied and for the different input positions are calculated. The waveguide frequency response of the waveguide is obtained by

deconvolution, and the -3 dB bandwidth of the waveguide can subsequently be found for each particular launch condition and input position. The procedure of bandwidth estimation is depicted in Figure 4-22.

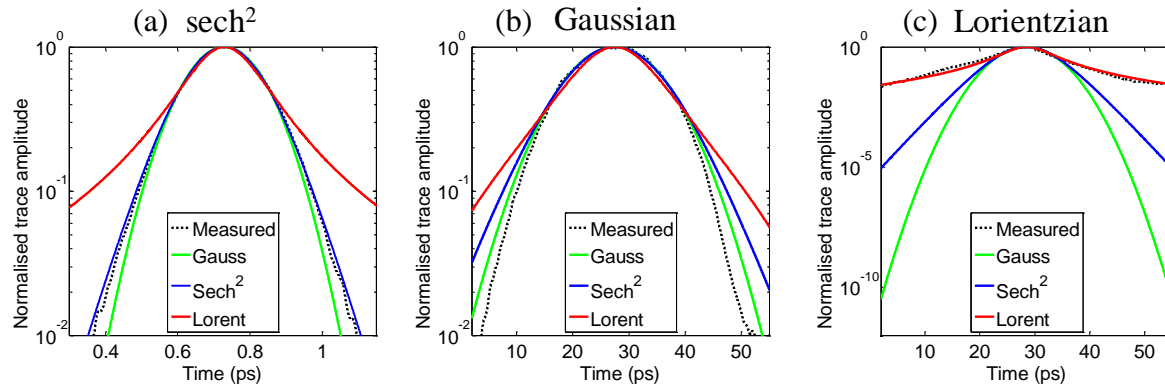


Figure 4-21 Examples of curve fitting: (a) original pulse of the laser source with sech^2 shape, and the structured pulses after propagation over the waveguides with (b) Gaussian and (c) Lorentzian shapes.

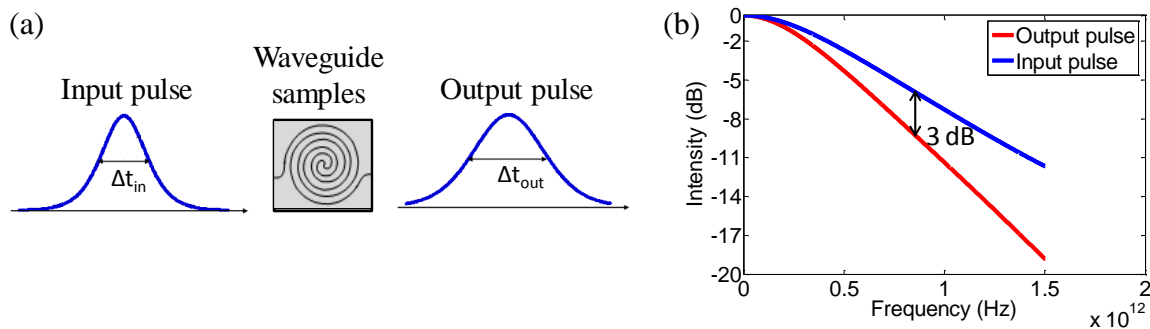


Figure 4-22 Illustrations of bandwidth estimation using pulse broadening method: (a) time-domain and (b) frequency-domain.

Figure 4-23 shows the -3 dB bandwidth of the two 105.5 cm long spiral waveguide samples and the respective normalised received power as a function of the horizontal offset under a 50/125 μm MMF launch with and without the use of the MM. The insertion loss [power difference between the point A and B in Figure 4-19(b)] is ~5.4 dB and ~6 dB for the SI spiral waveguide and ~5.3 dB and ~6.6 dB for the GI spiral waveguide under launch condition (i) and (ii) respectively.

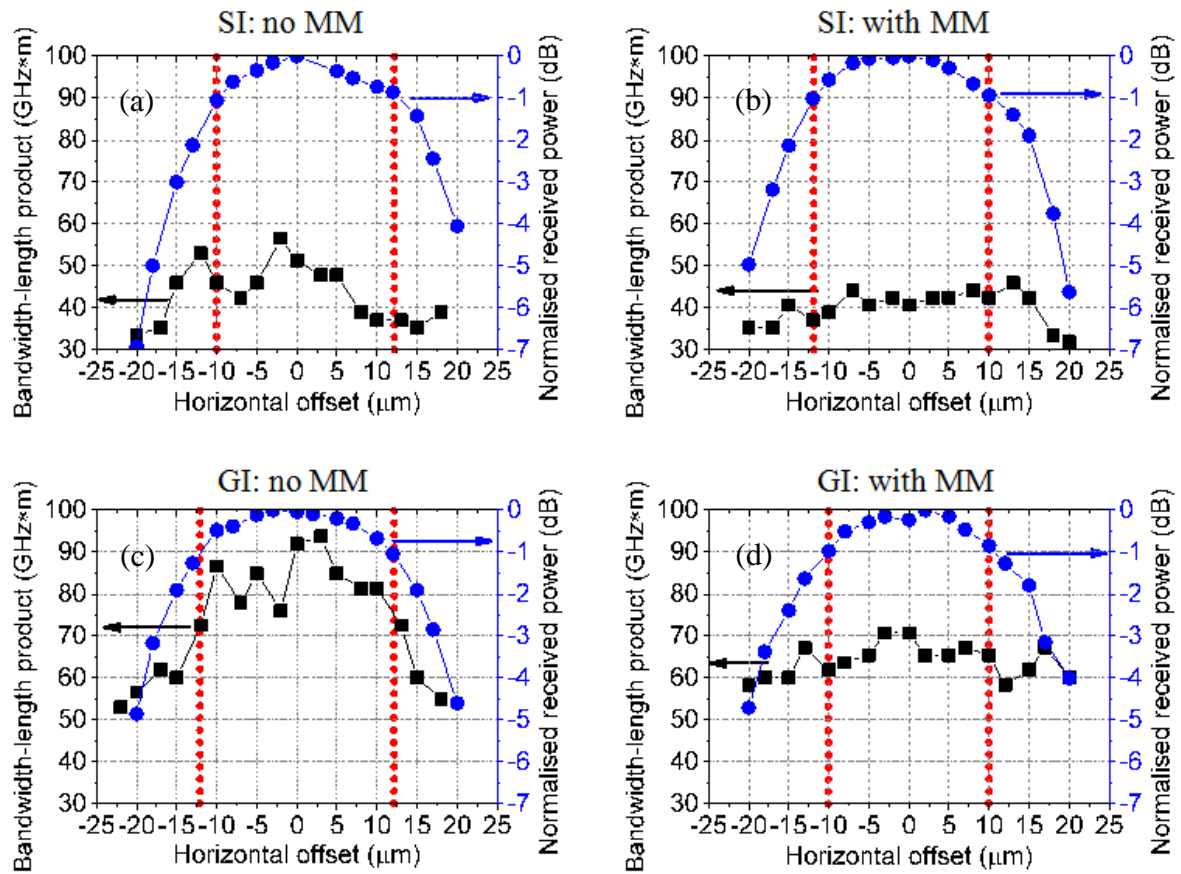


Figure 4-23 Experimental results of the -3 dB bandwidth for the 105.5 cm long spiral polymer multimode waveguides and respective normalised received power for a 50/125 μm MMF input with and without the MM: (a) SI waveguide with no MM, (b) SI waveguide with MM, (c) GI waveguide with no MM and (d) GI waveguide with MM ($\lambda = 850 \text{ nm}$).

The BLP of the SI and GI spiral waveguide is found to be $>40 \text{ GHz}\times\text{m}$ and $>70 \text{ GHz}\times\text{m}$ under the 50/125 μm MMF launch respectively with a -1 dB alignment tolerance up to $\sim \pm 10 \mu\text{m}$ [Figure 4-23(a) and (c)]. As expected, the SI waveguide exhibits lower bandwidth than the GI waveguide due to its larger modal volume. The waveguide bandwidth gradually reduces for larger input offsets, when a larger portion of the input power is coupled to higher-order modes at the waveguide input. A BLP of $\sim 40 \text{ GHz}\times\text{m}$ and $\sim 65 \text{ GHz}\times\text{m}$ is obtained for the SI and GI spiral waveguide across the offset range of $\pm 10 \mu\text{m}$ for the 50/125 μm MMF with a MM launch. As expected, the use of the MM degrades the bandwidth performance as a more uniform mode power distribution is generated at the waveguide input [Figure 4-20(b)], but also results in a more uniform bandwidth performance across input offsets [Figure 4-23 (b) and (d)] for both waveguides. Under a relatively overfilled launch, the induced spatial

offsets have a small effect on the measured bandwidth as the generated mode power distribution does not vary significantly across input offsets.

Similar measurements are carried out on the 19.2 cm long reference waveguides using a 10× microscope objective launch. The insertion loss of the SI and GI reference waveguide [power difference between the point A and B in Figure 4-19(c)] is ~2.2 dB and ~1.5 dB under such a launch. The input beam has a small spot-size and only excites a small number of modes inside the waveguide. This provides a restricted launch at the waveguide input, and thus an improved bandwidth performance is expected. To gain more physical insights into the bandwidth performance for different launches, the near-field images at the waveguide output of the SI and GI reference waveguide under the lens launch [Figure 4-24(a) and (b)] as well as the ones obtained at the output of two spiral waveguides under a 50/125 μm MMF launch without the MM are recorded using a CCD camera for comparison [Figure 4-24(c) and (d)]. These images indicate that a 10× lens launch can offer a highly selective mode excitation in the waveguide whereas a 50/125 μm MMF launch causes the distribution of a larger percentage of power towards the outer edge of the waveguide. A similar method of estimating bandwidth as the one used for the spiral waveguides is employed on these reference waveguides under the restricted launch condition.

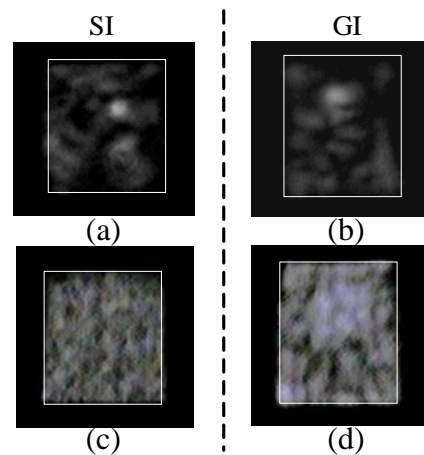


Figure 4-24 Near field images of the (a) SI and (b) GI reference waveguide under a restricted launch; and the (c) SI and (d) GI spiral waveguide under a 50/125 μm MMF launch.

Indeed, the obtained BLP for the 19.2 cm long reference waveguide is found to be >100 GHz×m for both SI and GI waveguide for a large range of input offsets. Figure 4-25 shows the range that provides such large bandwidth (>100 GHz×m) for each waveguide type. It is found to be $\sim 19 \times 8 \mu\text{m}^2$ in the lower bottom part of the waveguide core for the SI waveguide

and $\sim 18 \times 20 \mu\text{m}^2$ in the upper bottom part of the waveguide core for the GI waveguide. Figure 4-26 shows that the high-bandwidth region is also within the -1 dB alignment tolerances. Moreover, the high BLP areas match the higher refractive index of the waveguides at these input positions as the small input spot excites only the lower-order modes (Figure 4-18). The use of restricted launch condition is a useful tool for improving bandwidth performance and ensuring reliable operation in multimode waveguide systems. It has been widely used in MMF systems to meet specifications for Gigabit Ethernet (GbE) and 10 GbE data transmission [25].

Overall, the experimental results indicate that the GI waveguide exhibits superior bandwidth performance and offers more reliable operation than the SI waveguide. This is due to the lower number of modes guided in the GI waveguide and therefore the reduced levels of induced multimode dispersion. The obtained large area ($>10 \times 10 \mu\text{m}^2$) ensuring a BLP of $>100 \text{ GHz}\times\text{m}$ and high coupling efficiency on the GI waveguide, demonstrates that achievable launch conditioning and appropriate choice of refractive index profile can be implemented in such highly-multimoded waveguides to ensure a robust bandwidth performance across a large range of input positions.

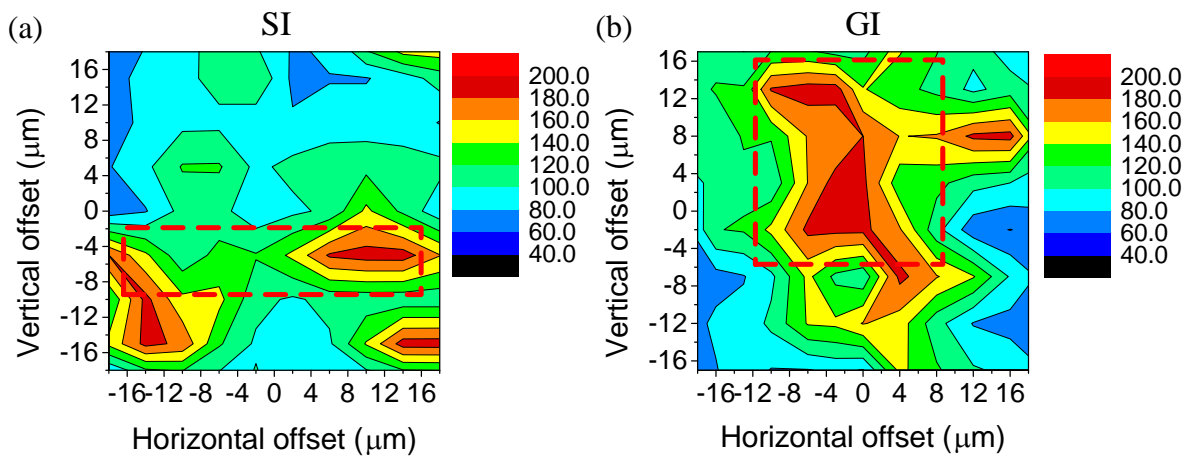


Figure 4-25 Experimental results of BLPs ($\text{GHz}\times\text{m}$) of the 19.2 cm long (a) SI and (b) GI under a $10\times$ microscope objective launch at $\lambda = 787 \text{ nm}$ (high BLP region noted in red dashed line).

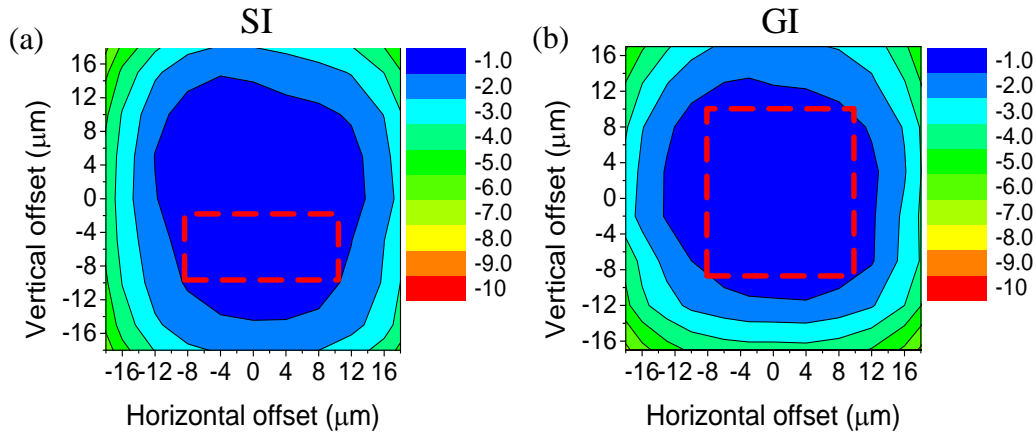


Figure 4-26 Normalised measured coupling loss (units in dB) of the 19.2 cm long SI and GI reference waveguide under a 10× microscope objective launch at $\lambda = 787$ nm (red dashed line indicates the high BLP region shown in Figure 4-25).

4.4.4 Simulation Results

The simulation is based on standard methods employed for studying MMF waveguides [26] and has been presented in more detail in Chapter 3. A mode solver FIMMWAVE (see section 3.7 in Chapter 3) is used to calculate the field profiles of the guided waveguide modes as well as their corresponding group refractive indices using the measured refractive index profiles of the waveguides. The modes of a 50/125 μm MMF are obtained using an analytic mode solver assuming the standard refractive index profile of a MMF as discussed in section 3.5.2 in Chapter 3 [27]. The number of modes for a standard 50/125 μm MMF is calculated to be 184 with a maximum principle mode number (PMN) of 29. The power is assumed to be distributed equally among the modes of the MMF patchcord with a $\text{PMN} \leq 15$ for the launch without the MM, and with a $\text{PMN} \leq 22$ for the launch with the MM as illustrated in Figure 4-27. The restricted launch is modelled with a Gaussian beam with a spot size of the measured value ($\text{FWHM} \sim 4 \mu\text{m}$). The power coupled to each waveguide guide for a given launch is calculated using overlap integrals. The suppression of higher-order modes due to the waveguide bends is taken into account by introducing mode selective loss, which is found by fitting the simulation with the experimental data of the received optical power across spatial offsets. Figure 4-28 depicts the curves of assumed mode selective loss while Figure 4-29 shows the comparisons between the simulated and actual received power for both SI and GI waveguide. The impulse response and the bandwidth of the waveguide can then be calculated using the mode group refractive indices and mode power. Therefore, the respective

waveguide bandwidth for each offset under each launch condition can be calculated from the obtained impulse response by repeating the process for the different launch conditions at different input positions.

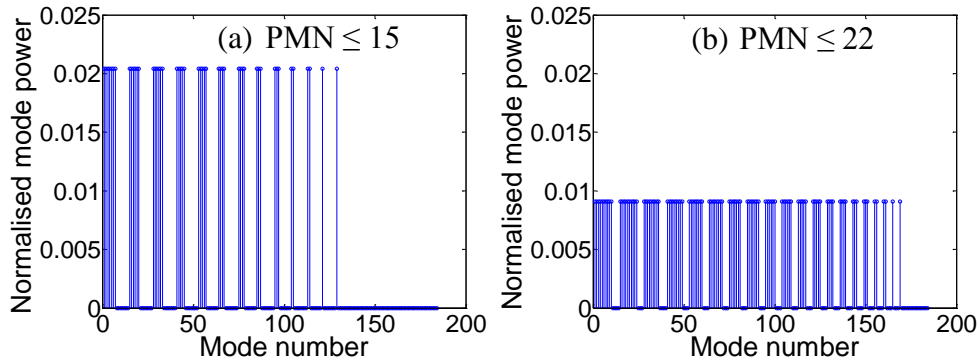


Figure 4-27 Assumed mode power distribution inside the input 50/125 μm MMF patchcord for condition: (a) a 50/125 μm MMF with no MM ($\text{PMN} \leq 15$) and (b) a 50/125 μm MMF with MM ($\text{PMN} \leq 22$).

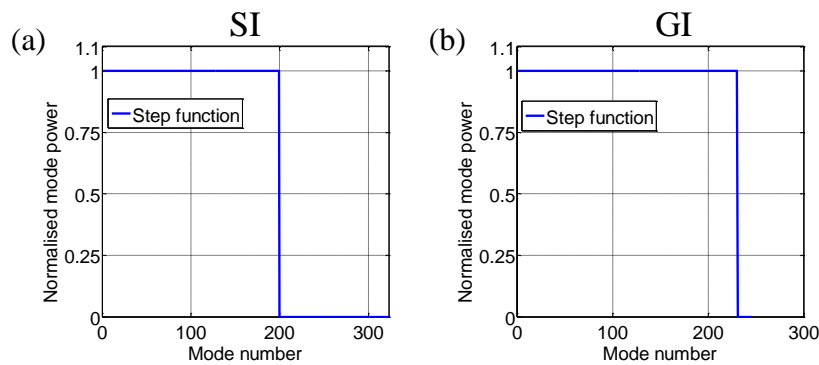


Figure 4-28 The curves of mode selective loss assumed for the (a) SI and (b) GI waveguide.

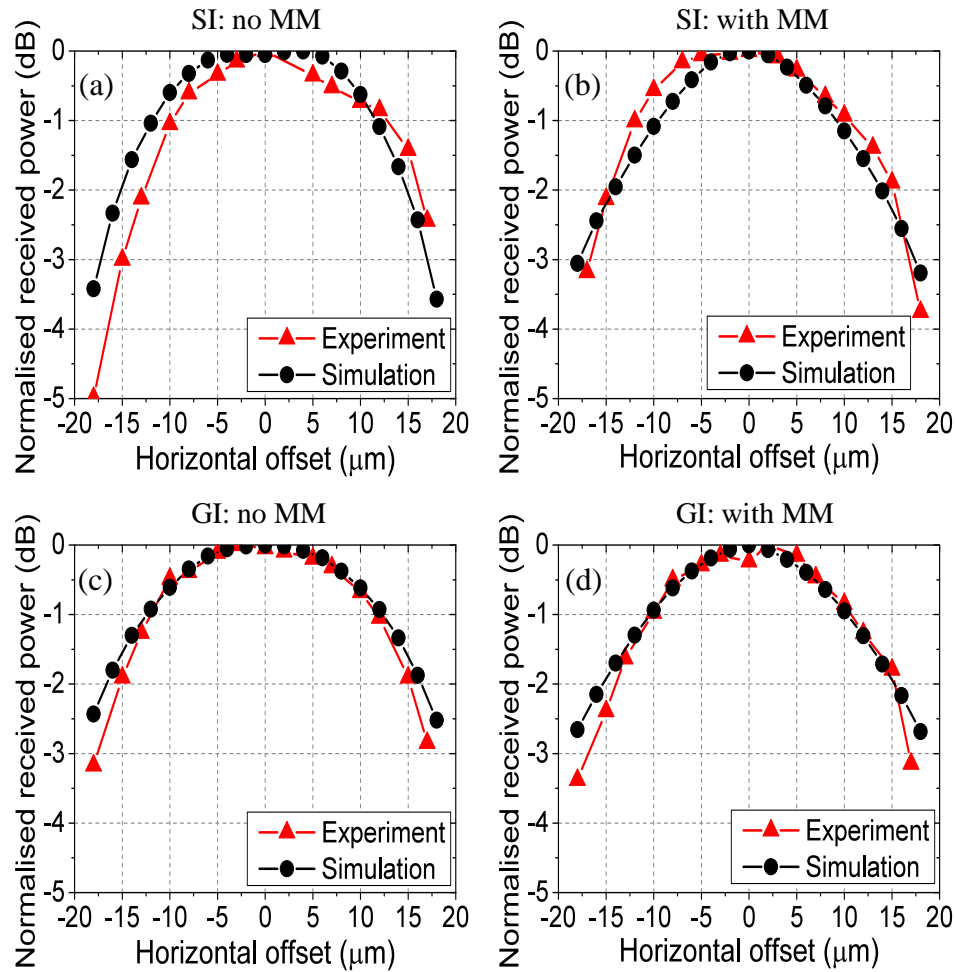


Figure 4-29 Normalised received power versus position of input 50/125 μm MMF:
(a) SI waveguide with no MM ($PMN \leq 15$), (b) SI waveguide with MM ($PMN \leq 22$), (c)
GI waveguide with no MM ($PMN \leq 15$) and (d) GI waveguide with MM ($PMN \leq 22$).

Figure 4-30 shows the bandwidth simulation results for the two spiral waveguides under the MMF launch. It can be seen that a similar behaviour is obtained to that of the experimental work. The simulation results for the reference waveguide under restricted launch are also shown in Figure 4-31. General agreement can be found between the high BLP region obtained from the simulation and the experimental observations. To better understand why the bandwidth is higher at high index region of the waveguide core under the restricted launch, some analysis from the perspective of mode power distribution excited inside the SI and GI waveguides is discussed below.

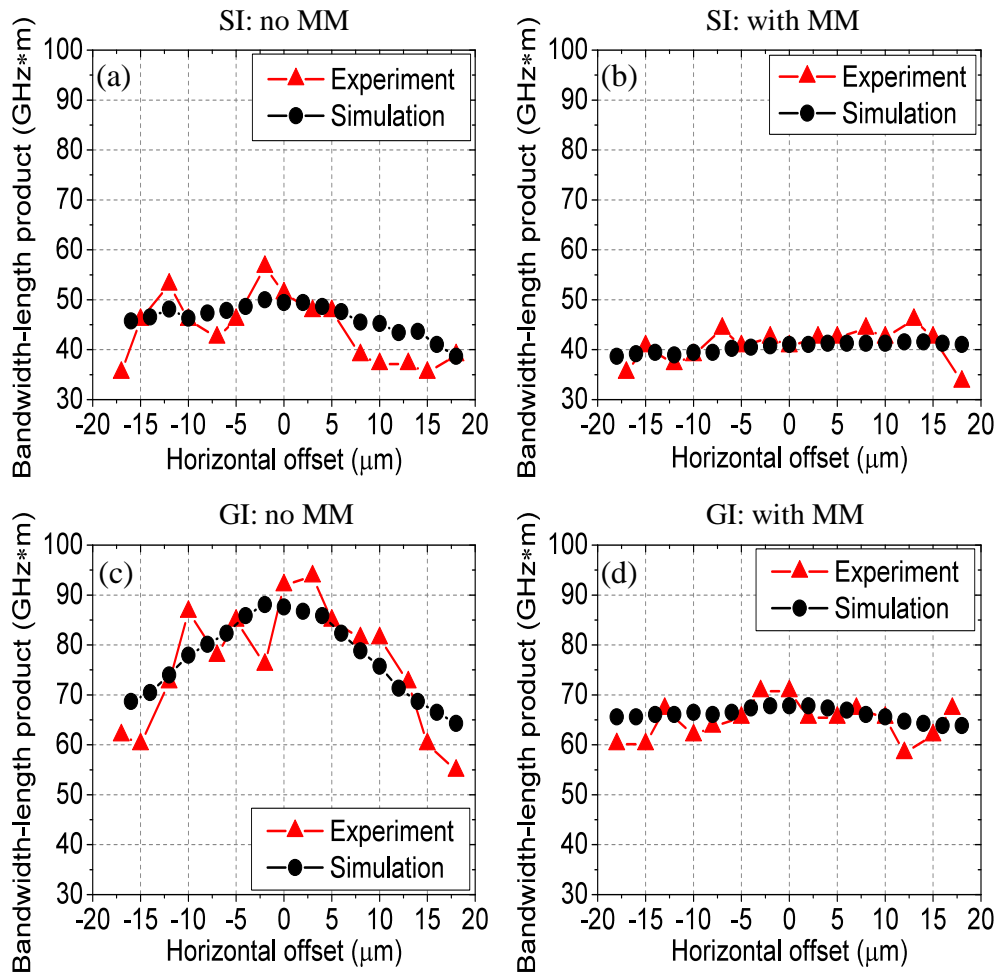


Figure 4-30 Simulation and experimental results of the -3 dB BLP (unit in GHz×m) for the 105.5 cm long spiral polymer multimode waveguides for a 50/125 μm MMF input with and without MM: (a) SI waveguide with no MM, (b) SI waveguide with MM, (c) GI waveguide with no MM and (d) GI waveguide with MM ($\lambda = 850$ nm).

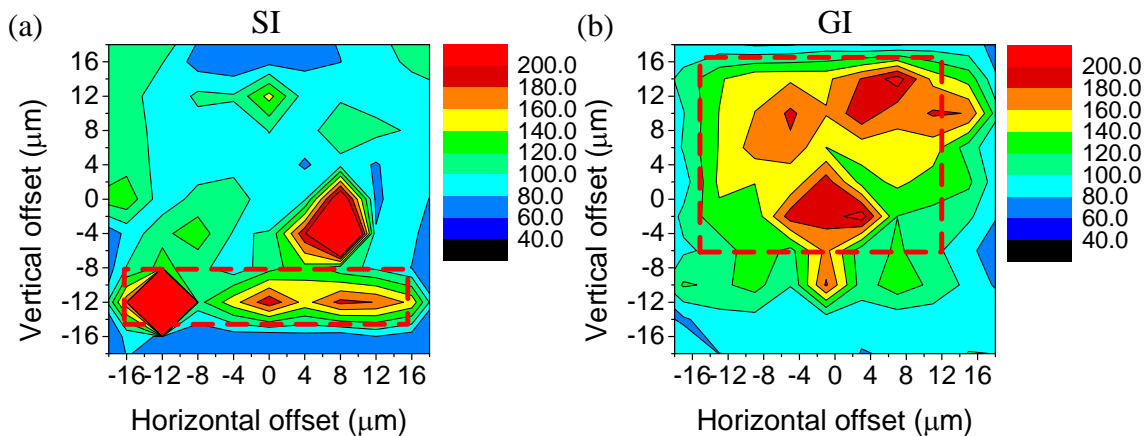


Figure 4-31 Simulation results of the -3 dB BLP (unit in GHz×m) of the 19.2 cm long reference polymer multimode waveguide for a 10× microscope objective launch ($\lambda = 787$ nm): (a) SI waveguide and (b) GI waveguide.

- SI waveguide

The mode profiles of the first 5 modes calculated using FIMMWAVE based on the measured refractive index profile are plotted in Figure 4-32. Figure 4-33(b) shows the mode power distribution at different launch positions under restricted launch for the SI waveguide. It can be seen that higher-order modes carry a large portion of the coupled input power when the input beam is launched at location 1 ($x = 0 \mu\text{m}$, $y = 0 \mu\text{m}$) where the index dip occurs in the middle of the core. Hence, the multimode dispersion is increased and the bandwidth is low at this particular position as shown in Figure 4-31(a). In comparison, when the launch position moves to location 4 ($x = -12 \mu\text{m}$, $y = -12 \mu\text{m}$) where the high index region appears, a smaller number of modes are excited and the majority of power is coupled into the lower-order modes, resulting in the largest bandwidth performance. Similarly, higher bandwidth values are expected at location 2 ($x = 8 \mu\text{m}$, $y = -4 \mu\text{m}$) and location 3 ($x = 0 \mu\text{m}$, $y = 12 \mu\text{m}$) where the lower-order modes are mostly excited given the particular index profile.

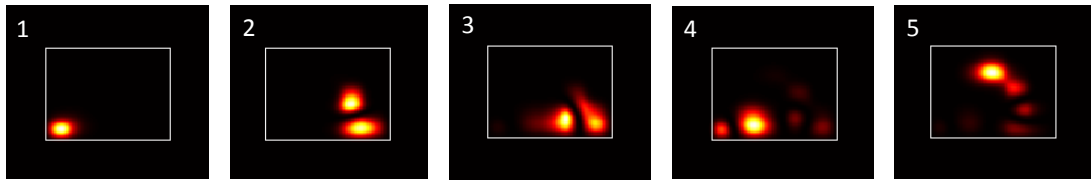


Figure 4-32 Mode profiles of the SI waveguide (first 5 modes).

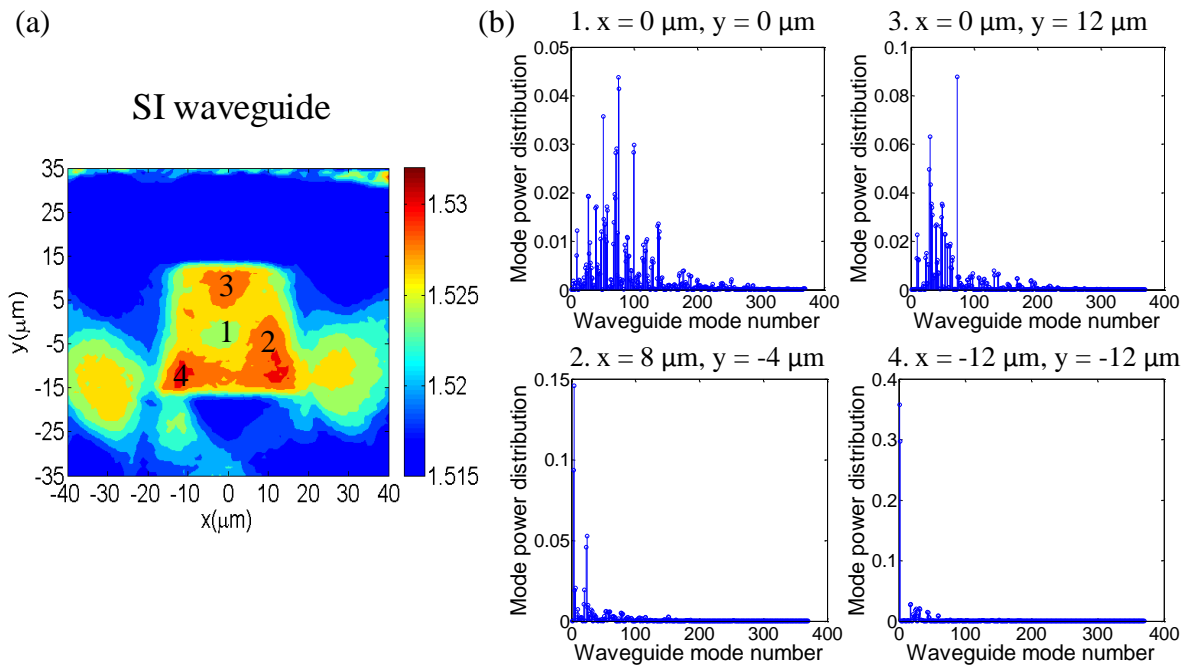


Figure 4-33 (a) Refractive index profile of the SI waveguide at 678 nm and (b) mode power distribution of the SI waveguide at varying locations under restricted launch.

- GI waveguide

Figure 4-34 and Figure 4-35 illustrate the mode profiles of the first few modes and the simulated mode power distribution at varying input positions of the GI waveguide under restricted launch respectively. As indicated in the refractive index profile, the lower-order modes of this waveguide lie in the upper side of the core (Figure 4-34). As a result, at locations 1-3, high bandwidth performance is expected as lower-order modes are mainly excited at these launch positions. This can be seen from the mode power distributions at the respective input offsets shown in Figure 4-35(b) where a large amount of power is coupled into the lower-order modes resulting in reduced multimode dispersion. In contrast, when the launch position is at the waveguide edge (location 4: $x = 0 \mu\text{m}$, $y = -16 \mu\text{m}$), it can be clearly seen that more power is distributed into the higher-order modes, which results in larger multimode dispersion and reduced bandwidth as can be observed in Figure 4-31(b).

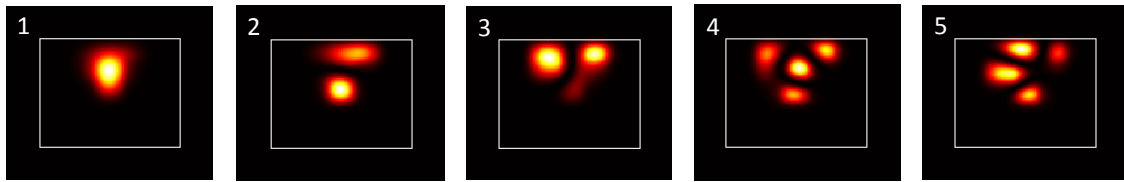


Figure 4-34 Mode profiles of the GI waveguide (first 5 modes).

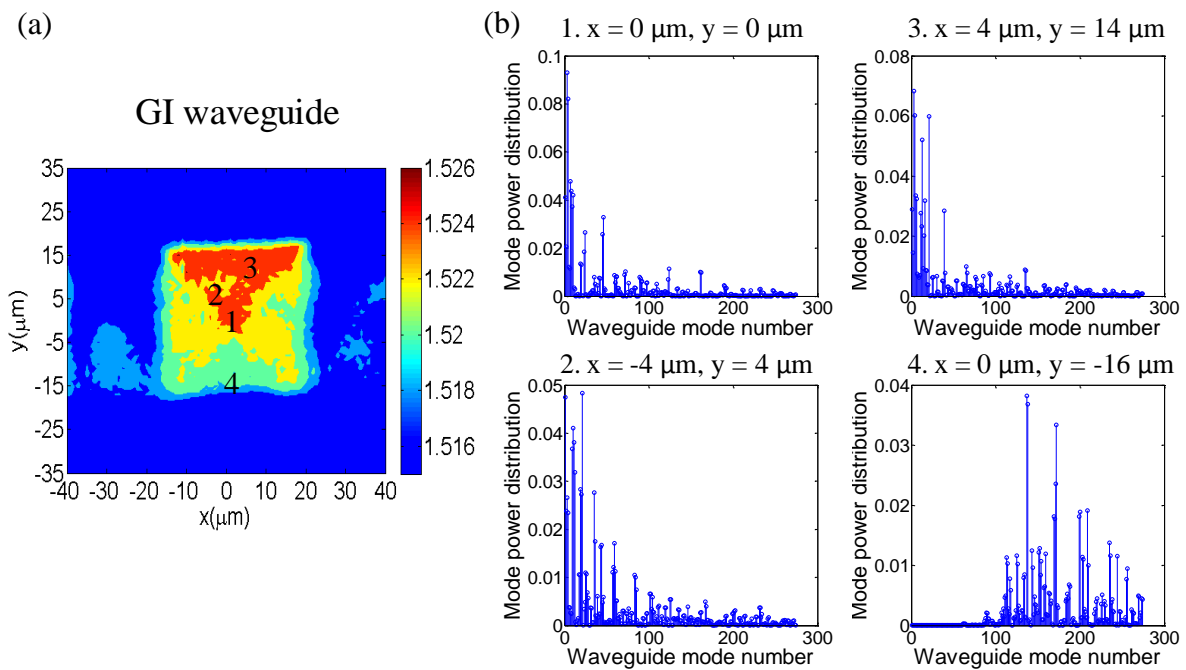


Figure 4-35 (a) Refractive index profile of the GI waveguide at 678 nm and (b) mode power distribution of the GI waveguide at varying locations under restricted launch.

These analyses provide an understanding of the bandwidth performance of the waveguides through the calculated mode power distribution for different input spatial offsets under a restricted launch condition. More experimental investigation will be conducted on straight waveguides samples to further confirm the feasibility of this simulation model in section 4.5.

4.4.5 Discussion

The successful fitting of the experimental bandwidth results indicates that the simulation studies can provide a good indication for launch design and dispersion engineering. For the particular studies presented here, however, it is practically challenging to know the exact mode power distribution at the waveguide input for the case of multimode launches and therefore calculate the induced dispersion unless specific launch conditioning schemes are employed. Nevertheless, such a model can at least provide a guideline of the expected waveguide performance as performed in the study of 10 GbE standards in MMF links [25]. However, it should be noted that there are a number of phenomena which have not been considered in the simulations but may affect the mode propagation inside the waveguide should much greater accuracy be required: (a) mode mixing is not considered; (b) the calculated mode profiles are based on an ideal straight waveguide whereas the actual mode profiles inside the complex long bending waveguide samples may differ. It has been previously found that multimode waveguide dispersion in different polymer material systems can be significantly affected by mode mixing with very short equilibrium lengths of ~ 10 cm observed in the experiment [6].

4.5 Short Pulse Measurement on Straight Waveguides

As mentioned in the previous section, the high bandwidth region of a waveguide under restricted launch conditions is expected to be located in the high index region of the core due to the excitation of the lower-order modes at the waveguide input. Although general agreement between the simulation and experimental results has been found on the reference waveguides, a difference can be partially attributed to the bending structure of the waveguides. Therefore, the bandwidth performance of straight waveguides is experimentally studied in this section in order to provide a more intuitive understanding of how the mode propagation in the guides affects the dispersion of these multimode waveguides.

4.5.1 Waveguide Samples

The dispersion of three waveguide samples with different refractive index profiles is measured under a restricted launch. The fabrication, index profile design and characteristics of the waveguide components with the three different refractive index profiles will be discussed in more detail in the next chapter. Here, the bandwidth performance of these waveguides is mainly concerned. The three straight waveguides are fabricated to exhibit similar refractive index profiles as illustrated in Figure 5-6 in Chapter 5. The straight waveguide samples are denoted as WG01, WG02 and WG03 with lengths of 9.1 cm, 9.6 cm and 7.4 cm respectively.

4.5.2 Experimental Results

The launch condition employed here is the same as launch condition (iii) mentioned in section 4.4.2, and experimental setup is illustrated in Figure 4-19(c). The bandwidth estimation of these straight waveguides follows the same procedures explained in section 4.4.3. In order to gain more insight into the guided modes in the waveguide, near field images are recorded at different launch positions. Figure 4-36(a) and (b) illustrate the refractive index profile and the measured bandwidth for WG01 respectively. As expected, the high BLP area of WG01 is located towards the upper side of the core, which agrees well with the location of high index region in the core. Moreover, the bandwidth variation can be justified by the near field images taken at the waveguide output. For example, the bandwidth is the largest at location 1 ($x = 0 \mu\text{m}$; $y = 17 \mu\text{m}$), at which lower-order modes are mostly excited resulting in the smallest multimode dispersion. As the input launch position moves down to location 3 ($x = 0 \mu\text{m}$; $y = -3 \mu\text{m}$), the bandwidth decreases as an increasing number of higher-order modes are excited as can be seen from the near field image at location 3. In contrast, when the input launch is focused at the edge of the core (location 6: $x = 20 \mu\text{m}$, $y = -22 \mu\text{m}$), it can be seen that a larger amount of power is distributed into the higher-order modes, and therefore the bandwidth is significantly reduced compared to that at location 1 as expected. In addition, a slight asymmetric behaviour can be observed on the bandwidth result, which can be justified by the near field image obtained at location 2 ($x = 20 \mu\text{m}$; $y = 12 \mu\text{m}$).

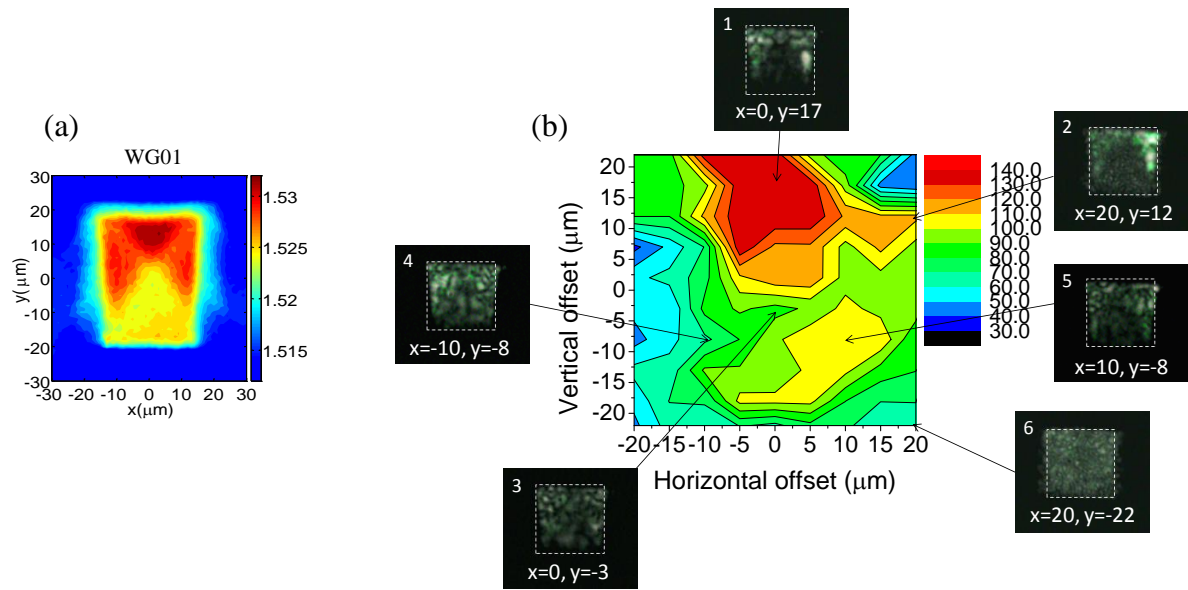


Figure 4-36 (a) Measured refractive index profile of WG01 at 678 nm and (b) experimental result of BLPs (GHz×m) of WG01 with the recorded near field images at different input positions inset.

The refractive index profile and the measured bandwidth for WG02 are shown in Figure 4-37(a) and (b) respectively. As the high index region is located toward the bottom of the waveguide core, high-bandwidth performance is expected when the input beam is launched in this region as seen in Figure 4-37(a). This is due to the fact that lower-order modes are primarily excited when the input launch lies within this particular high index area which can be shown by the near field image recorded at location 1 ($x = 0 \mu\text{m}$, $y = -5 \mu\text{m}$) and location 5 ($x = 0 \mu\text{m}$, $y = -20 \mu\text{m}$). The bandwidth is lower at location 5 than that at location 1 as slightly more higher-order modes are excited which can be noticed from the near field images at the respective locations. As the launch position moves toward the edges of the waveguide core, the bandwidth performance degrades gradually as more power is coupled into the higher-order modes in the waveguide that results in an increase of the induced multimode dispersion. The waveguide are more overfilled at location 6 ($x = 25 \mu\text{m}$, $y = 20 \mu\text{m}$), and hence the bandwidth is observed to be the lowest at this position. Moreover, it can be noticed that the bandwidth variation in the horizontal direction is higher than that in the vertical direction due to the larger horizontal index change as seen in the index profile. This can also be justified by the near field images recorded at the relevant locations. Figure 4-38(a) shows the index profile of WG03 while Figure 4-38(b) depicts the measured bandwidth of WG03 with the near field images captured. Similar behaviour can be found on WG03 compared to WG01 due to the similarity between the refractive index profiles of the two samples.

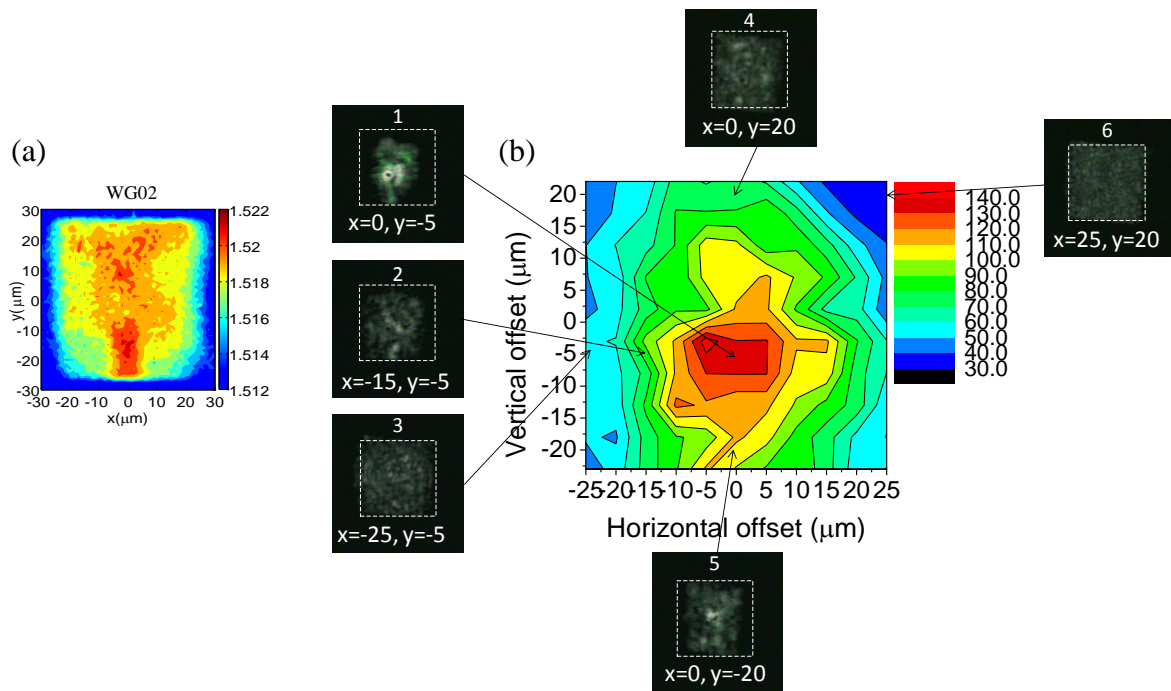


Figure 4-37 (a) Measured refractive index profile of WG02 at 678 nm and (b) experimental result of BLPs (GHz×m) of WG02 with the recorded near field images at different input positions inset.

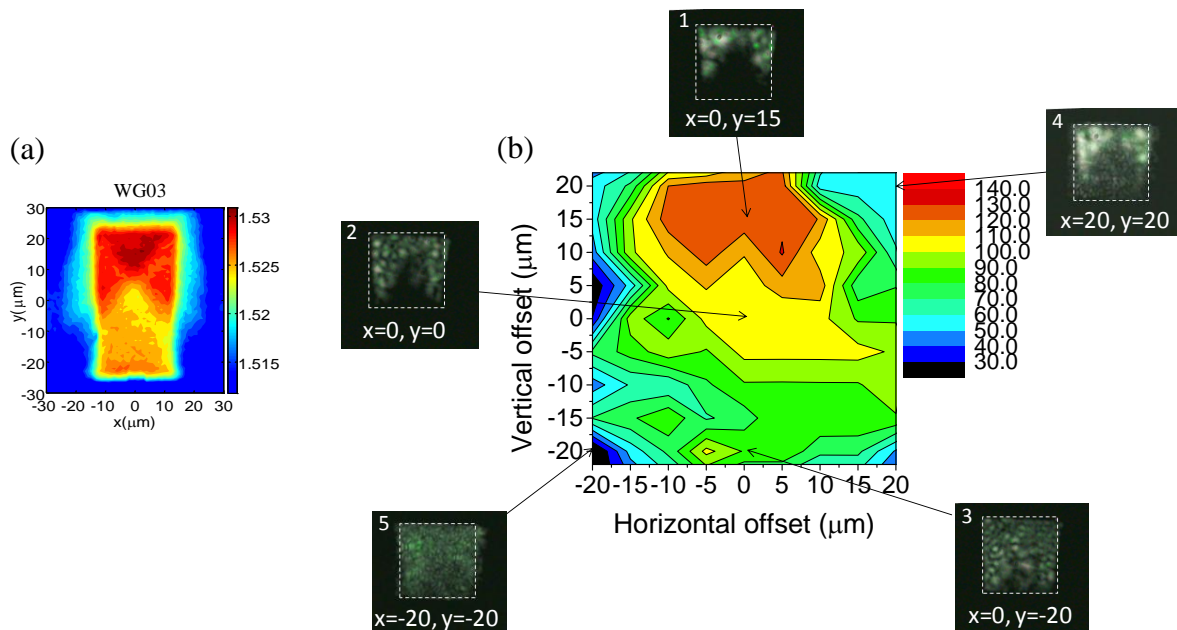


Figure 4-38 (a) Measured refractive index profile of WG03 at 678 nm and (b) experimental result of BLPs (GHz×m) of WG03 with the recorded near field images at different input positions inset.

Overall, the near field images agree well with the obtained bandwidth results of all three waveguide samples. These observations not only provide a straightforward understanding of dynamic performance of these guides but also confirm the viability of the simulation model developed. These results can provide very useful insights into the design of high-bandwidth waveguides by employing appropriate refractive index engineering. The results indicate that waveguides with high-bandwidth values and high input alignment tolerances can be achieved by carefully designing the shape of index profiles. It can also be noted that the BLP values of these straight waveguides are lower than those obtained on the reference waveguides, indicating again that the bending structure can be beneficial to the bandwidth performance due to the mode stripping properties of the bends. In addition, the waveguide loss performance is another limiting factor in the system design to ensure an adequate power budget. The effects of the refractive index engineering and waveguide layout on the waveguide loss and bandwidth performance will be further discussed in the next chapter.

4.6 Summary

This chapter presents the dispersion studies on the multimode polymer waveguides for use in board-level optical interconnections. The bandwidth studies on the 1.4 m and 1 m long spiral waveguides demonstrate an instrument-limited BLP value of at least 35 GHz×m under a wide range of launch conditions and for different input offsets. Time-domain measurements are further carried out to investigate the ultimate bandwidth of these waveguides and shown BLP values of >40 GHz×m and >70 GHz×m for the SI and GI waveguide respectively under a 50/125 μm MMF launch for an offset range of ±10 μm, and of >100 GHz×m using a restricted launch for an offset range of ~19 × 8 μm² and ~18 × 20 μm² for the SI and GI waveguide respectively. Moreover, the high bandwidth regions are well within -1 dB alignment tolerances. The simulation model based on the measured refractive index profile agrees well with the experimental results. These results indicate the potential of this technology and the capacity of transmitting data rates of 100 Gb/s over a single waveguide channel up to distances of 1 m with achievable launch conditioning schemes and appropriate refractive index engineering.

4.7 References

- [1] P. Westbergh, R. Safaisini, E. Haglund, J. S. Gustavsson, A. Larsson, and A. Joel, "High-Speed 850 nm VCSELs with 28 GHz Modulation Bandwidth for Short Reach

- Communication,” *Proc. SPIE*, vol. 8639, pp. 86390X–1–6, 2013.
- [2] R. Safaisini, E. Haglund, A. Larsson, J. S. Gustavsson, E. P. Haglund, and P. Westbergh, “High-Speed 850 nm VCSELs Operating Error Free Up To 57 Gbit/s,” *Electron. Lett.*, vol. 49, no. 16, pp. 1021–1023, Aug. 2013.
 - [3] D. Kuchta, A. Rylyakov, C. L. Schow, J. E. Proesel, C. Baks, P. Westbergh, J. S. Gustavsson, and A. Larsson, “64Gb/s Transmission over 57m MMF using an NRZ Modulated 850nm VCSEL,” *Opt. Fiber Commun. Conf.*, pp. 20–22, 2014.
 - [4] D. M. Kuchta, S. Member, A. V Rylyakov, C. L. Schow, J. E. Proesel, C. W. Baks, P. Westbergh, J. S. Gustavsson, and A. Larsson, “A 50 Gb / s NRZ Modulated 850 nm VCSEL Transmitter Operating Error Free to 90 °C,” *J. Light. Technol.*, vol. 33, no. 4, pp. 802–810, 2015.
 - [5] D. M. Kuchta, A. V Rylyakov, F. E. Doany, C. L. Schow, J. E. Proesel, C. W. Baks, P. Westbergh, J. S. Gustavsson, and A. Larsson, “A 71-Gb/s NRZ Modulated 850-nm VCSEL-Based Optical Link,” *IEEE Photon. Technol. Lett.*, vol. 27, no. 6, pp. 577–580, 2015.
 - [6] F. E. Doany, P. K. Pepeljugoski, A. C. Lehmanl, J. A. Kash, and R. Dangel, “Measurement of Optical Dispersion in Multimode Polymer Waveguides,” *LEOS Summer Top. Meet.*, p. MB4.4, 2004.
 - [7] X. Wang, L. Wang, W. Jiang, and R. Chen, “Hard-Molded 51 cm Long Waveguide Array with a 150 GHz Bandwidth for Board-Level Optical Interconnects,” *Opt. Lett.*, vol. 32, no. 6, pp. 677–679, 2007.
 - [8] T. Kosugi and T. Ishigure, “Polymer Parallel Optical Waveguide with Graded-Index Rectangular Cores and Its Dispersion Analysis,” *Opt. Exp.*, vol. 17, no. 18, pp. 15959–15968, 2009.
 - [9] J. V. DeGroot, Jr., “Cost-Effective Optical Waveguide Components for Printed Circuit Applications,” *Proc. SPIE*, vol. 6781, no. 2007, pp. 678116–1–678116–12, 2007.
 - [10] N. Bamiedakis, J. Chen, R. V. Penty, and I. H. White, “Bandwidth Studies on Multimode Polymer Waveguides for ≥ 25 Gb/s Optical Interconnects,” *IEEE Photon. Technol. Lett.*, vol. 26, no. 20, pp. 2004–2007, 2014.
 - [11] N. Bamiedakis, J. Beals, R. V. Penty, I. H. White, J. V. DeGroot, and T. V. Clapp, “Cost-effective Multimode Polymer Waveguides for High-speed On-board Optical Interconnects,” *IEEE J. Quantum Electron.*, vol. 45, no. 4, pp. 415–424, 2009.
 - [12] N. Bamiedakis, J. Chen, P. Westbergh, J. S. Gustavsson, A. Larsson, R. V. Penty, and I. H. White, “40 Gb/s Data Transmission Over a 1 m Long Multimode Polymer Spiral Waveguide for Board-Level Optical Interconnects,” *J. Light. Technol.*, vol. 33, no. 4, pp. 882–888, 2015.
 - [13] L. Raddatz, I. White, D. G. Cunningham, and M. C. Nowell, “An Experimental and Theoretical Study of the Offset Launch Technique for the Enhancement of the Bandwidth of Multimode Fiber Links,” *J. Light. Technol.*, vol. 16, no. 3, pp. 324–331, 1998.
 - [14] “Coherent, Inc.” [Online]. Available: <http://www.coherent.com/products/?1557/Chameleon-Family>.
 - [15] “TOPTICA.” [Online]. Available: http://www.toptica.com/products/ultrafast_fiber_lasers/femtofiber_pro.html.
 - [16] “MSHG1550-0.5-xx - Covesion Ltd.” [Online]. Available: www.covesion.com/assets/downloads/MSHG1550-0.5.pdf.
 - [17] L. Huang, S. P. Chong, A. Mills, D. Jones, and S. Tang, “Multiphoton Microscopy using Frequency-Doubled Compact Femtosecond Erbium-Doped Fiber Laser,” *Proc. SPIE*, vol. 8948, pp. 894826–1–6, 2014.
 - [18] K. Moutzouris, F. Sotier, F. Adler, and A. Leitenstorfer, “Highly Efficient Second, Third and Fourth Harmonic Generation From a Two- Branch Femtosecond Erbium Fiber Source,” *Opt.*

- Exp.*, vol. 14, no. 5, pp. 1905–12, 2006.
- [19] G. D. Boyd and D. a. Kleinman, “Parametric Interaction of Focused Gaussian Light Beams,” *J. Appl. Phys.*, vol. 39, no. 8, pp. 3597–3639, 1968.
- [20] “FR-103MN Autocorrelator Instruction Manual.”
- [21] J.-C. M. Diels, J. J. Fontaine, I. C. McMichael, and F. Simoni, “Control and Measurement of Ultrashort Pulse Shapes (in Amplitude and Phase) With Femtosecond Accuracy,” *Appl. Opt.*, vol. 24, no. 9, pp. 1270–1282, 1985.
- [22] P. Vasil’ev, *Ultrafast Diode Lasers: Fundamentals and Applications*. Artech House, 1995.
- [23] J. Chen, N. Bamiedakis, P. Vasil’ev, T. Edwards, C. Brown, R. Penty, and I. White, “High-Bandwidth and Large Coupling Tolerance Graded-Index Multimode Polymer Waveguides for On-board High-Speed Optical Interconnects,” *J. Light. Technol.*, vol. 34, no. 12, pp. 2934–2940, 2015.
- [24] K. I. White, “Practical Application of The Refracted Near-Field Technique for The Measurement of Optical Fibre Refractive Index Profiles,” *Opt. Quantum Electron.*, vol. 11, no. 19 79, pp. 185–196, 1978.
- [25] D. G. Cunningham and W.G. Lane, *Gigabit Ethernet Networking*. Macmillan technology series, 1999.
- [26] P. Pepeljugoski, S. Golowich, A. J. Ritger, P. Kolesar, and A. Risteski, “Modeling and Simulation of Next-Generation Multimode Fiber Links,” *J. Light. Technol.*, vol. 21, no. 5, pp. 1242–1255, 2003.
- [27] H. S. Mackenzie, “Evanescent Field Devices For Non-Linear Optical Applications,” University of Cambridge, 1987.

5 EFFECTS OF REFRACTIVE INDEX PROFILES ON WAVEGUIDE PERFORMANCE

This chapter examines the effects of refractive index profiles on the performance of passive waveguide components (e.g. bends, crossings, etc.) needed in the design of an optical backplane. The design and characterisation of these fundamental elements are introduced and experimental results such as loss and bandwidth performance are reported and discussed. The results indicate that low-loss and high-bandwidth (>47 GHz \times m) multimode polymer waveguide bends (<1 dB) and crossings (<0.02 dB/crossing) can be achieved using appropriate refractive index engineering, demonstrating the strong potential of this technology for high-performance board-level optical interconnects with high routing flexibility.

5.1 Introduction

The combination of refractive index engineering and launch conditioning has been shown to improve the bandwidth performance of the multimode polymer waveguides in Chapter 4. This chapter further investigates the effects of refractive index (RI) profiles on the performance of passive waveguide components such as bends and crossings. In Chapter 2, a wide range of optical coupling methods to launch light onto and receive light from the backplane has been described. It has been noted that much work has been done on the

demonstration of coupling schemes. In this work therefore, a focus is maintained on the waveguide components. The increasing interest of using multimode polymer waveguides in passive optical backplanes brings forward the need of high-performance passive waveguide components that can provide a cost-effective solution in achieving high-speed interconnection between electrical cards in blade servers and data storage systems. In particular, waveguides crossing through each other or having paths that change direction are inevitably required for optical backplane structures that seek to interconnect more than a few cards in blade servers. Examples of waveguide crossing techniques that have been proposed include the use of multiple optical layers [1] or mode-coupled waveguides [2] as shown in Figure 5-1(a) and (b). However, these out-of-plane structures inevitably introduce significant fabrication complexity. Hence, 2-D planar waveguide crossings are preferred in polymer backplane architecture as they can be readily patterned as seen in Figure 5-1(c). In addition, there are normally two approaches of forming on-board turns: bends and mirrors (Figure 5-2). Although mirrors may need a smaller board-area footprint and can potentially have lower losses, they typically require additional fabrication procedures and are vulnerable to sidewall roughness issues [3]. 90° waveguide bends have the advantages of simplicity from the fabrication point of view and enable interconnection by curved paths. Thus, 90° bent waveguides are mainly discussed here.

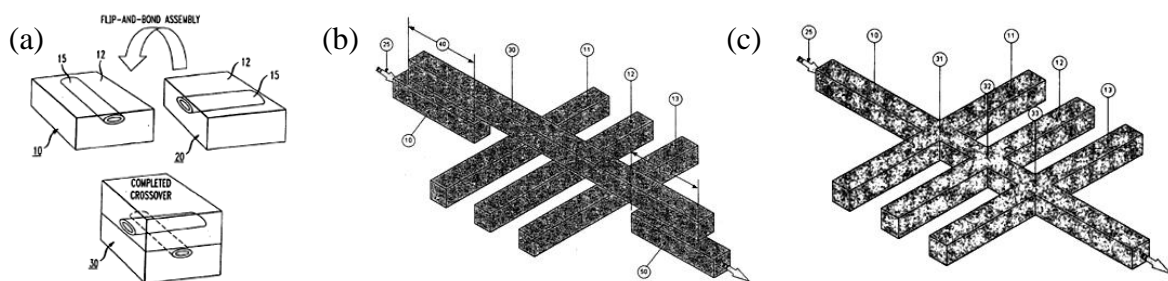


Figure 5-1 Example techniques for waveguide crossings: (a) multiple waveguide layers with flip-chip bonded [1], (b) multiple waveguide layers with directional coupler and (c) single waveguide layer [2].

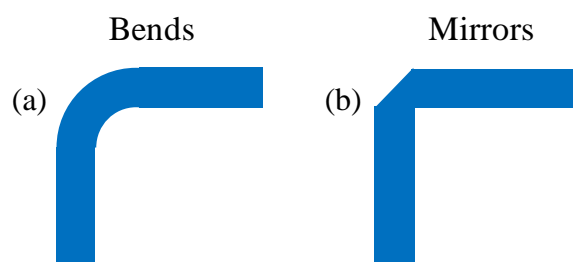


Figure 5-2 Schematics of the (a) 90° waveguide bends and (b) 90° waveguide mirrors.

These on-board passive waveguide components have significant advantages as they can enable non-blocking interconnection architectures and complex waveguide layouts such as a shuffle-style architecture [4]. Such a backplane is considered an appealing interconnection architecture by leveraging readily available components such as arrays of VCSELs and PDs as well as ribbon fibres discussed in Chapter 2. A shuffle scheme does not suffer from the power loss due to fan-out typically encountered in optical bus architectures [5] and transmitters with the same fixed wavelength can be used in contrast to multi-wavelength architectures [6], [7]. Furthermore, it allows any card to simultaneously operate multiple transmitters and therefore is strictly non-blocking. Figure 5-3(a) illustrates the shuffle interconnection architecture using arrays of transmitters and receivers at each node and a single waveguide for each possible link, while it is reconfigured allowing for the basic waveguide design elements (90° bends and crossings) for the formation of a planar shuffle backplane architecture as illustrated in Figure 5-3(b). For example, the 1-Tb/s aggregate-capacity 10-card optical backplane presented in [8] features ~ 1800 90° waveguide crossings and 100 90° waveguide bends.

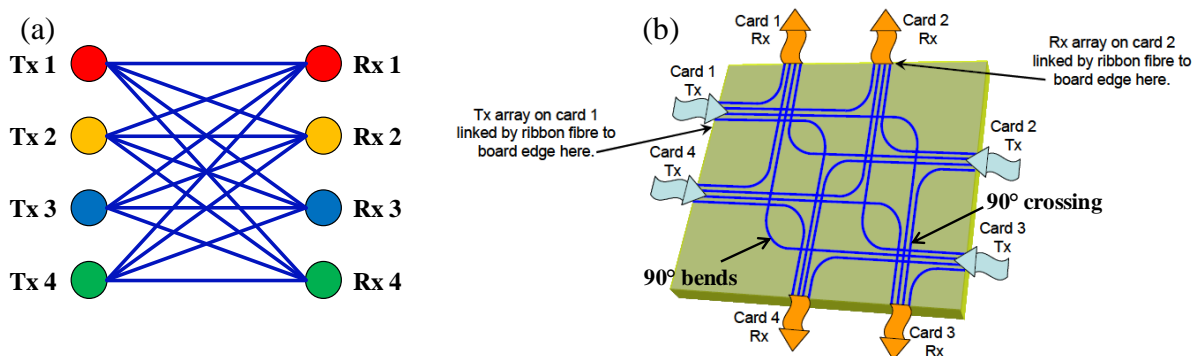


Figure 5-3 Schematic of shuffle interconnections: (a) basic shuffle interconnection concept and (b) reconfigured to utilise the basic elements (90° bends and crossings) required for complex backplane topologies [8].

However, the requirement for different high-performance components on an optical backplane may differ, and the design parameters (e.g. waveguide dimension, RI difference Δn and RI profile) of the devices depend on the specifications used in the backplane design. For instance, the two elementary waveguide components (e.g. bends and crossings) exhibit differing behaviour with respect to the waveguide RI difference Δn . Waveguide bends benefit from strong optical confinement at higher Δn , whereas waveguide crossings exhibit lower

loss for smaller Δn values due to the lower probability of being radiated away along the structure length owing to shallower ray angles [9].

In this chapter therefore, the goal is to make a full assessment of basic waveguide design elements that form the backplane and to understand how the engineering of refractive index profiles can influence the performance of these components. The design, fabrication and characterisation of a variety of multimode waveguide components are presented, including reference waveguides, spiral waveguides, 90° waveguide bends and 90°/45° waveguide crossings. The loss and bandwidth performance on these waveguides with different RI profiles are investigated under different launch conditions. Section 5.2 first presents the waveguide samples with different RI profiles employed in the studies. Section 5.3 then describes the experimental setups employed in the power transmission and dispersion measurements. Section 5.4 provides an overview of the theoretical approaches of calculating bending loss of multimode waveguides and presents the experimental results of the bending loss versus radius of curvature. Section 5.5 briefly introduces the theoretical method of calculating the waveguide crossing loss based on ray tracing technique and presents the power transmission studies of the waveguide crossings. Section 5.6 presents the bandwidth measurements of the waveguide components and discusses the effects of the bending and crossing structures on the bandwidth performance of the guides. Finally, section 5.7 summarises the results obtained and highlights the important conclusions from the work.

5.2 Multimode Polymer Waveguide Components

Three waveguide samples with different RI profiles are fabricated from siloxane materials provided by Dow Corning (core: Dow Corning WG-1020 Optical Waveguide Core and cladding: XX-1023 Optical Waveguide Clad) using standard photolithography processes. Each waveguide sample, denoted as WG01, WG02, and WG03, has various waveguide components fabricated on 8-inch silicon substrates (UV mask design is illustrated in the Appendix):

- Waveguides with four 90° bends, two of which have constant radius (17 mm) while the other two have a varying radius of 5, 6, 8, 11, 15 and 20 mm;
- Waveguides with a variable number of 90° and 45° crossings with number of crossings of 1, 5, 10, 20, 40 and 80;

- 16.25 cm long reference waveguides which include two 90° bends and one long 180° bend;
- 94.6 cm long spiral waveguides.

It should be noted that the characterisation of the components have been carried out by the author while the waveguide samples have been designed and fabricated by Dow Corning. Figure 5-4 illustrates the schematics of various waveguide components employed in the studies while Figure 5-5 shows the photographs of respective components illuminated with a red laser source. The RI profiles of the particular siloxane waveguides used in this work can be readily adjusted by slightly changing their fabrication parameters [10]. Figure 5-6 presents the measured refractive index profiles of the 3 waveguide samples using refractive near field method [11] while Table 5-1 summaries their characteristics (i.e., size and index values of core and cladding). As can be seen in Table 5-1, WG02 has the largest width of $\sim 50 \mu\text{m}$ and smallest index step difference (the difference between the minimum and maximum index) $\Delta n \sim 0.01$, while WG01 and WG03 have similar width of $\sim 30 \mu\text{m}$ and index difference $\Delta n \sim 0.02$. It can also be noted in Figure 5-6 that the higher RI region is located toward the bottom of the core for WG02, whereas the higher RI region lies in the upper side of the core for both WG01 and WG03.

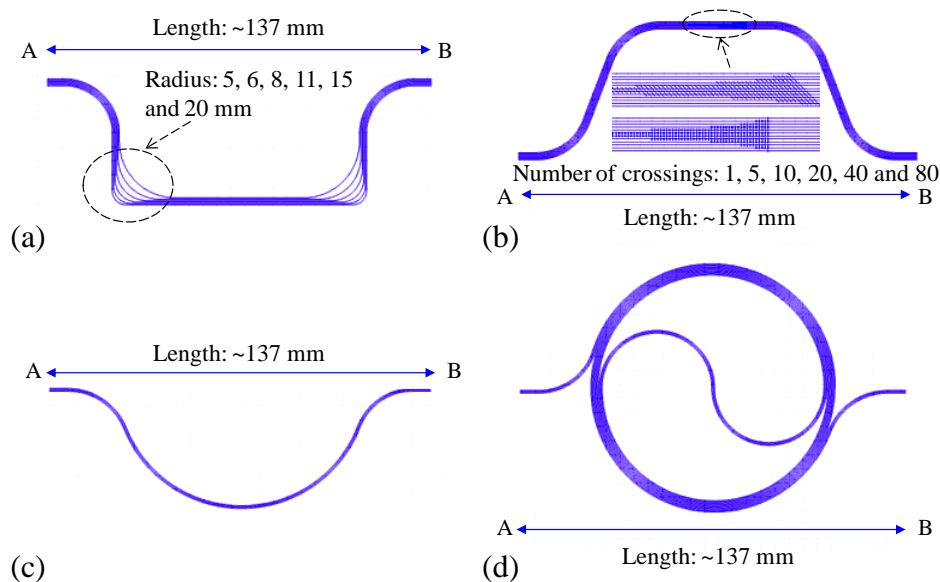


Figure 5-4 Schematics of the waveguide components used for the refractive index studies: (a) 90° waveguide bends, (b) 90° and 45° waveguide crossings, (c) reference waveguides and (d) spiral waveguides.

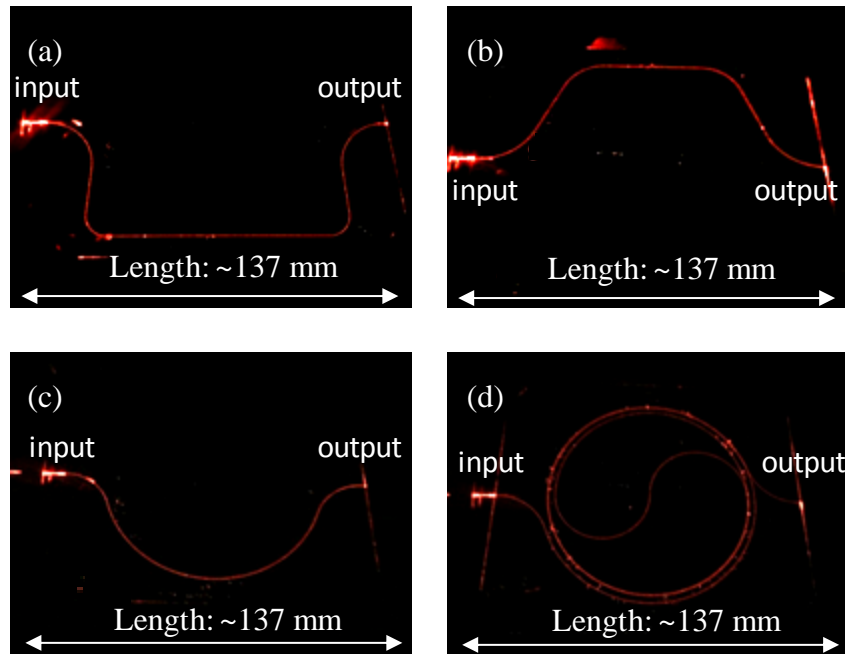


Figure 5-5 Photographs of (a) 90° waveguide bend ($R = 8$ mm), (b) 90° waveguide crossing (single crossing), (c) reference waveguide and (d) spiral waveguide illuminated with red light.

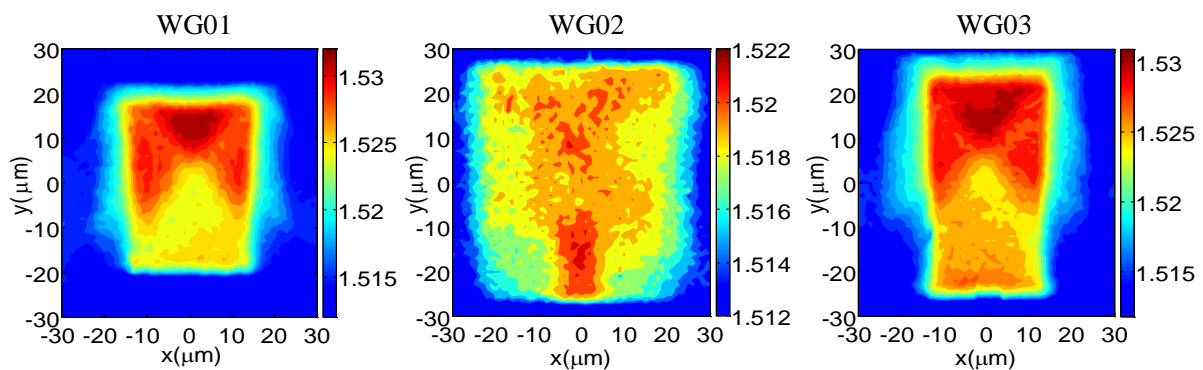


Figure 5-6 Measured RI profile of the 3 waveguide samples at 678 nm.

Table 5-1 Summary of the characteristics of 3 waveguide samples at 678 nm.

	WG01	WG02	WG03
n_{\max}	1.532	1.522	1.531
n_{cladding}	1.512	1.512	1.512
Core height (μm)	37	53	48
Core width (μm)	32	50	29

5.3 Experimental Setups

5.3.1 Power Transmission Studies

A number of measurements have been conducted on these polymer multimode waveguide components under different launch conditions. Figure 5-7 illustrates the experimental setup used in the power transmission measurements. A multimode 850 nm VCSEL is used as the light source, while a pair of microscope objectives [20× microscope objective (NA = 0.4) and 10× microscope objective (NA = 0.25)] is employed to couple the light into a fibre patchcord in order to obtain a high coupling efficiency. Three different types of fibres are employed at the waveguide input to generate different launch conditions, including: (i) a 9/125 μm SMF input, (ii) a 50/125 μm GI MMF input (NA = 0.2), and (iii) a 100/140 μm GI MMF input (NA = 0.29) used with a mode mixer (MM: Newport FM-1). The three different inputs employed provide launch conditions at the waveguide input ranging from a restricted launch to a more overfilled launch. The SMF launch excites the smallest number of modes, while the 100/140 μm MMF with the use of a MM offers the most overfilled launch condition producing a “worst-case” launch condition. The 50/125 μm MMF input provides a “medium” launch condition exciting a larger number of modes than the 9/125 μm SMF input and less than the 100/140 μm MMF launch corresponding therefore, to a relatively realistic launch condition that could be encountered in a real-world system.

The cleaved end of the input fibre is butt-coupled with the waveguide input facet while a 16× microscope objective (NA = 0.32) is used to collect the transmitted light at the waveguide output and deliver it to a large area optical power meter (HP 81525A). The 16× lens is chosen as its NA is larger than that of the waveguide, preventing any mode selective loss. For each measurement, the position of the input fibre is adjusted with a precision translation stage to maximise the power transmission through the waveguide components under test.

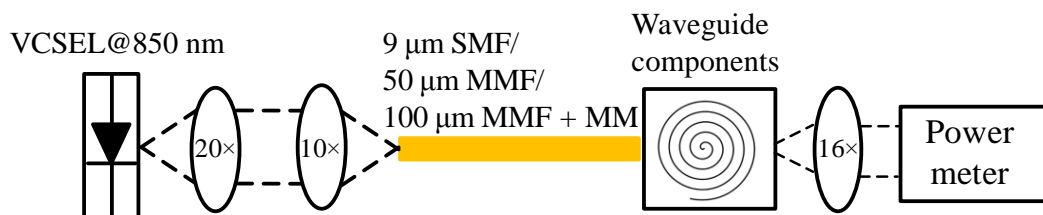


Figure 5-7 Experimental setup of the power transmission measurements.

Figure 5-8 depicts the far field intensities and the corresponding near field images of the cleaved end for the employed input types. The -13 dB intensity points (5% intensity value) in the far field plots indicate the NA of each employed input and are found to be: 0.13, 0.18 and 0.26 for the 9/125 μm SMF, 50/125 μm MMF and 100/140 μm MMF input respectively (see Table 5-2). It should be noted that the 9/125 μm SMF is not strictly single-moded at 850 nm and supports a small number of modes which can be seen in Figure 5-8(a) and Figure 5-8(b).

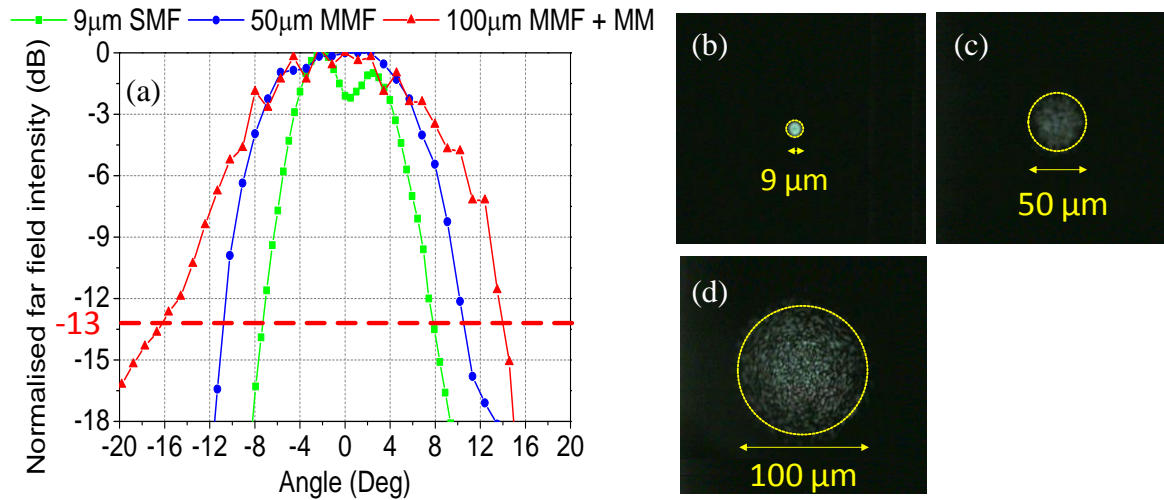


Figure 5-8 Far field intensity of different launch conditions: (a) a 9/125 μm SMF, a 50/125 μm MMF and a 100/140 μm MMF + MM; and near field images of input fibre for different launch conditions: (b) a 9/125 μm SMF, (c) 50/125 μm MMF and (d) 100/140 μm MMF + MM.

Table 5-2 Far field NA (5% intensity) of the various input fibres employed in the power transmission experiments.

Launch condition	5% intensity angle (-13 dB)	Far field NA (-13 dB)
9 μm SMF	7.5°	0.13
50 μm MMF	10.6°	0.18
100 μm MMF + MM	15°	0.26

5.3.2 Dispersion Studies

Time-domain measurements utilising the short pulse generation system 2 ($\lambda = \sim 787$ nm) mentioned in section 4.3.1 in Chapter 4 are conducted to examine the bandwidth performance of various waveguide components with different RI profiles under different launch

conditions. Figure 5-9 illustrates the experimental set-ups for the pulse broadening measurements. The short pulses are coupled into the waveguide components via a 10× microscope objective (NA = 0.25), a 50/125 μm MMF or a 100/140 μm MMF + a MM which approximates the launches used in the power transmission studies for direct comparisons between the loss and bandwidth performance of the waveguide samples. The near field images of the input for each launch condition studied are shown in Figure 5-10. The 10× microscope objective launch provides a restricted launch condition resulting in a Gaussian input with a spot size of $5 \pm 1 \mu\text{m}$ (FWHM). A 16× microscope objective (NA = 0.32) is used to collect the output light and deliver it to a matching autocorrelator as described in section 4.3.2 in Chapter 4 so as to detect the transmitted optical pulses.

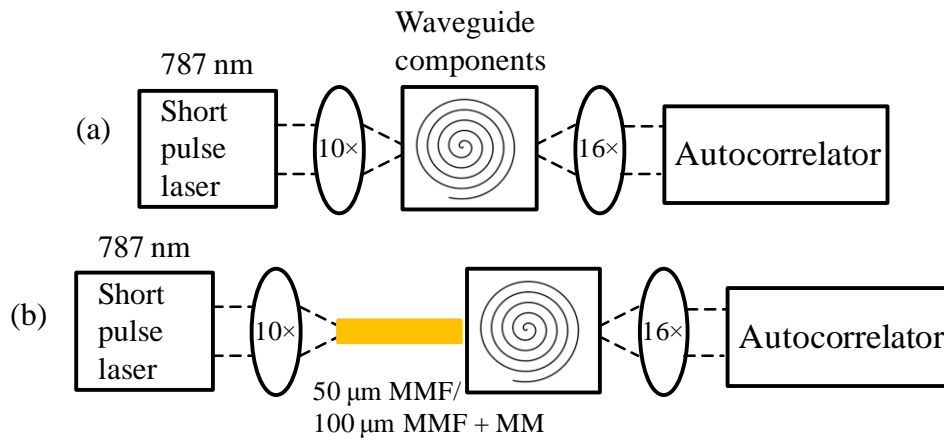


Figure 5-9 Experimental setups for short pulse measurement: (a) 10× microscope objective launch and (b) 50/125 μm or 100 μm + MM launch.

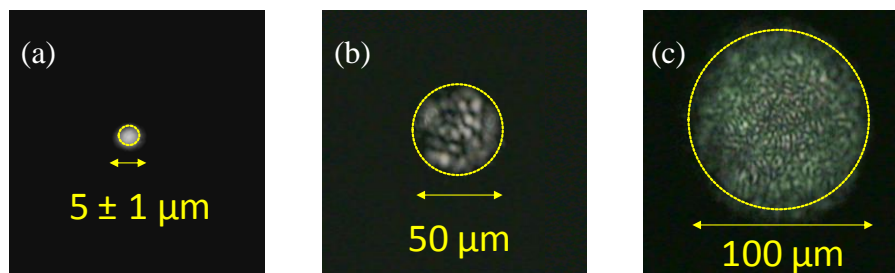


Figure 5-10 Near field images of the inputs for different launch conditions: (a) 10× microscope objective, (b) a 50/125 μm MMF and (c) a 100/140 μm MMF + MM.

5.4 90° Bent Waveguides

The use of bent waveguides can result in extra power loss in a system application. Therefore, it is important to design low-loss waveguide bends, which requires the modelling

of the transmission characteristics of the bent waveguides. There has been much interest on the studies of optical waveguide bends, and the understanding of the behaviour of these waveguide bends is not trivial. It has been known that two types of losses contribute to the loss induced in the bends: radiation loss and transition loss. It can be shown that all waveguide modes propagating in bent structures are “leaky” from a ray analysis as curved path of the waveguide bend geometry cannot guide electromagnetic energy without losing power [9], [12]. The total radiation loss depends on various factors such as waveguide dimension, the radius of curvature and index step difference. The radiation loss decreases as the light confinement in the guide and the radius of curvature increases. In addition, the transition loss occurs at the interface of the bent and straight waveguides. This is due to the mismatch of the supported mode profiles in the two waveguide structures as different waveguide sections have different electromagnetic solutions for the supported modes. The mode profiles of the curved waveguides are known to be offset towards the outer edge of the structure which differs from the mode profiles of the straight waveguides [9]. In [13], it is shown that the transition loss becomes dominant component for small radii.

There has been much study on the theoretical modelling approaches of calculating the loss mechanisms of these bent waveguides, and the modelling of multimode bending loss is particularly challenging. Different theoretical approaches have been proposed, including the effective index method (EIM), finite element method (FEM), beam propagation method (BPM) and ray tracing [13]–[18]. The bending losses can be accurately estimated using the 2-D equivalent method and numerical methods; however these methods have been mainly used for single mode structures as they require intensive computational power. The BPM simulation is more computationally efficient but it is a less accurate approach. Many researchers have used this method to analyse a 90° waveguide bend by dividing the waveguide bend into a series of short radial sectors within which a paraxial approximation may be valid [13]. However, in practice, the ray tracing technique is a more straightforward modelling method for highly multimoded structures (i.e. the dimension of the waveguide is considerably larger than the wavelength of the guided light). While the ray tracing model has been widely used for studying rectangular planar waveguides, tuning of the model parameters is typically required by comparing the simulation and experimental results as the model strongly depends on the input mode distribution. It should be noted that various theoretical models tend to fail increasingly to match the experimental results when the bend radius

decreases to a certain value while maintaining a good agreement with the experimental values for bends with large radius (greater than approximately 10 mm) [18], [19].

5.4.1 Theoretical Approach

Ray optics can provide a straightforward qualitative understanding of the light propagation inside the bends and derive a relationship between the physical parameters and the bending loss. Based on the 2-D geometric optics, the attenuation of every ray propagating around a waveguide bend can be calculated [17]. The power loss of each ray can be obtained using the power transmission coefficients T_i (i.e. the fraction of the incident ray power lost by reflection) of each reflection on the waveguide walls. In Figure 5-11(a), θ_i and θ'_i corresponds to the incident angle of each reflection at the outer and inner wall respectively. When the θ angle is low, the rays will experience reflections with smaller angles which results in less power loss as they propagate along the bend. Rays with larger angle θ suffer from higher loss due to the increasing attenuation coefficients and number of incident reflections on the wall. It is worth mentioning radiation caustic here to help understand the way different waveguide parameters affect the bending loss. In order to make sure that the phase velocity of the mode does not exceed the speed of light in the bulk material, the field that lies beyond a certain radius value is lost in the form of radiation. This radius is called radiation caustic at which the phase velocity increases beyond that of the guided mode as the mode accelerates around the bend as depicted in Figure 5-11(b) [20]. The smaller the radiation caustic is, the larger the radiation loss of the bend becomes.

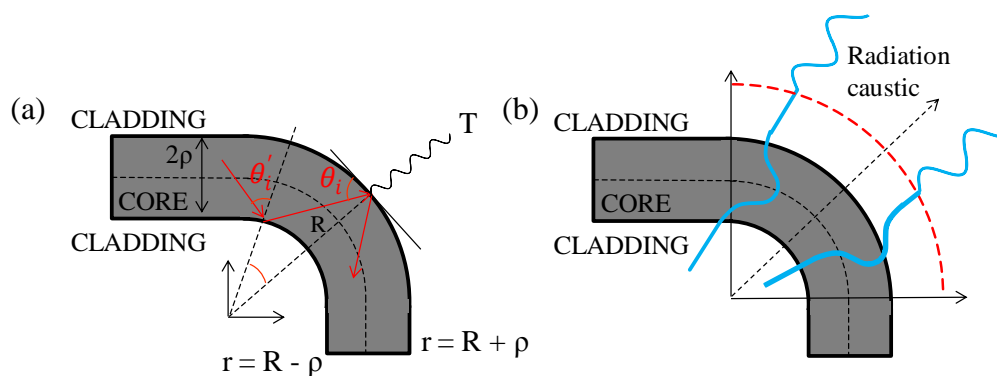


Figure 5-11 (a) Geometry of a waveguide bend and a typical ray in the core of a bent step-index guide and (b) illustrations of radiation caustic (red dashes), constant phase (dotted black arrow) and mode profile of the lowest order mode (blue).

The radiation caustic for a step-index planar waveguide bend is defined as Equation (5-1), which shows the effects of different waveguide parameters such as waveguide dimension, radius of curvature and index difference [9].

$$r_{rad} \approx R \cdot \left(\frac{n_{co}}{n_{cl}} \right) \cos \theta; \quad \cos \theta > (R - \rho) / (R + \rho) \quad (5-1)$$

where r_{rad} is the radius of the radiation caustic, R is the radius of curvature (to the centre of the waveguide width), ρ is the half width of the waveguide and θ is the incident angle between the ray and outer wall of the waveguide. It is known that the radiation loss decreases when the radiation caustic increases. Hence, by increasing the radius of curvature and the index difference between the core and the cladding, the radiation caustic increases resulting in a lower bending loss. In addition, Equation (5-1) indicates that larger θ (higher-order modes) suffer greater radiation loss than the smaller θ (lower-order modes). In theory, low-loss waveguide bends can be designed by altering these parameters.

Israel et al. [18], [19] derived an analytical expression for the power transmitted through a waveguide bend using ray optics concepts given as below:

$$T = 10 \cdot \log_{10} \left(1 - \frac{1}{2R} - \frac{t^2}{2R^2} - \frac{t^3}{2R^3} - \frac{t^4}{2R^4} \right) \quad (5-2)$$

where $t = (n_{co}^2 w) / (NA)^2$, w is the width of the waveguide and NA is the numerical aperture. It has been shown that this model can describe the experimental results adequately although it fails when $t / R > 0.5$. Figure 5-12(a) plots the bending loss of a 50 μm wide 90° waveguide bend with varying index steps between 0.015 and 0.03 while Figure 5-12(b) shows the loss of 90° waveguide bend with step index $\Delta n = 0.02$ for different waveguide widths from 20 to 50 μm . As expected, lower bending loss can be achieved using waveguide bends with larger index step and smaller waveguide width for bends with small radii.

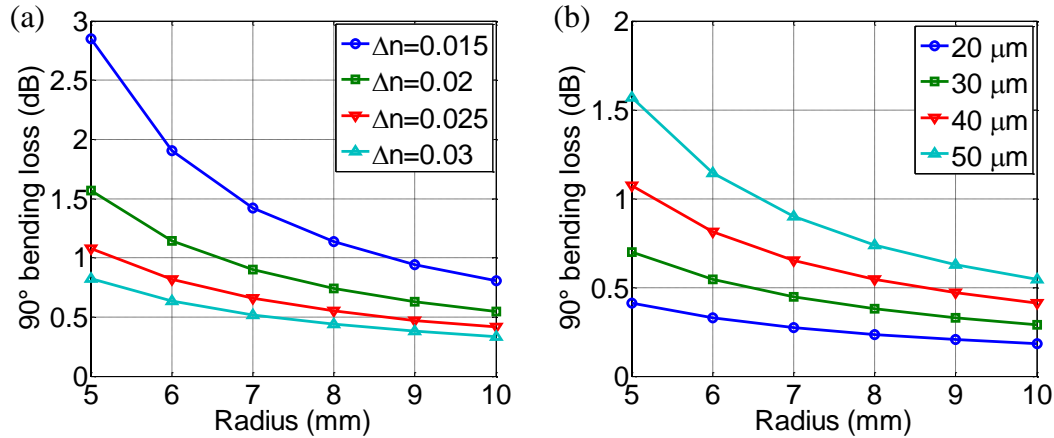


Figure 5-12 (a) Induced loss for a 90° waveguide bend with width of 50 μm for different index steps Δn and (b) induced loss for a 90° waveguide bend with step index $\Delta n = 0.02$ for different waveguide widths.

5.4.2 Experimental Results

Figure 5-13(a) illustrates total insertion loss of the 90° bending loss of 3 waveguides as a function of the bend radius measured under a 9/125 μm SMF, a 50/125 μm MMF and a 100/140 μm MMF + MM respectively. The loss shown in Figure 5-13(b) is normalised with respect to the insertion loss of the bend with the largest radius to compensate for the respective coupling and propagation loss. Table 5-3 summarises the radius needed to achieve bending loss of <1 dB of 3 waveguide samples under different launch conditions. As mentioned earlier, the bending loss depends on the index difference, dimension and input launch condition of the waveguide. As expected, the bending loss increases for decreasing bend radius. The 100/140 μm MMF + MM launch results in the highest bending loss whereas the SMF launch in the lowest as the 100 μm MMF couples larger percentage of optical power onto the higher-order waveguide modes which are more susceptible to radiation loss at the bends. The results also agree with the fact that lower loss can be achieved from waveguide bends which have smaller core size and larger index difference due to the increased mode confinement in the waveguide core. For example, WG02 exhibits the highest bending loss (bending loss of <1 dB for a radius of >10 mm even under the SMF launch) as it has a larger width of ~50 μm and smaller index difference of ~0.01, whereas WG01 and WG03 exhibit smaller losses (bending loss of <1 dB for a radius of >6 mm under both the SMF and 50 μm MMF launch, and >8 mm under the 100 μm MMF launch) due to their smaller width of ~35 μm and larger index difference of ~0.02 (see Table 5-1).

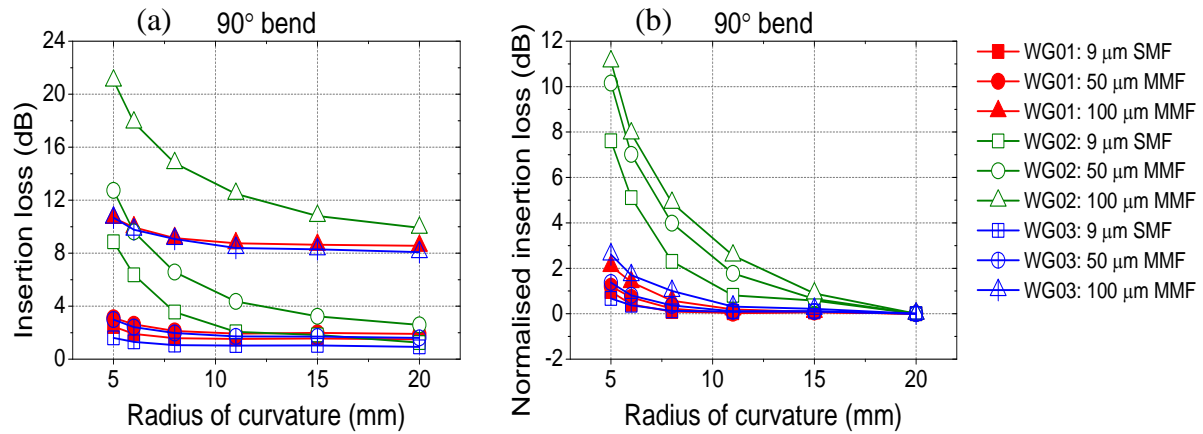


Figure 5-13 (a) Insertion loss of the 90° bends versus bending radius, and (b) normalised bending loss versus bending radius of 3 different waveguides under a 9/125 μm SMF, a 50/125 μm MMF and a 100/140 μm MMF + MM launch.

Table 5-3 The required radius for bending loss below 1 dB of 3 waveguides with different RI profiles under different launch conditions studied.

WG#	9 μm SMF	50 μm MMF	100 μm MMF + MM
WG01	> 6 mm	> 6 mm	> 8 mm
WG02	> 10 mm	> 11 mm	> 15 mm
WG03	> 5 mm	> 6 mm	> 8 mm

5.5 Waveguide Crossings

As discussed in the beginning of the chapter, while the waveguide bend is one crucial element for an optical backplane, the waveguide crossing is another important building block for any interconnection architecture as it can eliminate the need for an additional stacked optical layer, maximise the available on-board area and increase the interconnection density. Therefore, the use of a waveguide crossing in a backplane architecture can simplify the manufacturing process as the fabrication complexity typically encountered in the out-of-plane structures can be eliminated. However, these components need to exhibit low loss so as to meet the stringent power budget requirements for the applications of on-board interconnection architectures [21].

5.5.1 Theoretical Approach

Some studies on waveguide intersections have been reported in the literature; however most of the work focuses on single mode waveguides [22]–[24]. Theoretical approaches that have been commonly used to analyse the light propagation in the waveguide crossings include: (i) free-space expansion of the fundamental mode in the waveguide junction [23], (ii) the BPM [25] and (iii) ray tracing methods [26]. It has been shown that the waveguide crossing losses can be minimised by increasing the width of the waveguide and deploying larger crossing angles (e.g. 90° waveguide crossings) [27].

The electromagnetic method of computing the crossing loss is to calculate the input field expansion in the crossing region and then estimate the power coupled into the waveguide by using the overlap integral between the input field profile and the waveguide modes at the interface B depicted in Figure 5-14(a). However, the Gaussian approximation method in [22] cannot be applied for multimode waveguides as each mode will have different spreads at the interface. One possible way is to calculate the diffraction integrals of all guided waveguide modes and subsequently compute the power coupled to the output waveguide. Nevertheless, this approach is time and computation consuming.

Therefore, a more straightforward method of using geometric optics analysis is often preferred for the case of multimode waveguides [26]. The ray tracing model considers all possible rays inside the guides and computes the possibility of rays not being reflected totally at a sidewall (for the case of step-index profiles only). This probability turns out to depend on the spherical angles θ and φ of each ray and the waveguide width W . As illustrated in Figure 5-14(b), θ is the angle between the light beam and optical axis (z axis), and φ is the angle formed between the projection of the light beam on the x - y plane and x axis. For instance, Ray 1 (the ray propagating in the x - z plane when $\varphi = 0^\circ$) can be transmitted through the guide with a probability of 100%, whereas Ray 2 (the ray in the y - z plane when $\varphi = 90^\circ$) has no total internal reflection at the core-cladding interface and has the highest probability of being lost due to the crossings. In addition, the input launch conditions can be expressed using an intensity distribution $f(\theta)$. The total power transmitted through the structure can subsequently be calculated using the probabilities of the rays not lost on the way and the assumed input intensity distribution.

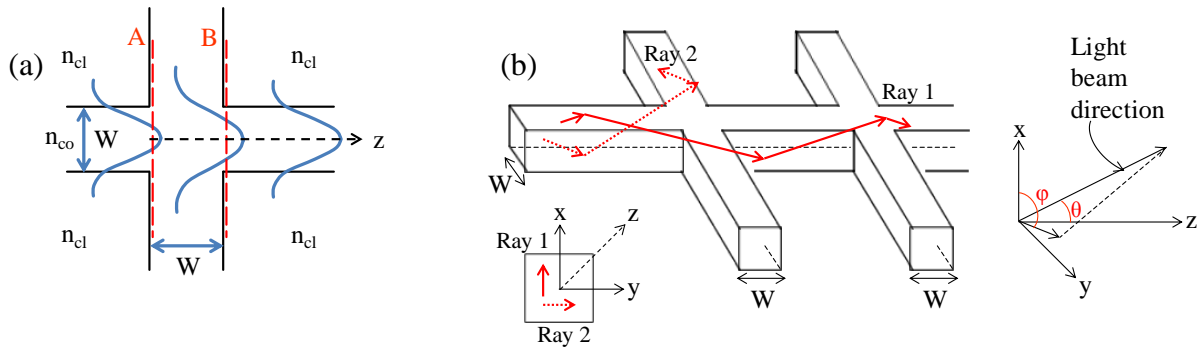


Figure 5-14 Illustration of theoretical modelling methods: (a) electromagnetic approach based on the free-space field expansion and (b) ray tracing technique based on the ray trajectories in the waveguide (Ray 1: solid line, Ray 2: dashed line).

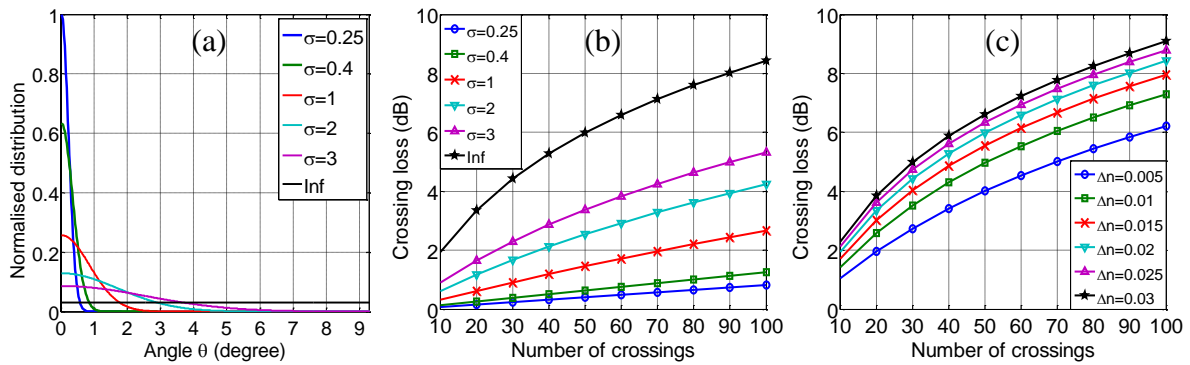


Figure 5-15 (a) Input power distributions used in the ray tracing model, (b) excess loss of waveguide crossings for a 50 μm wide waveguide, $\Delta n = 0.02$ for varying input power distribution and (c) excess loss of waveguide crossings for a 50 μm wide waveguide for varying index different Δn when the input power is “inf”.

The input ray distribution is chosen to be a Gaussian with a variable standard deviation σ . Figure 5-15(b) shows the calculated crossing loss as a function of the number of crossings under different input power distribution as illustrated in Figure 5-15(a) for a waveguide with $w = 50\mu\text{m}$ and $\Delta n = 0.02$, while Figure 5-15(c) shows the crossing loss as a function of the number of crossings under a uniform input power distribution with varying index steps. These results provide a useful insight into the relationship between the excess loss of the waveguide crossings and the number of crossings. A few observations can be made. First, the crossing loss is a mode-selective loss and it strongly depends on the input power distribution. Secondly, the crossing loss does not increase linearly with the number of crossings when the input power becomes more overfilled. This suggests that the higher-order modes are primarily attenuated at the initial stages of the structure. Thirdly, it should be noted that the

crossing loss can be reduced with a smaller index step difference Δn as the propagated rays have shallower θ angle and thus a lower probability of being lost on the way is expected. The ray tracing model provides a useful tool to interpret the experimental results obtained in the next section.

5.5.2 Experimental Results

The insertion loss of the 3 waveguide samples of a varying number of 90° and 45° waveguide crossings (1, 5, 10, 20, 40 and 80) is also measured for the three different launch conditions mentioned in section 5.3.1. Figure 5-16(a) and Figure 5-17(a) show the total insertion loss of the 90° and 45° waveguide crossings respectively under different launch conditions, while Figure 5-16(b) and Figure 5-17(b) present the normalised insertion loss obtained by normalising the insertion loss of each waveguide to the loss of the waveguide with the least number of crossings (i.e. single crossing). Similar behaviour can be observed on the both 90° and 45° waveguide crossings. The only difference is that the losses of 45° waveguide crossings are higher as the light is more likely to leak at the intersection.

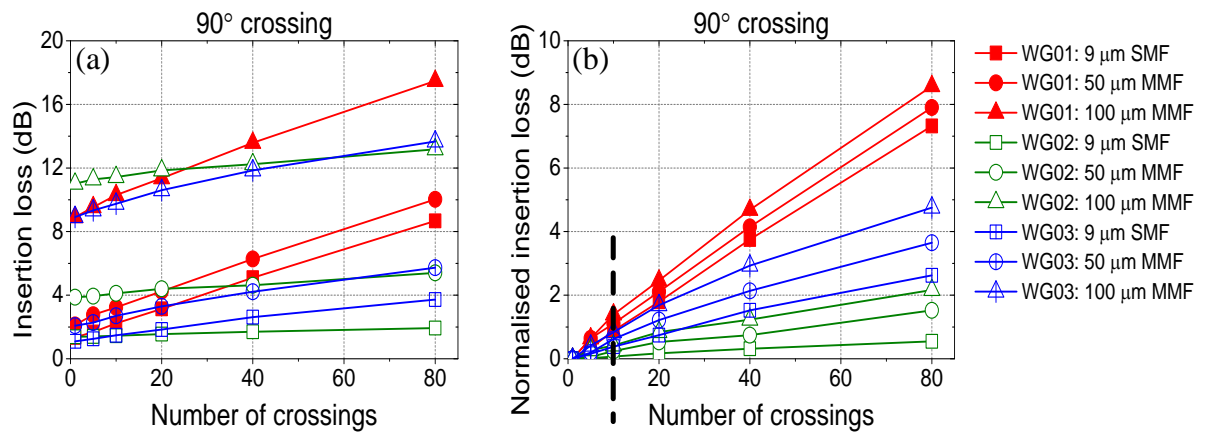


Figure 5-16 (a) Insertion loss of the 90° crossing versus the number of crossings, and (b) normalised insertion loss versus the number of crossings of 3 waveguides under a 9/125 μm SMF, a 50/125 μm MMF and a 100/125 μm MMF + MM launch.

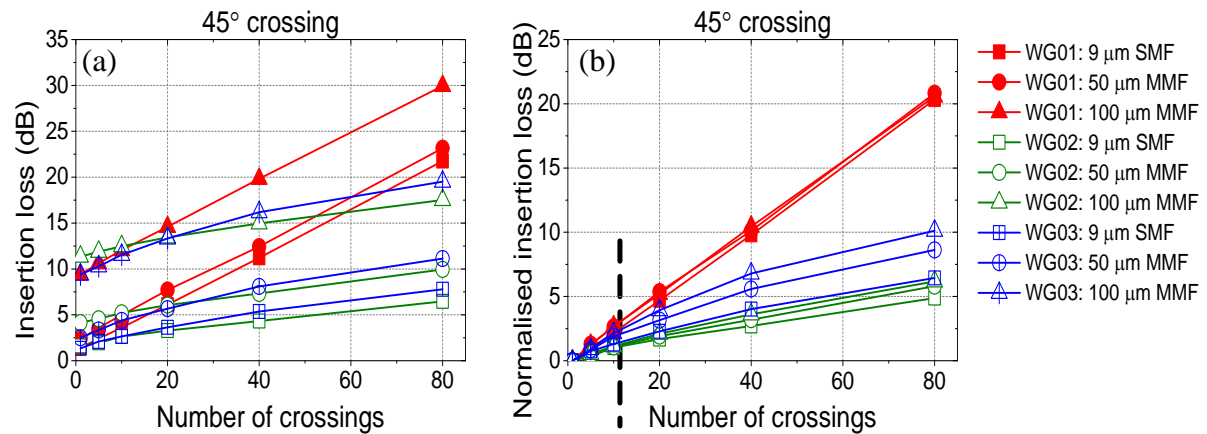


Figure 5-17 (a) Insertion loss of the 45° crossing versus the number of crossings, and (b) normalised insertion loss versus the number of crossings of 3 waveguides under a 9/125 μm SMF, a 50/125 μm MMF and a 100/125 μm MMF + MM launch.

The 100/140 μm MMF + MM launch results in the highest loss as it provides a more “overfilled” launch at the waveguide input, coupling more power into the higher order modes which are more susceptible to crossing losses. As expected and observed before, the crossing loss does not depend linearly on the number of crossings [28]. Higher-order modes exhibit higher crossing loss and are therefore primarily attenuated at the initial crossings closer to the waveguide input, while lower-order modes that exhibit a lower crossing loss coefficient are left to propagate in the remaining crossings. As a result, two different slope approximations that characterise the loss per crossing are extracted for each sample: for 1-10 crossings and for 20-80 crossings (see Figure 5-18, Table 5-4 and Table 5-5). In addition, WG02 and WG01 exhibit the lowest and highest losses per crossing due to their smallest and largest index step difference respectively. It should be noted that WG02 exhibits 90° crossing loss of ~0.02 dB/crossing under a 50/125 μm MMF launch, which is lower than the typical values shown on the traditional SI waveguide crossings (~0.03–0.06 dB/crossing) [26], [27].

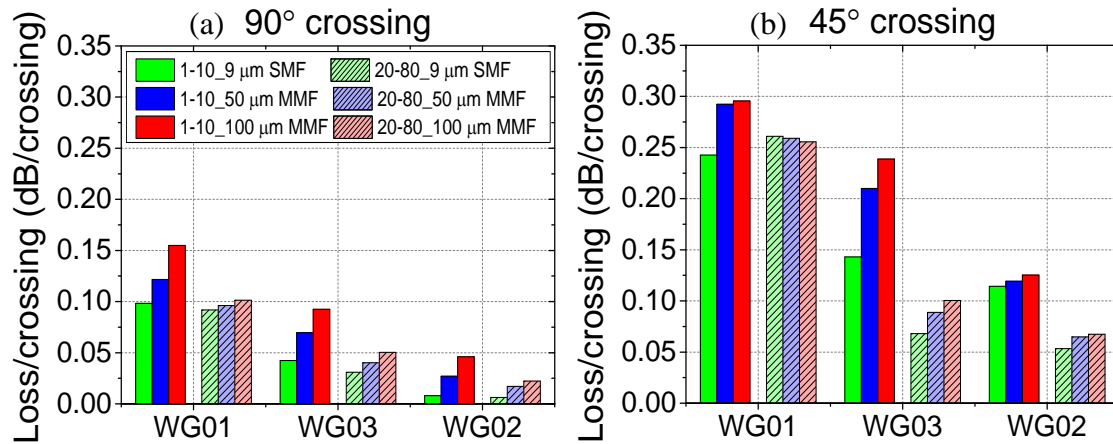


Figure 5-18 Loss/crossing of (a) 90° and (b) 45° degree crossings for 3 waveguides under a 9/125 μm SMF, a 50/125 μm MMF and a 100/140 μm MMF + MM launch.

Table 5-4 Loss per crossing of 90° crossings for 3 waveguides under a 9/125 μm SMF, 50/125 μm MMF and 100/140 μm MMF + MM launch.

Crossing#	9 μm SMF (dB/crossing)		50 μm MMF (dB/crossing)		100 μm MMF + MM (dB/crossing)	
	1-10	20-80	1-10	20-80	1-10	20-80
WG01	0.098	0.092	0.122	0.096	0.155	0.101
WG02	0.008	0.006	0.027	0.017	0.046	0.022
WG03	0.042	0.031	0.070	0.040	0.092	0.050

Table 5-5 Loss per crossing of 45° crossings for 3 waveguides under a 9/125 μm SMF, 50/125 μm MMF and 100/140 μm MMF + MM launch.

Crossing#	9 μm SMF (dB/crossing)		50 μm MMF (dB/crossing)		100 μm MMF + MM (dB/crossing)	
	1-10	20-80	1-10	20-80	1-10	20-80
WG01	0.243	0.261	0.292	0.259	0.296	0.256
WG02	0.114	0.053	0.119	0.065	0.125	0.067
WG03	0.143	0.068	0.210	0.089	0.239	0.100

5.6 Bandwidth Performance

5.6.1 Reference and Spiral Waveguides

Figure 5-19 and Table 5-6 illustrate the insertion losses of the reference and spiral waveguides with 3 different RI profiles under different launch conditions described in section 5.3.2. The values shown are the average values of 6 reference and 6 spiral waveguides on each waveguide sample. The reference waveguides are used as control samples to compare the loss performance of the waveguide components and measure their bandwidth.

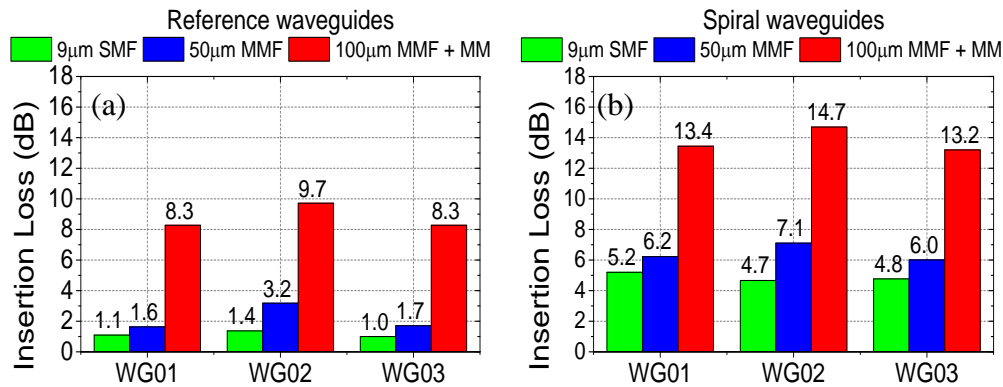


Figure 5-19 Insertion losses of (a) reference waveguides and (b) spiral waveguides under a 9/125 μm SMF, a 50/125 μm MMF and a 100/140 μm MMF + MM launch.

Table 5-6 Insertion losses (dB) of (a) reference waveguides and (b) spiral waveguides under a 9/125 μm SMF, a 50/125 μm MMF and a 100/140 μm MMF + MM launch.

WG#	9 μm SMF (dB)		50/125 μm MMF (dB)		100/140 μm MMF + MM (dB)	
	Reference	Spiral	Reference	Spiral	Reference	Spiral
WG01	1.1	5.2	1.6	6.2	8.3	13.4
WG02	1.4	4.7	3.2	7.1	9.7	14.7
WG03	1.0	4.8	1.7	6.0	8.3	13.2

Figure 5-20 shows the BLPs of the 3 different reference waveguides under a 10 \times microscope objective, a 50/125 μm MMF and a 100/140 μm MMF + MM launch. For all

launches, the input position is chosen so that the insertion loss is minimised. The 10 \times lens launch provides a restricted launch condition resulting, as expected, in the highest bandwidth, whereas the 100/140 μm MMF + MM provides a relatively overfilled launch condition that yields the lowest bandwidth. The 50/125 μm provides a launch condition that lies in between the restricted launch and overfilled launch, which is typically encountered in the real-world application. Under such a launch condition, as can be seen in Figure 5-19 and Figure 5-20, WG02 exhibits the largest insertion loss (~ 1.5 dB higher than that of WG01 and WG03), but also the largest bandwidth ($\sim 2.5\times$ over WG01 and WG03) due to its smaller Δn . A restricted launch input however, results in similar insertion loss values from all samples and high BLP values of >100 GHz \times m due to the low input coupling loss and the excitation of lower-order modes. Moreover, the 100 μm MMF + MM launch couples more power into the higher-order modes inside the input fibre, resulting in the highest insertion loss due to the high coupling loss and high attenuation of the higher-order modes excited inside the waveguides.

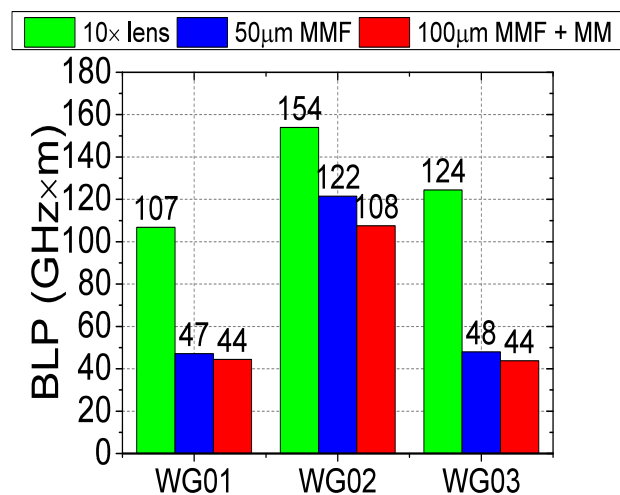


Figure 5-20 Bandwidth-length products of the 3 reference waveguides under a 10 \times microscope objective, a 50/125 μm MMF and a 100/140 μm MMF + MM launch.

Far field measurements are carried out on the reference waveguides to confirm the observations obtained from the bandwidth measurements. Figure 5-21 shows the far field intensity of the 3 reference waveguides in the horizontal direction under the different launch conditions, and Table 5-7 summarises the 5% intensity angle and the respective far-field NA of the 3 reference waveguides under the launch conditions employed. It can be seen that WG02 has the narrowest far field intensity while the WG01 and WG03 have the similar width of far field intensity, confirming the bandwidth measurement results as shown in Figure 5-20.

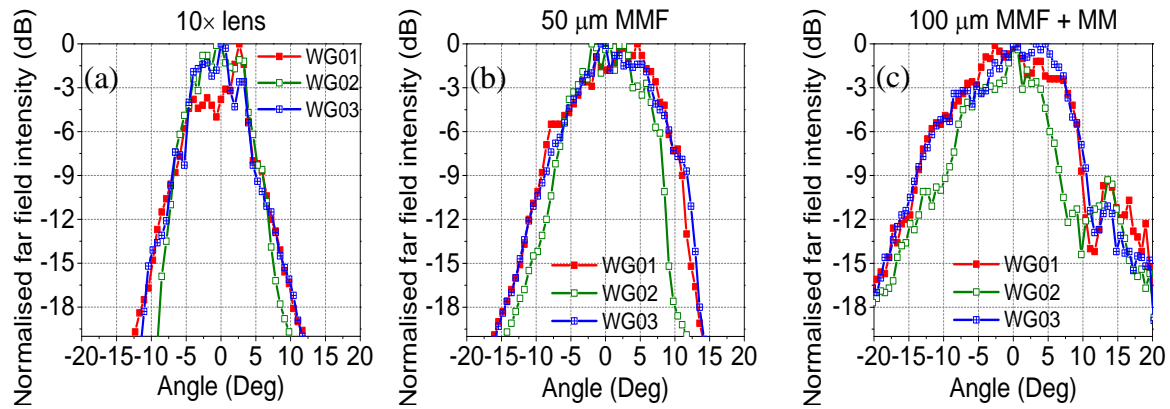


Figure 5-21 Far field intensity of the 3 reference waveguides in the horizontal direction under (a) a 10× microscope objective, (b) a 50/125 μm MMF and (c) a 100/140 μm MMF + MM launch.

Table 5-7 Far field NA (5% intensity) of 3 different waveguides under different launch conditions employed.

WG#	5% intensity angle (-13 dB)			Far field NA (-13 dB)		
	10× lens	50 MMF	100 MMF	10× lens	50 MMF	100 MMF
WG01	8.6°	11.6°	16.6°	0.15	0.20	0.29
WG02	7.4°	9.0°	12.3°	0.13	0.16	0.21
WG03	8.2°	12.1°	15.7°	0.14	0.21	0.27

5.6.2 90° Waveguide Bends and 90° Waveguide Crossings

As indicated in [29], the use of the spiral waveguides for the estimation of the waveguide bandwidth can be beneficial with respect to multimode dispersion as the higher waveguide modes are suppressed along the bends of the structure. In order to confirm this observation, the bandwidth of waveguides with different bending radius is also measured. Figure 5-22(a) shows the measured bandwidth of 90° bends with the different radius of curvature for the 3 waveguide samples with different RI profiles under the 50/125 μm MMF launch. For all 3 waveguides, the bandwidth increases as the bending radius decreases as the light is more likely to be radiated along the bends with smaller radius which can also be seen in Figure

5-13 resulting in the bandwidth increase. These results indicate that the bending structure is beneficial with respect to bandwidth performance increase.

A similar study is carried on the waveguide crossings. The use of larger number of waveguide crossings should improve the bandwidth performance of the waveguide components due to the attenuation of the higher-order modes. Figure 5-22(b) shows the bandwidth of 90° crossings versus the number of crossings under the 50/125 μm MMF launch. The bandwidth increases as the number of crossings increases and finally become saturated, indicating that the increasing number of crossings introduces larger loss on higher-order modes and therefore reduces the induced multimode dispersion. It can be seen that the bandwidth increase is larger for lower number of crossings, matching the non-linear relationship of the crossing loss as observed in Figure 5-16.

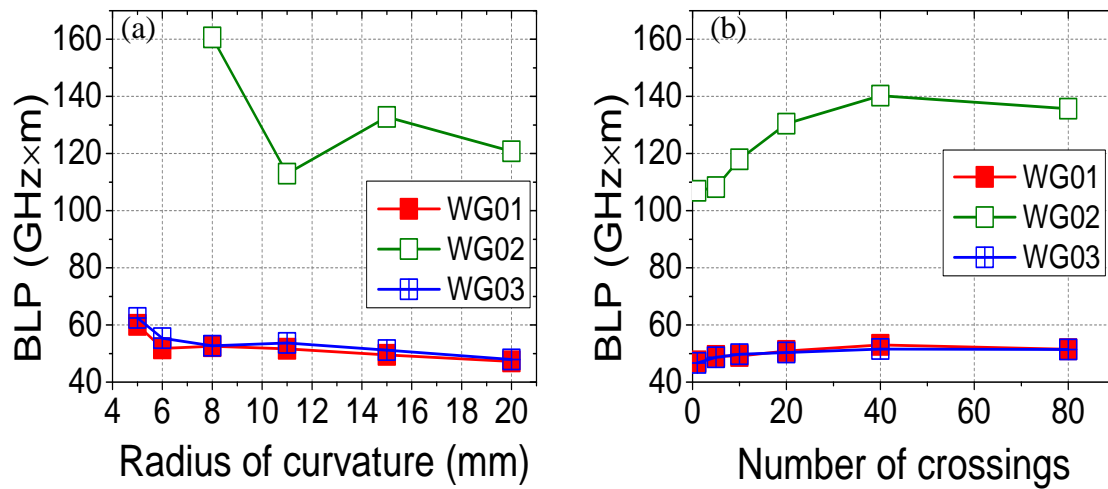


Figure 5-22 Bandwidth-length products of (a) 90° bends versus radius of curvature and (b) 90° crossings versus the number of crossings of 3 waveguides under the 50/125 μm MMF launch.

5.6.3 Discussion

The optimisation of loss and bandwidth becomes particularly important for the design of next-generation optical backplanes. It is clear that launch condition can play a role in optimising the insertion loss and bandwidth performance of passive waveguide components. Moreover, the performance trade-off with respect to the RI profile exists despite the fact that excellent optical transmission properties of the waveguide components are demonstrated. The insertion loss for a certain waveguide component can be minimised by varying the index

difference Δn , while adequate bandwidth is still available in order to enable high-speed operation given the tight power budget requirements in board-level optical links. For instance, reference waveguide WG02 exhibits the highest insertion loss but shows a much higher bandwidth ($\sim 120 \text{ GHz}\times\text{m}$) compared to WG01 and WG03 ($\sim 50 \text{ GHz}\times\text{m}$) owing to its lower Δn for a $50 \text{ }\mu\text{m}$ MMF input.

For waveguide bends, although WG02 exhibits the highest bandwidth, it also shows the highest insertion loss. For WG01 and WG03, their insertion losses are reasonably low while exhibiting adequate bandwidth. For comparison, the BLP values obtained for the respective straight waveguides under the similar launch condition ($50/25 \text{ }\mu\text{m}$ MMF) are also measured to be: WG01 $\sim 39 \text{ GHz}\times\text{m}$, WG03 $\sim 40 \text{ GHz}\times\text{m}$. The insertion loss of two straight waveguides with length from point A to B (Figure 5-4) is estimated to be 1.2 dB and 1.1 dB respectively under the $50/125 \text{ }\mu\text{m}$ MMF. As a result, it is found that a 1.55 times bandwidth improvement ($\text{BLP} > 60 \text{ GHz}\times\text{m}$) over the straight waveguides can be achieved for a bend radius of 5 mm, with a loss penalty of $\sim 1.9 \text{ dB}$. A smaller loss penalty is introduced for slightly larger bends, for example, an 11 mm bend radius ensures a $\text{BLP} > 50 \text{ GHz}\times\text{m}$ with an additional loss of $\sim 0.7 \text{ dB}$.

In addition, the results on the crossing waveguides indicate that a bandwidth enhancement up to 1.25 times can be achieved with a relatively low number of crossings ~ 10 , which corresponds to an additional loss of ~ 2 and 1.6 dB for the samples WG01 and WG03 respectively. It should be noted that the difference in bandwidth and loss performance observed between the straight waveguides and the waveguides with a single crossing is due to the presence of the input/output waveguide bends in the components under study.

Therefore, the results show the potential of increasing the bandwidth performance of these multimode waveguides employing refractive index engineering and waveguide layout (e.g. bend structures and waveguide crossings). Sufficient bandwidth for supporting $> 40 \text{ Gb/s}$ on-board data transmission can be achieved while maintaining low loss transmission characteristics. The results demonstrate the importance of refractive index profiles and intelligent layout in optical backplanes based on this multimode polymer waveguide technology and highlight its potential in board-level optical interconnects.

5.7 Summary

In summary, the studies reported in this chapter present multimode polymer waveguides (reference and spiral waveguides) and fundamental waveguide components (e.g. 90° waveguide bends and 90°/45° waveguide crossings) with different RI profiles. These waveguide elements are the building blocks of any complex on-board interconnection architecture. Measurements of insertion loss and bandwidth performance of these waveguides are conducted under different launch conditions. A theoretical approach using a simple ray tracing technique is introduced as it provides a useful insight of the behaviour of highly multimoded waveguide components. It has been demonstrated that 90° waveguide bends with excess loss below 1 dB for radius larger than 6 mm and 90° crossings with crossing loss less than 0.02 dB/crossing while exhibiting adequate BLP values of larger than 47 GHz×m can be achieved under a 50 µm MMF launch by varying the index differences and waveguide dimensions. In addition, it is shown that the bandwidth performance can be enhanced by utilising bending and crossing structures in the waveguide layout. This study provides an insight on the effects of refractive index engineering on multimode polymer waveguides. It is shown that the choice of refractive index profiles, waveguide dimensions and waveguide layout should be dependent of the requirements of each specific application in order to optimise both the loss and bandwidth performance of these multimode polymer waveguides. It is possible to provide optimised loss performance for a particular waveguide layout while ensuring adequate interconnection bandwidth in the link by employing appropriate refractive index engineering. Overall, the results obtained in this chapter can enable the extraction of useful guidelines for the waveguide fabrication based on the desired waveguide layouts, demonstrating the strong potential of this multimode polymer waveguide technology and their highly flexible structural design for the development of low-loss and high-bandwidth passive optical backplane using refractive index engineering.

5.8 References

- [1] M. D. Feuer and N. J. Frigo, “Method for fabricating optical devices by assembling multiple wafers containing planar optical waveguides,” 2007.
- [2] A. Telkamp and R. Bindrup, “Low-loss optical waveguide crossovers using an out-of-plane waveguide,” 2007.
- [3] R. L. Espinola, R. U. Ahmad, F. Pizzuto, M. J. Steel, and M. Osgood, “A study of high-index-contrast 90 waveguide bend structures,” *Opt. Exp.*, vol. 8, no. 9, pp. 517–528, 2001.
- [4] N. Bamiedakis, A. Hashim, R. V. Penty, and I. H. White, “Regenerative polymeric bus

- architecture for board-level optical interconnects,” *Opt. Exp.*, vol. 20, no. 11, p. 11625, 2012.
- [5] X. Wang and R. T. Chen, “Optical Bus for Intra and Inter-Chip Optical Interconnect,” *LEOS 19th Work. Interconnect. Within High Speed Digit. Syst.*, 2008.
 - [6] A. Wonfor, “Low Cost Blade Server: An Investigation,” 2007.
 - [7] J. Beals, N. Bamiedakis, A. Wonfor, R. V. Penty, and I. H. White, “Polymer Waveguides for Low-Cost Optical Backplanes,” Pittsburgh, PA, USA, 2007.
 - [8] J. Beals, N. Bamiedakis, A. Wonfor, R. V. Penty, I. H. White, J. V. DeGroot, K. Hueston, T. V. Clapp, and M. Glick, “A Terabit Capacity Passive Polymer Optical Backplane Based on a Novel Meshed Waveguide Architecture,” *Appl. Phys. A*, vol. 95, no. 4, pp. 983–988, 2009.
 - [9] A. W. Snyder and J. D. Love, *Optical Waveguide Theory*. Chapman & Hall, 1983.
 - [10] B. W. Swatoski, C. Amb, M. G. Hyer, R. S. John, and W. K. Weidner, “Graded index silicone waveguides for high performance computing,” *IEEE Opt. Interconnects Conf.*, vol. 2, pp. 133–134, 2014.
 - [11] K. I. White, “Practical Application of The Refracted Near-Field Technique for The Measurement of Optical Fibre Refractive Index Profiles,” *Opt. Quantum Electron.*, vol. 11, no. 19 79, pp. 185–196, 1978.
 - [12] F. Ladouceur and J. D. Love, *Silica-based Buried Channel Waveguides and Devices*. Chapman & Hall, 1996.
 - [13] I. Papakonstantinou, K. Wang, D. R. Selviah, and F. A. Fernández, “Transition, Radiation and Propagation Loss in Polymer Multimode Waveguide Bends,” *Opt. Exp.*, vol. 15, no. 2, pp. 669–679, 2007.
 - [14] E. A. J. Marcatilli, “Bends in optical dielectric waveguides,” *Bell Syst. Tech. J.*, vol. 48, pp. 2103–2132, 1969.
 - [15] S. Kim and Anand. Gopinath, “Vector analysis of optical dielectric waveguide bends using finite-difference method,” *J. Light. Technol.*, vol. 14, no. 9, pp. 2085–2092, 1996.
 - [16] V. Subramaniam, G. N. De Brabander, D. H. Naghschi, and J. T. Boyd, “Measurement of mode field profiles and bending and transition losses in curved optical channel waveguides,” *J. Light. Technol.*, vol. 15, no. 6, pp. 990–997, 1997.
 - [17] C. Winkler, J. D. Love, and A. K. Ghatak, “Loss calculations in bent multimode optical waveguides,” *Opt. Quantum Electron.*, vol. 11, pp. 173–183, 1979.
 - [18] S. Musa, A. Borreman, A. A. M. Kok, M. B. J. Diemeer, and A. Driessen, “Experimental study of bent multimode optical waveguides,” *Appl. Opt.*, vol. 43, no. 30, pp. 5705–5707, 2004.
 - [19] H. Kelderman, M. Diemeer, L. Hilderink, and A. Driessen, “Bends in polymeric multimode waveguides,” *Eur. Conf. Integr. Opt.*, pp. 1–4, 2007.
 - [20] G. T. Palocz, “Polymer integrated optics: device architectures and fabrication methods,” California Institute of Technology, 2005.
 - [21] A. F. Benner, P. K. Pepeljugoski, and R. J. Recio, “A Roadmap to 100G Ethernet at the enterprise data center,” *IEEE Appl. Pract.*, no. November, pp. 10–17, 2007.
 - [22] J. D. Love and F. Ladouceur, “Excess loss in singlemode right-angle X junctions,” *Electron. Lett.*, vol. 28, no. 3, pp. 221–222, 1992.
 - [23] S. J. Hewlett, F. Ladouceur, and J. D. Love, “On the right-angle X-junction diffraction model,” *Opt. Quantum Electron.*, vol. 27, no. 4, pp. 261–266, 1995.
 - [24] R. T. Deck, A. L. Sala, Y. Sikorski, and B. G. Bagley, “Loss in a rectangular optical waveguide induced by the crossover of a second waveguide,” *Opt. Laser Technol.*, vol. 34, no. 5, pp. 351–356, 2002.
 - [25] A. Capobianco, B. Costantini, and C. G. Someda, “BPM modelling of planar right-angle X

- junctions,” *Electron. Lett.*, vol. 29, no. 9, p. 753, 1993.
- [26] T. Sakamoto, H. Tsuda, M. Hikita, T. Kagawa, K. Tateno, and C. Amano, “Optical interconnection using VCSELs and polymeric waveguide circuits,” *J. Light. Technol.*, vol. 18, no. 11, pp. 1487–1492, 2000.
- [27] D. A. Zauner, A. M. Jorgensen, T. A. Anhoj, and J. Hübner, “High-density multimode integrated polymer optics,” *J. Opt. A Pure Appl. Opt.*, vol. 7, no. 9, pp. 445–450, 2005.
- [28] A. Hashim, N. Bamiedakis, R. V. Pentty, and I. H. White, “Multimode Polymer Waveguide Components for Complex On-Board Optical Topologies,” *J. Light. Technol.*, vol. 31, no. 24, pp. 3962–3969, 2013.
- [29] N. Bamiedakis, J. Chen, P. Westbergh, J. S. Gustavsson, A. Larsson, R. V. Pentty, and I. H. White, “40 Gb/s Data Transmission Over a 1 m Long Multimode Polymer Spiral Waveguide for Board-Level Optical Interconnects,” *J. Light. Technol.*, vol. 33, no. 4, pp. 882–888, 2015.

6 HIGH SPEED DATA TRANSMISSION ON MULTIMODE WAVEGUIDES

This chapter presents the investigation of high-speed data transmission over multimode polymer waveguides for board-level optical interconnections. A thorough theoretical study of NRZ and multilevel modulation scheme PAM-4 is described. A basic system model is developed to assess each element in a waveguide-based optical link and to evaluate the feasibility of such multimode systems to support very high-speed data transmission. Feed-forward equalisers and decision-feedback equalisers are also briefly discussed. Record data transmissions of 40 Gb/s NRZ and 56 Gb/s PAM-4 over a 1 m long multimode polymer spiral waveguide are demonstrated both theoretically and experimentally. These results clearly indicate the capabilities of these highly-multimoded waveguides to support on-board data transmission rates of >40 Gb/s for use in next-generation short-reach optical interconnections.

6.1 Introduction

Previous chapters in this thesis report studies of the bandwidth performance of multimode polymer waveguides, and it has been theoretically and experimentally shown that these waveguides exhibit sufficient bandwidth to support very high on-board data transmission (>40 Gb/s). This chapter presents system level studies using the waveguides for application

in short-reach board-level optical interconnects. Two types of modulation scheme are discussed in this chapter: NRZ and PAM. Normally, NRZ is the main modulation scheme used in commercial short-reach optical communication links due to its simple implementation and low power consumption. In keeping with the low cost requirements for the links, high-speed VCSELs and PDs are used, 25 Gb/s commercial versions already becoming available [1], [2]. In this chapter, record 40 Gb/s NRZ-based data transmission over a 1 m long multimode polymer spiral waveguide is demonstrated for the first time.

As the demand for increasing data rates grows however, NRZ-based links for >40 Gb/s impose stringent requirements on the performance of active optoelectronic devices (VCSELs, PDs) as well as electronic circuits [3]. In addition, the transmission distance may become limited by the modal dispersion in a multimode waveguide at very high data rates if NRZ modulation is employed [4]. Therefore, in order to further increase the data rates and extend the reach of the multimode waveguides based systems, multilevel modulation schemes have attracted significant interest in recent years owing to their higher spectral efficiency [4]. In short-reach datacommunication links, high power consumption is undesirable so an important consideration in selecting the modulation scheme is the complexity of modulator, demodulator and driver circuits. PAM-4 offers lower implementation complexity compared with many other multilevel modulation formats [5]. For instance, 56 Gb/s real-time PAM-4 transmitters and receivers have been demonstrated using CMOS electronic circuits [6], [7]. Although multilevel modulation formats have been demonstrated for MMF links, their use in short-reach polymer waveguide-based optical interconnects has not yet been investigated [8], [9]. Therefore, PAM-4 modulation is investigated using multimode polymer waveguides for application in board-level optical interconnections. A record 56 Gb/s data transmission over a similar 1 m long spiral waveguide using PAM-4 scheme is presented via simulation and experimental demonstration.

This chapter is structured as follows. Section 6.2 introduces NRZ and PAM-N modulation schemes. Section 6.3 presents a simulation of a waveguide-based optical link consisting of a transmitter, waveguide channel and receiver as well as equalisation techniques, while the link power budget analysis is introduced in section 6.4. Bit-error-ratio (BER) calculations for both NRZ and PAM-4 modulation schemes are presented in section 6.5. Section 6.6 reports the simulation results of each stage in the system, while section 6.7 compares the performance of both modulation schemes using power budget analysis. Section 6.8 presents the experimental

results of 40 Gb/s NRZ and 56 Gb/s PAM-4 over a 1 m long multimode polymer spiral waveguide. Finally, section 6.9 concludes the chapter.

6.2 Modulation Schemes

NRZ and PAM are basic modulation schemes. NRZ is most widely used in optical communication systems due to its easy implementation and simple clock recovery circuit design. Although multilevel modulation formats have been studied for optical communications for many years [10], they were not adopted in high-speed links such as in the 10G Ethernet standard. In recent years, however multilevel modulation schemes have been proposed for the 40G/100G optical datacommunication links [11], and PAM has been regarded as a most promising candidate for 400G Ethernet by the IEEE P802.3bs 400 Gb/s Ethernet Task Force [12].

6.2.1 Non-Return-To-Zero (NRZ)

NRZ is a binary code in which 1s and 0s represent binary high and low states. Unlike return-to-zero (RZ), NRZ does not return to zero before the next bit is transmitted. Figure 6-1(a) illustrates NRZ signals in time domain. If the bit rate of NRZ is R (bits/sec), the symbol period $T = 1/R$. The bandwidth of the signal is defined as the frequency at first null which is equal to R (Hz) (i.e. bandwidth $B = R$). Since the bandwidth efficiency is defined as R/B , the bandwidth efficiency of a NRZ signal is 1 bps/Hz [13].

6.2.2 Pulse Amplitude Modulation (PAM-N)

PAM-N is one of the most basic digital modulation schemes [see Figure 6-1(b)]. The data is encoded in the amplitude of a series of signal pulses. PAM-N has N distinct levels to encode m bits of data (i.e. $N = 2^m$). For example, a PAM-4 signal has 4 levels (i.e. $N = 4$) and each symbol has 2 bits (i.e. $m = 2$).

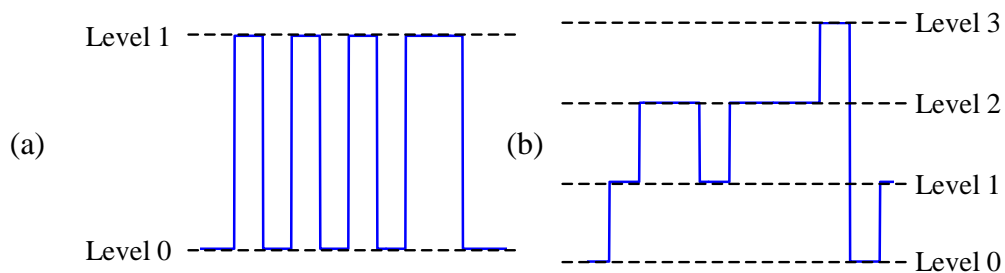


Figure 6-1 Illustration of (a) NRZ and (b) PAM-4 signals.

A mapping table is used to map the symbols of a PAM-N signal to the binary sequences. Table 6-1 illustrates the mapping between the natural binary and Gray code. The Gray code often provides better performance than natural code due to less errors as Gray code has the pattern that the adjacent symbols only differ by one bit resulting in minimum transition error [14], although it is usually easier to implement the natural code in real-world applications [4]. Therefore, Gray code is preferred in the simulation model discussed later in the chapter.

Table 6-1 Natural and Gray codes for PAM-4.

Symbol	0	1	2	3
Natural Binary	00	01	10	11
Gray Code	00	01	11	10

If the bit rate of a PAM-N signal is R (bits/sec), the symbol rate is R/m (bits/sec). The required bandwidth therefore for a PAM-N signal is $1/m$ that of an NRZ signal. Thus, the bandwidth efficiency of PAM-N signals is $R/B = R/(R/m) = m$ bps/Hz. For instance, the bandwidth efficiency of PAM-4 and PAM-8 is 2 bps/Hz and 3 bps/Hz respectively, better than that of NRZ.

6.3 Simulation Modelling

This section presents basic modelling of each element used in a multimode waveguide based system for the purpose of evaluating its high-speed performance. This model provides a useful basis for planning the experimental demonstration presented in section 6.8 of this chapter. The block diagram of the simulation is shown in Figure 6-2. The transmitter and receiver employed are modelled using parameter values shown by actual state-of-the-art active components. The experimental bandwidth measurements of the waveguides presented in Chapter 4 are also used for system modelling. More details on the parameters of each component can be found in section 6.6. The equalisation technique, an important signal processing technology to compensate the bandwidth limits of different elements in the system, is also briefly discussed in this section.

In the simulation, ideal NRZ and PAM-4 signals are fed into a VCSEL which is assumed to have a Gaussian response. The output of the VCSEL propagates through the waveguide which is also modelled using a Gaussian response. A 4th-order Bessel Thomson (BT) filter is employed to model the receiver that collects the output light from the waveguide. Finally, a

feed-forward equaliser and a decision-feedback equaliser are used to reduce the intersymbol interference (ISI). The simulation is based on time domain and thus sampling is used. The simulation of the system performance is carried out using MATLAB. The details of each block are discussed as follows.

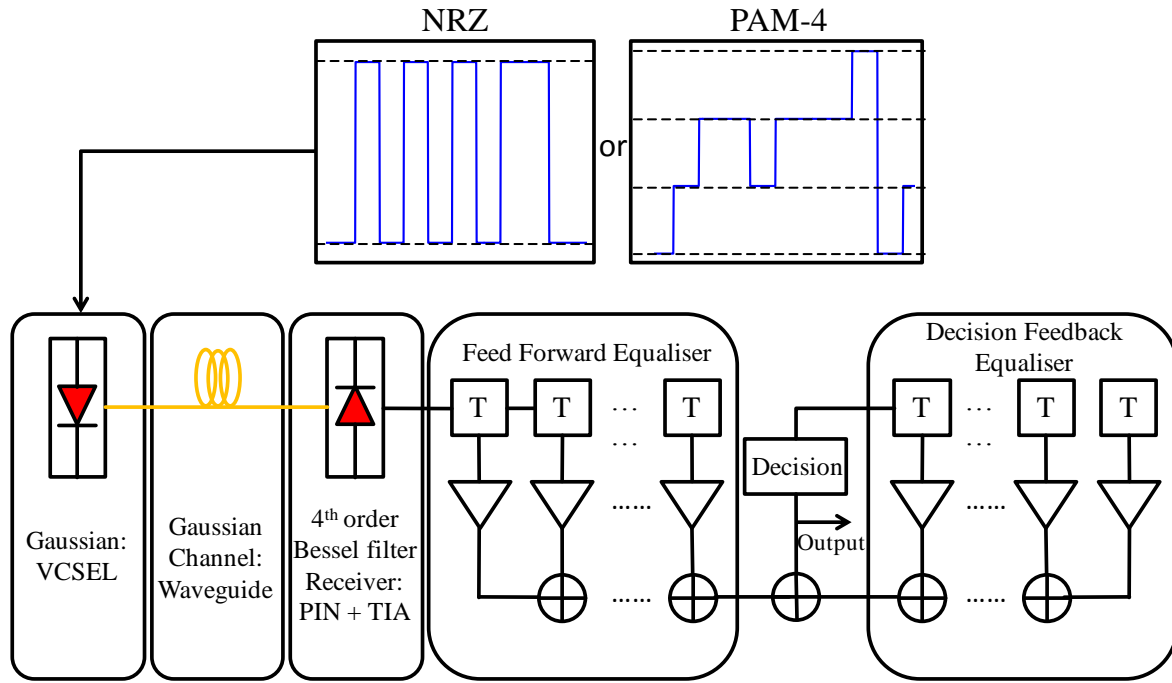


Figure 6-2 Block diagram of the simulation model used for the system evaluation.

6.3.1 VCSEL Transmitter

The impulse response of a VCSEL can be modelled using rate equations [15]. However it is modelled as a Gaussian filter here for simplicity and the impulse response is given by [16]:

$$h(t) = \frac{1}{\sigma\sqrt{2\pi}} \exp\left(-\frac{t^2}{2\sigma^2}\right) \quad -\infty \leq t \leq \infty \quad (6-1)$$

where σ is the RMS pulse width that can characterise the pulses.

On this basis the 10% - 90% rise time can be calculated from Equation (6-2), as:

$$t_r = \sigma \left(\text{erf}^{-1}(0.9) - \text{erf}^{-1}(0.1) \right) \approx 2.564\sigma \quad (6-2)$$

and the 20% - 80% rise time is given by:

$$t_r = \sigma \left(\text{erf}^{-1}(0.8) - \text{erf}^{-1}(0.2) \right) \approx 1.683\sigma \quad (6-3)$$

Taking the Fourier transform of Equation (6-1), the normalised frequency response can be obtained as:

$$H(f) = \exp\left(-2\pi^2 f^2 \sigma^2\right) \quad 0 \leq f \leq \infty \quad (6-4)$$

which has -3 dB bandwidth of:

$$BW_{-3} = \frac{\sqrt{0.3 \ln 10}}{2\pi\sigma} \approx \frac{0.1323}{\sigma} \quad (6-5)$$

and -6 dB bandwidth of:

$$BW_{-6} = \frac{\sqrt{0.6 \ln 10}}{2\pi\sigma} \approx \frac{0.1871}{\sigma} \quad (6-6)$$

6.3.2 Waveguide Channel

Waveguide response is also modelled using Gaussian response shown in Equation (6-1) in section 6.3.1.

6.3.3 Receiver

The receiver should be chosen to eliminate the noise outside the signal bandwidth and minimise the ISI. In the simulation, the receiver is modelled using a 4th order Bessel-Thomson filter (PD + TIA + LPF) in order to be consistent with model used in the IEEE 802.3aq Task Force [17], [18]. It meets the Nyquist criterion, which describes the condition when no ISI is introduced during the recovery of the original modulated signal [19]. The frequency response of the 4th order Bessel-Thomson filter is expressed as [17]:

$$H(f) = \frac{105}{105 + 105s + 45s^2 + 10s^3 + s^4} \quad (6-7)$$

where $s = j(2.144f / f_{3dB})$.

6.3.4 Overall System Response

The total bandwidth of a composite system can be expressed with a simple expression for the case that several components in the system have Gaussian frequency responses [16]:

$$BW_{sys}^{-2} = BW_1^{-2} + BW_2^{-2} + BW_3^{-2} \dots \quad (6-8)$$

where BW_{sys} represents the total system bandwidth and BW_i denotes the bandwidth of each component. It can be clearly seen that the bandwidth of the total system is limited by the slowest component in the link. Although some systems may not have Gaussian frequency response in practice, this relationship can still provide an illustration of the evolution of system frequency response.

6.3.5 Equalisation

The Nyquist criterion specifies a condition when the original transmitted symbol can be recovered without ISI. However the transmitted symbol may spread in the time domain after the transmission channel due to its limited bandwidth. Thus, the current symbol may be affected by previous symbols, causing ISI and this breaks the Nyquist criterion. Therefore, an equalisation filter needs to be used to compensate for the distortion caused in the channel in order to recover the symbol [19]. Two types of equalisation techniques are briefly introduced, including feed-forward equalisation (FFE) and decision-feedback equalisation (DFE).

ISI occurs in a dispersive channel which causes a blur or mixture of symbols as illustrated in Figure 6-3. ISI can occur at both ends of the symbols. As shown in Figure 6-3, pre-cursor ISI comes from the later arrived symbols (on the left side), while post-cursor ISI comes from the earlier symbols (on the right side). A finite impulse response (FIR) filter can be used to recover the pre-cursor ISI as it gathers the ISI information from the later arrived symbols, whereas the post-cursor ISI relies on the information from the earlier arrived symbols which requires a feedback mechanism in order to extract the ISI information. This can be done using an infinite impulse response (IIR) filter. More details on the implementations of the FIR and IIR filters using FFE and DFE will be discussed in the following.

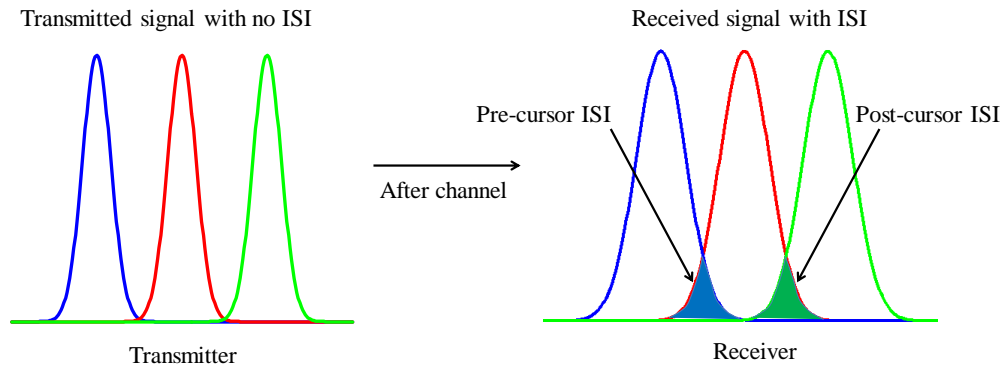


Figure 6-3 Illustration of pre-cursor ISI and post-cursor ISI in a dispersive channel.

- Feed-Forward Equalisation (FFE)

The structure of a FIR filter can be used for an N-tap FFE as illustrated in Figure 6-4. The FFE corrects the information of received waveform itself and not the logical decision made on the waveform. So no logical decisions are made in the FFE algorithm [20].

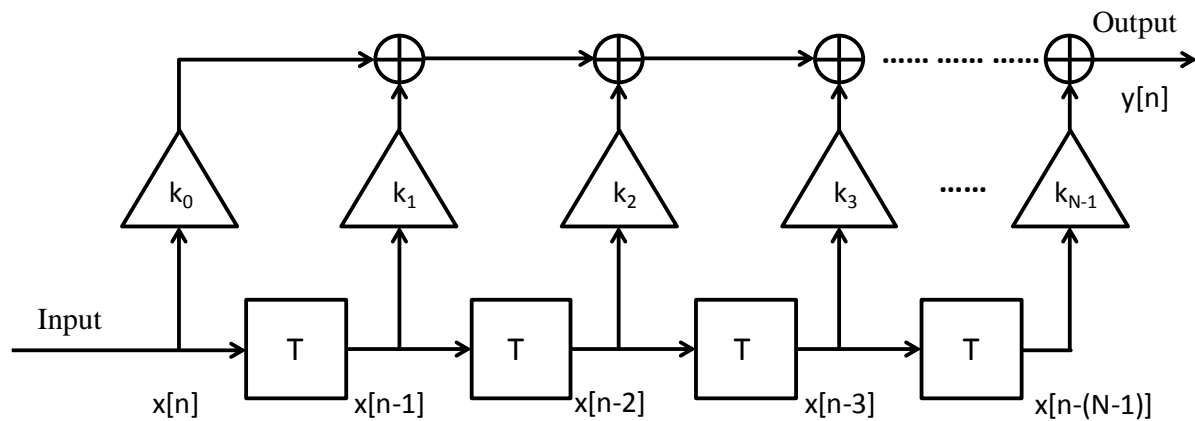


Figure 6-4 Schematic diagram of an FIR T-spaced N-tap FFE.

The input signal is sampled at the symbol rate and then delayed by $(N-1) \cdot T$. Then the recovered symbols are the superposition of those delayed samples multiplied by the corresponding tap values. The values of the taps are predetermined using training sequence. The minimum-mean-square-error (MMSE) algorithm is used here for equaliser adaption [21].

For an N-tap FFE, the input sample sequence is:

$$\{x[n], x[n-1], x[n-2], x[n-3], \dots, x[n-(N-1)]\}$$

The corresponding tap values are:

$$\{k_0, k_1, k_2, k_3, \dots, k_{N-1}\}$$

Then the recovered symbol is given as:

$$\begin{aligned} y[n] &= k_0 x[n] + k_1 x[n-1] + k_2 x[n-2] + k_3 x[n-3] + \dots + k_{N-1} x[n-(N-1)] \\ &= \sum_{i=0}^{N-1} k_i x[n-i] = \hat{x}[n-(N-1)] \end{aligned} \quad (6-9)$$

Here, $y[n]$ is the recovered symbol of $\hat{x}[n-(N-1)]$.

- Decision Feedback Equalisation (DFE)

The basic structure of an M-tap DFE is similar to an IIR filter as shown in Figure 6-5. The decisions available for the symbol at the present time must come from the information of the earlier symbols as the decisions made for the received symbols are fed back to the current symbol. Therefore, the DFE can be used to remove the post-cursor ISI as it extracts information from earlier symbols via a feedback structure. The recovered symbol is obtained by the superposition of the decisions multiplied by the individual tap values.

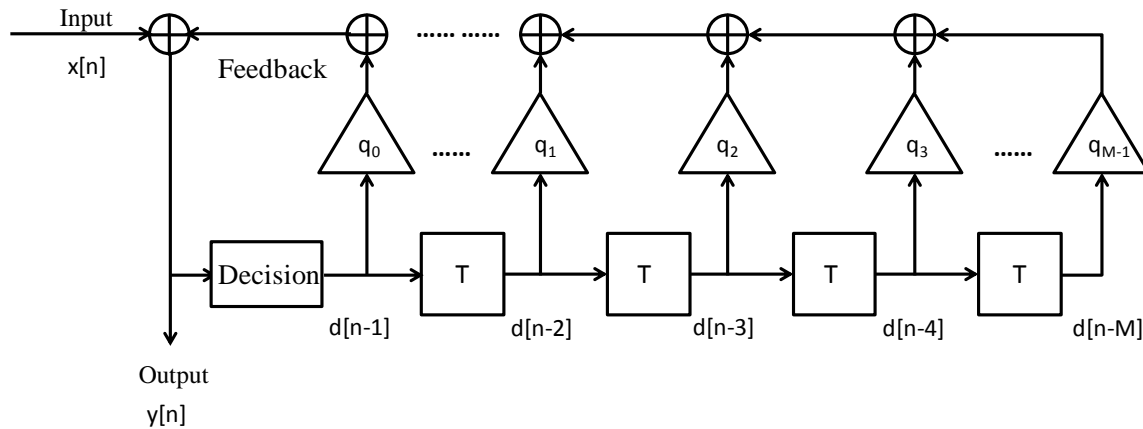


Figure 6-5 Schematic diagram of an IIR T-spaced M-tap DFE.

For an M-tap DFE, the input sample sequence is:

$$\{d[n-1], d[n-2], d[n-3], \dots, d[n-M]\}$$

The corresponding tap values are:

$$\{q_0, q_1, q_2, q_3, \dots, q_{M-1}\}$$

Then the recovered symbol is given as:

$$\begin{aligned}
 y[n] &= x[n] + q_0 d[n-1] + q_1 d[n-2] + q_2 d[n-3] + \cdots + q_{M-1} d[n-M] \\
 &= x[n] + \sum_{i=0}^{M-1} q_i d[n-i-1] = \hat{x}[n]
 \end{aligned} \tag{6-10}$$

where $\hat{x}[n]$ is the recovered symbol of $x[n]$.

If we connect the input of the DFE $x[n]$ to the output of the FFE, the above equation needs to be shifted by $(N-1)$:

$$\begin{aligned}
 y[n-(N-1)] &= x[n-N+1] + q_0 d[n-N] + q_1 d[n-N-1] + q_2 d[n-N-2] + \cdots + q_{M-1} d[n-N-M+1] \\
 &= x[n-N+1] + \sum_{i=0}^{M-1} q_i d[n-N-i] \\
 &= \sum_{i=0}^{N-1} k_i x[n-i] + \sum_{i=0}^{M-1} q_i d[n-N-i] = \hat{x}[n-(N-1)]
 \end{aligned}$$

The combination of FFE and DFE for an N -tap FFE and M -tap DFE system is illustrated as Figure 6-6. $x[n]$ is the symbol received at the present time, and $x[n-(N-1)]$ is the symbol to be recovered.

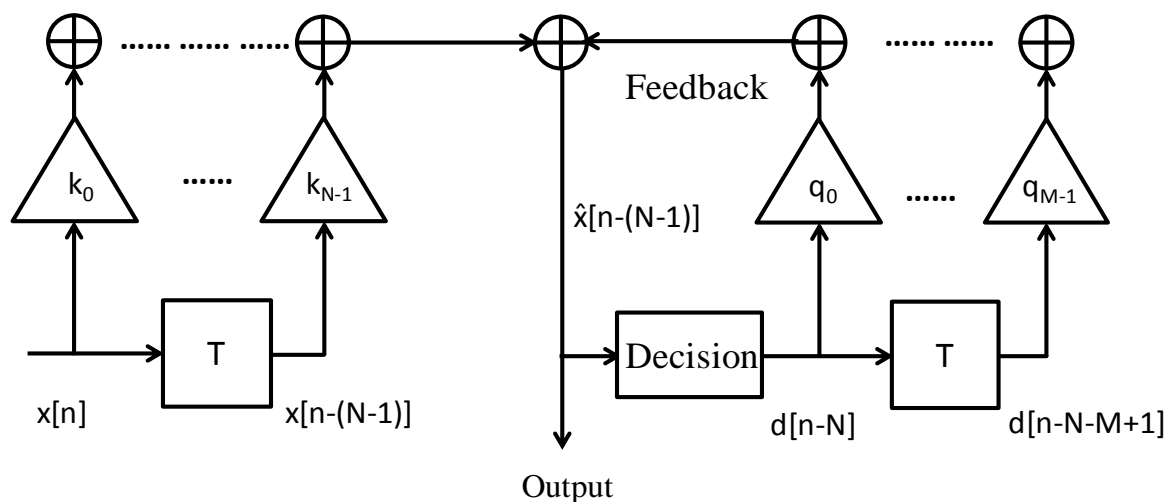


Figure 6-6 Schematic diagram of a T-spaced N -tap FFE and T-spaced M -tap DFE equaliser.

6.4 Link Power Budget

The link power budget is defined as the difference between the maximum transmitting power and minimum receiver sensitivity. To achieve a specified BER performance, total power penalty of the system must not exceed the link power budget.

Link power budget analysis is a useful tool to evaluate if a system can meet the specified requirement, and it also provides a guideline for the experimental work presented later in this chapter. A reference BER of 10^{-12} is assumed in the following simulation in this chapter unless otherwise stated. Four main power penalties are considered in the simulation model as illustrated in Figure 6-7, including attenuation, ISI penalty (including noise enhancement penalty and residual ISI), relative intensity noise (RIN) penalty and multilevel penalty. The system margin is obtained by subtracting the total power penalty (i.e. the accumulation of all of the power penalties) from the link power budget. This allows one to determine whether a system is feasible to achieve the required BER performance or not.

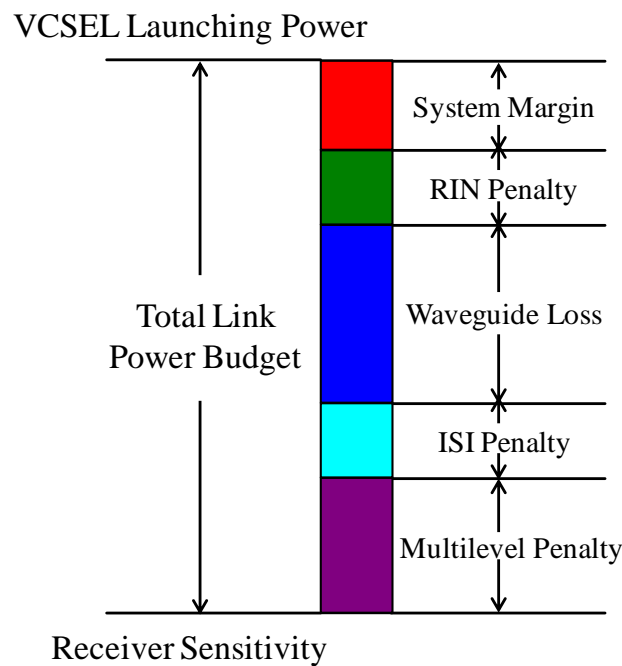


Figure 6-7 Link power budget model for multilevel modulation schemes in waveguide based transmission systems.

- Multilevel Penalty:

Multilevel modulation schemes inevitably introduce multilevel penalty [22]. Assuming that the received signals have the same power, the eye opening between each adjacent level for the multilevel signal is only a fraction of that of the NRZ signal. Therefore, an extra

power is needed so as to achieve the same BER performance, which results in the multilevel penalty. Theoretically, the modulation penalty for PAM-4 is $10 \cdot \log(3) = \sim 4.77$ dB, because it has one third of the eye opening of an NRZ signal.

- ISI Penalty:

The ISI penalty is defined here as the BER degradation after the receiver or the equalisers if equalisation technique is applied. For the case of equalisation, it consists of two types of penalties: residual ISI penalty and noise enhancement penalty.

(i) Residual ISI Penalty

It is not possible to remove all the ISI by using equalisation as the equaliser tap settings obtained using MMSE algorithm may not give a perfect signal recovery. The degraded BER performance due to this ISI penalty is defined as residual ISI penalty.

(ii) Noise Enhancement Penalty

As a result of the FFE, noise is enhanced by the combined tap weights, which leads to noise enhancement. DFE does not introduce noise enhancement.

The new noise after enhancement can be calculated as:

$$\sigma'^2 = \sigma^2 \times \sum_{i=0}^{N-1} k_i^2 \quad (6-11)$$

where k is the FFE tap values: $k = \{k_0, k_1, k_2, k_3, \dots, k_{N-1}\}$, and σ^2 (A^2) is the receiver noise.

Two BER curves can be obtained using the noise without (σ^2) and with (σ'^2) the equalisers. The difference between the average received optical powers for the same value of BER is equivalent to the noise enhancement penalty which can be expressed as:

$$\text{Noise Enhancement (in dB)} = 10 \times \log \left[\sqrt{\sum_{i=0}^{N-1} k_i^2} \right] \quad (6-12)$$

It can be seen that additional noise is introduced during the process of removing ISI using equalisation techniques. This noise enhancement degrades the overall signal-to-noise ratio resulting in a power penalty. It should be noted that the Equation (6-12) is only valid for the case when thermal noise dominates the overall receiver noise.

- Waveguide Loss:

The power of the incident light decreases as it propagates through the channel (waveguide in this case). It satisfies the following expression:

$$P_L = P_0 \cdot e^{-\alpha L} \quad (6-13)$$

where P_0 and P_L are the launching optical power into the channel and the optical power after the channel, respectively. α is the attenuation coefficient in m^{-1} .

The Equation (6-13) can also be expressed in the logarithm form:

$$10 \log \frac{P_L}{P_0} = -\alpha L \quad (6-14)$$

- Relative Intensity Noise (RIN) Penalty

RIN is due to fluctuations in the output intensity of the laser as illustrated in Figure 6-18. Spontaneous emission leads to intensity and phase fluctuations in the coherent field established inside the laser cavity by stimulated emission. As a result of phase uncertainty, the intensity and phase of the optical field change randomly. Therefore, the RIN comes from the spontaneous emission [23].

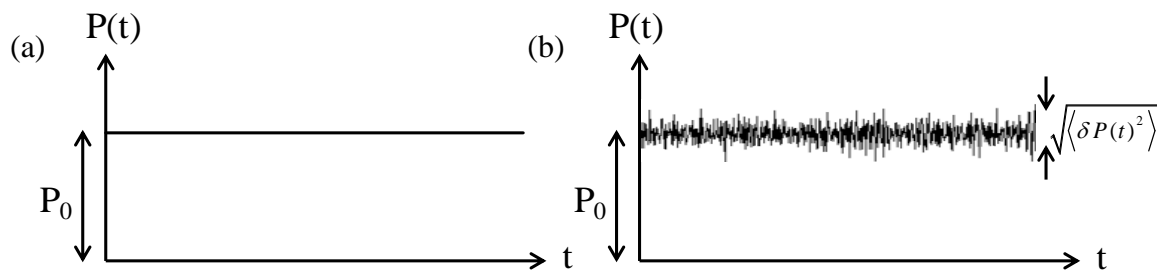


Figure 6-8 (a) Ideal laser output power with DC bias and (b) real laser output power with intensity noise [24].

RIN is defined as the mean square intensity fluctuation divided by the square of average intensity of the laser output. Also, RIN is usually normalized to 1-Hz bandwidth, which makes it easier to compare the intensity fluctuations under different receiver bandwidths. The linear form of the RIN is expressed as follows [24], [25]:

$$RIN = \frac{\langle \delta P(t)^2 \rangle}{P_0^2 \cdot \Delta f} [1/\text{Hz}] \quad (6-15)$$

where $\delta P(t)$ is the optical intensity fluctuations, $\langle \rangle$ denotes the time average, P_0 is the DC optical power, and Δf is the noise bandwidth (detection system bandwidth).

RIN is often written in the form of dB/Hz shown in Equation (6-16). The higher the RIN value is, the higher the RIN penalty is.

$$RIN[\text{dB/Hz}] = 10 \log \left(\frac{\langle \delta P(t)^2 \rangle}{P_0^2} \right) [\text{dB}] - 10 \log (\Delta f [\text{Hz}]) \quad (6-16)$$

The estimated the RIN-induced power penalty is [26]:

$$\sigma_{RX} = \sqrt{\Delta f_{RX} \cdot 10^{RIN/10}} \quad (6-17)$$

where Δf_{RX} is the receiver bandwidth (approximately 0.75 times the symbol rate).

For an NRZ signal without equalisation, the RIN power penalty in dB can be written as [27]:

$$P_{RIN_NRZ} = 10 \cdot \log \left(\sqrt{\frac{1}{1 - Q^2 \cdot \sigma_{RX}^2 / ISI_{RX}^2}} \right) \quad (6-18)$$

where $ISI_{RX} = B/A$ (A: nominal level without ISI, B: vertical eye opening with ISI) as illustrated in Figure 6-9.

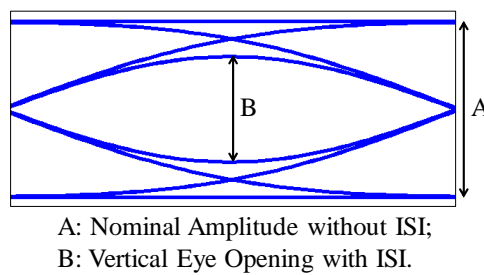


Figure 6-9 Plot of eye diagram at the optical receiver.

For an NRZ signal with equalisation, the RIN power penalty in dB needs to be modified to:

$$P_{RIN_NRZ_D} = 10 \cdot \log \left(\sqrt{\frac{1}{1 - Q^2 \cdot [\sigma_{RX}^2 \cdot NEF]}} \right) \quad (6-19)$$

where NEF is noise enhancement factor, defined as the output noise variance divided by the input noise variance (in linear units).

Similarly, for PAM-N signal without equalisation, the RIN power penalty in dB can be written as:

$$P_{RIN_PAM-N} = 10 \cdot \log \left(\sqrt{\frac{1}{1 - Q^2 \cdot (M-1)^2 \cdot \sigma_{RX}^2 / ISI_{RX}^2}} \right) \quad (6-20)$$

For PAM-N signal with equalisation, the RIN power penalty in dB needs to be modified as:

$$P_{RIN_PAM-N_D} = 10 \cdot \log \left(\sqrt{\frac{1}{1 - Q^2 \cdot (M-1)^2 [\sigma_{RX}^2 \cdot NEF]}} \right) \quad (6-21)$$

- System Margin

After subtracting all of the penalties from the system power budget, the remaining budget is the system margin. The larger the system margin is, the more freedom of power degradation a system has. A system is only feasible when the system margin is positive.

6.5 Bit-error-ratio (BER) Calculation

There is a possibility of bit errors due to noise and interference. BER is defined as the number of bit errors divided by the total number of transmitted bits within a time interval [28]. This section introduces the procedures for calculating BER for both NRZ and PAM-N modulation schemes [29].

- NRZ

The sampled receiver output signal $R(t)$ is expressed as:

$$R(t) = S(t) + N(t) \quad (6-22)$$

where $S(t)$ is the sampled signal amplitude and $N(t)$ is a Gaussian random variable with zero mean and variance σ^2 . Thus, $R(t)$ is a Gaussian random variable with a mean value $S(t)$. As shown in Figure 6-10, S_1 and S_0 represent the mean value of the sampled output signal $R(t)$ at

the decision point for binary 1 and 0, respectively. The probability density function (PDF) is expressed as:

$$f(R|S_\alpha) = \frac{1}{\sqrt{2\pi}\sigma_\alpha} \exp\left\{-\frac{(R-S_\alpha)^2}{2\sigma_\alpha^2}\right\} \quad (6-23)$$

where the subscript $\alpha \in \{0,1\}$ represents binary 0 or binary 1, and σ_α^2 is the noise power of binary 0 or binary 1.

Then the BER can be expressed as:

$$BER = P(S_1)P(\text{error} | S_1) + P(S_0)P(\text{error} | S_0) \quad (6-24)$$

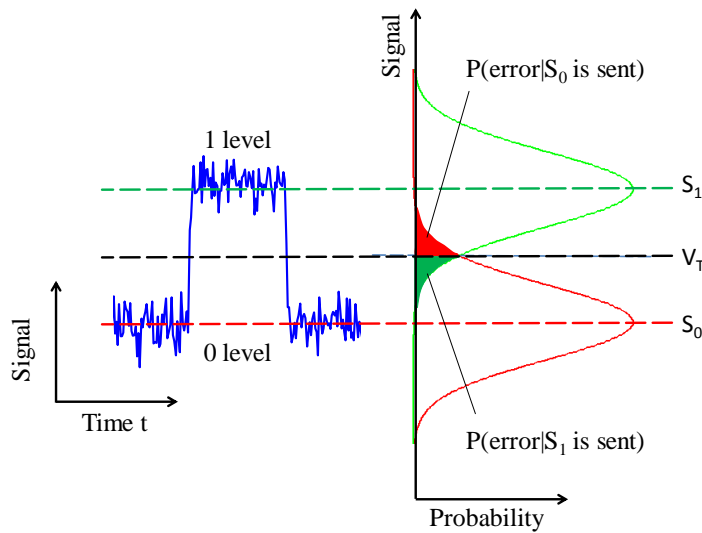


Figure 6-10 Gaussian probability density functions of binary 1s and 0s with the fluctuating signal illustrated at the receiver (the colour regions represent the probability of error).

where $P(S_1)$ and $P(S_0)$ are the probabilities of bit S_1 and S_0 is sent respectively,

$P(\text{error} | S_1)$ represents the probability of error due to the receiving S_0 when S_1 is sent, and

$P(\text{error} | S_0)$ represents the probability of error due to that receiving S_1 when S_0 is sent.

$P(\text{error} | S_1)$ and $P(\text{error} | S_0)$ are given by:

$$\begin{aligned}
P(\text{error} | S_1) &= \frac{1}{\sqrt{2\pi}\sigma_1} \int_{-\infty}^{V_T} \exp\left\{-\frac{(S-S_1)^2}{2\sigma_1^2}\right\} dS \\
P(\text{error} | S_0) &= \frac{1}{\sqrt{2\pi}\sigma_0} \int_{V_T}^{\infty} \exp\left\{-\frac{(S-S_0)^2}{2\sigma_0^2}\right\} dS
\end{aligned} \tag{6-25}$$

where V_T is the threshold level between S_1 and S_0 . An optimum threshold is used here to minimise the BER.

$$V_T = \frac{S_1 + S_0}{2} \tag{6-26}$$

And we assume equal probability for sending binary symbol S_1 and S_0 , i.e.

$$P(S_1) = P(S_0) = \frac{1}{2}.$$

Hence,

$$\begin{aligned}
BER &= \frac{1}{2} Q\left(\frac{-V_T + S_1}{\sigma_1}\right) + \frac{1}{2} Q\left(\frac{V_T - S_0}{\sigma_0}\right) \\
&= \frac{1}{4} \operatorname{erfc}\left(\frac{-V_T + S_1}{\sqrt{2}\sigma_1}\right) + \frac{1}{4} \operatorname{erfc}\left(\frac{V_T - S_0}{\sqrt{2}\sigma_0}\right)
\end{aligned} \tag{6-27}$$

$$\text{where } Q(z) = \frac{1}{\sqrt{2\pi}} \int_z^{\infty} e^{-\lambda^2/2} d\lambda = \frac{1}{2} \operatorname{erfc}\left(\frac{z}{\sqrt{2}}\right).$$

It is also assumed that thermal noise is the dominant receiver noise:

$$\sigma_1 = \sigma_0 = \sigma_{\text{Thermal}}$$

Thus, Equation (6-27) can be re-written into the following form for simplicity:

$$BER = \frac{1}{2} \operatorname{erfc}\left(\frac{|S_{\alpha} - V_T|}{\sqrt{2}\sigma_{\text{thermal}}}\right) \tag{6-28}$$

In the simulation, 64 sampling points per bit are used. The BER value for each of the 64 sampling point β is calculated by taking the average of the BER error functions for all of the bits within the received data, given by:

$$BER(\beta) = \frac{\sum \frac{1}{2} \operatorname{erfc}\left(\frac{|S_\alpha - V_T|}{\sqrt{2}\sigma_{\text{thermal}}}\right)}{\text{number of bits}} \quad (6-29)$$

The optimum BER is the BER value at the sampling point when the BER is minimum.

$$BER_{\text{optimum}} = \min(BER(\beta)) \quad (6-30)$$

The curve of BER versus the average received optical power can be obtained by repeating the above BER analysis for different average received optical powers.

- PAM-N

The principle used in NRZ can be extended to multilevel modulation. The sampled output signal is expressed as:

$$R(t) = S_\alpha(t) + N_\alpha(t) \quad (6-31)$$

where $\alpha \in \{1, 2, 3, \dots, N\}$ and N denotes the number of levels. $S_\alpha(t)$ is the sampled signal amplitude of symbol α and $N_\alpha(t)$ is a Gaussian random variable with zero mean and variance σ_α^2 . So $R(t)$ is a Gaussian random variable with a mean value $S_\alpha(t)$. S_α represents the mean value of the sampled output signal $R(t)$ at the decision point for symbol α .

As illustrated in Figure 6-11, the symbol-error-ratio (SER) can be divided into three parts, including the first symbol S_1 (leftmost side), the last symbol S_N (rightmost side) and the symbols S_α ($\alpha = 2, 3, \dots, N-1$) in the middle.

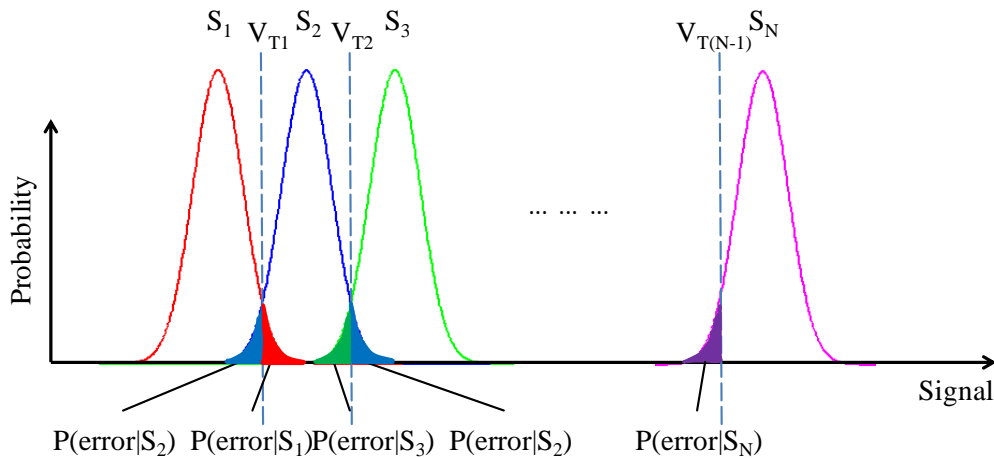


Figure 6-11 Gaussian probability density functions of multilevel signals.

There is only one colour region in the first and last symbol. $P(\text{error} | S_1)$ and $P(\text{error} | S_N)$ are given by:

$$\begin{aligned} P(\text{error} | S_1) &= \frac{1}{\sqrt{2\pi}\sigma_1} \int_{V_{T1}}^{+\infty} \exp\left\{-\frac{(S-S_1)^2}{2\sigma_1^2}\right\} dS \\ P(\text{error} | S_N) &= \frac{1}{\sqrt{2\pi}\sigma_N} \int_{-\infty}^{V_{T(n-1)}} \exp\left\{-\frac{(S-S_N)^2}{2\sigma_N^2}\right\} dS \end{aligned} \quad (6-32)$$

Assuming the probability of sending each level of a symbol is equal, i.e. $P(S_\alpha) = \frac{1}{N}$.

Hence,

$$\begin{aligned} SER_1 &= P(S_1) P(\text{error} | S_1) \\ &= \frac{1}{N} Q\left(\frac{V_{T1} - S_1}{\sigma_1}\right) \\ &= \frac{1}{2N} \operatorname{erfc}\left(\frac{V_{T1} - S_1}{\sqrt{2}\sigma_1}\right) \end{aligned} \quad (6-33)$$

$$\begin{aligned} SER_N &= P(S_N) P(\text{error} | S_N) \\ &= \frac{1}{N} Q\left(\frac{-V_{T(n-1)} + S_N}{\sigma_N}\right) \\ &= \frac{1}{2N} \operatorname{erfc}\left(\frac{-V_{T(n-1)} + S_N}{\sqrt{2}\sigma_N}\right) \end{aligned} \quad (6-34)$$

where $Q(z) = \frac{1}{\sqrt{2\pi}} \int_z^\infty e^{-\lambda^2/2} d\lambda = \frac{1}{2} \operatorname{erfc}\left(\frac{z}{\sqrt{2}}\right)$.

As shown in Figure 6-11, there are two colour regions in the symbols between the first and the last symbol. So the SER should be approximately twice of that of the first or last symbol.

$$\begin{aligned}
P_1(\text{error} | S_\alpha) &= \frac{1}{\sqrt{2\pi}\sigma_\alpha} \int_{-\infty}^{V_{T(\alpha-1)}} \exp\left\{-\frac{(S-S_\alpha)^2}{2\sigma_\alpha^2}\right\} dS \\
P_2(\text{error} | S_\alpha) &= \frac{1}{\sqrt{2\pi}\sigma_\alpha} \int_{V_{T\alpha}}^{+\infty} \exp\left\{-\frac{(S-S_\alpha)^2}{2\sigma_\alpha^2}\right\} dS
\end{aligned} \tag{6-35}$$

Hence,

$$\begin{aligned}
SER_\alpha &= P(S_\alpha) \{P_1(\text{error} | S_\alpha) + P_2(\text{error} | S_\alpha)\} \\
&= \frac{1}{N} \left\{ Q\left(\frac{-V_{T(\alpha-1)} + S_\alpha}{\sigma_\alpha}\right) + Q\left(\frac{V_{T\alpha} - S_\alpha}{\sigma_\alpha}\right) \right\} \\
&= \frac{1}{2N} \operatorname{erfc}\left(\frac{-V_{T(\alpha-1)} + S_\alpha}{\sqrt{2}\sigma_\alpha}\right) + \frac{1}{2N} \operatorname{erfc}\left(\frac{V_{T\alpha} - S_\alpha}{\sqrt{2}\sigma_\alpha}\right)
\end{aligned} \tag{6-36}$$

The total symbol error ratio therefore is:

$$SER_{Total} = \sum_{\alpha=1}^N SER_\alpha \tag{6-37}$$

Pre-determined threshold levels are used to put the received data into corresponding symbol levels, and then the new decision threshold levels can be calculated as:

$$V_{T\alpha} = \frac{\overline{S_\alpha} + \overline{S_{\alpha+1}}}{2} \tag{6-38}$$

where $\overline{S_\alpha}$ is the average value of all of the symbols received at level α .

In this simulation, 64 sampling points per symbol are used. The SER at each sampling point β for symbol level α is calculated by taking the average value of all of the $SER(\beta)$ at symbol level α , given by:

$$SER_\alpha(\beta) = \frac{\sum_{\text{All symbols } \alpha} SER_\alpha(\beta)}{\text{Number of symbols } \alpha} \tag{6-39}$$

Hence, the total SER at sampling point β is:

$$SER_{Total}(\beta) = \sum_{\alpha=1}^N SER_{\alpha}(\beta) \quad (6-40)$$

The optimum SER is the SER value at the sampling point that produces the minimum SER.

$$SER_{optimum} = \min(SER(\beta)) \quad (6-41)$$

The corresponding BER for a certain SER is calculated as:

$$BER_{optimum} = \frac{SER_{optimum}}{\log_2 N} \quad (6-42)$$

For example, $N = 4$ for PAM-4. Finally, the above SER analysis process can be repeated for different average received optical powers so that the curve of BER versus the average received optical power can be obtained.

6.6 Simulation Results

Table 6-2 shows the values of major parameters used in the simulation for each element in the waveguide-based optical link. These values are chosen to match the devices likely employed in the experiments and the actual state-of-the-art components readily available in the market. It should be noted that the parameter values chosen in the simulation are conservative in order to gain a useful insight on the feasibility of high-speed on-board optical links based on the multimode waveguide technology. As presented in Table 6-2, a VCSEL is modelled using a Gaussian low pass filter with a bandwidth of ~25 GHz based on the characteristics of the devices in the experiments [30]. A laser RIN of -130 dB/Hz is assumed for multimode devices [31]. The maximum output power is ~10 dBm [30]. The waveguide is modelled with a Gaussian response with a BLP of 35 GHz×m. This is a “worst-case” value obtained from the bandwidth measurements in Chapter 4. The waveguide loss is assumed to be ~0.06 dB/cm which is slightly larger than the 0.04 dB/cm typically reported on these polymer waveguides to account for the additional bending losses that occur in the 1 m long spiral waveguide employed in the experiments. The input and output total coupling losses are assumed to be ~3 dB. A 4th-order Bessel Thomson filter is used to model the frequency response of the receiver and the transimpedance amplifier (TIA). An optical receiver with a -

3 dB frequency of 22 GHz and a responsivity of 0.4 A/W is used in the model based on a commercially-available receiver (New Focus 1484-A-50) with a sensitivity of ~ 5.5 dBm for a BER of 10^{-12} .

Table 6-2 List of parameters for each component used in the simulation model.

Transmitter	Channel	Receiver	Equalisation
Gaussian Response	Gaussian Response	4 th order Bessel Response	
VCSEL:	Waveguide:	PIN photodiode + TIA	Equalisers
Wavelength: 850 nm	Loss: 0.06 dB/cm	Cut-off frequency: 22 GHz	Minimum Mean Square Error (MMSE) equaliser
Bandwidth: 25 GHz	Bandwidth: 35 GHz×m	Responsivity: 0.4 A/W	consists of 7-tap FFE and
Output power: 10 dBm	Coupling loss: 3 dB	Sensitivity: -5.5 dBm	5-tap DFE
RIN: -130 dB/Hz			

The system link is investigated at 40 Gb/s and 56 Gb/s using NRZ coding and 56 Gb/s using PAM-4 modulation scheme. A thermal noise dominated receiver with identical noise power spectral density is assumed as a reference which gives a sensitivity of -5.5 dBm at BER of 10^{-12} for a NRZ receiver. This reference noise power spectral density is used throughout the simulation model to enable comparison of the performance using different modulation formats.

6.6.1 Signal Generation

In the simulation, a $2^7 - 1$ pseudo-random bit sequence (PRBS) pattern is used to model the short run length codes in data communication links. The original modulation signal is generated using an ideal rectangular pulse shaping filter with an oversampling ratio of 64. The eye diagrams of the ideal NRZ signals at 40 Gb/s and 56 Gb/s and PAM-4 signals at 56 Gb/s are shown in Figure 6-12. This ideal modulation signal is used to assess the responses of the VCSEL, waveguide and receivers by convolving with their respective impulse responses defined in section 6.3.1 to 6.3.3.

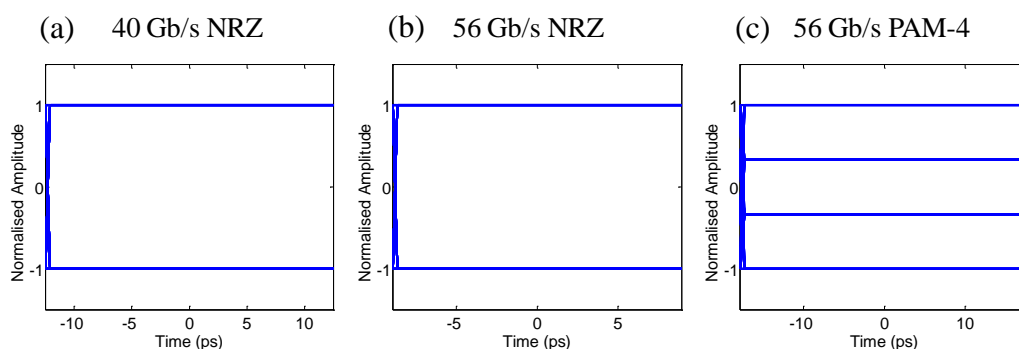


Figure 6-12 Eye diagrams of the ideal signals: (a) NRZ at 40 Gb/s, (b) NRZ at 56 Gb/s and (c) PAM-4 at 56 Gb/s.

6.6.2 Signal After VCSEL

Figure 6-13 shows the eye diagrams of the transmitted signals for NRZ at 40 Gb/s and 56 Gb/s and for PAM-4 at 56 Gb/s. As can be seen from the eye diagrams, PAM-4 signals have smaller vertical eye openings between the two adjacent levels compared to NRZ signals in terms of the absolute amplitude for a given received optical power. PAM-4 systems also generally have smaller ISIs as PAM-4 systems have half of the symbol rate of NRZ systems. However, PAM-4 schemes also introduce large multilevel power penalty and thus the signal-to-noise ratio of the overall system is not necessarily better than typical NRZ schemes. This will be further illustrated in the following sections.

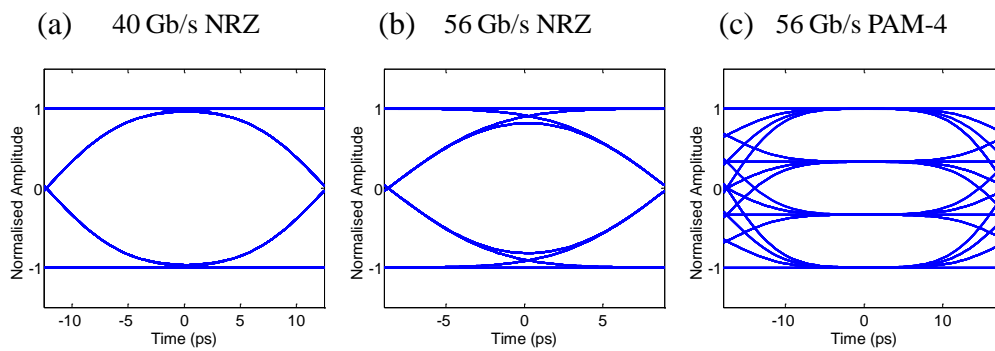


Figure 6-13 Eye diagrams of the transmitted signals after VCSEL: (a) NRZ at 40 Gb/s, (b) NRZ at 56 Gb/s and (c) PAM-4 at 56 Gb/s.

6.6.3 Signal After Waveguide

Figure 6-14 shows the signals after propagation of various waveguide lengths (0.5 m, 1 m and 1.5 m) for NRZ at 40 Gb/s and 56 Gb/s and for PAM-4 at 56 Gb/s. Eye closures gradually increase as the propagation length increases. Clear eye openings can be observed for NRZ signals at 40 Gb/s even after the transmission of a 1.5 m waveguide, however, obvious eye closure can be noticed at higher data rates of 56 Gb/s. In comparison, the ISIs of PAM-4 signals exhibit less increase than NRZ signals as the waveguide length increases due to the lower signal bandwidths.

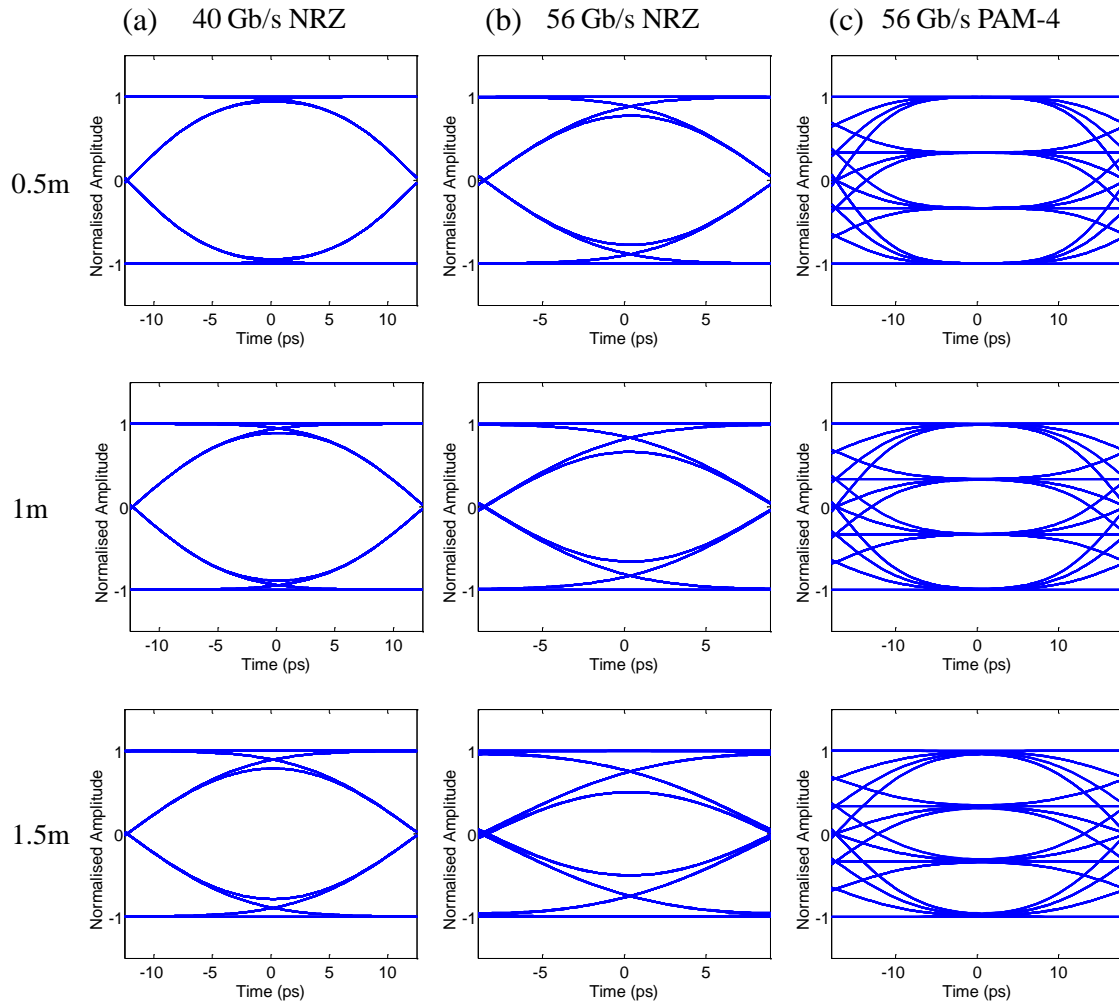


Figure 6-14 Eye diagrams of signals after propagation of waveguide lengths of 0.5m, 1 m and 1.5 m for (a) NRZ at 40 Gb/s, (b) NRZ at 56 Gb/s and (c) PAM-4 at 56 Gb/s.

6.6.4 Signal After Receiver

Figure 6-15 shows the received signals at the receiver end for NRZ at 40 Gb/s and 56 Gb/s and for PAM-4 at 56 Gb/s after the transmission of different waveguide lengths of 0.5 m, 1 m and 1.5 m respectively. Good eye openings can still be achieved after a 1.5 m long waveguide at 40 Gb/s using NRZ scheme. However, severe eye closures can be observed beyond a 1 m long waveguide when the data rates increase to 56 Gb/s. Without the use of equalisation, PAM-4 signals still show relatively good eye openings for all waveguide lengths studied at 56 Gb/s. At higher data rates, the NRZ signals exhibit higher ISIs than PAM-4 signals. When a point is reached where the ISI penalty exceeds the intrinsic multilevel penalty of PAM-4 signals, the multilevel modulation schemes starts to show the advantages over NRZ scheme in the overall system signal-to-noise ratio.

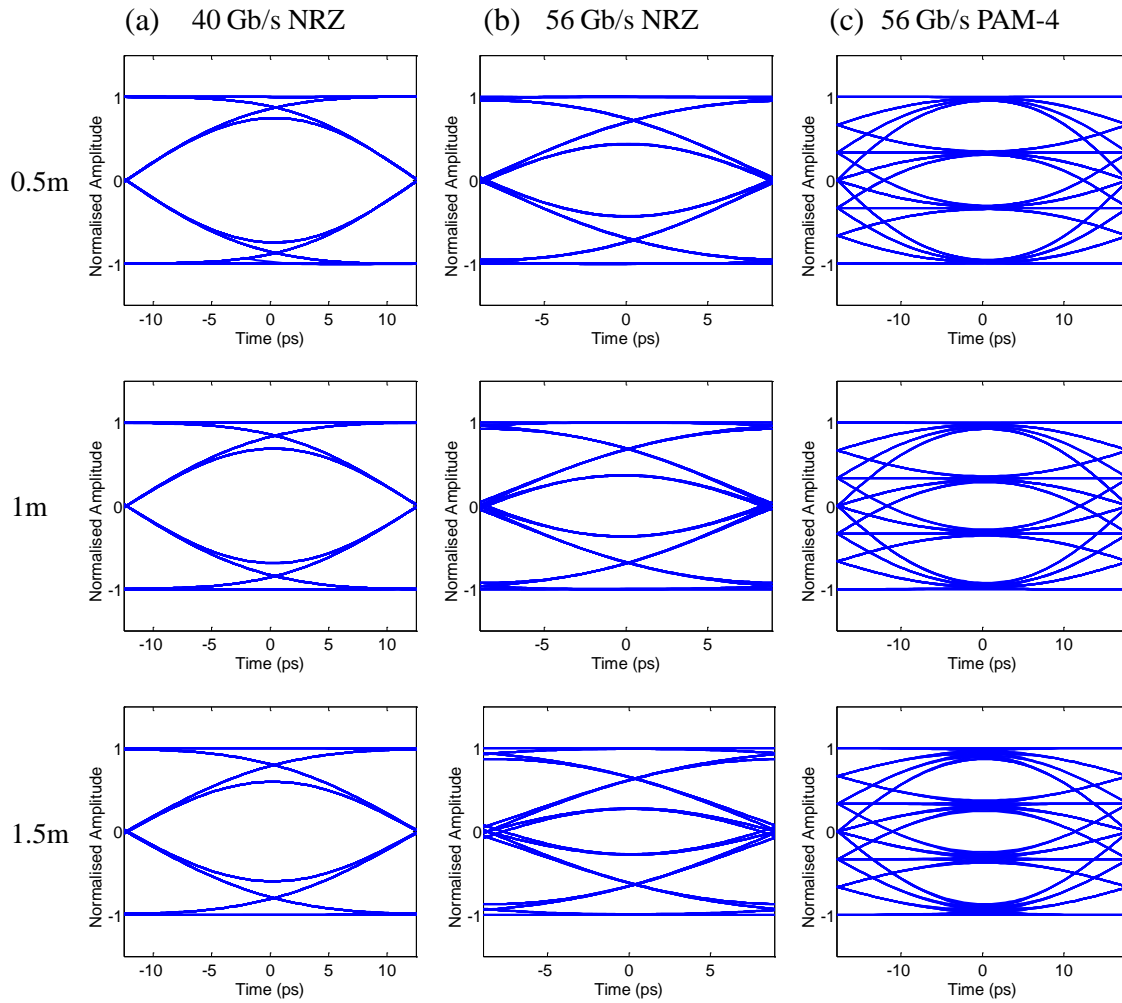


Figure 6-15 Eye diagrams of the signals after the receiver after propagation of waveguide lengths of 0.5m, 1 m and 1.5 m for (a) NRZ at 40 Gb/s, (b) NRZ at 56 Gb/s and (c) PAM-4 at 56 Gb/s without the use of equalisers.

6.6.5 Signal After Equalisation

As shown in Figure 6-15, different levels of eye closures can be observed after the receiver for both modulation schemes at different data rates due to the limited bandwidth of the available active devices. Nevertheless, ISI can be removed using equalisation techniques. In this simulation, an equaliser with 7-tap T-spaced FFE and 5-tap T-spaced DFE is used as an example in order to be consistent with IEEE 802.3aq Task Force [32]. The implementation of the equalisers is introduced in section 6.3.5. The signals after equalisation are plotted in Figure 6-16. Clear eye openings can be observed. For example, the closed eyes for 56 Gb/s NRZ signals after propagation of 1 m and 1.5 m long waveguide with no equalisation can be recovered with the use of such equalisers. However, equalisation introduces noise

enhancement penalty as explained in section 6.4. PAM-4 scheme can exhibit better performance than NRZ when the noise enhancement penalty of NRZ scheme exceeds the multilevel power penalty induced. This will be further discussed in the next section.

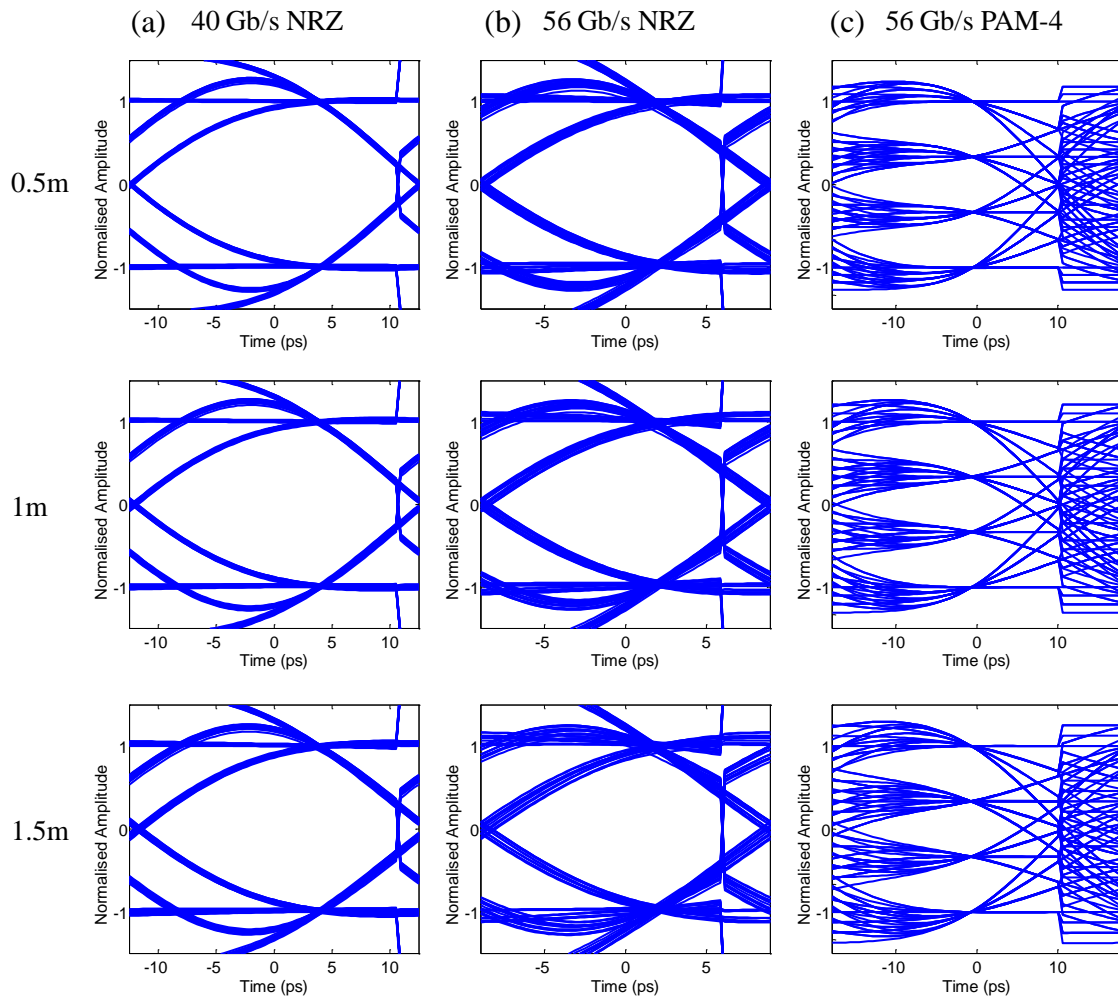


Figure 6-16 Eye diagrams of the signals after the receiver after propagation of waveguide lengths of 0.5m, 1 m and 1.5 m for (a) NRZ at 40 Gb/s, (b) NRZ at 56 Gb/s and (c) PAM-4 at 56 Gb/s with the use of a 7-tap FFE and 5-tap DFE equaliser.

6.7 Power Budget Analysis

By calculating the differences between the received optical power for various output signals and the reference signal, different power penalties can be found and the system power budget can be subsequently obtained. The total system power budget is 12.5 dB based on the parameters employed in section 6.6. The performance of both NRZ and PAM-4 links is discussed below for 0.5 m, 1 m and 1.5 m long waveguides at data rates of 40 Gb/s and 56 Gb/s with and without the use of equalisation. The available system margins for both

schemes are calculated and compared in this section. The obtained results indicate the possibilities of transmitting such high data rates over these multimode waveguides using both NRZ and PAM-4 schemes, and establish the theoretical foundation for the experimental demonstrations presented in the next section.

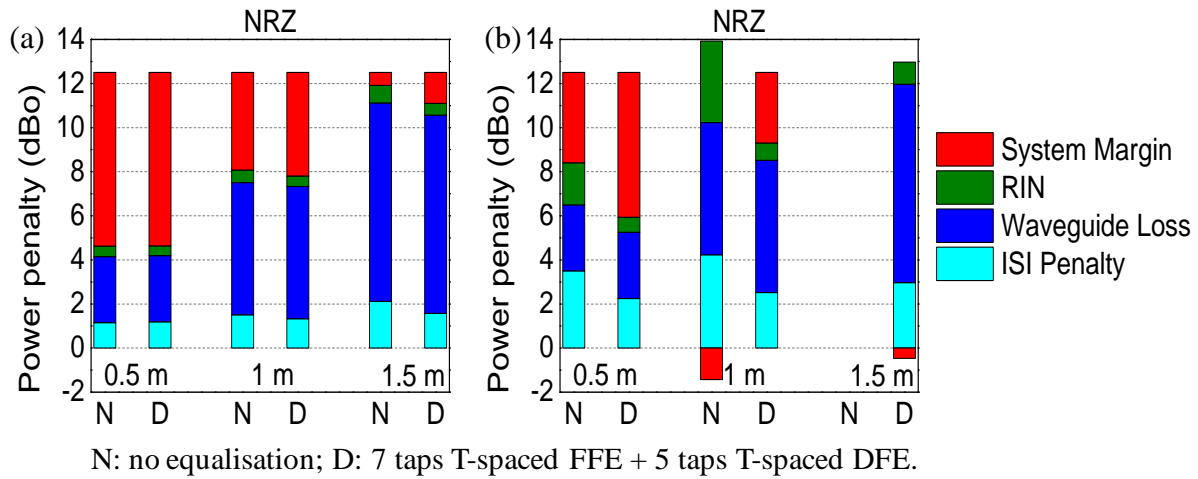


Figure 6-17 Power budget for NRZ signals at (a) 40 Gb/s and (b) 56 Gb/s for waveguide lengths of 0.5 m, 1 m and 1.5 m, respectively.

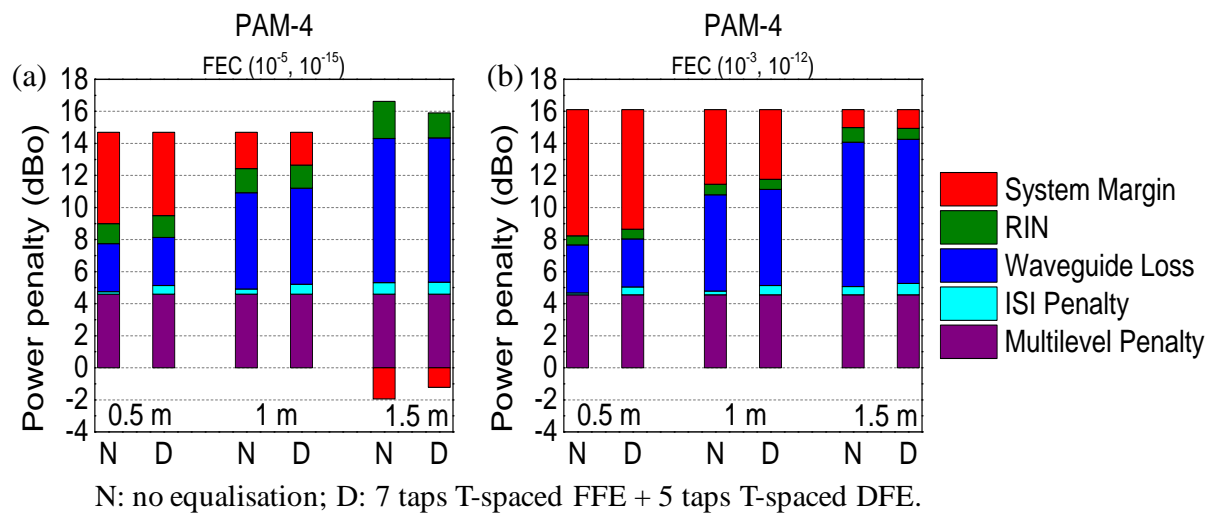


Figure 6-18 Power budget for PAM-4 signals at 56 Gb/s with the use of (a) FEC(10⁻⁵, 10⁻¹⁵) and (b) FEC(10⁻³, 10⁻¹²) for waveguide lengths of 0.5 m, 1 m and 1.5 m, respectively.

Without using forward error correction (FEC), NRZ can support up to a 1.5 m waveguide length with and without equalisation at bit rates of 40 Gb/s as shown in Figure 6-17(a). The system margins are ~7.9 dB (7.9 dB), 4.4 dB (4.7 dB) and 0.6 dB (1.4 dB) for a 0.5 m, 1 m and 1.5 m long waveguide respectively without (with) the use of equalisation. Equalisation

does not make a major difference for short link up to 1 m at low data rates as the induced noise enhancement penalty is comparable to the ISI penalty of the respective link without the use of equalisation. However, it can be noticed that equalisation results in an improved system margin of ~ 0.8 dB when the link length increases to 1.5 m. At a higher data rate of 56 Gb/s, the equalisation technique becomes essential to ensure the feasibility of the link. Although NRZ can support 0.5 m waveguide transmission at 56 Gb/s, the use of equalisers can improve the system margin by ~ 2.5 dB. For the 1 m and 1.5 m links, the NRZ scheme is not sufficient to support 56 Gb/s over such long waveguides. Using equalisation, the system is feasible for 56 Gb/s NRZ data transmission with a system margin of ~ 3.2 dB for a 1 m long waveguide, but it fails to meet the power budget requirement for a 1.5 m long waveguide at such data rates.

For relatively low data rates (e.g. 40 Gb/s) and short links up to 1 m, NRZ modulation is sufficient as system margins of >4 dB can be seen [Figure 6-17(a)]. Multilevel modulation is not able to compete with NRZ at this data rate and link length due to its high multilevel penalty. However, as the data rates and link lengths increase, equalisation techniques are required to remove the ISIs of NRZ signals. In Figure 6-17(b), it can be seen that the noise enhancement penalty and residual ISI penalties gradually increase as the link length increases. At a certain point, when the ISI penalty of NRZ scheme exceeds the multilevel penalty of PAM-4, the multilevel modulation scheme starts to outperform the NRZ scheme.

The PAM-4 scheme requires the use of FEC in order to gain extra power budget. Two different FEC schemes (10^{-5} and 10^{-3}) are considered for the PAM-4 modulation format. In comparison to the common 10^{-3} FEC scheme, a more stringent link performance is required for the 10^{-5} FEC scheme but a lower latency can be achieved. The simulation results show that the 56 Gb/s PAM-4 link is feasible for both FEC schemes for the waveguide links of 0.5 m and 1 m without the need of equalisation. For the 0.5 m link, the system exhibits the largest margin of ~ 5.7 dB and 7.9 dB for 10^{-5} and 10^{-3} FEC scheme respectively with no equalisation. A system margin of ~ 2.3 and 4.6 dB can be achieved with a 10^{-5} and 10^{-3} FEC threshold for the 1 m long waveguide link with no equalisation. The system is only feasible with 10^{-3} FEC and a system margin of ~ 1.1 dB is achieved for the longest 1.5 m waveguide link. It can also be seen that the use of equalisation does not affect the system performance significantly in this case, indicating that equalisation is not necessary for implementation of such links operating at the data rates studied. This can be justified from the good eye openings shown in Figure 6-15(c) due to the reduced symbol rate and thus the relaxed

requirements of the component bandwidth. The noise enhancement penalty turns out to be comparable to the ISI penalty without the use of equalisation at such data rates.

6.8 Experiments

In section 6.7, it has been theoretically shown that it is feasible to achieve high-speed transmission of 40 Gb/s NRZ and 56 Gb/s PAM-4 over a 1 m long multimode waveguide without the need for equalisation. In this section, high-speed data transmission using both NRZ and PAM-4 modulation schemes are evaluated experimentally. A record error-free ($\text{BER} < 10^{-12}$) 40 Gb/s data transmission over a 1 m long spiral waveguide using NRZ scheme is first presented, followed by the demonstration of a record 56 Gb/s using PAM-4 modulation over a similar waveguide. An estimated BER of 10^{-5} is achieved using PAM-4, which is within low-latency FEC limits. Open eye diagrams are recorded in both experiments without the use of any equalisation. The experimental results are in good agreement with the simulation results.

6.8.1 40 Gb/s NRZ

Error-free 25 Gb/s data transmission has been demonstrated over a 1.4 m long spiral waveguide discussed in section 4.2.1. Due to the high insertion loss (~ 13 dB) of this waveguide, the high-speed performance of the system is limited by the available power budget rather than the bandwidth of the components. Therefore, the 1 m long spiral waveguide designed for low loss operation (details discussed in section 4.2.2) is utilised to demonstrate the potential of achieving even higher data transmission over such waveguides. The bandwidth performance of this 1 m long waveguide has been studied thoroughly in Chapter 4, and it has been shown that this waveguide exhibits a BLP of at least 35 GHz \times m for a wide range of launch conditions studied and a robust performance in the presence of input offsets. These experimental results indicate that these multimode waveguides have enough bandwidth to support data rates of 40 Gb/s. In this section therefore, the theoretical calculations presented in section 6.7 is experimentally proved to be sensible and a record data rate of error-free ($\text{BER} < 10^{-12}$) 40 Gb/s over such a 1 m long waveguide is reported [33].

6.8.1.1 Experimental Setup

Figure 6-19 shows the setup employed in the data transmission experiments. An 850 nm VCSEL with bandwidth of ~ 25 GHz (oxide aperture is 9.5 μm) is used as the light source

[30], while the receiver employs a 50/125 μm MMF pigtailed photodiode with a bandwidth of ~ 30 GHz (VIS D30-850M). The VCSEL is directly modulated via a 40 GHz bias tee and a 40 GHz RF probe by a 2^7-1 PRBS. This short bit sequence is generated by an Anritsu pattern generator (MP1800A) in order to emulate the short run length block codes typically employed in datacommunication links (e.g. 8B10B) [34]. A pair of 16 \times microscope objectives (NA = 0.32) is employed to couple the emitted light from the VCSEL directly into the waveguide to minimise the coupling losses. A 50/125 μm MMF is used at the waveguide output to collect the transmitted light with the use of index-matching gel at the output facet to further minimise coupling losses. At the receiver end, a multimode VOA (Agilent NA7766A) is used to adjust the average optical power level and introduce optical loss comparable to the insertion loss of the waveguide in the back-to-back link. The received electrical signals are amplified by a 40 GHz SHF amplifier (SHF 807) at the photodiode end, while a digital communication analyser (Infiniium 86100A) is used to observe the electrical waveforms and a bit error ratio tester (BERT: Anritsu MP1800A) is employed to perform BER measurements. The link without the spiral waveguide (back-to-back) is also set up for comparison [Figure 6-19(b)]. The emitted light from the VCSEL source is collected using a cleaved 50/125 μm MMF and a short fibre patchcord is used to deliver the light to the photodiode via the VOA. The total insertion loss of the 1 m long spiral waveguide [power difference between points A and B in Figure 6-19(a)] is measured to be approximately 9 dB, which includes the propagation and coupling losses. The insertion loss of the VOA is ~ 1.9 dB.

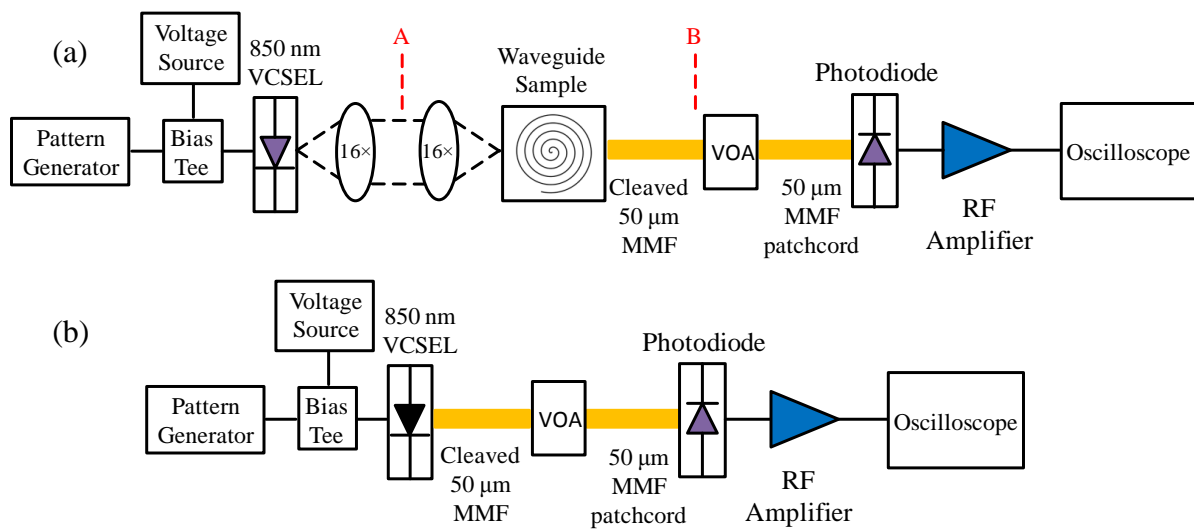


Figure 6-19 Experimental setup for (a) the waveguide link and (b) the back-to-back optical link.

6.8.1.2 Experimental Results

The data transmission experiments are carried out at the data rates of 25 Gb/s, 36 Gb/s and 40 Gb/s. The performance of both the back-to-back link and the link with the 1 m long spiral waveguide is assessed. The VCSEL operating conditions (current bias, modulation amplitude) are appropriately adjusted for each data rate in order to achieve optimum link performance. Typical values employed in the experiments are ~14.6 mA bias current and ~1.2 Vpp RF modulation amplitude. The received eye diagrams for the back-to-back and waveguide link are shown in Figure 6-20. Open eye diagrams are obtained for all data rates. Some small additional dispersion and noise can be noticed due to the insertion of the waveguide in the link. The bandwidth limitation of the active devices in the link causes the relative eye closure observed at higher data rates (36 and 40 Gb/s) as it can be also observed in the eye diagrams obtained in the back-to-back link.

BER measurements are also conducted on both optical links. Error-free ($\text{BER} < 10^{-12}$) data transmission is achieved over the waveguide link for all data rates up to 40 Gb/s. Figure 6-21 shows the obtained BER curves as a function of the average received optical power for both the waveguide and back-to-back link. A small power penalty is due to the insertion of the waveguide in the link and is found to be ~0.4 dB for 25 Gb/s, and ~0.8 dB for 36 Gb/s and 40 Gb/s for a BER of 10^{-9} .

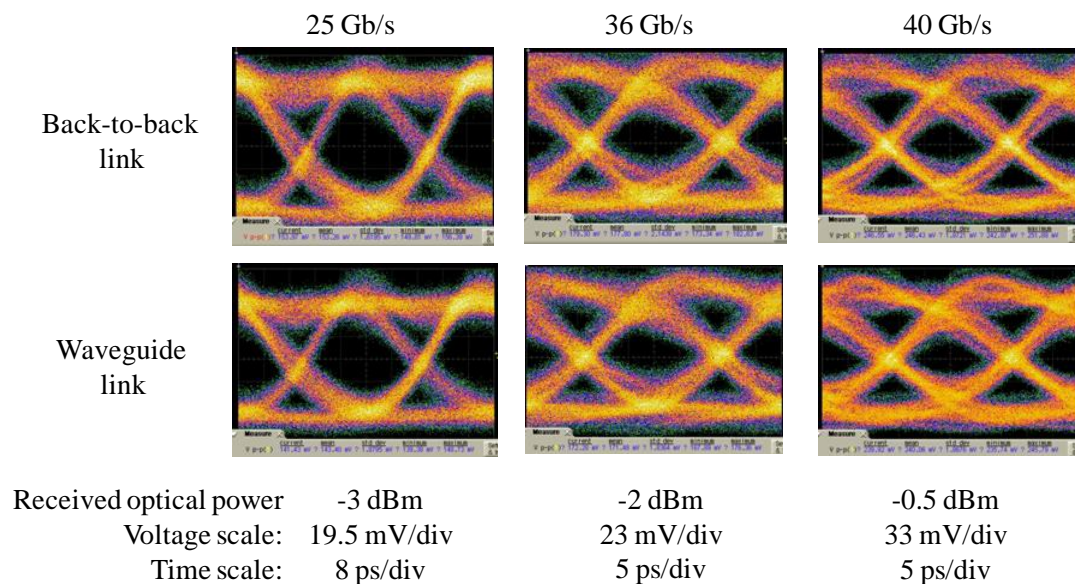


Figure 6-20 Received eye diagrams for optical back-to-back and the waveguide links at 25 Gb/s, 36 Gb/s and 40 Gb/s. Average received optical power noted for each data rate as well as the respective voltage and time scales of the recorded waveforms.

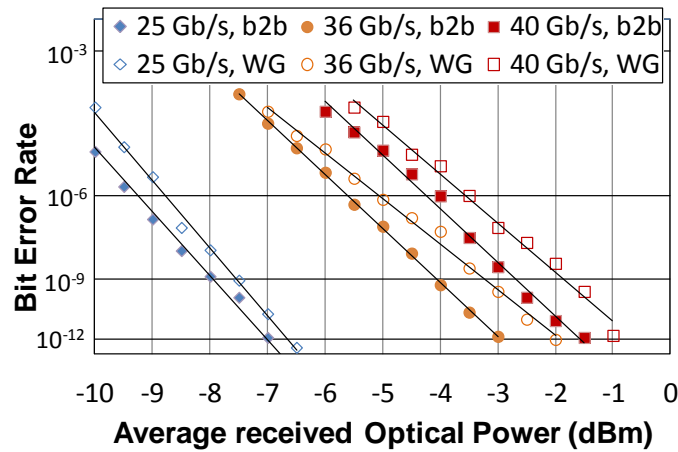


Figure 6-21 BER curves for the optical back-to-back (b2b) link and the link with the 1 m long spiral waveguide (WG) obtained at 25, 36 and 40 Gb/s.

In addition, the effect of the input offsets on the high-speed performance of this 1 m long spiral waveguide is also examined. The robustness of the link performance across different input offsets raises an important concern for real-world applications. It has been previously shown that the dynamic performance of this waveguide does not degrade significantly in the presence of the spatial offsets with a BLP of >35 GHz \times m. Consequently, the dynamic performance of the waveguide is assessed by shifting the launch position, and it has been experimentally determined that no significant transmission impairments in the link are observed for the data rates under consideration.

A similar setup as shown in Figure 6-19(a) is used in this offset experiment, while the input $16\times$ lens is placed on a translation stage and a displacement sensor is employed to control the spatial offsets. The received power is recorded using an optical power meter head (HP 81525A). Eye diagrams are recorded for both the back-to-back link and waveguide link at data rates of 25 Gb/s and 40 Gb/s for varying spatial offsets as shown in Figure 6-22 and Figure 6-24 respectively. The VOA is used to fix the average optical power level for both data rates in order to compensate the induced coupling loss by the input offsets. Good eye openings can be observed for both data rates across different offsets. In addition, BER measurements at varying offsets for both data rates are carried out. Figure 6-23(a) and Figure 6-25(a) show the BER curves versus average received optical power at different offsets, while Figure 6-23(b) and Figure 6-25(b) present the respective power penalties across offsets for data rates of 25 Gb/s and 40 Gb/s respectively. -1 dB alignment tolerance is up to $\sim\pm 10$ μ m. Relatively constant power penalties with little variation of $\sim\pm 0.1$ dB are observed at different launch positions, and are found to be ~ 0.4 dB for 25 Gb/s and ~ 0.8 dB for 40 Gb/s

for a BER of 10^{-9} . These results clearly demonstrate the potential of this technology for use in board-level optical interconnects and its robust performance of supporting high data rates up to 40 Gb/s for a large range of input offsets of $>\pm 10 \mu\text{m}$ despite its highly-multimoded nature.

(I) 25 Gb/s

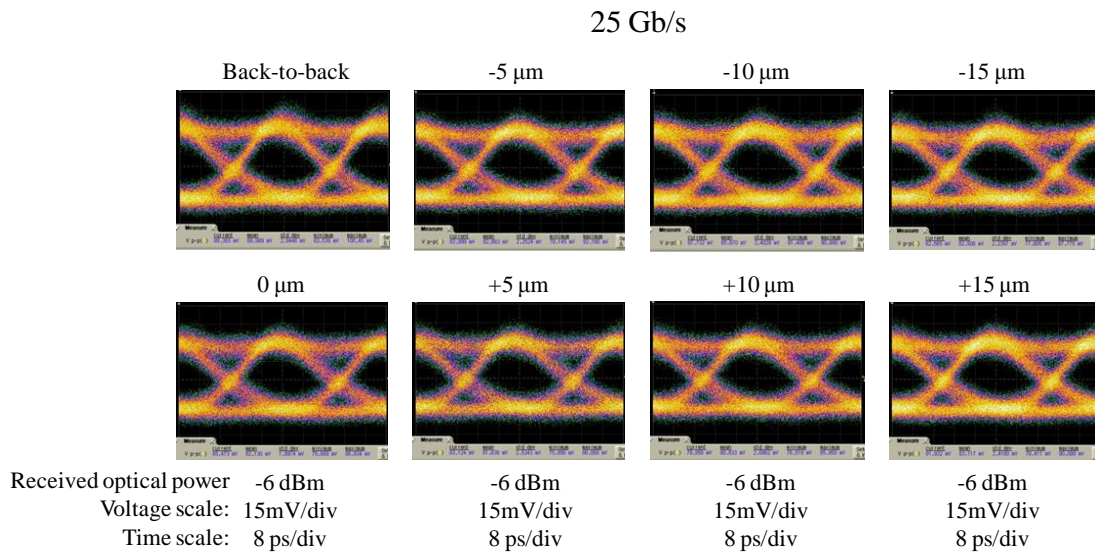


Figure 6-22 Received eye diagrams for optical back-to-back and the waveguide links at 25 Gb/s for different horizontal offsets. Average received optical power as well as the respective voltage and time scales of the recorded waveforms noted.

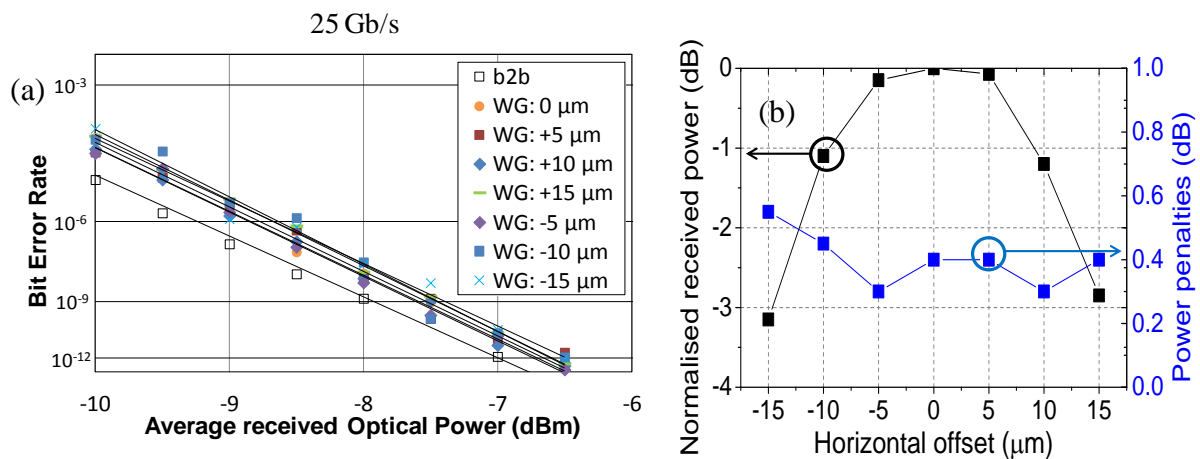


Figure 6-23 (a) BER curves for the optical back-to-back (b2b) link and the link with the 1 m long spiral waveguide (WG) at different horizontal offsets, and (b) normalised received power and power penalties for a BER of 10^{-9} as function of input offsets obtained at 25 Gb/s.

(II) 40 Gb/s

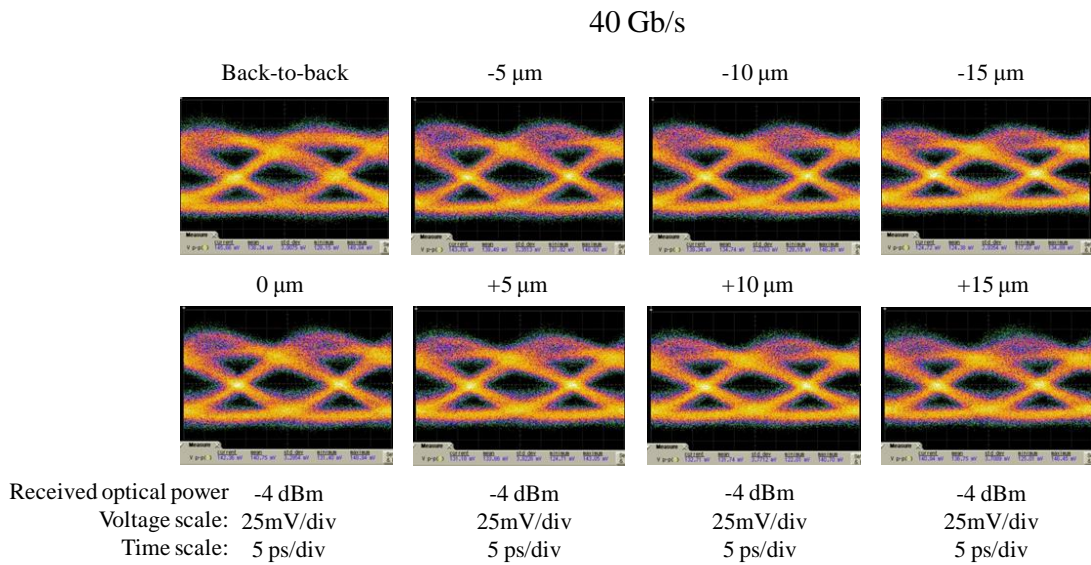


Figure 6-24 Received eye diagrams for optical back-to-back and the waveguide links at 40 Gb/s for different spatial offsets. Average received optical power as well as the respective voltage and time scales of the recorded waveforms noted.

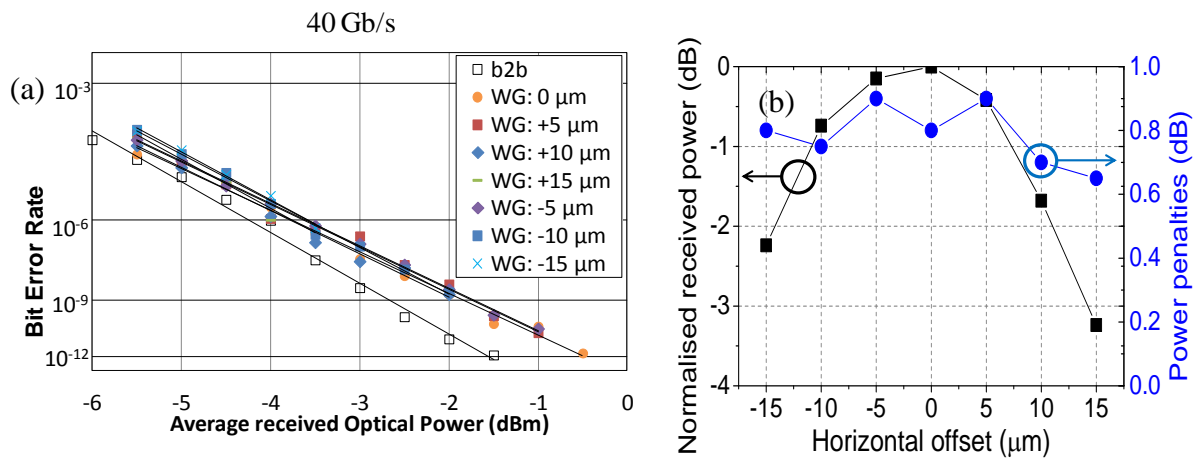


Figure 6-25 (a) BER curves for the optical back-to-back (b2b) link and the link with the 1 m long spiral waveguide (WG) at different horizontal offsets, and (b) normalised received power and power penalties for a BER of 10^{-9} as function of input offsets obtained at 40 Gb/s.

6.8.2 56 Gb/s PAM-4

After the successful demonstration of record 40 Gb/s data transmission over a 1 m long multimode spiral waveguide, we are interested in further increasing the interconnection

capacity of such waveguide-based systems. Either a greater number of on-board optical links or higher data rates over each waveguide channel are required to achieve so. We have shown that these waveguides have enough bandwidth to support even 100 Gb/s data rates over a single channel in Chapter 4. However, the implementation of such high data rates on-board strictly requires very high-specification of active devices such as VCSELs and photodiodes as well as the driving electronic circuits in order to ensure RF signal integrity. Significant engineering challenges still remain for the RF system design, and cost and complexity issues also occur at such high on-board data rates. Therefore, it is necessary to find an alternative way to achieve high data rate transmission over each waveguide channel so as to avoid the need of very high-performance electronic and photonic components. In section 6.7, the feasibility of 56 Gb/s data transmission over a 1 m long waveguide has been theoretically assessed using advanced modulation formats such as PAM-4 modulation scheme. In this section, advanced modulation format is successfully demonstrated experimentally on short-reach waveguide-based optical interconnects. For the first time, data transmission of 56 Gb/s using PAM-4 is demonstrated over the 1 m long multimode polymer waveguide (waveguide parameters discussed in section 4.4.1). It should be noted that the experimental work presented below is done in collaboration with Dr. Nikos Bamiedakis.

6.8.2.1 Experimental Setup

Figure 6-26 illustrates the setup for the data transmission experiment. The VCSEL employed is an 850 nm multimode with a bandwidth of ~25 GHz [35]. The two data outputs of a pattern generator (Anritsu MP1800A) are employed to generate the 4-level PAM modulation signal. Discrete RF components such as a 6 dB attenuator and a variable electrical delay line are used to delay the two output signals. The PAM-4 modulation signal is generated by appropriately attenuating and re-combining the two signals with an inductive RF coupler, and is fed to the VCSEL via a high-bandwidth RF probe and a bias tee. A pair of 16× microscope objective (NA = 0.32) is used to couple the emitted light into the waveguide while at the waveguide output a cleaved 50/125 μm MMF patchcord is employed to collect the transmitted light. Index matching gel is used at the waveguide output to minimise the coupling losses. The total insertion loss of the 1 m long spiral waveguide is measured to be ~7 dB. At the receiver end, the multimode optical module of a digital sampling oscilloscope (DSA8300, Tektronix 80C15) is employed. A VOA is inserted in the optical link in order to adjust the received optical power. For comparison, the link without the waveguide (back-to-back) link is also tested.

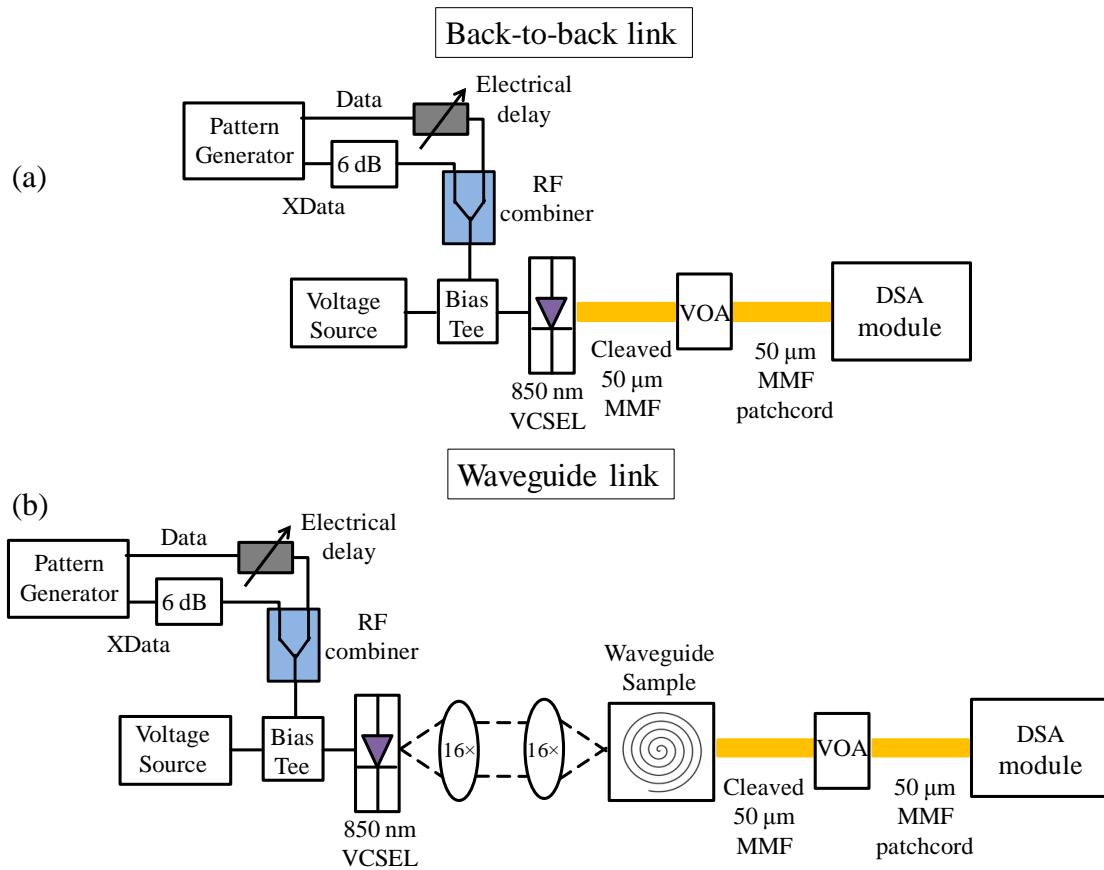


Figure 6-26 Experimental setup of (a) the back-to-back and (b) the waveguide link.

6.8.2.2 Experimental Results

The open eye diagrams of 28 Gbaud PAM-4 (56 Gb/s aggregate bit rate) are recorded using the sampling oscilloscope in both the back-to-back and waveguide links (Figure 6-27). Clear four levels can be seen in both links. A Q-factor analysis is used to estimate the BER as proper BER measurements cannot be conducted given the available receiver module in this experiment. The histograms of recorded eye diagrams at different received optical power levels are analysed. Figure 6-28(a) shows the histogram of a recorded eye diagram while Figure 6-28(b) presents the estimated BER curve as a function of the average received optical power for both optical links. An estimated BER of 10^{-5} is achieved while a power penalty of ~ 1 dB is introduced due to the insertion of the waveguide in the link. This result is in good agreement with the simulation results presented in section 6.7. The performance of the link allows the application of low-latency FEC schemes. The results clearly demonstrate the potential of using advanced modulation formats (e.g. PAM-4) to boost data transmission rates over each waveguide channel without the need for high-performance optoelectronic components and complex RF layout design.

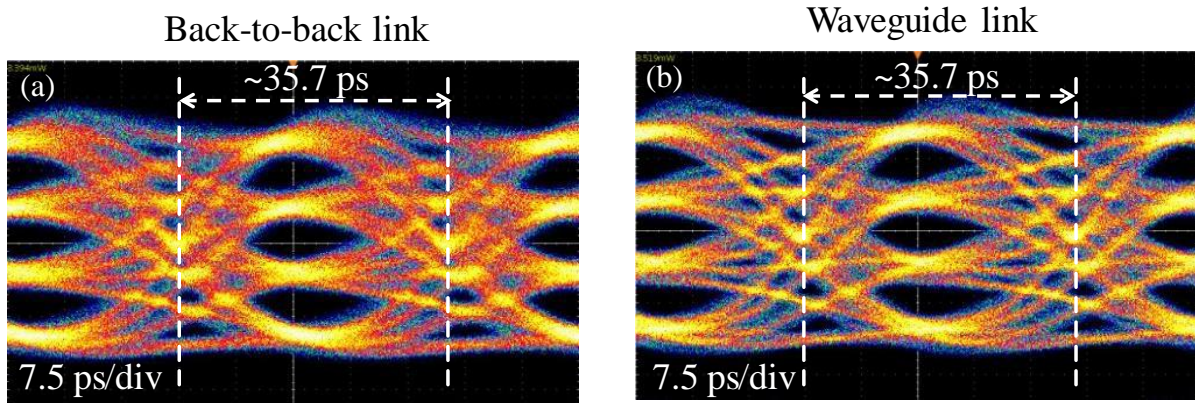


Figure 6-27 Recorded 28 Gbaud (56 Gb/s) eye diagrams for the (a) back-to-back and (b) the waveguide link [36].

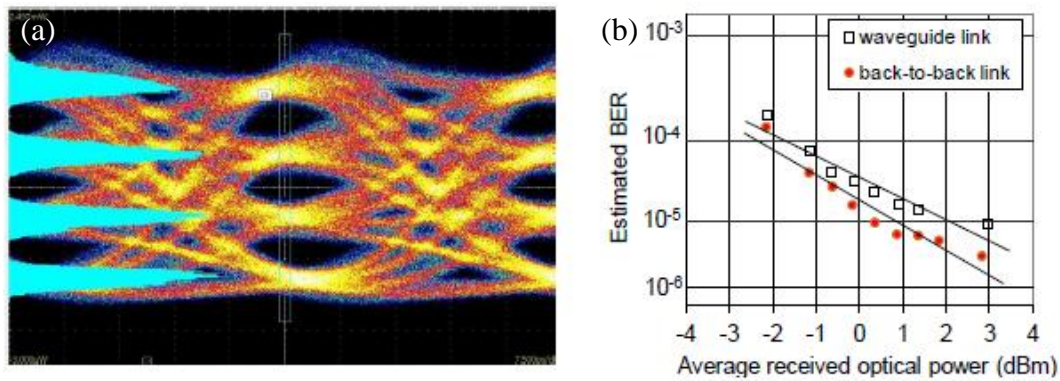


Figure 6-28 Estimated BER using Q-factor analysis [36].

6.9 Summary

This chapter investigates the high-speed data transmission over the multimode polymer waveguides for use in board-level optical interconnects. Both NRZ and PAM-4 modulation schemes are reviewed, and a system simulation model is developed to assess and compare the performance of the two different modulation schemes for use on these waveguides. The VCSEL transmitter and multimode waveguide are modelled as low-pass filters with Gaussian responses, while a 4th-order Bessel Thomson filter is used to model the receiver. The parameters are chosen from the components that are likely to be employed in the experiments. Equalisation, an important technique to remove ISI in the system, is also discussed. FFE and DFE equalisers are studied and a 7-tap T-spaced FFE and 5-tap T-spaced DFE equaliser is implemented in the simulation model. BER calculation procedures of both modulation schemes are discussed, and link power budget analysis is also introduced to categorise different power penalties in the waveguide-based optical link. The simulation

results have shown that 40 Gb/s NRZ can be achieved up to a 1.5 m long waveguide regardless the employment of equalisation, while the use of equalisers can extend the data rate to 56 Gb/s up to a 1.5 m link length. Alternatively, the use of modulation schemes such as PAM-4 is proposed to achieve very high data rates (>40 Gb/s) to avoid the need of high-specification optoelectronic components and complex RF system design. The simulation has shown that data transmission of 56 Gb/s using PAM-4 modulation scheme over a 1.5 m long waveguide is feasible with the 10^{-3} low-latency FEC applied without the use of equalisation. Record NRZ 40 Gb/s and PAM-4 56 Gb/s data transmissions over a 1 m long spiral waveguide are further demonstrated experimentally, which is in good agreement with the simulation results. These results certainly show the potential to use this technology for very high-speed on-board optical interconnects despite using highly-multimoded waveguides, and clearly demonstrate their capability for transmitting on-board data rates of >40 Gb/s over distances of 1 m.

6.10 References

- [1] M. Chacinski, N. Chitica, S. Molin, N. Lalic, and O. Sahlen, "25.78 Gbps Data Transmission with 850nm Multimode VCSEL Packaged in QSFP Form Factor Module," *Opt. Fiber Commun. Conf. Expo. Natl. Fiber Opt. Eng. Conf. (OFC/NFOEC)*, 2013, p. OW1B.1, 2013.
- [2] N. Bamiedakis, R. V. Pentty, and I. H. White, "25 Gb/s Data Transmission over a 1.4 m Long Multimode Polymer Spiral Waveguide," *Cleo 2014*, p. STu1G.7, 2014.
- [3] C. Cole, "Beyond 100G Client Optics," *IEEE Commun. Mag.*, vol. 50, no. 2, pp. 58–66, 2012.
- [4] K. Szczerba, P. Westbergh, J. Karout, J. S. Gustavsson, Å. Haglund, M. Karlsson, P. a. Andrekson, E. Agrell, and A. Larsson, "4-PAM for High-Speed Short-Range Optical Communications," *J. Opt. Commun. Netw.*, vol. 4, no. 11, pp. 885–894, 2012.
- [5] J. L. Wei, J. D. Ingham, D. G. Cunningham, R. V. Pentty, S. Member, and I. H. White, "Performance and Power Dissipation Comparisons Between 28 Gb/s NRZ, PAM, CAP and Communication Applications," *J. Light. Technol.*, vol. 30, no. 20, pp. 3273–3280, 2012.
- [6] C. Xiong, D. Gill, J. Proesel, J. Orcutt, W. Haensch, and W. M. J. Green, "A Monolithic 56 Gb/s CMOS Integrated Nanophotonic PAM-4 Transmitter," in *2015 IEEE Optical Interconnects Conference (OI)*, 2015, p. MC3.
- [7] K. D. Sadeghipour, P. D. Townsend, and P. Ossieur, "Design of a Sample-and-Hold Analog Front End for a 56Gb/s PAM-4 Receiver Using 65nm CMOS," *IEEE Int. Symp. Circuits Syst.*, pp. 1606–1609, 2015.
- [8] K. Szczerba, P. Westbergh, M. Karlsson, A. Larsson, and P. a. Andrekson, "60 Gbits Error-Free 4-PAM Operation With 850 nm VCSEL," *Electron. Lett.*, vol. 49, no. 15, pp. 953–955, 2013.
- [9] K. Szczerba, P. Westbergh, M. Karlsson, P. a. Andrekson, and A. Larsson, "70 Gbps 4-PAM and 56 Gbps 8-PAM Using An 850 nm VCSEL," *J. Light. Technol.*, vol. 33, no. 7, pp. 1395–1401, 2015.
- [10] S. Walklin and J. Conradi, "Multilevel Signaling for Increasing The Reach of 10 Gb/s Lightwave Systems," *J. Light. Technol.*, vol. 17, no. 11, pp. 2235–2248, 1999.

- [11] M. Sharif, J. K. Perin, and J. M. Kahn, "Modulation Schemes for Single-Laser 100 Gb/s Links : Single-Carrier," *J. Light. Technol.*, vol. 33, no. 20, pp. 4268–4277, 2015.
- [12] "IEEE P802.3bs 400 Gb/s Ethernet Task Force." [Online]. Available: <http://www.ieee802.org/3/bs/>.
- [13] G. P. Agrawal, *Fibre-Optics Communication Systems*, Third Edit. John Wiley & Sons, Inc., 2002.
- [14] K. SANKAR, "Binary to Gray code conversion for PSK and PAM." [Online]. Available: <http://www.dsblog.com/2008/05/11/binary-to-gray-code-conversion-psk-pam/>.
- [15] W. Nakwaski, "Principles of VCSEL designing," *Opto-Electronics Rev.*, vol. 16, no. 1, pp. 18–26, 2007.
- [16] G. D. Brown, "Bandwidth and Rise Time Calculations for Digital Multimode Fiber-optic Data Links," *J. Light. Technol.*, vol. 10, no. 5, pp. 672–678, May 1992.
- [17] I. H. White, D. G. Cunningham, and C. H. Kwok, "Shannon Capacity Calculation on Multimode Fibres," *IET Optoelectron.*, vol. 3, no. 3, pp. 149–157, Jun. 2009.
- [18] "IEEE P802.3aq 10GBASE-LRM Task Force." [Online]. Available: <http://www.ieee802.org/3/aq/>.
- [19] G. Liang, "Transmission Capacity Improvement for High Speed Multimode Waveguide Links Using Advanced Optical Launch and Multimode Modulation Schemes," University of Cambridge, 2013.
- [20] B. A. Robert Lashlee, "Introduction to Feed-Forward Equalization (FFE) and Decision Feedback Equalization (DFE)." [Online]. Available: <http://www.canadianelectronics.ca/articles/introduction-to-feed-forward-equalization-ffe-and-decision-feedback-equalization-dfe-part-2>.
- [21] D. G. Cunningham, A. Technologies, R. V Johnson, and F. Corporation, "Exact Expressions For Tap Weights And Noise Enhancement For A FFE (3, T) Assuming The Pulse Response Of The 32 Gigabit Fibre Channel Optical Link Model," no. April, pp. 1–9, 2012.
- [22] L. Geng, J. Wei, R. V. Penty, I. White, and D. G. Cunningham, "3 Gbit/s LED-Based Step Index Plastic Optical Fiber Link Using Multilevel Pulse Amplitude Modulation," *Opt. Fiber Commun. Conf. Fiber Opt. Eng. Conf. 2013*, p. OTh4A.1, 2013.
- [23] G. P. Agrawal, "Noise in Semiconductor Lasers and Its Impact on Optical Communication Systems," *SPIE*, vol. 1376, no. 2, pp. 224–235, 1990.
- [24] S. E. Hashemi, "Relative Intensity Noise (RIN) in High-Speed VCSELs for Short Reach Communication Master of Science Thesis in Photonics Engineering," Chalmers University of Technology, 2012.
- [25] L. A. Coldren and S. W. Corzine, *Diode Lasers and Photonics Integrated Circuits*. New York, USA: John Wiley & sons, 1995.
- [26] "Impact of Transmitter RIN on Optical Link Performance Impact of Transmitter RIN on Optical Link Performance." [Online]. Available: <http://pdfserv.maximintegrated.com/en/an/AN3470.pdf>.
- [27] "Fibre Channel - Methodologies for Signal Quality Specification - MSQS," 2010.
- [28] E. A. Lee and D. G. Messerschmitt, *Digital Communication*, Second Edi. Kluwer Academic Publishers, 1993.
- [29] Q. Sun, "Novel Optical Launch Techniques for High-speed Extended-reach Multimode-fibre Datacommunication Links," University of Cambridge, 2010.
- [30] P. Westbergh, R. Safaisini, E. Haglund, J. S. Gustavsson, A. Larsson, and A. Joel, "High-Speed 850 nm VCSELs With 28 GHz Modulation Bandwidth For Short Reach Communication," *Proc. SPIE*, vol. 8639, pp. 86390X–1–6, 2013.

- [31] I. White, J. Ingham, and R. Penty, "Systems Aspects of Optical Technologies for Use in Datacommunications," *Opt. Fiber Commun. Conf. Fiber Opt. Eng. Conf. 2011*, p. OMM1, 2011.
- [32] J. D. Ingham, R. V. Penty, and I. H. White, "10 Gb/s Transmitter-Based Equalization For Extended-Reach Multimode-Fiber Datacommunication Links," *OFC/NFOEC 2007*, p. OTuL4, 2007.
- [33] N. Bamiedakis, J. Chen, R. V. Penty, I. H. White, P. Westbergh, and A. Larsson, "40 Gb/s Data Transmission over a 1 m Long Multimode Polymer Spiral Waveguide," in *European Conference on Optical Communication*, 2014, p. P.4.7.
- [34] J. D. Ingham, R. V. Penty, and I. H. White, "Carrierless Amplitude and Phase Modulation for Low-Cost, High-Spectral-Efficiency Optical Datacommunication Links," in *OSA/OFC/NFOEC*, 2011, p. OThZ3.
- [35] B. Kögel, J. S. Gustavsson, E. Haglund, R. Safaisini, A. Joel, P. Westbergh, M. Geen, R. Lawrence, and A. Larsson, "High-Speed 850 nm VCSELs with 28 GHz Modulation Bandwidth Operating Error-Free Up To 44 Gbit/s," *Electron. Lett.*, vol. 48, no. 18, pp. 1145–1147, 2012.
- [36] N. Bamiedakis, J. Wei, J. Chen, P. Westbergh, A. Larsson, R. V. Penty, and I. H. White, "56 Gb/s PAM-4 Data Transmission Over a 1 m Long Multimode Polymer Interconnect," *Conf. Lasers Electro-optics*, p. STu4F.5, 2015.

7 CONCLUSIONS AND FUTURE WORK

This chapter provides a summary of the contents presented in this dissertation by recapitulating the important findings and results of each chapter, and gives directions for future work.

7.1 Conclusions

Optics provides an alternative solution to the interconnection bandwidth bottleneck foreseen in future data centres and supercomputers due to the inherent disadvantages of existing copper wires. Polymer waveguides are a promising technology for board-level optical interconnects that have received considerable interest from both academic and industrial research laboratories worldwide as they satisfy the requirements of cost-effective manufacturing processes and compatibility with conventional electronic PCBs. To date, the field has evolved from the study of fundamental nature of optical transmissions in various waveguide structures to the demonstration of complex backplane architectures. In this thesis, a particular facet of this field has been selected for investigation – the demonstration of high-bandwidth multimode polymer waveguides and high-speed data transmission over such waveguides. All of this work tries to advance this technology for real-world adoption by addressing commercial concerns of a promising technology including issues of cost, manufacturing and reliability. To this end, fundamental waveguide modelling is developed, waveguide parameters and design guidelines are formalised, and possible approaches to

achieving high-bandwidth performance are suggested to meet the requirements aforementioned. Each chapter has sought to focus on one particular aspect of this mission.

Chapter 1 discusses the challenges faced by traditional electrical links for use in future computing systems. The argument of using optical interconnects is made to solve the severe obstacles that electrical interconnects face such as dramatically increased loss, crosstalk, power consumption and limited bandwidth as data rates increase. Optics can enable high-speed short-reach interconnects while eliminating many of the problems encountered by electrical links. The cost-bandwidth analysis determines that the board-level interconnects will be the next step for the transition from electrical to optical, and hence polymer waveguides are selected for use in the next-generation high-speed interconnections at the board level.

Chapter 2 introduces different material systems commonly used for board-level optical interconnects. Polymer materials are identified as an excellent choice, of which Dow Corning siloxane material is identified as particularly interesting due to its superior characteristics including sufficiently low cost, excellent mechanical, thermal and optical properties appropriate for use at wavelength of 850 nm and suitability for direct integration on PCBs. Waveguide structures can be fabricated using conventional methods such as photolithography and embossing onto various types of substrates (FR4, silicon and glass). Active devices such as VCSELs and photodiodes suitable for board-level optical interconnects are briefly discussed. Two main coupling methods of coupling light in and out of polymer waveguides (out-of-plane and butt-coupling schemes) are introduced, while a review of the state-of-the-art demonstrators in polymer waveguide technology is presented. It can be noticed that almost all reported demonstrators employ short straight parallel waveguides (<20 cm) with maximum data transmission rates of 25 Gb/s achieved, however the fundamental waveguide characteristics such as dimensions, index step, refractive index profile and waveguide dispersion are rarely investigated in details. In addition, the deployment of advanced modulation formats on short-reach optical interconnects has not yet been demonstrated.

Chapter 3 introduces the fundamental design parameters and optical transmission properties of the multimode polymer waveguides studied in this thesis. The theoretical modelling based on ray tracing method and electromagnetic treatment is described. The coupling efficiency as well as the associated alignment tolerances of low-cost butt-coupling configurations employing SMF and MMF is estimated for a wide range of waveguide parameters (waveguide widths $20\text{ }\mu\text{m} \leq w \leq 60\text{ }\mu\text{m}$, and index steps $0.005 \leq \Delta n \leq 0.03$). The

SMF launch provides negligible coupling efficiency (approximately equal to Fresnel loss) and large alignment tolerances of the order of the waveguide half width. The use of MMF results in higher coupling losses which strongly depend on the mismatch of the numerical aperture between waveguide and fibre and their relative dimensions. The experimental results agree well with the simulation results. Furthermore, a theoretical evaluation of the waveguide dispersion is carried out. It is shown that the chromatic dispersion is less significant to the link bandwidth for the link lengths under consideration. Rather, multimode dispersion can limit the dynamic performance of the link and strongly depends on the launch conditions. The restricted launch can offer a BLP of larger than 100 GHz×m for the waveguide parameters under consideration. The overfilled BLP of the waveguides is found to be in the range from 7 to 50 GHz×m, and the overfilled MMF launches provide BLP values approximately similar to the worst-case scenario of an overfilled waveguide. Appropriate design rules can be derived to ensure low coupling loss and sufficient link bandwidth for a specific application. Overall, this chapter provides a concrete theoretical foundation for the experimental investigation in the waveguide dispersion to be presented in the next chapter.

Chapter 4 presents the experimental results on the dispersion of the multimode polymer waveguides. Two approaches are employed to investigate the modal dispersion, including frequency-domain (S_{21}) and ultra-short pulse measurements. The frequency-domain measurements on the 1.4 m and 1 m long spiral waveguide demonstrate the instrument-limited BLP values of at least 35 GHz×m for a wide range of launch conditions and in the presence of input spatial offsets. Time-domain measurements are introduced along with the brief discussion of femtosecond lasers and autocorrelators. Two short pulse generation systems are employed so as to allow more detailed studies with a range of launch conditions. The short pulse generation system one utilises a commercial femtosecond Ti:Sapphire laser operating at a wavelength of 850 nm while the second system employs a femtosecond erbium-doped TOPTICA fibre laser source operating at a wavelength of ~1574 nm and a frequency-doubling crystal in order to generate second-harmonic short pulses at the wavelength of ~787 nm. Matching autocorrelators are used as receivers. The ultimate bandwidths of the waveguides are revealed using this approach, and the BLP values are found to be in excess of 40 GHz×m and 70 GHz×m for the SI and GI waveguide respectively for a 50/125 µm MMF launch across an offset range of ± 10 µm, and of >100 GHz×m using a 10× microscope objective launch for an offset range of $\sim 19 \times 8$ µm² and $\sim 18 \times 20$ µm² for the SI and GI waveguide respectively. The high BLP regions are well within -1 dB alignment

tolerances. Simulation results using the theoretical model developed in Chapter 3 based on the real measured refractive index profiles show a good agreement with the experimental results. These results indicate the capacity of these multimode polymer waveguides to support on-board data rates of 100 Gb/s and beyond over a single waveguide channel using achievable launch conditioning schemes and appropriate refractive index engineering.

Chapter 5 further investigates the effects of refractive index profiles on the performance of various multimode waveguides and waveguide components. The loss and bandwidth performance of multimode polymer waveguides (reference and spiral waveguides) and functional waveguide elements (90° waveguide bends and 90°/45° waveguide crossings) with different refractive index profiles are fabricated and characterised under different launch conditions. 90° waveguide bends with excess loss below 1 dB for radius of >6 mm and 90° crossings with crossing loss of <0.02 dB/crossing while exhibiting adequate BLP in excess of 47 GHz×m are demonstrated for a 50 µm MMF input using appropriate refractive index engineering. In addition, bending and crossing structures in the waveguide layout are shown to enhance the bandwidth performance. For example, it is possible to achieve a 1.55 times bandwidth improvement (BLP>60 GHz×m) over conventional straight waveguides using a waveguide bend with radius of 5 mm at the cost of a loss penalty of ~1.9 dB for a 50 µm MMF launch. Slightly larger bends with a radius of 11 mm can ensure a BLP>50 GHz×m with a smaller loss penalty of ~0.7 dB. The results obtained using crossing waveguides show that the bandwidth can be increased by up to 1.25 times using a comparably low number of crossings of ~10 with an extra loss of ~1.6 dB. These results indicate the possibility of designing waveguides with low interconnection loss and sufficient link bandwidth using appropriate refractive index engineering, although the choice of refractive index profiles is dependent on each specific application. Overall, the use of refractive index engineering and intelligent waveguide layout is shown to enhance further the performance of these highly-multimoded polymer waveguides.

Chapter 6 demonstrates the high-speed data transmission over the multimode polymer waveguide based optical links with the aim of further pushing the electrical-to-optical boundary. A system model is first developed to compare the performance of both NRZ and PAM-4 modulation schemes for use on short-reach optical interconnects. The VCSEL transmitter and waveguide channel are modelled as Gaussian responses while the receiver is modelled as a 4th-order Bessel Thomson filter with all parameters chosen from the actual components likely employed in the experiments. Equalisation techniques such as FFE and

DFE are also studied and implemented in the simulation model. BER calculation procedures for both modulation schemes are presented while different power penalties in the waveguide-based optical link are characterised and calculated using link power budget analysis. The simulation results show that 40 Gb/s NRZ can be achieved over a 1.5 m long waveguide with and without the use of equalisation although the data rate can be extended to 56 Gb/s over the same length of waveguide using equalisers. In addition, multilevel modulation schemes such as PAM-4 are shown to further increase the data rates without the need of high-specification active devices and sophisticated RF design. The simulation demonstrates the feasibility of transmitting 56 Gb/s data rates over a 1.5 m long waveguide with 10^{-3} low-latency FEC without the need of equalisers. Furthermore, record 40 Gb/s NRZ-based data transmission over a 1 m long spiral waveguide is experimentally demonstrated with a power penalty of ~ 0.8 dB for a BER of 10^{-9} . No significant performance impairments (rather constant power penalties of $\sim \pm 0.1$ dB) across spatial offsets up to ± 15 μm are observed. Finally, 56 Gb/s PAM-4-based data transmission over a similar 1 m long spiral waveguide is demonstrated for the first time. An estimated BER of 10^{-5} is obtained while a power penalty of ~ 1 dB is introduced. The experiments are in good agreement with the theoretical calculation. The obtained results clearly demonstrate the capability of these multimode waveguides to support on-board data rates of >40 Gb/s over distances of 1 m despite their highly-multimoded nature.

7.2 Future Work

The work presented in this thesis constitutes an expansion of the on-going development of cost-effective high-performance board-level optical interconnects based on multimode polymer waveguides. However, there are still a number of issues that need to be further studied in order to advance the work addressed in this thesis. In summary, the suggested studies include the further improvement of the waveguide modelling, the deployment of advanced launch conditions, the optimisation of the refractive index profiles and waveguide layout, the demonstration of 100 Gb/s data transmission and the development of all-plastic optical circuits.

7.2.1 Waveguide Modelling

A more accurate evaluation of optical transmission characteristics of the waveguide-based system is required in order to gain further insight into the light propagation inside the

fabricated multimode waveguide samples particularly for the long complex spiral waveguides. For instance, sidewall surface roughness can be further taken into account in the waveguide modelling. Mode mixing can occur due to the sidewall deformations, and therefore the induced multimode dispersion may be affected. A number of approaches have been proposed to study the effect induced including ray tracing [1] and coupled mode theory [2], [3]. Statistical properties of the roughness can be typically used to describe the properties of surface roughness owing to its random nature. In addition, further investigations are required to quantify the magnitude of mode mixing phenomena inside these waveguides.

Moreover, another important issue that is sometimes forgotten is the stability of the available bandwidth of these waveguides. Therefore, an investigation of the stress analysis and the change of refractive index profiles of the waveguides versus temperature is needed as the variation with temperature (if any) of the refractive indices can significantly affect the mode profiles and propagation constants of the guide modes and hence the induced multimode dispersion as well as coupling loss. This index variation with temperature can be subsequently incorporated into the current model to gain more insight into the change of bandwidth performance of these waveguides in real-world applications where the range of temperatures the waveguide links operate at is essential in commercial products.

7.2.2 Launch Conditions

In Chapters 3 and 4, it has been shown that the bandwidth performance of the multimode polymer waveguides is highly launch condition dependent. The restricted launch results in the highest bandwidth among the launch conditions studied in the thesis due to the excitation of lower-order modes. Similarly, alternative launch conditions may be employed for use on these waveguides to further increase the bandwidth by exciting the higher-order modes. For example, some advanced launch methods such as adaptive launches [4], [5] and twin-spot launches [6] [Figure 7-1(a)] were developed to improve the bandwidth performance of MMFs. However, these launches do not eliminate the modal dispersion completely and hence do not fully employ the ultimate bandwidth of MMF links. In 2010, a novel launch condition known as Hermite-Gaussian line launch was proposed to minimise the modal dispersion providing improved differential modal delay [7] [Figure 7-1(b)]. Based on this, a Hermite-Gaussian square launch was further proposed to reduce the coupling loss while maintaining a similar level of bandwidth [8] [Figure 7-1(c)]. It has been demonstrated that only one mode group in the GI MMF that exhibits similar propagation constant is excited under a carefully

designed Hermite-Gaussian beam, and therefore intermodal dispersion can be effectively eliminated resulting in a high bandwidth. Moreover, the Hermite-Gaussian launches can be implemented using phase masks that have simple structures and are easy to fabricate [8].

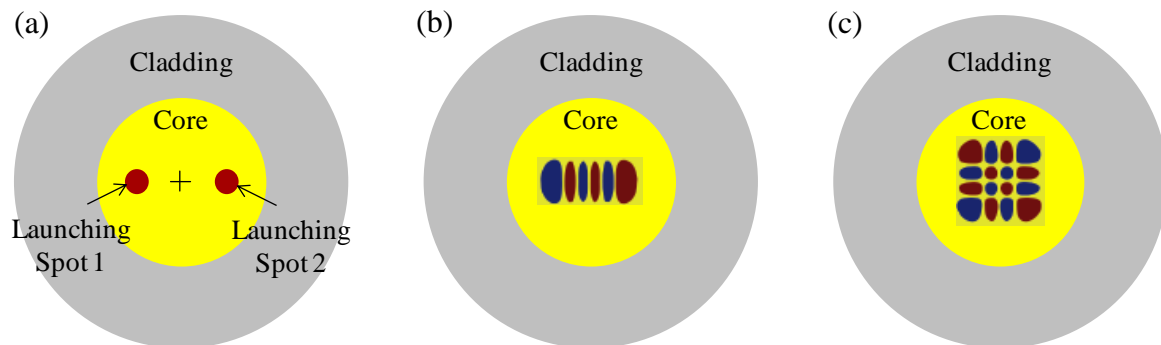


Figure 7-1 Schematic diagram of (a) twin-spot launch, (b) Hermite-Gaussian (5, 0) line launch and (c) Hermite-Gaussian (3, 3) square launch. The two different colours in (b) and (c) represent two phases with a difference of 180°.

The feasibility of the deployment of these advanced launch conditions on the multimode polymer waveguides to further enhance their available bandwidth has not yet been investigated. Further theoretical calculation and experimental demonstrations are required.

7.2.3 Optimisation of Refractive Index Profiles and Waveguide Layout

It has been shown in Chapter 5 that refractive index profiles can significantly vary the loss and bandwidth performance of these multimode polymer waveguides. However, the optimised refractive index profiles that can offer maximum bandwidth while ensuring low loss interconnection are yet to discover. For example, rather than having the index profiles with high index values concentrated on either lower bottom or upper bottom side of the waveguide core, it is worth investigating the performance of waveguides with different parabolic index shapes with varying coefficients of squire-law profile typically seen in the conventional GI MMFs. Furthermore, the successful fabrication of the optimised index profiles is another important issue by employing traditional photolithography processes as it might be difficult to precisely control the refractive index profiles with a particular design parameter. Preliminary work toward this goal has been recently reported in [9].

In addition, it is shown that the bandwidth of the multimode waveguides can be enhanced by employing bending structure due to the mode stripping properties of the bend. However, this approach inevitably introduces additional loss. A trade-off between the bending radius

and induced optical loss clearly exists, and the optimised radius is yet to prove. Furthermore, the combination of waveguide structure and refractive index engineering may offer an optimised bandwidth and loss performance.

Therefore, more investigation into the design, fabrication and characterisation of the multimode polymer waveguides with a wide range of refractive index profiles and different layouts are worth carrying out. Nevertheless, the theoretical model developed and the experimental approaches employed in this thesis can certainly lay a foundation for any future studies.

7.2.4 Toward 100 Gb/s Data Transmission

- Advanced Modulation Schemes

It is unlikely that NRZ can support 100 Gb/s data rates using the existing low-bandwidth active devices unless VCSELs and PDs with higher bandwidth in the order of ~60 GHz become available. It has been demonstrated that multilevel modulation format such as PAM-4 can achieve higher data rates using low-bandwidth devices with FEC. Higher data rates can be further achieved with the use of equalisation. Therefore, electronic equalisation can be used in future real-time data transmission over these waveguides. Moreover, FFE/DFE equalisers used in the simulation model may be disadvantaged by being placed after the dominant noise sources in the optical link [Figure 7-2(a)]. Transmitter-based equalisations have been shown to improve the link performance by reducing the noise enhancement caused by the FFE in the receiver side [10] [Figure 7-2(b)], which can be incorporated into the current system model. In addition to PAM-4, PAM-8 is worth investigating and the comparison between the two schemes needs to be conducted.

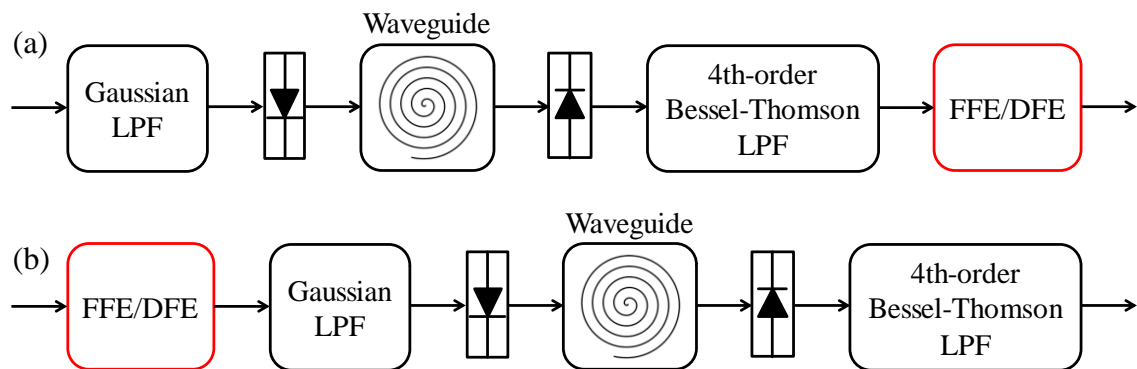
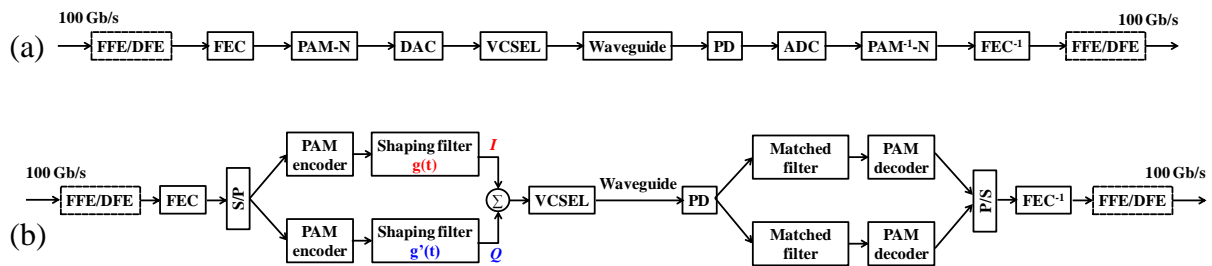


Figure 7-2 Schematic diagrams of the waveguide link configurations: (a) an “Rx-FFE/DFE” link and (b) a “Tx-FFE/DFE” link.

Furthermore, carrierless amplitude and phase modulation (CAP), initially used in communication links over electrical cables, may also be used on short-reach optical interconnects. It allows the use of low-cost transversal filters to generate multilevel and orthogonal pulse shapes without the need for mixers. Therefore, it has attracted particular interest in high-speed optical communications recently. For instance, a CAP-16 system has two channels in-phase (I) and quadrature (Q) compared to a PAM-4 system. Symbols in I or Q channels are generated, and then injected into two orthogonal shaping filters. The combined signal from the I and Q channels is used to drive the VCSEL. On the receiver side, match filters with the corresponding shaping filter are used to recover the I and Q channels. The architectures of both PAM and CAP systems are illustrated in Figure 7-3 while Table 7-1 summaries the system parameters for different modulation schemes considered for use in board-level optical interconnects.

Overall, the combination of appropriate choice of advanced modulation formats, equalisation and FEC can be a promising approach toward 100 Gb/s on-board data transmission in the near future.



DAC/ADC: digital to analogue/analogue to digital conversion; S/P: serial to parallel conversion; P/S: parallel to serial conversion.

Figure 7-3 Schematic diagrams of the transmission systems: (a) PAM-4 and (b) CAP-16 or CAP-64 [11].

Table 7-1 100 Gb/s system parameters for various modulation schemes.

	NRZ	PAM-4	PAM-8	CAP-16	CAP-64
Bit rate (Gb/s)	100	100	100	100	100
Symbol rate (Gbaud)	100	50	33.3	25	16.7
Spectral efficiency (bps/Hz)	1	2	3	4	6

- Wavelength-division Multiplexing (WDM)

In addition to using single wavelength as mentioned above, WDM is believed to be another potential approach to further increase the on-board data rates by using multiple wavelengths over the same polymer waveguide. WDM systems can be categorised into two types, coarse WDM (CWDM) and dense WDM (DWDM). CWDM is one possible way of achieving 100 Gb/s by using 4 wavelengths with each operating at 25 Gb/s. Currently developed VCSELs at 850 nm, 980 nm, 1100 nm, 1300 nm and 1550 nm [12] can be used as the potential sources as it is relatively easy to separate the large wavelength spacing at the receiver end (Figure 7-4).

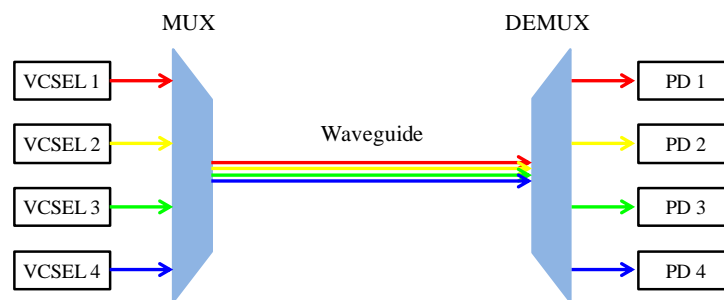


Figure 7-4 System diagram of wavelength-division multiplexing.

In addition, high-speed tunable VCSELs operating at wavelength of around 850 nm with tuning range of 24 nm have been demonstrated in the laboratory enabling the applications of DWDM [13]. Moreover, novel passive devices such as wavelength multiplexers and demultiplexers based on polymer materials are essential to enable the deployment of WDM schemes on board-level optical interconnects. Some preliminary work on the design of a novel two dimensional integrated optics (2DIO) devices has been carried out [14], [15] (Figure 7-5). Further investigation is required for the design, fabrication and characterisation of such 2DIO devices based on multimode polymer waveguides. Overall, the potential to further increase the achievable link capacity by employing WDM schemes to on-board optical links is worth exploring.

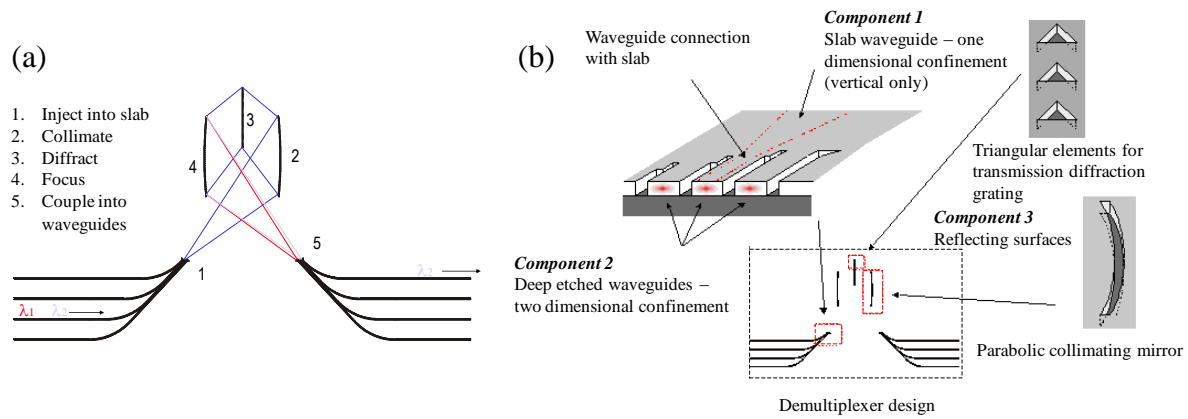


Figure 7-5 2DIO demultiplexer devices (a) device operation and (b) device components [15].

- Spatial Multiplexing

As opposed to using one single waveguide channel, spatial multiplexing is an alternative approach to achieve 100 Gb/s and beyond on-board data transmission by employing multiple parallel links. As illustrated in Figure 7-6(a), individual waveguide layer can be stacked on top of each other to form a multilayer waveguide structure. This structure, in conjunction with VCSEL arrays and PD arrays, can significantly increase the system capacity. However, there are a few challenges for this approach. One issue is that it is difficult to precisely align each stacked layer in both horizontal and vertical directions, and therefore a suitable fabrication process is worth investigating. Even though a number of multilayer optical structures have been demonstrated, most of the reported structures are only stacking optical waveguides without suitable coupling schemes employed to enable the out-of-plane and inter-plane signal transmission [16]. For instance, if 45° mirrors are to use, coupling losses may experience some variation for different layers of waveguide as the coupling efficiencies depend on the vertical distances between the VCSELs/PDs and the mirrors. In addition to the out-of-plane coupling, the design and fabrication of 45° mirrors is crucial to enable the inter-plane coupling for the communications between different layers [Figure 7-6(b) and (c)] [17]. Limited work has been reported to tackle these issues, and hence this area still offers room for innovation.

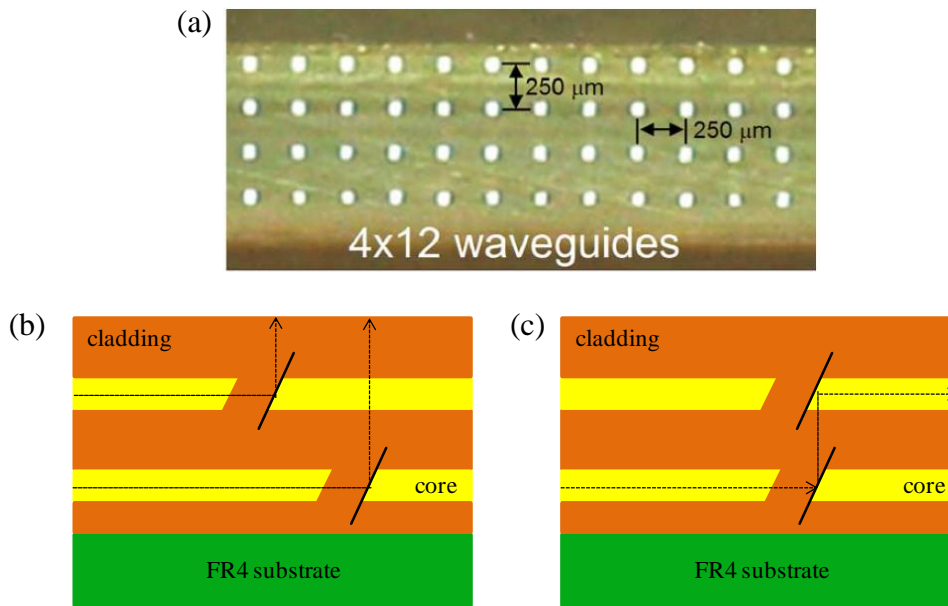


Figure 7-6 (a) Cross-sectional of 2-dimensional 4×12 waveguide array, (b) two-layer out-of-plane coupling configuration and (c) two-layer inter-plane coupling configuration [16], [17].

7.2.5 All-plastic Optical Circuits

Currently, most commercially available optical systems use inorganic lasers, LEDs and PDs. Organic materials can potentially provide an alternative solution due to their lower cost and higher flexibility. In fact, organic electronics has attracted particular interests since polymer-based LEDs were reported by Friend's group in 1990 [18]. Organic light emitting diodes (OLEDs) and organic photodiodes (OPDs) have gradually become mature and ready to use as commercial devices over the past few years. However, most of the OLEDs are used in the lightings and display applications while OPDs are mainly applied in the area of solar cells. Therefore, their applications in optical communications can lead to a very interesting research area. One of the main advantages of OLEDs and OPDs is that they can be readily fabricated on various substrates including polymers using low-cost ink-jet printing fabrication process.

The combination of polymer waveguides, OLEDs and OPDs can provide huge advantages in fabricating all plastic flexible optical integrated systems for future short-reach datacommunication systems. An OLED fabricated directly on a polymer waveguide have been demonstrated as shown in Figure 7-7(a) [19], while Figure 7-7(b) illustrates the proposed concept of fabricating both OLEDs and OPDs on a polymer waveguide substrate

[20]. Currently, the demonstrated transmission speed based on this configuration is in the range of several hundreds of megahertz due to the limited modulation bandwidth of the active devices. In order to further increase the data rates, advanced modulation formats and equalisation techniques discussed in Chapter 6 can be employed. The bandwidth studies of the polymer waveguides presented in this thesis can provide a guideline for future waveguide-based optical links using OLEDs and OPDs. The demonstration of fully integrated all-plastic optical circuits operating at much higher speed (e.g. gigahertz regime) is yet to be addressed.

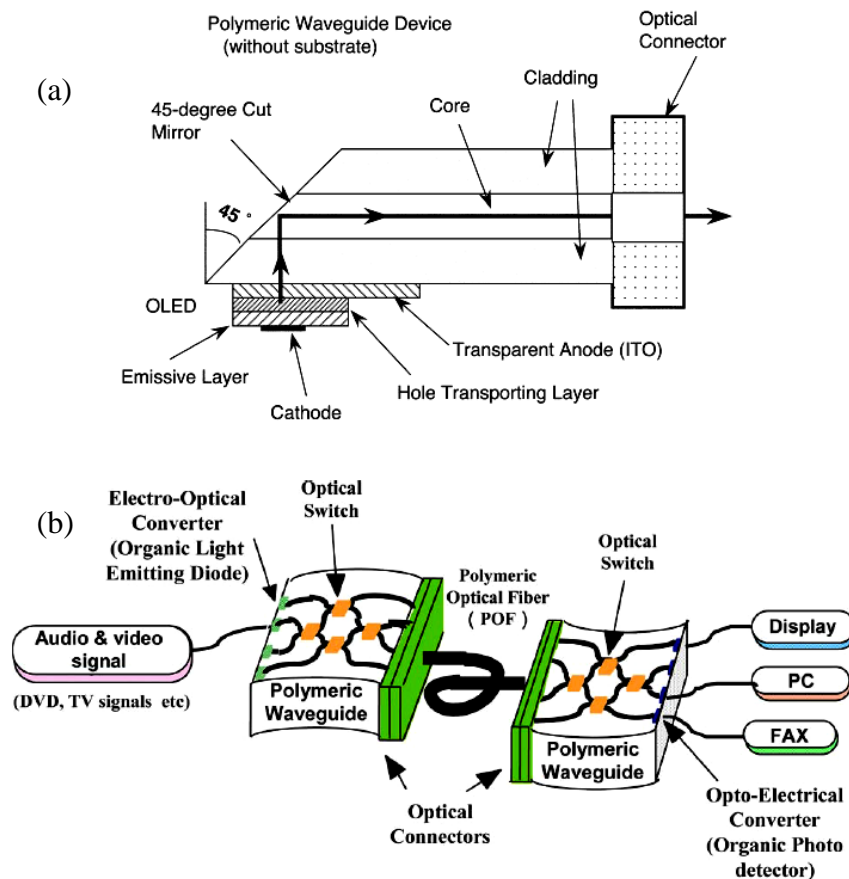


Figure 7-7 (a) An integrated OLED with polymer waveguide and (b) schematic of proposed optical plastic integrated devices: OLED and OPD formed directly on a polymer substrate [19], [20].

To conclude, the work presented in this thesis appears to be a promising candidate to solve the interconnection bandwidth bottleneck for use in future systems. Clearly, this work may be extended into many directions. It is greatly encouraging that some of the future promises mentioned above are being explored by the colleagues at the University of Cambridge as well as other groups at various institutions and industries worldwide. It is

hoped that the deployment of this technology will become a reality for use in real-world applications in the near future.

7.3 References

- [1] E. Griesse, "Reducing EMC Problems Through an Electrical/Optical Interconnection Technology," *IEEE Trans. Electromagn. Compat.*, vol. 41, no. 4, pp. 502–509, 1999.
- [2] A. W. Snyder and J. D. Love, *Optical Waveguide Theory*. London: Chapman & Hall, 1983.
- [3] F. Ladouceur and J. D. Love, *Silica-Based Buried Channel Waveguides and Devices*. London: Chapman & Hall, 1995.
- [4] X. Shen, J. M. Kahn, and M. A. Horowitz, "Compensation for Multimode Fiber Dispersion by Adaptive Optics," *Opt. Lett.*, vol. 30, no. 22, pp. 2985–2987, 2005.
- [5] R. A. Panicker, J. M. Kahn, and S. P. Boyd, "Compensation of Multimode Fiber Dispersion Using Adaptive Optics via Convex Optimization," *J. Light. Technol.*, vol. 26, no. 10, pp. 1295–1303, 2008.
- [6] Q. Sun, J. D. Ingham, R. V. Penty, I. H. White, and D. G. Cunningham, "Twin-Spot Launch for Enhancement of Multimode-Fiber Communication Links," *Conf. Lasers Electro-Optics*, p. CWM6, 2007.
- [7] C. H. Kwok, R. V. Penty, I. H. White, and D. G. Cunningham, "Novel Passive Launch Scheme for Ultimate Bandwidth Improvement of Graded-Index Multimode Fibers," *Opt. Fiber Commun. Conf.*, p. OWA3, 2010.
- [8] L. Geng, S. Lee, K. William, R. V. Penty, I. H. White, and D. G. Cunningham, "Symmetrical 2-D Hermite-Gaussian Square Launch for High Bit Rate Transmission in Multimode Fiber Links," *Opt. Fiber Commun. Conf.*, p. OWJ5, 2011.
- [9] T. Ishigure, K. Shitanda, and Y. Oizumi, "Index-Profile Design for Low-Loss Crossed Multimode Waveguide for Optical Printed Circuit Board," *Opt. Exp.*, vol. 23, no. 17, pp. 22262–22273, 2015.
- [10] J. D. Ingham, R. V. Penty, and I. H. White, "10 Gb/s Transmitter-Based Equalization for Extended-reach Multimode-fiber Datacommunication Links," *Opt. Fiber Commun. Conf.*, p. OTuL4, 2007.
- [11] J. L. Wei, J. D. Ingham, D. G. Cunningham, R. V. Penty, S. Member, and I. H. White, "Performance and Power Dissipation Comparisons Between 28 Gb/s NRZ, PAM, CAP and Communication Applications," *J. Light. Technol.*, vol. 30, no. 20, pp. 3273–3280, 2012.
- [12] M. Cooke, "Short- and Long-Reach of New VCSEL Applications," *Technology focus: Lasers*, 2001. [Online]. Available: [http://www.semiconductor-today.com/features/Semiconductor Today - Feb2011 - VCSELS.pdf](http://www.semiconductor-today.com/features/Semiconductor%20Today%20-%20Feb2011%20-%20VCSELS.pdf).
- [13] A. Larsson, J. S. Gustavsson, Å. Haglund, B. Kögel, J. Bengtsson, P. Westbergh, E. Haglund, and P. P. Baveja, "High-Speed Tunable and Fixed-Wavelength VCSELs for Short-Reach Optical Links and Interconnects," *Proc. SPIE*, vol. 8276, pp. 82760H–1–9, 2012.
- [14] R. P. Thilakumara, R. V. Penty, and I. H. White, "Modeling of Reflection-Transmission Grating Based 2DIO Wavelength Router," *J. Light. Technol.*, vol. 24, no. 9, pp. 3439–3447, 2006.
- [15] C. N. Morgan, I. H. White, R. V. Penty, and S. Yu, "Silica Two-Dimensional Integrated Optics for WDM Datacommunication Applications," *15th Annu. Meet. IEEE Lasers Electro-Optics Soc.*, vol. 1, pp. 291–292, 2002.
- [16] R. Dangel, C. Berger, R. Beyeler, L. Dellmann, M. Gmür, R. Hamelin, F. Horst, T. Lamprecht,

- T. Morf, S. Oggioni, M. Spreafico, and B. J. Offrein, "Polymer-Waveguide-Based Board-Level Optical Interconnect Technology for Datacom Applications," *IEEE Trans. Adv. Packag.*, vol. 31, no. 4, pp. 759–767, 2008.
- [17] N. Hendrickx, "Multilayer Optical Interconnections Integrated on a Printed Circuit Board," Ghent University, 2009.
- [18] J. H. Burroughes, D. D. C. Bradley, A. R. Brown, R. M. Marks, K. Mackay, R. H. Friend, P. L. Burns, and A. B. Holmes, "Light Emitting Diodes Based on Conjugated Polymers," *Nature*, vol. 347, no. 6293, pp. 539–541, 1990.
- [19] Y. Ohmoria, M. Hikita, H. Kajii, T. Tsukagawa, K. Yoshino, M. Ozaki, A. Fuji, S. Tomaru, S. Imamura, H. Takenaka, J. Kobayashi, and F. Yamamoto, "Organic Electroluminescent Diodes as a Light Source for Polymeric Waveguides - Toward Organic Integrated Optical Devices," *Thin Solid Films*, vol. 393, pp. 267–272, 2001.
- [20] Y. Ohmori and H. Kajii, "Organic Devices for Integrated Photonics," *Proc. IEEE*, vol. 97, no. 9, pp. 1627–1636, 2009.

